Testing and Modeling Mechanical Properties of Ex Vivo Trabecular Bone

by

Luisa A. Meyer

A dissertation submitted in partial fulfillment of

the requirements for the degree of

Doctor of Philosophy

(Mechanical Engineering)

at the

UNIVERSITY OF WISCONSIN – MADISON

2016

Date of final oral examination: 05/02/2016

This dissertation is approved by the following members of the Final Oral Committee:
    Heidi-Lynn Ploeg, Associate Professor, Department of Mechanical Engineering
    Melih Eriten, Assistant Professor, Department of Mechanical Engineering
    Karen E. Hansen, Associate Professor, School of Medicine and Public Health
    Tim Osswald, Professor, Department of Mechanical Engineering
    Krishnan Suresh, Associate Professor, Department of Mechanical Engineering

ProQuest Number: 10110975

ProQuest 10110975

Abstract

An osteoporotic fracture occurs approximately every three seconds. Worldwide, this sums to nearly 9 million annual fractures caused by osteoporosis—a systemic, degenerative skeletal disorder that is characterized by low bone mass and increased bone tissue fragility. Although the individual and economic burden of osteoporosis nearly outweighs that of most cancers and many chronic illnesses, the existing methods for treatment are insufficient and many who are at risk remain undiagnosed. To develop improved osteoporosis treatments, prevent osteoporotic fractures, and promote bone health throughout the aging process, it is imperative to understand bone biomechanical behavior and the factors contributing to bone mechanotransduction and adaptation. Consequently, the first objective for the presented research was to characterize the effects and interactions of mechanical stimulus and biochemical signaling activity on the modeling and remodeling response of bovine and human trabecular bone through the use of *ex vivo* organ culture. The second objective for the research was to simulate the mechanical behavior and dynamic remodeling response of bone tissue through the use of finite element analyses and analytical cell population models. Collectively, the presented research illustrated that bone modeling and remodeling can be affected by the amount and type of applied mechanical stimulus and biochemical exposure. In addition, the research showed that, despite current limitations, simulation and prediction of bone response to applied stimulus is feasible with additional development of existing models.

Acknowledgements

~

First and foremost, I would like to sincerely thank Prof. Heidi-Lynn Ploeg for initiating my interest in bone and joint biomechanics and for her patience, direction, and assistance in my graduate schoolwork. I genuinely appreciate the unique learning environment I was provided under her guidance that allowed me the freedom to develop my own research goals, conduct experiments, and to achieve intellectual milestones. The independence and confidence I gained through my graduate journey working with Prof. Ploeg is truly invaluable.

I would also like to thank members of my thesis committee, Prof. Melih Eriten, Prof. Karen Hansen, Prof. Tim Osswald, and Prof. Krishnan Suresh for their input, and supervision. My collaborators, Dr. Juan Vivanco, Dr. Michael Johnson, Dalton Hess, Dr. Robert Blank, Prof. Yvan Petit, Annie Levasseur, Prof. Diane Cullen, Scott Hetzel, Dr. Matthew Squire, Nick Keuler, and Dr. Everett Smith have been instrumental to my success as a graduate student and their assistance and support are greatly appreciated. I would like to thank those previously and presently in the Bone and Joint Biomechanics and Neuromuscular Biomechanics Labs for enhancing my experience as a graduate student through both technical discussions and recreational activities.

I would also be lost without those who have taken time to provide me with advice and guidance during my graduate schoolwork and as such I am grateful to Prof. Thomas Crenshaw, Dr. Deborah Gilbert, Dr. Monica Usrey, Prof. Robert Hamers, and Mark Zager for their mentorship, guidance, and invaluable words of wisdom.

Finally, my greatest gift has truly been that of my family and friends, who have supported me throughout my journey in graduate school and encouraged me to dream big and pursue my goals despite the challenges. I am infinitely grateful for my colleagues and friends, Caitlyn Collins, Scott Sokn, and Carrie Francis, who not only provided me with valuable technical feedback on my work, but also ensured that I maintained sanity throughout graduate school and even managed to make my experience enjoyable. I am thankful for my lifelong friend, Katie, who provided me with such resolute reassurance and positivity that, without, I would not have persevered. I owe innumerous thanks to my parents, Scott and Morelia, who fostered my interest in engineering and passion for learning and have supported me in all my endeavors no matter how crazy. I am thankful for my brother, Scott Jr., for being a constant source of cheer and assurance regardless of the circumstances. I am also grateful for Gail and Michael Anderson for their benevolence and affirmation through difficult times. Finally, and most especially, I would like to thank my partner, Steven, for his unwavering love, support, encouragement, and understanding on both the good days and the bad.

Thank you, all.

Table of Contents

List of Figures

List of Tables

Chapter 1

1. Introduction

1.1 Background

In the United States, more than 50% of all reported injuries are musculoskeletal [1]. It is estimated that an osteoporotic fracture occurs every 3 seconds which adds to 8.9 million fractures annually worldwide [2]. Osteoporosis is a debilitating health condition in which bone mineral density decreases. Reduction in the bone mineral density leads to deterioration of bone's microstructure which in turn leads to the decline in skeletal resilience and increased likelihood of bone fracture [3]. Currently, about 55% of adults over the age of 50 years are affected with osteoporosis [4]. Of the aforementioned 55%, about 50% of the women and 25% of the men will experience some bone fracture in their remaining lifetime [4]. Individuals who suffer bone fracture as a result of osteoporosis during old age are have a much higher risk of premature mortality and a three to four fold higher risk for subsequent fractures [5,6]. Osteoporosis related fractures accounted for about $19 billion in medical expenditures in 2005 and is predicted to escalate to $25 billion by the year 2025 [6]. Although osteoporosis treatments exist, there is no known cure or infallible prevention scheme.

Understanding bone biomechanical behavior is imperative for developing methods for promoting bone health throughout the aging process, and thus averting fractures and improving treatment options. Many researchers have recognized the disparity in knowledge regarding bone mechanics and have thus put forth effort to characterize the material and mechanical properties of bone. Although many studies have been conducted that investigate relevant parameters related to material and mechanical properties, much is still unknown. One potential limitation is the lack of research funding. At present, less than 2% of the National Institute of Health budget is dedicated to musculoskeletal research despite the expected increases in musculoskeletal conditions over the next two decades [1].

The prediction of trabecular bone's biomechanical (biological and mechanical) behavior has long eluded researchers and orthopaedic specialists in part due to bone's non-homogeneity and its anisotropic, nonlinear biomechanical behavior [8]. Although many studies have been dedicated to studying this complex biological material, few have examined the biomechanical properties of live bone at the tissue level. Understanding mechanics and modeling/remodeling mechanisms of live bone at the tissue level would greatly aid in developing methods for preventing and treating bone diseases. Finite Element Analysis (FEA) used in conjunction with live bone tissue experimentation would yield both morphological and material property information about bone on the micro and macro level, in addition gaining information about remodeling in response to various stimuli. Knowledge of the modeling and remodeling mechanisms, specifically understanding how to predict modeling and remodeling, would contribute greatly to the development of improved osteopenia and osteoporosis treatments and provide insight on prevention strategies. In addition, bone response predictive abilities would aid in the design of patient specific implants, and improved surgical success.

Chapter 2

2. Summary of Research

2.1 Motivation and Goals

The goal of this research is to improve understanding of the underlying mechanics and mechanisms of bone turnover in order to inform methods for predicting the time-dependent macro and micro level remodeling response of human trabecular bone tissue mechanical and biochemical stimuli. Specifically, the project aim is to observe how human bone tissue responds to mechanical and biochemical stimuli and quantify this response by documenting its changes in mechanical, biochemical, and morphological properties *ex vivo*. Upon completion of the *ex vivo* studies, FEA and analytical modeling of the bone can be compared to the results from the *ex vivo* study.

2.2 Objectives and Specific Aims

The overall objectives for this research are to:

1. Assess and characterize bone tissue adaptation through the use of a controlled *ex vivo* testing environment

2. Model bone structural, material, and biochemical properties of the bulk tissue and of its constituents to determine multi-scale tissue contributions to bulk tissue mechanical properties and predict bone tissue response and adaptation to applied stimulus.

The specific aims designed to address **Objective 1** are as follows:

1.1: Measure and characterize the mechanical properties and the change in mechanical properties of *ex vivo* trabecular bone tissue in response to mechanical and biochemical stimuli.

1.2: Measure and characterize the biochemical response of *ex vivo* trabecular bone tissue to mechanical and biochemical stimuli.

1.3: Assess the morphological properties of *ex vivo* trabecular bone tissue.

The specific aims designed to address **Objective 2** are as follows:

2.1: Determine local stresses and strains of human trabecular bone tissue resulting from applied mechanical load using a finite element (FE) model that reflects the structural and mechanical properties of human trabecular bone measured *ex vivo.*

2.2: Simulate *ex vivo* bone tissue adaptation to mechanical and biochemical stimulus by developing an algorithm that models biochemical and cellular changes of human trabecular bone tissue.

2.3 Document Structure

This document includes 11 chapters and an appendix. Chapter One presents the motivation for the research in trabecular bone mechanics. Chapter Two outlines the objectives for this particular research in understanding trabecular bone mechanics. Chapter Three provides a literature review of existing knowledge of bone composition and behavior and serves as a concise introduction to the field of bone tissue research. The chapter also includes brief summaries of various methods that can be used to assess trabecular bone tissue structure, mechanics, and behavior.

Chapter Four describes the use of a bone loading and bioreactor system to observe the *ex vivo* response of bovine trabecular tissue to mechanical loading and pharmacological introduction of biochemical factors. Portions of this work were presented at the 2012 and 2013 American Society for Bone and Mineral Research annual meetings and the World Congress of Biomechanics in 2014. The full study was published in Bone in February of 2016 [9].

Chapter Five describes the use of a bone loading and bioreactor system to observe the *ex vivo* response of human trabecular bone tissue to mechanical loading and pharmacological inhibition of biochemical factors. A portion of this work was presented at the American Society for Bone and Mineral Research annual meeting in October of 2015 and at the Orthopedic Research Society annual meeting in March of 2016.

Chapter Six describes an analysis of the morphological properties of human trabecular bone tissue. Specifically, the research aims to elucidate the relationship between trabecular bone mechanical properties and bone trabecular structure and biochemistry. A portion of this work will be presented at the European Society of Biomechanics annual meeting in July of 2016.

Chapter Seven details the use of finite element methods to assess the macro-, micro-, and nano-level mechanical properties of injection molded bioceramic scaffolds sintered at multiple temperatures. The purpose of this project was to determine if the results of experimental testing could be reproduced using finite element analyses. A portion of this work was presented at the 2015 annual meeting for Computer Methods in Biomechanics and Biomedical Engineering.

Chapter Eight presents the use of finite element methods to model human trabecular tissue. The developed model is compared to results from the *ex vivo* study outlined in Chapter Five. The purpose of this project is to set the ground work for future development of micro-level finite element analyses that investigate trabecular strain in order to predict areas of bone remodeling.

Chapter Nine presents an algorithm developed for the purpose of simulating human bone modeling and remodeling. This work incorporates an empirical approach to bone cellular activity and biochemistry to predict human bone turnover in response to a mechanical stimulus. A portion of this work was presented at the annual conference for Computer Methods in Biomechanics and Biomedical Engineering in 2015.

Chapter Ten describes the adaptation of viscoelastic models to mathematically approximate the mechanical behavior of human trabecular bone tissue. This developed model is compared to the results

from the *ex vivo* study presented in <u>Chapter Five</u>. The purpose of this project is to supplement the development of a predictive model for simulating human bone tissue.

Finally, <u>Chapter Eleven</u> outlines the overall conclusions from the research projects presented in the preceding chapters and offers perspective on areas where future research can and should be conducted.

Chapter 3

3. Literature Review

3.1 Bone Composition and Structure

The function of bone includes mechanical support of the biological system, protection of the vital organs, facilitation of movement, mineral storage, calcium homeostasis, and blood cell formation. There are two types of bone—cortical (also called compact) and trabecular (also called cancellous) bone which are distinguished by their location in the skeletal system, and by material and mechanical properties [10]. Cortical bone forms the outer layer of all boney structures [10]. Trabecular bone, which accounts for approximately 80% of bone surface area in the human body but only about 20% of total bone mass, generally fills the interior of a boney structure and tends to be concentrated in areas frequently subjected to compressive forces [11,12]. The structure of bone is shown in Figure 3.1. Trabecular bone has high porosity, ranging anywhere from 75-95% [12]. Cortical bone has little porosity, ranging from 5-10% [12]. Each has a matrix of both a mineral and an organic phase. The mineral phase is composed of hydroxyapatite, calcium, and small amounts of sodium, magnesium, and fluoride [13]. The organic matrix contains type I collagen, non-collagenous proteins, proteoglycans, and numerous growth factors [14].
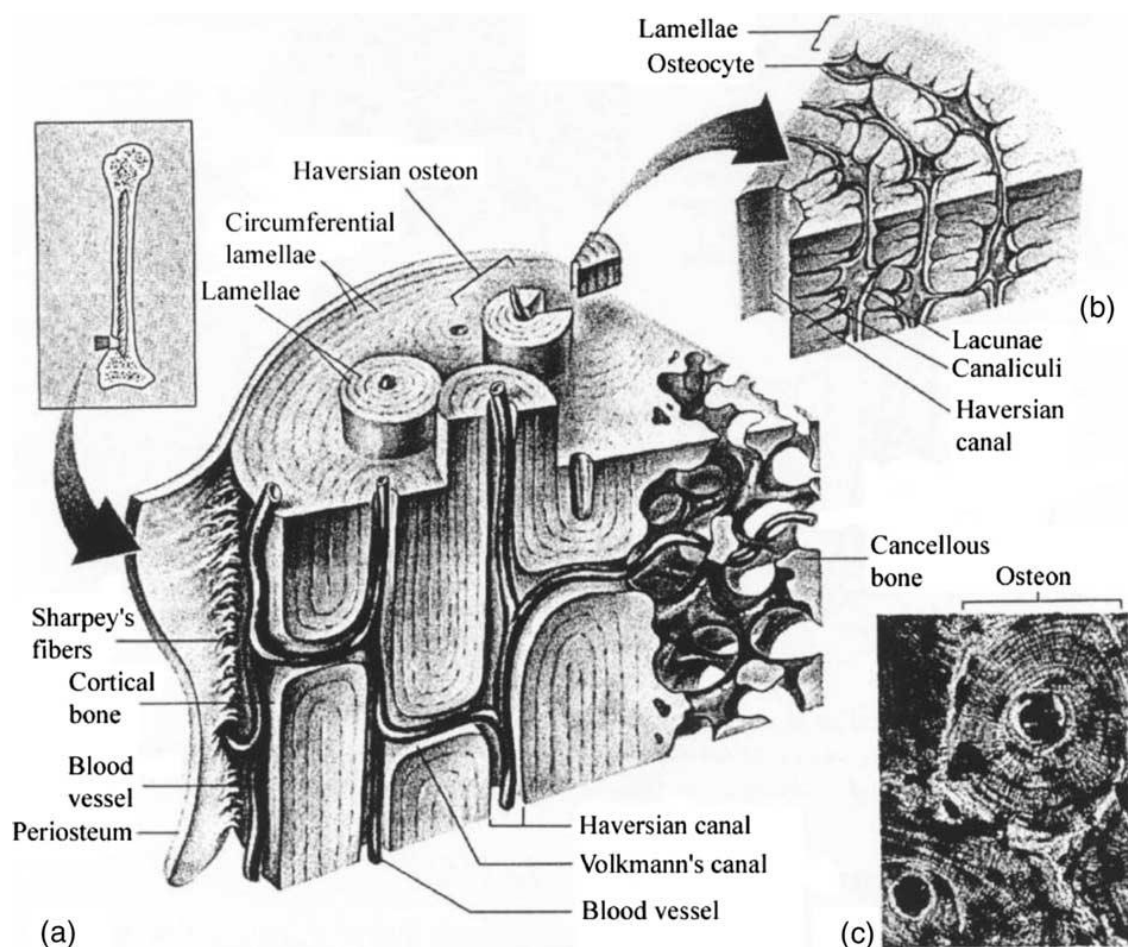
Figure 3.1 - Structure and location of trabecular and cortical bone[15]

There are four bone cell types: osteoclasts, osteoblasts, lining cells and osteocytes [16]. Osteoclasts are multinucleated bone-resorption cells. Osteoclasts resorb existing bone, leaving resorption cavities where bone had previously resided [16]. Osteoblasts are bone-forming cells. These develop from mesenchymal stem cells that transform into osteoblasts. Bone-lining cells are quiescent osteoblast cells. Osteoblasts line the resorption cavities and produce osteoid (collagenous matrix) in the wake of the osteoclasts' resorption [16]. Deactivated osteoblasts become osteocytes which make up 95% of all bone cells. [16]. Bone cells communicate with via gap junctions which allow them to respond and adapt to biochemical and mechanical stimuli [17].

3.2 Bone Mechanical and Material Properties

Bone forms the vertebrate skeleton and provides structural support for gravitational resistance and ambulatory endeavors. For bipedal mammals, such as humans, compressive loads are experienced in the lower limbs during walking, running and jumping. These physiological loads typically occur at a frequency of 2-5 Hz, at a magnitude of two to ten times body weight which corresponds to peak bone strain that ranges from -1,000 to -5,000 $\mu\varepsilon$ [18–20]. In addition to compressive loading, long bones are also subjected to bending due to skeletal architecture and moments produced during physical activities [14,21]. Depending on whether bone is axial or appendicular, it can also be subjected to torsion or combined modes of loading but is most resilient in compression and bending [22,23].

In addition to being a heterogeneous composite, like other biological connective tissue, bone is also viscoelastic which implies its load response is both rate and temperature dependent [23]. Mechanostat Theory, developed by Frost, postulates that bone adaptation is related to the stimulus within a certain range (Figure 3.2) [24–26]. Excessive or insufficient loading outside of this ideal range results in either bone fracture (overuse) or resorption (disuse) [25]. The stimulus intensity is considered a function of the magnitude of a load on the bone, the frequency of the load application, and the total number of loading cycles [27,28].
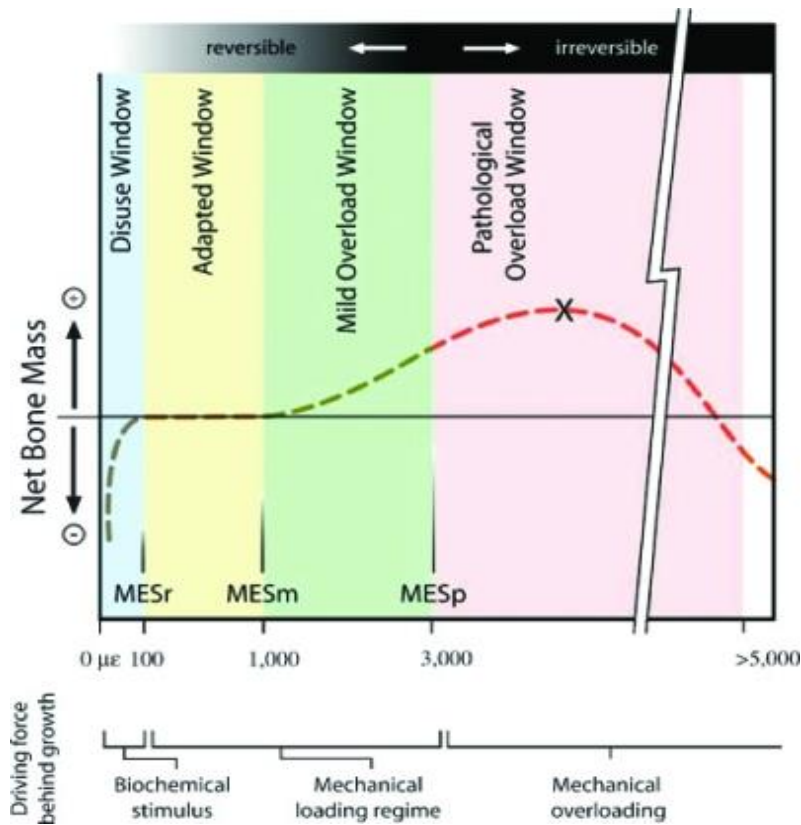
Figure 3.2 - Usage window of mechanical stimulation of bone according to Mechanostat Theory, where MESr, MESm, and MESp correspond to the remodeling, modeling, and pathological mechanical thresholds. Biochemical stimuli are required to initiate and perpetuate adaptation below the MESr threshold. Between MESr and MESm, the dominant driving force is mechanical loading. Above the MESp threshold, irreversible damage can occur from the mechanical force, whereas above the threshold, the mechanical loading is reversible (adapted from [29])**.**

3.3 Bone Modeling and Remodeling

Bone optimizes its stiffness to reduce fracture risk while maintaining minimal bone mass through modeling and remodeling [30,31]. Remodeling of bone is site specific and hypothesized to be locally mediated [32]. Between 30-40% of bone remodeling is site-specific for replacing bone which has been mechanically compromised due to microcracks from fatigue or impact [11]. Modeling forms bones through activation of osteoblasts; whereas, remodeling activates osteoclasts and osteoblasts in a sequence that reforms bone [33,34]. The remodeling process consists of six stages: activation, resorption, reversal, formation, mineralization, and quiescence. Osteoclasts begin to form resorption cavities in the bone

causing activated osteoblasts to follow in their wake, filling the cavities with osteoid and organic matrix material (Figure 3.3) [33,35]. After roughly 30 days, mineralization begins to occur and calcium phosphate and calcium carbonate in the form of hydroxyapatite and other minerals are deposited in the osteoid. Finally, paracrine signaling molecules deactivate the osteoblasts which become osteocytes embedded within the bone microstructure [35,36]. The whole process can take 100 to 400 days. The remodeled bone section is maintained by the osteocytes and the lining cells return to a quiescent stage until activated by another stimulus to start the remodeling process again.
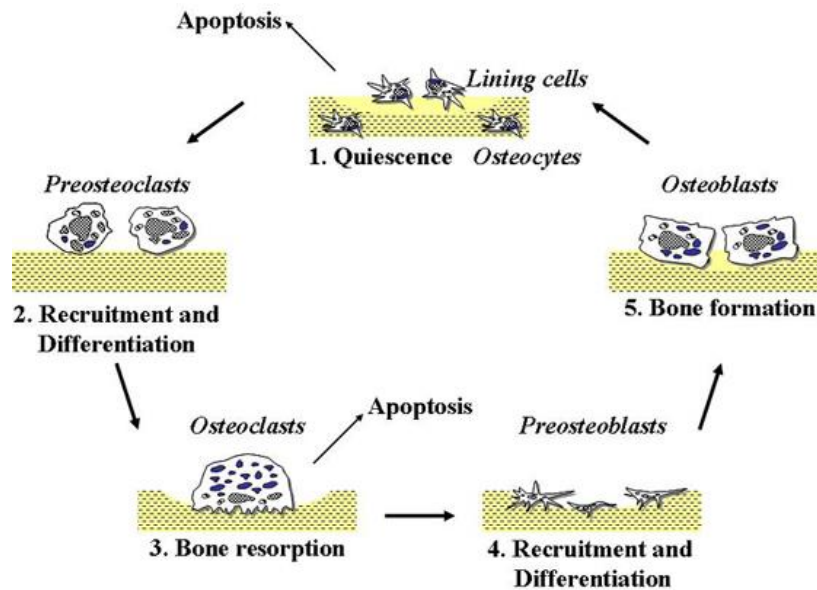
Figure 3.3 - Stages of bone remodeling, excluding mineralization[36]

3.4 Methods for Directly Evaluating Bone Mechanics

Mechanical and material properties of bone can be determined through experimentation with destructive testing of cadaveric tissue or by testing bone *in vitro*, *in vivo*, and *ex vivo*. Cadaveric testing, while generally the easiest to setup and conduct, is not appropriate for understanding the biomechanics of living tissue [37]. In addition to the tissue lacking the active modeling/remodeling response, cadaveric tissue can be more brittle compared to living tissue due to lower water content, depending on the tissue preparation. More appropriately, testing can be done on living bone cells or living tissue. On the cellular

level, *in vitro*, it is possible to examine bone's response to load and biochemical stimuli; however, the observed response is typically modeling and not remodeling. In addition, cultured bone cells are typically not as differentiated as naturally occurring tissue so little to no information can be gathered regarding the mechanical or material properties of the bone [18]. On the tissue level, it is possible to conduct testing *in vivo* where the tissue remains in its original physiological environment. Methods can include strain gage implantation or use of external fixators to determine bone displacement in response to load both quasi-statically and dynamically [38–40]. Such methods are extremely invasive, typically only capable of providing information about the bone surface, and are prone to placement error and interference from nearby soft tissues [41–44]. Finally, it is possible to test tissue *ex vivo*—outside the body but in a simulated physiological environment typically with bioreactor systems [45,46]. The use of bioreactors further allows for parallel use of mechanical testing apparati. Specifically, use of a uniaxial compression loading system in conjunction with bone tissue bioreactors allows for simultaneous application of simulated physiological loads and treatment with biochemical factors [46–48]. Remodeling response can then be tracked by monitoring biochemical, mechanical properties and morphological adaptations with time [46–48].

3.5 Imaging Methods for Evaluating Bone

The most traditional methods for non-invasively assessing bone structure include x-rays, dual photon energy x-ray absorptiometry (DXA), and computed tomography (CT) [49,50]. Typically, these methods are used to measure bone mineral density (BMD) and infer bone mechanical integrity from those measurements to diagnose or predict structural bone diseases and disorders, including osteoporosis and osteopenia [50]. Though DXA is a low-dose (< 0.5 mSv) technique and scanners are readily available in most clinics and used for many research applications, there are multiple issues associated with using DXA scans alone to estimate bone mechanical properties [51]. The final output of a DXA scan is a one-dimensional set of body composition values that have been converted from a projected two dimensional

image of the scanned object. Scans from DXA screening are affected by multiple factors including additional mineral content in the body resulting from various pathologies including kidney disease, aortic calcification, and degenerative spinal changes [49,51]. Furthermore, depending on the patient population, DXA results are interpreted differently due to known variances in fracture risk at higher BMD values [52].

Use of CT scans to image bone allows for three-dimensional (3D) evaluation of the tissue [53–57]. The data provided by CT scanning is a stack of high resolution image slices of the scanned object. The density of the voxels (three dimensional pixels) in each slice can be correlated to the density of the scanned tissue [56,57]. This is a distinct advantage over DXA scanning since it allows for enhanced assessment of bone structure and its material properties. To generate CT images, a higher radiation dose is required (~8 mSv for abdominal scans) and can potentially be more harmful to the scanned recipient [58]. Additionally, clinical CT cannot provide sufficiently high resolution to accommodate micro-level evaluation of bone structure since voxel sizes are operating in the range of a few millimeters [54,57,59].

Peripheral quantitative CT (pQCT) scans are an alternative method for obtaining 3D images of appendicular bone tissue. Resolutions of 17-800 µm can be attained depending on the scanner and allow for detailed images of bone microstructure [60]. Scanning with pQCT allows for lower radiation doses (1-5 µSv), although higher resolutions require higher doses [58]. Use of micro-CT (µCT) scans is also a possible method for evaluating bone tissue in high resolution (4-100 µm) [60,61]. Although µCT scanning can easily capture micro-level bone structures including trabecular dimensions and is well-suited for *ex vivo* purposes, it has a few considerable limitations. Scanning on the micro-level is limiting due to the amount of radiation necessary to achieve such high resolutions, the small bore size of available scanners, and the necessary computing power to produce images of macro-scale skeletal portions [54,57,58].

3.6 Modeling Bone Structure and Mechanics

Finite element analysis (FEA) or the finite element method (FEM) is a computational tool for determining approximate solutions to complex boundary value problems [62]. Applications for FEA are varied including mechanical and thermal calculations for large structures, automotive design, and biological systems.

In the late 1980s and early 1990s, orthopaedic surgeons equipped with improved medical imaging technology—namely dual-energy x-ray absorptiometry (DEXA)—were finding that hip replacement surgeries were failing or requiring revisions much earlier than anticipated due to bone resorption at the implantation site [63,64]. To address this problem, van Rietbergen *et al.*, investigated the comparative mechanical properties of femoral bone tissue and manufactured total hip stems [65]. This assessment was conducted by using CT scans of canine femurs to generate a finite element (FE) model with which to simulate body forces on an implanted femoral head. The FEM was implemented in conjunction with a strain based (assumed normal strain as only stimulus) remodeling algorithm based on Mechanostat theory (shown in Figure 3.2). The study concluded that large differences between bone and implant stiffness resulted in extreme bone resorption due to "stress shielding", and suggested that more compliant implants be used clinically [65]. Unfortunately, the study was limited by the remodeling algorithm which considered strain as the sole remodeling stimulus, suboptimal mesh quality, and lack of microlevel bone mechanics [65].

More than a decade later, researchers are still attempting to quantify bone mechanics and characterize bone remodeling. Various methods have included imaging based methods which implement DEXA, clinical CT, peripheral computed tomography (pQCT), and micro computed tomography (µCT) to determine approximate bone stiffness. Clinical CT based FE methods are dependent on empirical relationships between bone mineral density to mechanical properties. [66]. Others have developed

methods for incorporating traditional FE meshing with voxel-based methods (Figure 3.4) to both
accommodate minute changes in geometry in addition to reducing computational time [67]

A   **B**
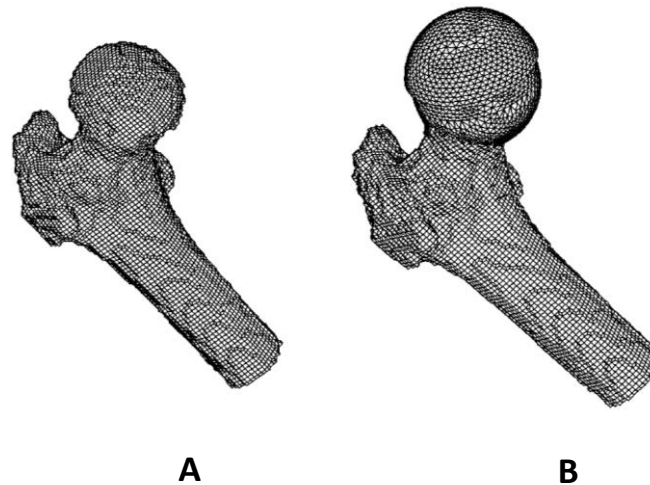
Figure 3.4 - A) Voxel-based of femoral head B) Mesh of femoral head using quadratic tetrahedral elements. Figure adapted from Schmitt *et al.* [67]

Crawford *et al.* compared bone mineral density (as determined from DXA and QCT scans) strength prediction methods and FEM strength prediction using voxel-based meshes [66]. The individual compressive strengths of pQCT scanned vertebral samples were estimated using voxel-based FEM and densitometric data from the scans. To validate the computational results, the vertebrae were tested until failure in compression. It was determined that the voxel-based FE model provided superior estimates of each specimen's compressive strength compared to estimates based on bone density alone [66]. Similarly, in 2008, van Rietbergen *et al.* found that FEA was superior than densitometric methods in predicting the location and magnitude of failure-inducing loads in wrists of postmenopausal women [68]. Voxel-based FE models were generated from pQCT images of wrists prior to fracture and used to predict the location and magnitude of the failure-inducing load [68].

Given that CT-based mesh FE models provide improved estimation of bone strength (non-destructively) over traditional bone densitometric methods, researchers have attempted to expand the use of FEA to not just estimating mechanical properties but also to predict areas of bone remodeling. Kotha and Müller *et al.* predicted location specific strain and resulting bone formation in rat ulnas using FEM. Strain results from the FEA were validated with *in vivo* mechanical data from strain-gaged rat ulnas and bone formation was determined from histological analysis of a sacrificed subset of the tested subjects [69]. The researchers found that areas determined to be subjected to higher compressive strain in the FE model highly correlated with a greater bone formation aligned with the bone axis as determined from histology [69].

As an alternative to FEA, it is possible to describe bone mechanical properties by determining analytical and semi-analytical models for the micromechanical properties and interactions of bone tissue using multi-scale continuum mechanics [70–72]. These models account for the hierarchical structure of bone since it is based on the relative volumes of various bone constituents and their individual mechanical properties and interactions. A variation on these continuum mechanics approaches allows for changes in the volume fractions of bone constituents (namely bone cell populations) and thus prediction of bulk bone volume evolution with time [70,71]. Scheiner *et al.* developed mathematical models to describe the activation, deactivation, differentiation, necrosis rates of osteoblasts, osteoclasts, osteocytes, and other biological factors integral to bone modeling and remodeling [71]. Based on empirical relationships and experimental data, they generated a system of mathematical relationships that altogether describe the mechano- and biological regulation of bone remodeling. The researchers concluded, however, that the model requires additional factors to completely and accurately describe the major signaling pathways between bone cell types and the mechanisms they employ to sense mechanical stimulus [71]. While the exact factors were not identified, the researchers did continue to add that their use of strain energy density (SED) is likely not completely representative of the mechanical stimulus interaction in bone's anabolic and catabolic system since both of their analytical models for these systems implement the same SED

variable. In addition, their model is purely based on strain thresholds from Mechanostat theory and does not predict bone's fatigue response such as in the case of stress fractures [71].

Chapter 4

4. Exposure to Big Endothelin-1 in Bovine Sternal Cores Mimics Mechanical Loading

 Additional document authors are MG Johnson[1], DM Cullen[2], JF Vivanco[3], RD Blank[4,5], H-L Ploeg[6], EL Smith[7]

[1]Department of Medicine, University of Wisconsin – Madison, [2]Department of Biomedical Sciences, Creighton University, [3]Facultad de Ingeniería y Ciencias, Universidad Adolfo Ibáñez-Chile, [4]Department of Medicine, Medical College of Wisconsin, [5]Department of Endocrinology, The Clement J. Zablocki VA Medical Center, Milwaukee, WI, [6]Department of Mechanical Engineering, University of Wisconsin – Madison, [7]Department of Population Health Sciences, University of Wisconsin-Madison,

4.1 Abstract

Increased bone formation resulting from mechanical loading is well documented; however, the interactions of the mechanotransduction pathways are less well understood. Endothelin-1, a ubiquitous autocrine/paracrine signaling molecule promotes osteogenesis in metastatic disease. In the present study, it was hypothesized that exposure to big endothelin-1 (big ET1) and/or mechanical loading would promote osteogenesis in ex vivo trabecular bone cores. In a 2×2 factorial trial of daily mechanical loading (-2000 $\mu\epsilon$, 120 cycles daily, "jump" wave-form) and big ET1 (25 ng/mL), 48 bovine sternal trabecular bone cores were maintained in bioreactor chambers for 23 days. The bone cores' response to the treatment stimuli was assessed with percent change in core apparent elastic modulus (E_{app}), static and dynamic histomorphometry, and prostaglandin E2 (PGE2) secretion. Two-way ANOVA with a post hoc Fisher's LSD test found no significant treatment effects on E_{app} (p=0.25 and 0.51 for load and big ET1, respectively). The E_{app} in the "no load + big ET1" (CE, 13±12.2%, p=0.56), "load + no big ET1" (LC, 17±3.9%, p=0.14) and "load + big ET1" (LE, 19±4.2%, p=0.13) treatment groups were not statistically

different than the control group (CC, 3.3%±8.6%). Mineralizing surface (MS/BS), mineral apposition (MAR) and bone formation rates (BFR/BS) were significantly greater in LE than CC (p=0.037, 0.0040 and 0.019, respectively). While the histological bone formation markers in LC trended to be greater than CC (p=0.055, 0.11 and 0.074, respectively) there was no difference between CE and CC (p=0.61, 0.50 and 0.72, respectively). Cores in LE and LC had more than 50% greater MS/BS (p=0.037, p=0.055 respectively) and MAR (p=0.0040, p=0.11 respectively) than CC. The BFR/BS was more than two times greater in LE (p=0.019) and LC (p=0.074) than CC. The PGE2 levels were elevated at 8 days post-osteotomy in all groups and the treatment groups remained elevated compared to the CC group on days 15, 19 and 23. The data suggest that combined exposure to big ET1 and mechanical loading results in increased osteogenesis as measured in biomechanical, histomorphometric and biochemical responses.

4.2 Introduction

Mechanical loading is a well-known stimulus in the process of bone modeling, remodeling and homeostasis; however, the interactions of the mechanotransduction pathways are less well understood [19,73–77]. Frost suggested that bone has an internal mechanical set point that controls bone's response to mechanical stimuli that he termed the mechanostat. He postulated the existence of a strain set point; with ambient strains below it eliciting bone resorption and ambient strains above it eliciting bone formation [78,79]. Studies by the authors and others on ex vivo cultured trabecular bone cores exposed to mechanical bulk strains of -2000 to -4000 $\mu\epsilon$ found, in comparison to controls, increased percent change in apparent elastic modulus (E_{app}), histological and biological markers of bone formation, demonstrating that bone's response to load can be recapitulated in an organ culture sys-tem [46,48,80–83]. Ex vivo testing provides a controlled environment, without systemic effects, to investigate mechanotransduction in live bone.

Bone modeling and remodeling are affected by genetic factors in addition to mechanical stimulus. The discovery that low-density lipoprotein receptor-related protein 5 (LRP5) gene mutations alter skeletal

mass provided a direct demonstration that skeletal mass is under genetic control. These findings demonstrate that the WNT signaling pathway occupies a central role in regulating mechanotransduction in bone [84–87]. In particular, the WNT inhibitor sclerostin (SOST) is expressed by mature osteocytes, and its expression is inhibited in response to mechanical loading [88]. In addition to the WNT pathway, mechanotransduction is also modulated by prostaglandins, parathyroid hormone (PTH) and a variety of identified and unidentified molecules (reviewed in [87,89,90]). If any of these signaling pathways are up- or down-regulated, bone formation and resorption are affected. Increased levels of prostaglandin E2 (PGE2) and PTH each decrease SOST gene expression [91,92].

Previously, we demonstrated that big endothelin-1 (big ET1) increased osteoblast mineralization in vitro and changed the expression of multiple miRNA known or hypothesized to affect expression of proteins that affect bone physiology, including SOST [93]. These results showed that big ET1 regulated SOST in a post-transcriptional manner [93].

A segment of mouse chromosome 4 harbors a gene or genes that modulate the magnitude of the bone modeling response to experimental loading [94]. We identified endothelin converting enzyme 1 (Ece1) as a candidate gene within the quantitative trait loci bmd7 on mouse chromosome 4 which is responsible for 40% of the variation in bone size, strength and density between the recombinant congenic mice strains HCB8 and HCB23 [95–97].

The purpose of this study was to investigate the biomechanical, histomorphometric and biochemical responses of ex vivo cultured bovine trabecular bone cores to exposure to big ET1 in conjunction with regular mechanical loading. The authors have demonstrated in previous studies that big ET1 added to cell culture increased osteogenesis [93]; however, it is yet to be shown that the cell culture result translates to a similar finding in trabecular bone organ culture. In the current study it was hypothesized that exposure to big ET1 and/or mechanical loading would promote osteogenesis in bovine trabecular bone organ culture.

4.3 Materials and Methods

In a 2×2 factorial trial of big ET1 (25 ng/mL) and daily mechanical loading (-2000 µε, 120 cycles daily, "jump" waveform), 48 bovine sternal trabecular bone cores were maintained in bioreactor chambers for 23 days. The cores were equally allocated to four groups based on rank order of their apparent elastic modulus (E_{app}) so that each group had approximately the same average E_{app}: CC (no load + no big ET1), CE (no load + big ET1), LC (load + no big ET1), and LE (load + big ET1). Cores in the CE and LE treatment groups were given 25 ng/mL of big ET1 daily. The concentration of big ET1 used in the current experiment was approximately equivalent to the lowest published concentration of active ET1 used in cell culture experiments [98]. Cores in the LC and LE treatment groups were loaded (-2000 µε, 120 cycles daily, "jump" waveform) through the bioreactors' sapphire pistons using ZETOS Bone Loading and Bioreactor System (ZETOS) [18,45,46,48,80–82,99]. Bone formation in the cores was assessed with E_{app}, static and dynamic histomorphometry, and PGE2 secretion.

4.3.1. Preparation and culture of bovine trabecular bone cores

A bovine sternum was removed from one 13±1 month old animal obtained from a local slaughterhouse. The animal was determined to be free of disease and infection. Within an hour of slaughter, sample preparation started under sterile conditions. Individual trabecular bone cores (10 mm diameter by 5 mm high) were excised from the sternum by machining according to the procedure developed by Smith and Jones [18,45,46,48,80–82]. The cylindrical axis for all cores was oriented along the cranial-caudal axis of the sternum. After machining, the cores were washed twice with culture medium to remove any residual bone left from the machining process and to minimize the risk of infection. A total of 52 bone cores were prepared from the single bovine sternum. The stiffest 48 cores were selected for the experiment.

After excision, machining, and washing, each bone core was inserted into a polycarbonate bioreactor chamber between two sapphire pistons. After preparation, the bone cores were allowed to

recover for 48 h before initiating the load and big ET1 treatments on day 1 of the experiment. While in these chambers, the bone cores were supplied with circulating culture medium (6.6 mL/h) using two 24-channel peristaltic pumps (model Ismatec ISM939D, IDEX Health & Science SA, Glattburgg, Switzerland); maintained at 37 °C and a pH of 7.2–7.3 throughout the 23-day experiment. A separate sterile test tube containing 5 mL of the culture medium was allocated to each bioreactor and replaced every 24 h. The culture medium, standard Dulbecco's Modified Eagle Medium, contained: 10% fetal calf serum, 2 mM of glutamine, 50,000 U/L each of streptomycin and penicillin G, 10 μg/mL of Vitamin C, 0.12 g/L of sodium bicarbonate, and 10 mM of HEPES. Calcein dye (60 μg/mL) for double labeling was added to the culture medium on days 9 and 19 and allowed to perfuse for 24 h.

4.3.2 Load treatment and mechanical analysis

The loading regimen for each of the cores in the LC and LE treatment groups consisted of daily dynamic loading. Each core was cyclically loaded in compression to a maximum change in bulk strain of 2000 με every 0.5 s for 120 cycles for 23 days [9–13,30–32]. The dynamic loading implemented in the study mimicked a "jump" wave-form, the shape of which was determined from normative human jump data [100]. The vertical ground reaction forces from the jump trials were used to define the shape of a "jump" waveform which is simulated in ZETOS (Figure 4.1). In this study, the average time to achieve maximum change in bulk strain was 0.375 s; therefore, the average strain rate during this period was approximately -5000 με/s.

To monitor bone core response for E_{app}, each specimen was tested quasi-statically at a rate of 0.04–0.08 με/s, with a maximal bulk compressive strain of 4000 με on days 1 and 23 of the study. The axial stiffness (K_{axial}) of the cores was measured with this quasi-static compression (Figure 4.2) through the bioreactors' sapphire pistons using ZETOS [18,45–48,80–82,99]. To ensure contact between the loading piston and bone core, a preload of 10 N was applied before quasi-static testing and the dynamic loading stimulus. For each loading trial, force and deformation data were recorded. The bone cores' E_{app}

was determined assuming Hooke's Law (Eq. 1) [11,12,101–103]; where, F is the measured axial force, L is the core height (5 mm), δ is the axial deformation, and A is the cross-section area (78.5 mm^2).
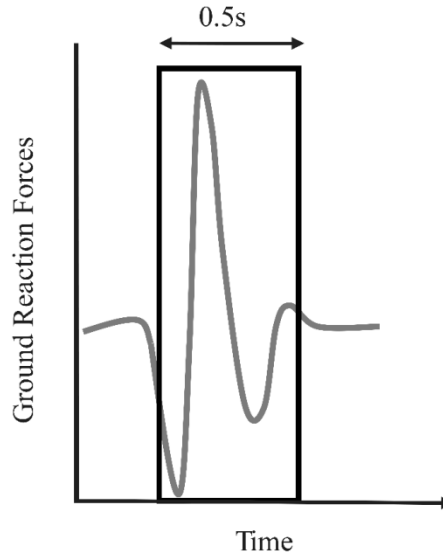
Figure 4.1 - "Jump" waveform as determined from normative data of vertical ground reaction forces from subject trials [100]**. Highlighted portion shows specific waveform that was used in the study representative of landing after a jump.**

$$\text{Equation 4.1} \quad E_{app} = \frac{FL}{\delta A}$$

The K$_{axial}$ for each core was determined from the slope of the linear region of the F-δ curve (Figure 4.2 and 4.3). A custom-made code in MATLAB (MathWorks Inc., Natick, MA) was used to determine the slope of the most linear region. An iterative algorithm performed linear regressions of the curve that gave both a coefficient of determination greater than 0.9 and maximized the number of data points in the regression analysis.
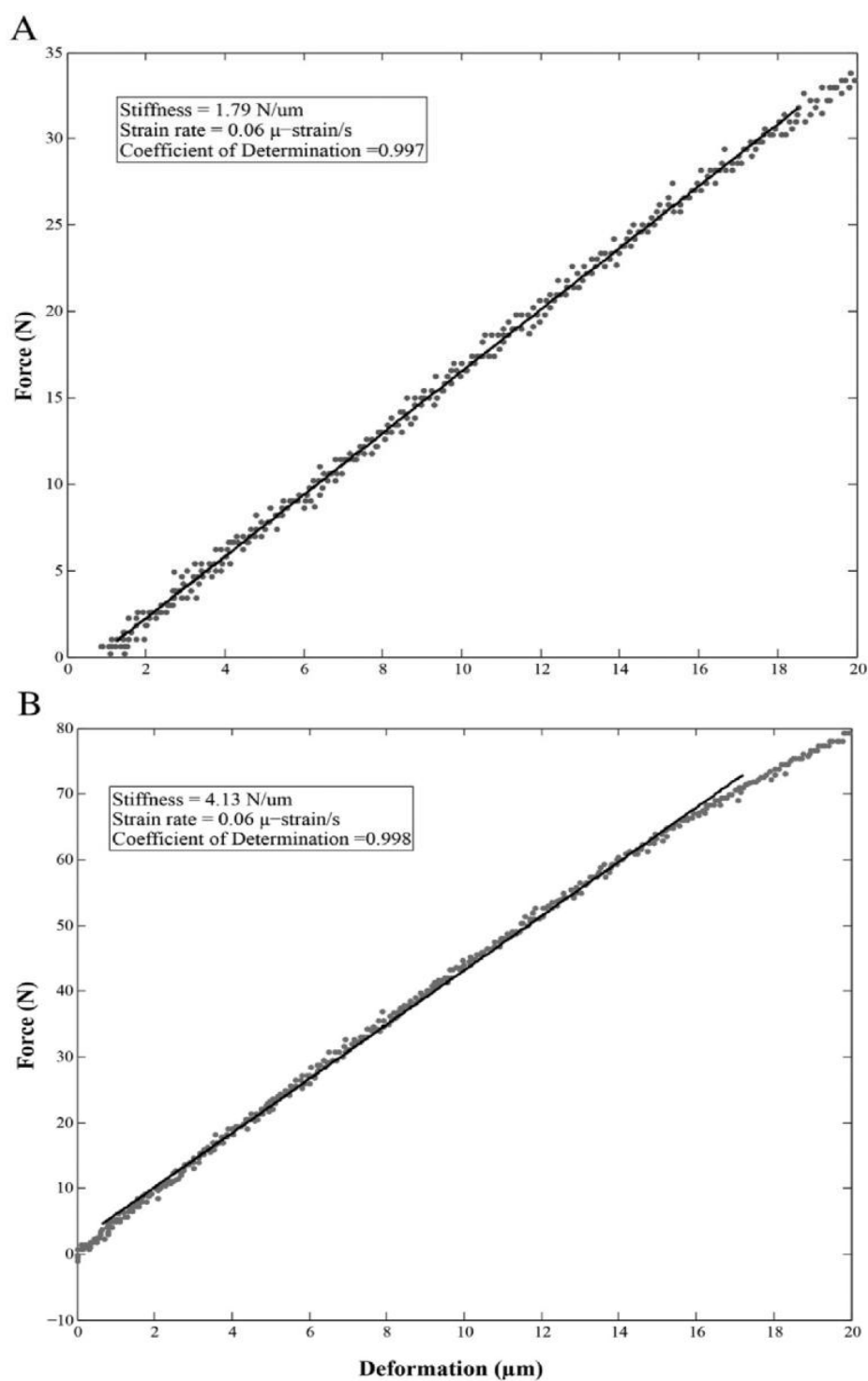
Figure 4.2 - Sample force versus deformation plots from quasi-static loading of representative bovine cores of groups CC and CE on day 23 of live bone study. Linear fit demonstrates axial stiffness to determine apparent elastic modulus. Groups are: CC (no load + no big ET1) and CE (no load + big ET1).
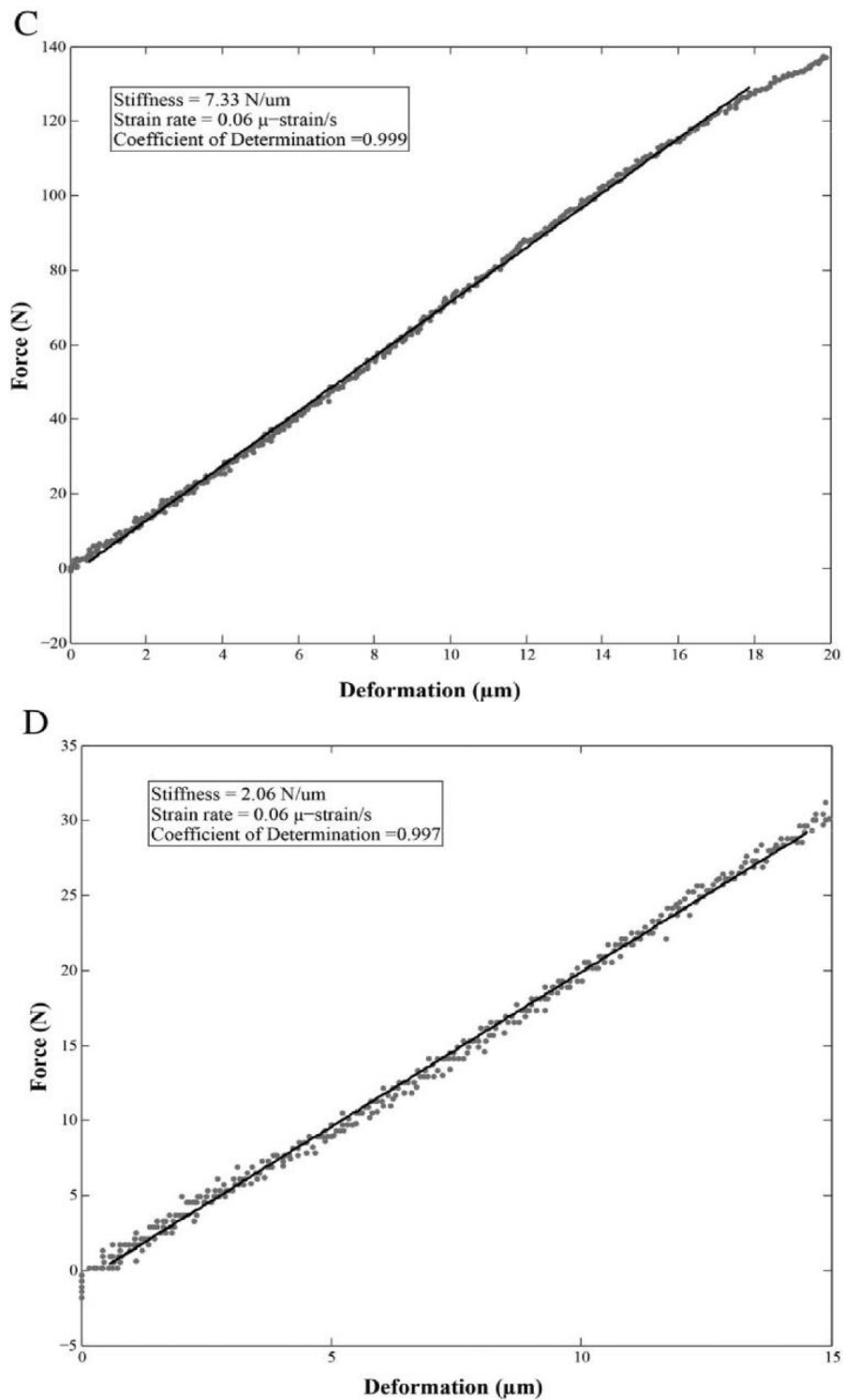
C

Stiffness = 7.33 N/um
Strain rate = 0.06 μ−strain/s
Coefficient of Determination =0.999

D

Stiffness = 2.06 N/um
Strain rate = 0.06 μ−strain/s
Coefficient of Determination =0.997

Figure 4.2 - Sample force versus deformation plots from quasi-static loading of representative bovine cores of groups LC and LE on day 23 of live bone study. Linear fit demonstrates axial stiffness to determine apparent elastic modulus. Groups are: LC (load + no big ET1) and LE (load + big ET1).

4.3.3 Histological and biochemical analyses

At the conclusion of the study, each bone core was extracted from its bioreactor and placed in 70% ethanol for static and dynamic histomorphometry using standard measures [58,104]. Over 14 days, the cores were dehydrated in graded ethanols and acetone, and then embedded individually in modified methylmethacrylate. The embedded cores were cut in half along the long axis (Leica SP1600 Saw Microtome, Buffalo Grove, IL). Thin sections (5 and 8 μm) were cut from the center of the core parallel to the direction of force application (Leica 2255 Rotary Microtome, Buffalo Grove, IL). One slide was examined without further staining under ultra-violet light; a second slide was stained with Goldner's trichrome stain. Each set of slides was given a random number to obscure specimen identity from the observer. Sections were analyzed using a light/epifluorescent microscope and a video camera interfaced with BIOQUANT TCW software (Bioquant Image Analysis Corp., Nashville, TN). The magnification for measurements was calibrated at the start of the study. Single label lengths were measured at 200× magnification; and, double label distances were measured at 400× magnification. The unstained specimen was used for assessing fluorochrome labeling, bone volume (BV/TV) and dynamic measurements of bone formation. The Goldner's stained section was used for static measurements of bone area. For data collection, a standard area (16 mm2) was outlined in the central region of the slide containing only cancellous bone and marrow. Mineralizing surface (MS/BS, %) was calculated as $100 \times (0.5$ single labeled surface length + double labeled surface)/bone surface. The mineral apposition rate (MAR, μm/day) was calculated from distance between calcein labels over the interlabel time (10 days). Bone formation rate (BFR/ BS, $\mu m^3/\mu m^2$/year) was calculated from MAR $\times$ (MS/BS), and extrapolated to a year by multiplying by 365 days/year. Bone specimens without double-labels were assigned a MAR of 0.3 μm/day [104]. Prostaglandin E2 secretions were measured in 5 mL of culture medium collected at 24 hour intervals and stored at −80 °C on days 0, 2, 4, 8, 12, 15, 19, and 23 using Prostaglandin E2

parameter Assay Kit (R&D Systems Inc., Minneapolis, MN, USA) according to the manufacturer's protocol.

4.3.4 Statistical analysis

One-way analysis of variance (ANOVA) and two-tailed two-sample t-tests were used to test that there was no difference between groups' mean E_{app} on day 1, and groups' mean BV/TV measured at the end of the experiment. From the 48 bone cores, seven samples with E_{app} on day 1 less than 40 MPa (one from CC, one from CE, two from LC and three from LE) were not included in the statistical analyses as their stiffness was outside the calibration range (E_{app}=40-1500 MPa) of ZETOS. Four additional bone cores (one each from CC and CE and two from LC) were not included in the histological analysis due to damage of the cores in tissue preparation. The percent change in E_{app} (E_{app}=100×($E_{app,day23}$-$E_{app,day1}$)/$E_{app,day1}$) was calculated for each core between days 1 and 23 and averaged for each group. Four cores, one from LE and three from CC groups, had E_{app} outside two standard deviations of their group's mean and were excluded from the statistical analysis of E_{app}. The effects of load and big ET1 on E_{app}, MS/BS, MAR and BFR/BS were determined using two-way ANOVA and post hoc Fisher's least significant difference (LSD) test. Prostaglandin E2 measurements from all samples in a group were averaged to estimate the PGE2 secretion for time points 0, 2, 4, 8, 12, 17, 19 and 23 days. The effects of load and big ET1 on PGE2 secretion were determined using two-way ANOVA with time as a repeated measure (RM) and the Holm–Šídák test for multiple comparisons. A significance level, α=0.05, was used for all statistical analyses. Normal probability plots confirmed the normality of all data. All statistical analyses were performed with Minitab version 15 (Minitab Inc., State College, PA).

4.4 Results

The initial mean E_{app} and standard error of all 41 bones cores was E_{app}=136±12.8 MPa with no statistical difference between groups (Table 4.1). Bone volume measured at the end of the experiment was also not different between groups (BV/TV=16.8±0.74%) (Table 4.1). Two-way ANOVA with a post hoc

Fisher's LSD test found no significant treatment effects on E_{app} (p=0.25 and 0.51 for load and big ET1, respectively). The E_{app} in the CE (13±12.2%, p=0.56), LC (17±3.9%, p=0.14) and LE (19±4.2%, p=0.13) treatment groups were not statistically different than the CC group (3.3% ± 8.6%) (Table 4.1 and Figure 4.4A).

Two-way ANOVA with a post hoc Fisher's LSD test found no difference between CC groups and CE or LC treatment groups in all histological bone formation markers (Table 4.1 and Figure 4.4B and Figure 4.5C & 4.5D). However, greater MS/BS and BFR/BS in LC treatment group compared to CC group approached significance in (p=0.055 and p=0.074, respectively). The LE treatment group was significantly greater in MS/BS, MAR and BFR/BS than CC group (p=0.037, 0.0040 and 0.019, respectively). Cores in LE and LC treatment groups had more than 50% greater MS/ BS (p=0.037, p=0.055 respectively) and MAR (p=0.0040, p=0.11 respectively) than CC group. The BFR was more than two times greater in LE (p=0.019) and LC (p=0.074) treatment groups than CC group. The MAR and BFR of the cores in the LE treatment group were larger than the CE treatment group by 66% (p=0.021) and 98% (p=0.044), respectively. The LC and LE treatment groups were not different from each other for any of the bone formation markers. Two-way ANOVA with RM found PGE2 levels were elevated at 8 days post-osteotomy in all groups and the treatment groups remained elevated compared to the CC group on days 15, 19 and 23 (Figure 4.6).

Table 4.1 - Mean and standard error of the day 1 apparent elastic modulus (E$_{app}$), percent change in apparent elastic modulus (ΔE$_{app}$) from day 1 to 23, bone volume (BV/TV) mineralizing surface (MS/BS), mineral apposition rate (MAR), and bone formation (BFR/BS) for each group. Asterisks represent statistical difference with α=5% significance compared to CC, where n is sample size, CC (no load + no big ET1), CE (no load + big ET1), LC (load + no big ET1), and LE (load + big ET1).

Measurement		*CC*	*CE*	*LC*	*LE*
E$_{app}$ (MPa)	Day 1	135 (24)	132 (19)	144 (30)	149 (28)
	n	11	11	10	9
ΔE$_{app}$ (%)	Days 1-23	-1.7 (7.5)	13 (12.2)	**17 (3.9)***	**19 (4.2)***
	n	10	11	10	8
	p-value	-	0.34	0.041	0.041
BV/TV (%)	Day 23	17.9 (1.6)	16.5 (1.6)	16.5 (0.86)	16.2 (1.8)
	n	10	10	8	9
MS/BS (%)	Days 9-19	14 (3.1)	16 (2.9)	22 (3.9)	**23 (2.0)***
	p-value	-	0.61	0.055	0.037
MAR (μm/day)	Days 9-19	0.89 (0.21)	1.08 (0.23)	1.4 (0.24)	**1.8 (0.14)***
	p-value	-	0.50	0.11	0.0040
BFR/BS (μm^3/μm^2/yr)	Days 9-19	63 (24)	76 (22)	131 (38)	**151 (16)***
	p-value	-	0.715	0.074	0.019
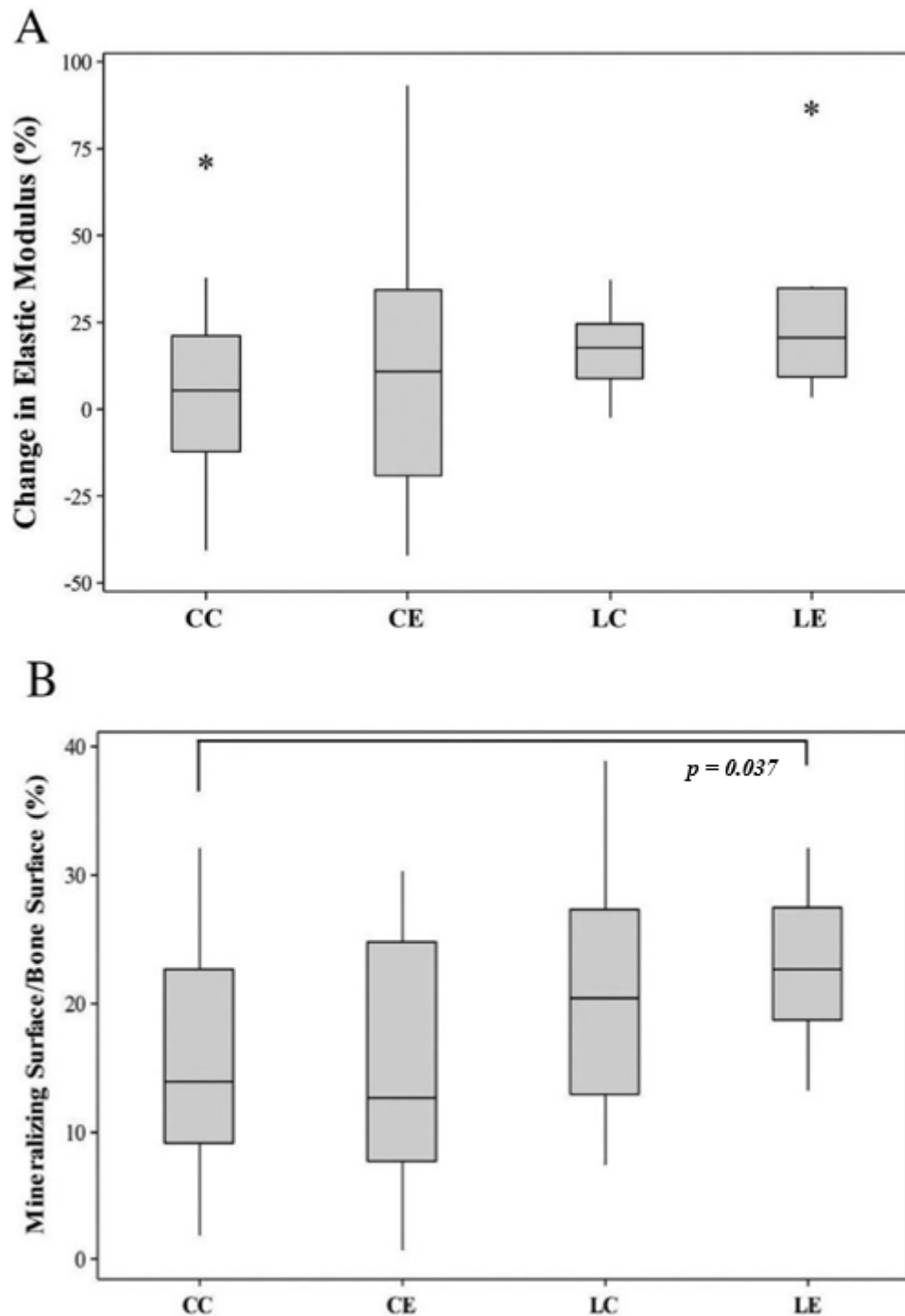
Figure 4.4 - Percent change in apparent elastic modulus between days 1 and 23; B) mineralizing surface. Graphs represent medians, first and third quartiles, and the lowest/highest datum with 1.5 interquartile lower/higher range for each treatment group. Asterisks indicate outliers (CC outlier greater than 100% is not shown). Horizontal bars indicate statistically significant difference with α=5% significance. Groups are: CC (no load + no big ET1), CE (no load + big ET1), LC (load + no big ET1), and LE (load + big ET1).

C

D
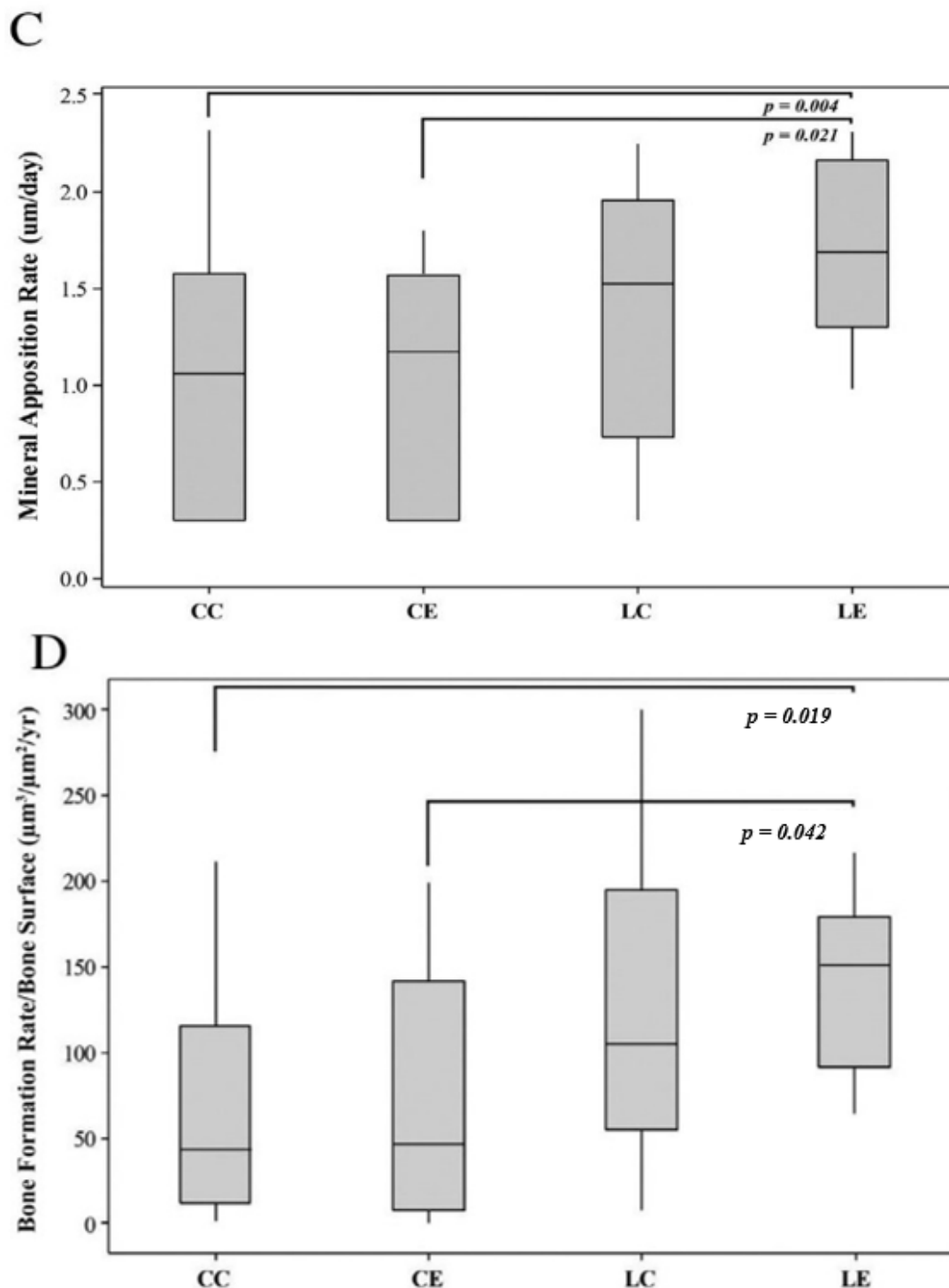
Figure 4.5 - C) mineral apposition rate between days 9 and 19; D) bone formation rate between days 9 and 19. Graphs represent medians, first and third quartiles, and the lowest/highest datum with 1.5 interquartile lower/higher range for each treatment group. Asterisks indicate outliers (CC outlier greater than 100% is not shown). Horizontal bars indicate statistically significant difference with α=5% significance. Groups are: CC (no load + no big ET1), CE (no load + big ET1), LC (load + no big ET1), and LE (load + big ET1).
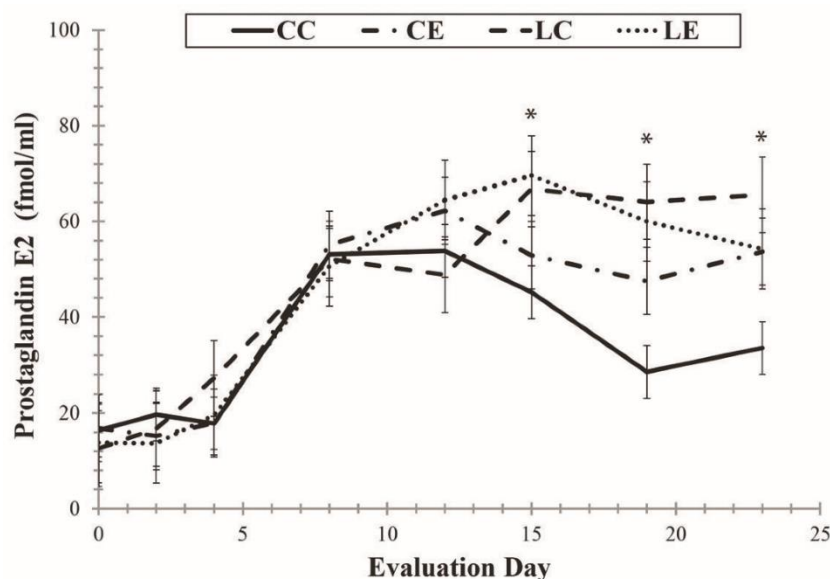
Figure 4.6 - Prostaglandin E2 secretion measured from culture medium sampled daily over duration of experiment. Data represent mean and standard error for each treatment group. Asterisks indicate statistically significant difference in all treatment groups from CC with α = 5% significance using Holm-Šídák test for multiple comparisons. Groups are: CC (no load + no big ET1), CE (no load + big ET1), LC (load + no big ET1), and LE (load + big ET1).

4.5 Discussion

Bone modeling and remodeling in response to mechanical stimuli are controlled by the interactive relationship of stem cells, osteoblasts, osteocytes and osteoclasts, in differentiation, formation, maintenance and resorption in bone [90]. Recent studies have shown that bioreactor systems are advantageous for bridging the experimental gap between in vitro cell culture and animal or clinical studies [105,106]. Ex vivo organ culture allows investigations of whole tissues without disrupting the interactions among neighboring cells and the extracellular matrix [107]. The ZETOS Bone Loading and Bioreactor System (ZETOS) allows isolation and maintenance of trabecular bone cores with active and viable stem cells, osteoblasts, osteocytes, osteoclasts necessary to maintain bone homeostasis [18,45,48,80–83,99]. Bone formation in response to mechanical and biochemical stimuli during a multi-

week experiment was assessed by measuring changes in axial stiffness of bone cores, using the ZETOS mechanical testing apparatus, and secretions of metabolic biomarkers [18,45,48,80–82,99]. Static and dynamic histomorphometry was used to trace morphological changes resulting from modeling and remodeling [18,48,82]. Contributors to mechanical stimulus are the magnitude of the load ($\mu\epsilon$), the rate of load application ($\mu\epsilon/s$), the number of loading cycles, and the rest periods between loads [19,73,77]. Previous ex vivo studies have investigated the impact of mechanical loading on trabecular bone including human, bovine, and ovine and found that these species respond similarly to mechanical load [46,48,80,82].

Endothelin-1 (ET1) was first recognized as a highly potent vasoconstrictive agent [108]. The active molecule consists of 21 amino acids and is produced by cleavage of the 34 amino acid, inactive big ET1, by a variety of proteases [109,110]. The ET1 signaling pathway is ancient and found, along with Notch [111], Hedgehog [112], and WNT [113] pathways, as far back in the evolutionary lineage as Hydra [114]. Like the other ancient pathways, the ET1 signaling axis is critical for development. Global ablation of any of the ET1 signaling axis genes leads to developmental lethality with ablation of ET1, the endothelin receptors type A (ETA) and B (ETB) type receptor, and Ece1 leading to multiple abnormalities in neural crest-derived structures [115–117]. The ablation of ETA causes a decrease in trabecular volume in postnatal development [118]. The secretion of ET1 impacts local cell growth and differentiation and has been shown to promote mineralization by osteoblasts and disorganized bone growth in osteoblastic metastases of breast and prostate cancer [93,119–121].

This is the first study to explore the potential impact of big ET1 expo-sure and mechanical stimulus on osteogenesis in ex vivo cultured trabecular bone cores. The data suggest that combined exposure to big ET1 and mechanical loading results in increased osteogenesis as measured in biomechanical, biochemical and histomorphometric responses. Treatment with big ET1 and daily dynamic loading increased E_{app}, MS/ BS, MAR and BFR/BS in bovine trabecular bone cores in comparison to CC group. Also, the study results suggested that trabecular bone expo-sure to big ET1

evoked similar responses to mechanical loading, quantified by E_{app} and PGE2 secretion in the treatment groups compared to the CC group.

Both treatments, big ET1 and load, significantly affected the secretion of PGE2 on days 15, 19, and 23. PGE2 levels were elevated at 8 days post-osteotomy in all groups and the treatment groups remained elevated compared to the CC group on days 15, 19 and 23. The initially elevated levels of PGE2 secretion were a reflection of the healing process induced by the osteotomy [122]. That the secretion of PGE2 remained elevated in all treatment groups, in comparison to the control group, implies that big ET1 and mechanical load are similar in their stimulation of trabecular bone [123–125]. The PGE2 secretion results support the E_{app} and histological findings. While SOST could not be measured in this study because ELISAs for bovine SOST are not available, other studies have found elevated PGE2 decreased expression of SOST resulting in an increase in WNT signaling and an increase in bone formation [91,92]. We have also previously demonstrated that addition of exogenous big ET1 to mouse osteoblasts decreases SOST secretion [93]. Therefore the PGE2 findings are consistent with the E_{app} and histological results from the current study.

Although all treatment groups showed an overall increase in E_{app} from day 1 to 23 of the study, the E_{app} in the treatment groups com-pared to CC group were not statistically significant. The increase in E_{app} was reflected in the histological analysis. Bone formation was greater in LE treatment group compared to CC and CE groups, with LC treatment group trending to greater bone formation and no significant difference between the CE and CC groups.

Previous studies with a similar experimental setup and sample size to the current study reported a statistically significant difference in E_{app} due to loading [46,48,80,82]. Type II error may be associated with some of the lack of statistical significance in the measured effects, a result of high variance and low sample sizes. Although 48 samples (twelve per group) may be sufficient to reduce type II error in ex vivo testing of trabecular bone cores [46,48,80,82], eleven samples (one to four per group) in the current study were not included in the statistical analyses of the E_{app} and histological results. Variance in the data could

have arisen from a number of sources including the inherent variability in trabecular tissue and loss of connectivity caused by excision [12,101–103]. In this study, the mechanical behavior (E_{app} and ΔE_{app}) of trabecular bone cores was assessed. It is important to keep in mind that the E_{app} of the cores is dependent on bone volume fraction and trabecular orientation. These parameters are highly variable in trabecular bone (Table 4.1) and could not be assessed at the start of the experiment without interfering with the sterility and viability of the specimens. The orientation of the trabecular structure relative to the tested load direction may have varied between cores depending on their in situ location in the sternum. The sternum is a non-weight bearing bone, where muscle pull may vary along the length of the sternum. However, use of a single bovine sternum enabled all cores to be harvested from one animal, avoiding variance due to genetics.

Potential sources of error in compression testing of trabecular bone include machine compliance, end artifacts and side artifacts [47,126–128]. Several steps in the mechanical testing procedure were designed to reduce these errors and sources of variance. The ZETOS loading sys-tem has been calibrated for E_{app} range of 40 to 1500 MPa [45,99]. Reference bodies tested within this range demonstrated a 3% accuracy in E_{app} [99]. Standard ZETOS specimen dimensions (10 mm diameter, 5 mm height) meet the main goal of maintaining core viability for several weeks [18,46], and are adequate for continuum assumptions [47,126–128] as required for equations of Hooke's Law. The aspect ratio of the bone cores (0.5) although favorable for maintaining viability could increase end artifacts in the measurement of E_{app} because of specimen-platen interface conditions and structural end artifacts [47,126–128]. The F-δ curves (Fig. 2) did not reveal a large "toe" region indicating machine compliance and possible end-artifact errors have been minimized.

Despite the study's limitations, the results of the current study align with those of previous loading studies. Increased secretion of PGE2 has been reported following mechanical stimulation of osteocytes [124,125] and bone [123], a similar result to the increased PGE2 secretion in all treatment groups in the current study. Ex vivo experiments on bovine trabecular tissue under dynamic loading with

a maximum bulk strain of −4000 με found an average increase in the E_{app} of approximately 50% over the course of 21 days [46]. The comparatively lower observed change in E_{app} in the present study (17–19%) may be due to the lower applied strains (-2000 με) or normal biological variation between different animals. Endres and co-workers experimented with the level of dynamic loading, finding a direct dose–response relationship for bulk strains between -1000 and -4000 με [82]. Similarly, comparative histological bone formation markers have been reported: MAR 0.94±05 μm/day [48]; MAR 0.53±0.08 μm/day [129]; and MS/BS 25±5%, MAR 1.0±0.3 μm/day, and BFR/BS 100±11 μm/year [83].

Previous in vivo studies demonstrated that -1000 to -2500 με corresponds to physiological strain levels experienced during walking and other daily activities; however, compressive strains as high as 3000 to 5000 με have been measured during high intensity activities [19,130–132]. In these studies, strain was measured in vivo from strain gauges fixed to the outer surface of the cortex during physiological activities. In contrast, in the current study, strain was determined from the bulk compression of the trabecular bone core, including the initial non-linear "toe" region of the force-deformation curve that remained be-yond the 10 N preload. Therefore, the actual strain of the bulk of the bone core may be less than calculated. The loading of the trabeculae in the bone core is complex and depending on their morphology and orientation include tensile, compressive, bending and shear strains. A recent numerical study found 2.2–12% of total bone in bone cores, under -2000 με bulk strain, experienced local trabeculae strains between -1000 and -3000 με [83]. To determine the relationship between the bulk strain of the bone core and local strain in the trabeculae micro computed tomography based finite element analysis is required, and is the subject of a subsequent study.

4.6 Conclusion

This study successfully showed that combined exposure to big ET1 and mechanical loading promoted osteogenesis in ex vivo bovine trabecular bone. Specifically, MAR, BFR/BS and PGE2 secretion were higher in LE treatment group compared to CC group. The findings will be used to design

studies on ex vivo human trabecular tissue with the goal of investigating mechanotransduction signaling pathways and the role of big ET1 in bone modeling and remodeling.

Chapter 5

5. Human Trabecular Bone Response to Mechanical Loading is Dependent on Endothelin-1 Signaling

 Additional document authors are MG Johnson[1], EL Smith[2], MW Squire[3], KE Hansen[3,4], RD Blank[5,6], H-L Ploeg[7]

[1]Department of Medicine, University of Wisconsin – Madison, [2]Department of Population Health Sciences, University of Wisconsin – Madison, [3]University of Wisconsin Hospital and Clinics, [4]University of Wisconsin – Madison School of Medicine and Public Health, [5]Department of Medicine, Medical College of Wisconsin, [6]Department of Endocrinology, The Clement J. Zablocki VA Medical Center, Milwaukee, WI [7]Department of Mechanical Engineering, University of Wisconsin – Madison

5.1 Abstract

It is widely recognized that mechanical loading promotes bone modeling, remodeling, and homeostasis; however, the interactions of the mechanotransduction pathways are not as well understood. Research has demonstrated that the WNT signaling pathway, the activity of which is indicated by secretion of certain genes including endothelin (ET1) and sclerostin (SOST), plays a critical role in regulating mechanotransduction. SOST is a WNT signaling antagonist and is tonically secreted by osteocytes. The purpose of this study was to investigate if pharmacological antagonism of the endothelin receptor A would inhibit relevant mechanotransduction pathways leading to bone modeling and remodeling in human trabecular bone. The study hypothesis was tested by conducting a 2x2 factorial trial whereby human trabecular bone cores were subjected to daily mechanical loading (-3000 µε, 120 cycles daily) and 10 µM BQ-123, an endothelin receptor A antagonist. Forty eight cores (5 mm x 10 mm) were obtained from two donors (1 male, 1 female) undergoing total hip arthroplasty and allocated to four groups: control (CC), control+BQ-123 (CB), load+control (LC) and load+BQ-123 (LB). Each specimen,

maintained individually in a bioreactor, was tested quasi-statically with a maximal bulk compression of 4000 µε on days 1,8,15, and 22 of the study to measure E_{app}. Culture medium from each sample was analyzed for secretion of insulin-like growth factor (IGF1), SOST, and ET1 on days 0, 8, 11, 18, and 25. Biochemical and mechanical data were analyzed by Kruskal-Wallace tests, followed by paired analysis via Wilcoxon tests. Significant differences were found in IGF1, SOST and ET1 secretion over time and between the LC and LB groups. The LB group showed increased secretion of SOST and ET1 and decreased secretion of IGF1. The percent change in E_{app} over the duration of the experiment was not significantly different between groups, however, the mean percent change in E_{app} in the LC group (28 ± 6.4 %, p=0.096) tended to be higher than the other groups (CC $32\pm7.2\%$, CB $10\pm3.6\%$, LB $17\pm5.6\%$). The results also show that blockade of ET1 signaling is associated with an increase in SOST secretion in response to mechanical load. Increases in IGF1 secretion in response to mechanical load and the decrease in secretion when ET1 signaling is blocked suggest that ET1 signaling interacts with pathways that respond to mechanical load. The increase in ET1 secretion in the CB and LB groups indicates the presence of a feedback loop. The study results imply that ET1 signaling is required for transduction of mechanical into biochemical signals during the anabolic response of bone to mechanical load.

5.2 Introduction

Bone modeling, remodeling, and homeostasis are stimulated in part by mechanical loading—a process which has been well studied in literature [19,73–75,77]. Bone tissue response to mechanical stimulus is dependent on the level of stimulus [26,78]. At the cellular level, bone tissue is largely thought to respond to applied strain, wherein strain below a set point causes bone resorption and applied strains above that set point cause bone formation [26,78]. Multiple studies conducted on *ex vivo* trabecular bone tissue showed that applied bulk strains ranging from -2000 to -4000 µε caused greater increases in the apparent elastic modulus (E_{app}) compared to samples not exposed to an applied mechanical stimulus [9,46,48,80–82]. In addition, many of these studies simultaneously found increased presence of

biochemical and histological markers of bone formation [9,46]. These findings demonstrate that 1) *ex vivo* testing is a productive method for studying factors affecting to bone mechanotransduction in an environment that is controlled and excludes systemic effects and 2) illustrates that bone's known response to mechanical stimulus can be replicated in an *ex vivo* culture system.

Literature has also demonstrated that bone modeling, remodeling, and homeostasis are largely affected by genetic and biochemical factors in addition to mechanical stimulus. Multiple studies have demonstrated that the WNT signaling pathway, a family of secreted proteins that regulate the activity and life cycles of cells, plays a primary role in regulating bone mechanostransduction [84–87,133]. The WNT pathway is controlled by cellular secretion of select inhibitors including proteins from the sclerostin (SOST) and Dickkopf (DKK) families, the expression of which are inhibited in response to mechanical loading [88,89,133,134]. These factors bind to low-density lipoprotein receptor-related protein 5 (LRP5), and are markers of WNT pathway activity [84,86–88,92,135]. Factors including prostaglandins, parathyroid hormone (PTH), and insulin growth factors (IGF) reduce SOST expression and contribute to bone mechanotransduction [87–89,92].

Prior studies have investigated the effects of endothelin on bone tissue turnover. An *in vitro* study conducted by Johnson *et al.* found that exposure to big endothelin-1 (ET1) increases osteoblast mineralization compared to control [93]. This exposure also caused changes in the expression of several miRNA that are known or hypothesized to influence expression of proteins affecting bone physiology [93]. A further study conducted by Meyer *et al.* found that ET1 exposure to bone tissue *ex vivo* also resulted in increased mineralization, increased bone formation, and increases in mechanical properties [9].

Since ET1 exposure has been shown to affect cell signaling pathways in bone in previous studies, the purpose of this study was to investigate if ET1 signaling is essential for physical and biochemical responses of bone to mechanical loading. The study hypothesis was that pharmacological antagonism of endothelin receptor A would inhibit mechanotransduction pathways leading to modeling and remodeling in human trabecular bone.

5.3 Materials and Methods

The study hypothesis was tested by conducting a 2x2 factorial trial of daily mechanical loading (3000 µε, 120 cycles daily, "jump" waveform) and endothelin receptor A (ET_A) antagonism (10 µM BQ-123) with 48 human hip trabecular bone cores. Using a protocol that was approved by the Institutional Review Board at the University of Wisconsin – Madison and after obtaining consent, 2 human femoral heads were obtained from 2 donors (48-year-old male, 68-year-old female) undergoing total hip arthroplasty. The 48 obtained bone cores were maintained in individual bioreactors for 25 days. Excised bone cores were allocated equally to four study groups according to the rank order of their measured apparent elastic modulus (E_{app}): CC (no load + no ET1 block), CB (no load + ET1 block), LC (load + no ET1 block), and LB (load + ET1 block). The groups were assembled such that each group had approximately the same mean E_{app} and number of cores from each donor hip. Cores in the CB and LB group were given BQ-123 daily and cores in the LC and LB groups were loaded daily (-3000 µε, 120 cycles, "jump" waveform) through the bioreactors' sapphire pistons sing the ZETOS Bone Loading and Bioreactor System (ZETOS) [45,99]. Bone modeling and remodeling was assessed by tracking changes in E_{app} (ΔE_{app}) and secretions in SOST, DKK1, IGF1, ET1, and prostaglandin E2 (PGE2).

5.3.1 Preparation and culture of human trabecular bone cores

Two human femoral heads were obtained from one 48 year old male and one 68 year old female who were undergoing total hip arthroplasty (THA). Sample preparation was initiated within 30 minutes of femoral head extraction during the THA surgery. Trabecular bone cores (5 mm height, 10 mm diameter) were excised under sterile conditions from each femoral head based on the procedure developed by Smith and Jones [45]. The fovea was identified for each femoral head and 7 mm slices were in parallel directions using a diamond band saw (Exakt, Norderstedt, Germany). Cores 10 mm in diameter were then excised from each slice using a custom diamond-tipped coring bit. Excised cores were then milled on both terminal ends along the cylindrical axis such that each core had a uniform, final height of 5 mm.

After the cores were through the machining process, each was washed twice using culture medium to remove residual bone debris and to minimize infection risk. Each bone core was placed in a polycarbonate bioreactor immediately following excision, machining, and washing (Figure 5.1). The cores were then individually tested in quasi-static axial compression to a maximum strain of -4000 µε to determine the axial stiffness (K_{axial}) and E_{app}. A total of 58 bone cores were excised and the stiffest 48 were selected for the experiment.
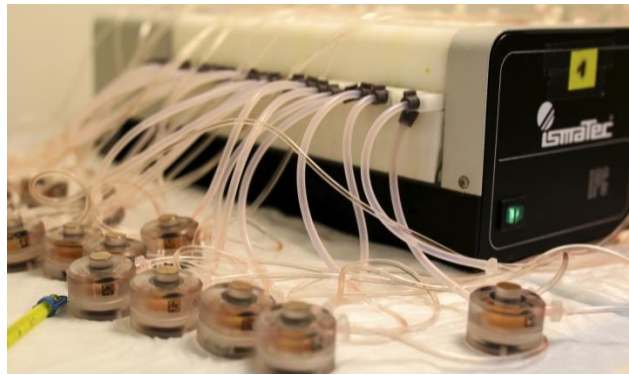
Figure 5.1 - Bone cores in polycarbonate bioreactors with culture medium perfused with peristaltic pumps.

After excision and initial Eapp measurement, the bore cores were rested for 48 hours before initiating treatments. Whilst inside the bioreactors, each bone core was supplied with culture medium that was continually perfused through the chamber (6.6 mL/hr) by two 24-channel peristaltic pumps (Ismatec ISM939D, IDEX Health & Science SA, Glattburgg, Switzerland) and maintained at 37°C and a pH of 7.2-7.3 for the duration of the 25-day experiment. Each bone core was allocated a separate, sterile 5 mL supply of culture medium that was replaced daily. Dulbecco's Modified Eagle Medium was used for the culture medium and consisted of 10% fetal calf serum (FCS), 2 mM glutamine, 10 mM HEPES, 0.12 g/L sodium bicarbonate, 10 µg/mL Vitamin C, and 50,000 U/L each of streptomycin and penicillin G [136].

5.3.2 Mechanical and Biochemical Treatment Application and Analysis

Bone cores in the LC and LB treatment groups were subjected to daily dynamic mechanical loading. The ZETOS was used to apply the dynamic loading—a cyclic compression pattern that resulted

in a maximum change in bulk strain of 3000 με every 0.5 seconds for 120 cycles every loading application [46,48,80,82,137]. This loading pattern simulated a "jump" waveform determined from normative human jump data that had been characterized during a previous study [100]. To track the mechanical response of the bone cores, each sample was evaluated on a weekly basis (days 1, 8, 15, 22) during the study to measure E_{app} and calculate ΔE_{app}. Measurements were achieved by testing each individual core quasi-statically (0.04-0.08 με/sec) to a maximum of -4000 με. Compression was applied through the sapphire pistons in the bioreactors encasing the bone cores. Prior to conducting quasi-static testing or applying the dynamic loading stimulus, each bone core was preloaded to 10 N to ensure it was contacting the loading piston. Force and deformation data were recorded during each quasi-static test and dynamic loading circuit. Using Hooke's Law (Equation 1), the E_{app} for each core was determined using the measured axial force F, the bone core height L, the axial deformation δ, and the bone core cross-sectional area A. The precise bone core dimensions were determined at the end of the study from micro-computed tomography (μCT) scans of the bone cores (Siemens microCATII, 34 μm, 80 kVp, 50 μA). The force-displacement data and the bone core dimensions were used to calculate K_{axial} for each bone core by implementing a custom program within MATLAB (MathWorks, Inc., Natick, MA) to calculate the slope of the linear region of the F-δ curve. The linear regressions calculations were accomplished through an iterative process whereby the coefficient of determination (≥ 0.9) and number of included data points were simultaneously maximized.

$$\textbf{Equation 5.1} \qquad E_{app} = \frac{FL}{\delta A}$$

Culture medium from each bone core were changed daily and collected on days 0, 8, 11, 18, and 25. The collected media were analyzed using enzyme linked immunosorbent assays (ELISA) to determine secreted amounts of SOST, DKK1, ET1, IGF1, and PGE2.

5.3.3 Statistical Analysis of Collected Data

The change in E_{app} ($\Delta E_{app} = 100$ x ($E_{app, \text{ day } 22}$- $E_{app, \text{ day } 1}$)/ $E_{app, \text{ day1}}$) for each bone core was calculated between days 1 and 22. The means and standard deviations were determined for each group. Values that were more than three standard deviations from the mean were considered as outliers and were excluded from statistical analyses. Normality probability plots were generated for all data sets and confirmed a lack of normality. For both the mechanical (E_{app}, ΔE_{app}) and biochemical (SOST, DKK1, ET1, IGF1, PGE2) data sets, the effects of loading and ET1 blockade were determined using Kruskal-Wallace tests. Paired comparisons were conducted with Wilcoxon tests. A significance level of $\alpha = 0.05$ was used for all statistical analyses. All statistical analyses were performed using R (R Foundation for Statistical Computing, Vienna, Austria).

5.4 Results

The mean and standard error of E_{app} for all 48 cores across all treatment groups was $E_{app} = 309 \pm$ 37.7 MPa with no statistical differences between groups. Kruskal-Wallace tests found a significant treatment effect on ΔE_{app} resulting from ET1 blockade (p=0.022) but no significant effect from mechanical loading (p= 0.965). Wilcoxon tests showed significant changes in E_{app} between days 1 and 22 in all treatment groups (p = 0.000, 0.001, 0.000, and 0.005 for the CC, CB, LC, and LB groups, respectively). Further testing showed no significant differences in ΔE_{app} were found between groups though ΔE_{app} tended to be higher in the LC group (28±6.4 %, p=0.096) compared to the other treatment groups (CC 32±7.2%, CB 10±3.6%, LB 17±5.6%) (Figure 5.2). Examining the patients separately resulted in near significance between the LC (39±12%) and LB (7.4±5.6%) and between the LC and CB (4.6±4.0%) groups from patient 1 (p=0.095 and 0.1508, respectively) (Figure 5.3).
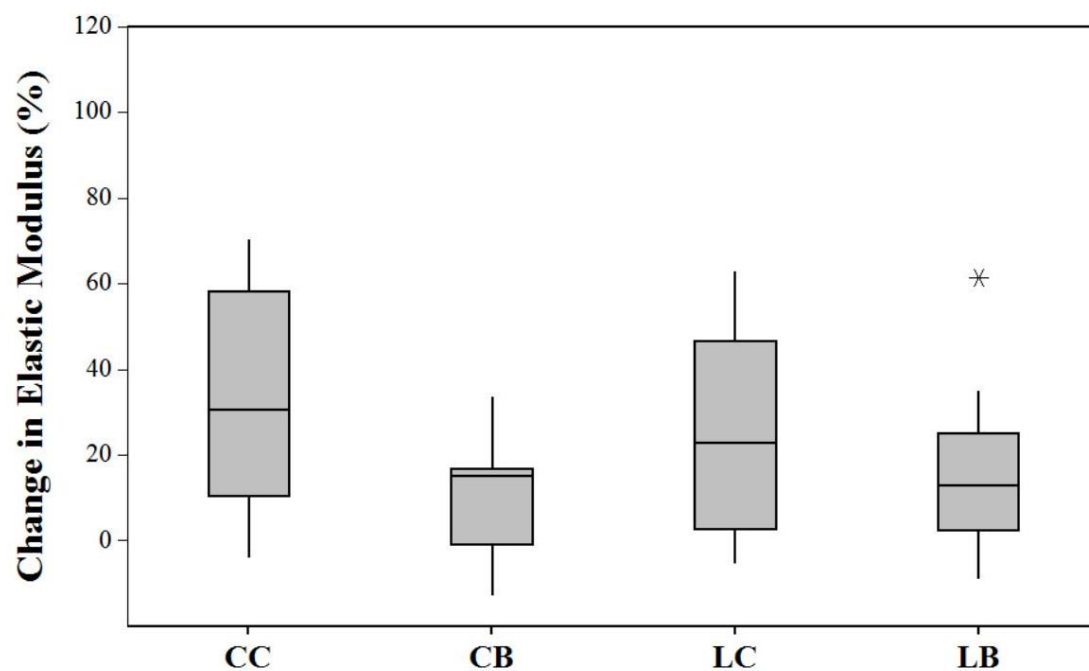
Figure 5.2 - Change in elastic modulus between days 1 and 22 for both patients in all treatment groups. Asterisk indicates a determined outlier. Graph shows medians, first and third quartiles, and the lowest/highest datum within 1.5 interquartile lower/higher range.
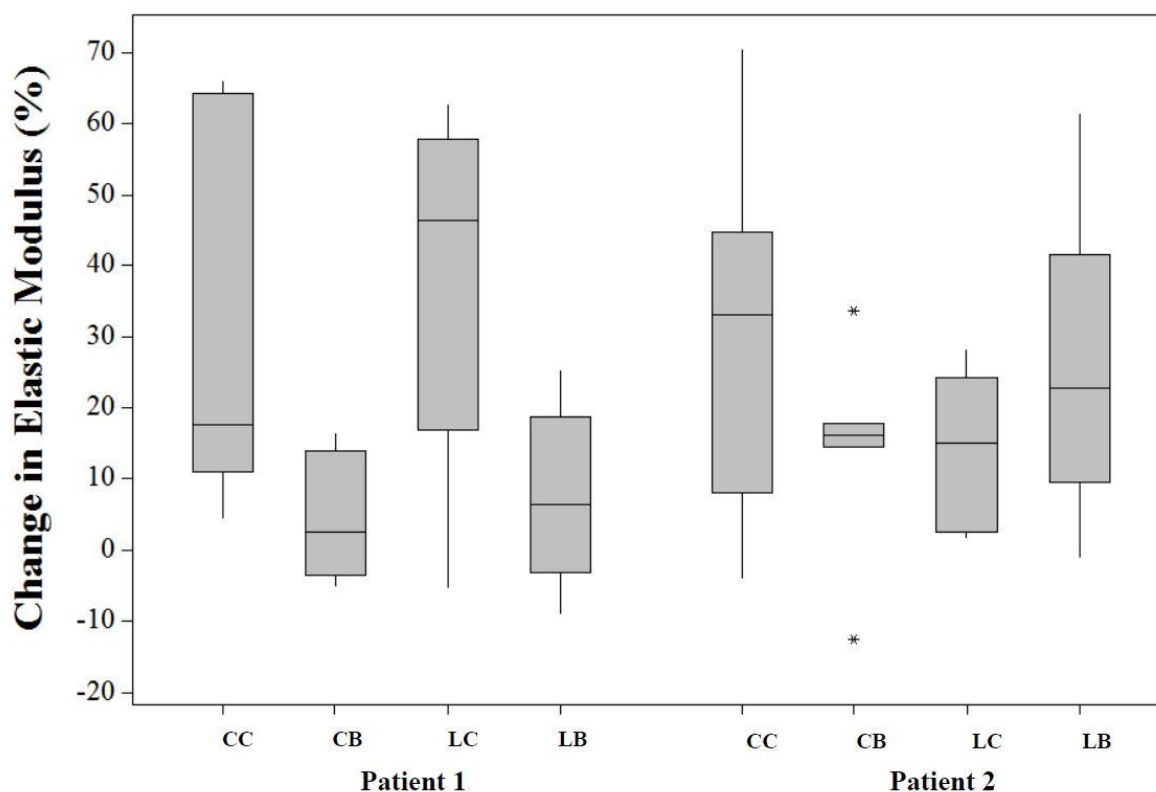
Figure 5.3 - Change in elastic modulus between days 1 and 22 for each patient in each treatment group. Asterisks indicate outliers. Graph shows medians, first and third quartiles, and the lowest/highest datum within 1.5 interquartile lower/higher range.

Kruskal-Wallace tests found significant effects of treatment on ET1 secretion on days 8, 11, and 18 (p=0.024, 0.0002, and 0.006, respectively). Wilcoxon tests found significant increases from baseline in ET1 secretion on days 18 and 25 in the CB (p=0.001, 0.002) and LB (p=0.005, 0.009) groups (Figure 5.4). Significant differences were also found on days 8, 11, and 18 between CB and LC groups (p=0.008. 0.00008, 0.0009) and the LC and LB groups (p=0.024, 0.011, 0.026). The patients were also examined separately, and no significant differences were found between patients in any group at any time point (Figure 5.5).
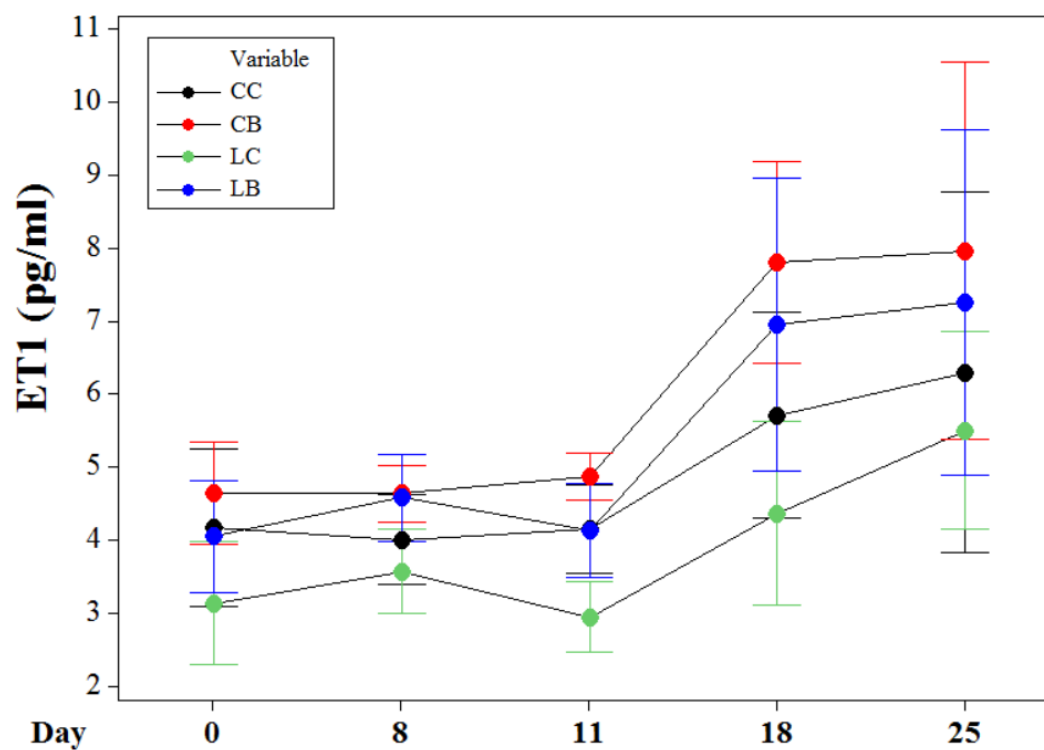
Figure 5.4 - ET1 secretion in all groups as measured at given time points. Error bars show 95% confidence interval for each time point.
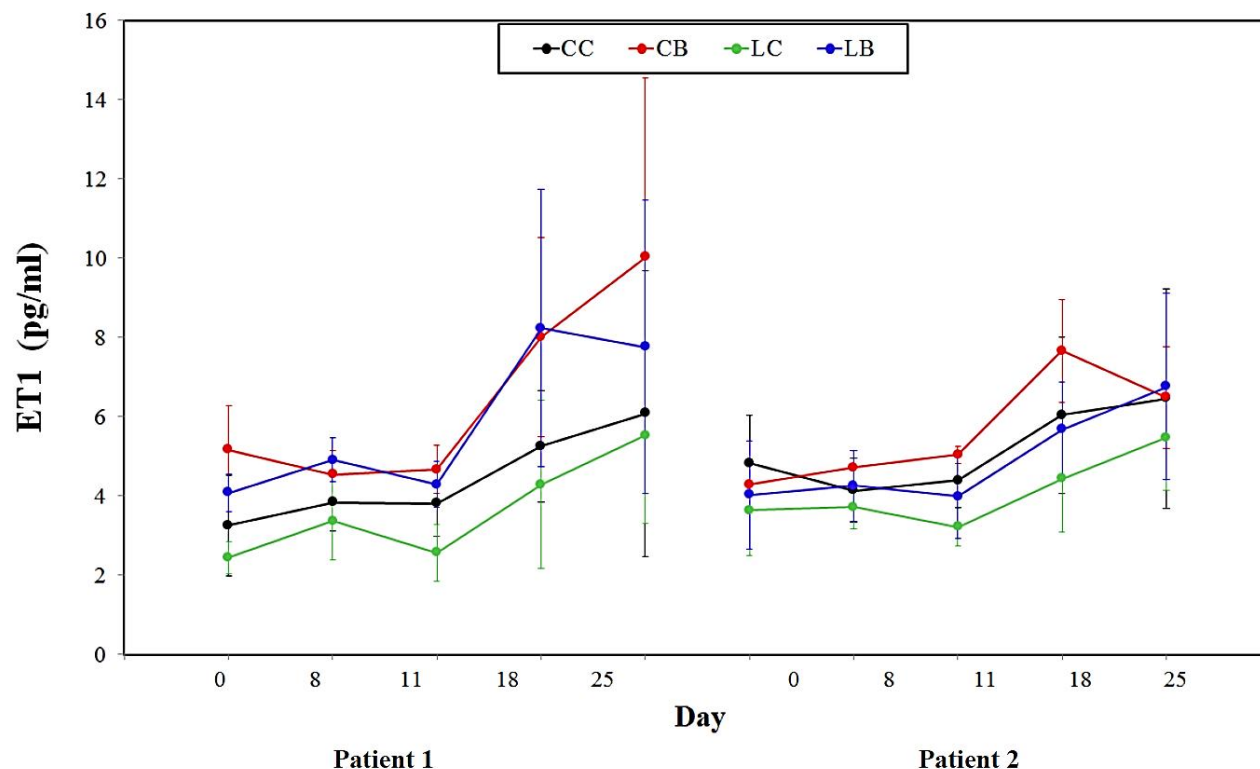
Figure 5.5 - ET1 secretion for both patients in all treatment groups as measured at given time points. Error bars show 95% confidence interval for each time point.

Kruskal-Wallace tests found significant effects of treatment on SOST secretion on days 8 (p=0.007). Wilcoxon tests found significant increases from baseline in SOST secretion on days 8, 11, 18 and 25 in the CB (p=0.000, 0.007, 0.003, 0.001) and LB (p=0.005, 0.016, 0.003, 0.0005) groups (Figure 5.6). Significant differences were also found on days 8, 11, and 18 between CB and LC groups (p=0.008, 0.008, 0.00009) and on days 8 and 18 between the LC and LB groups (p=0.0008, 0.01). The patients were also examined separately, and no significant differences were found between patients in any group at any time point (Figure 5.7).
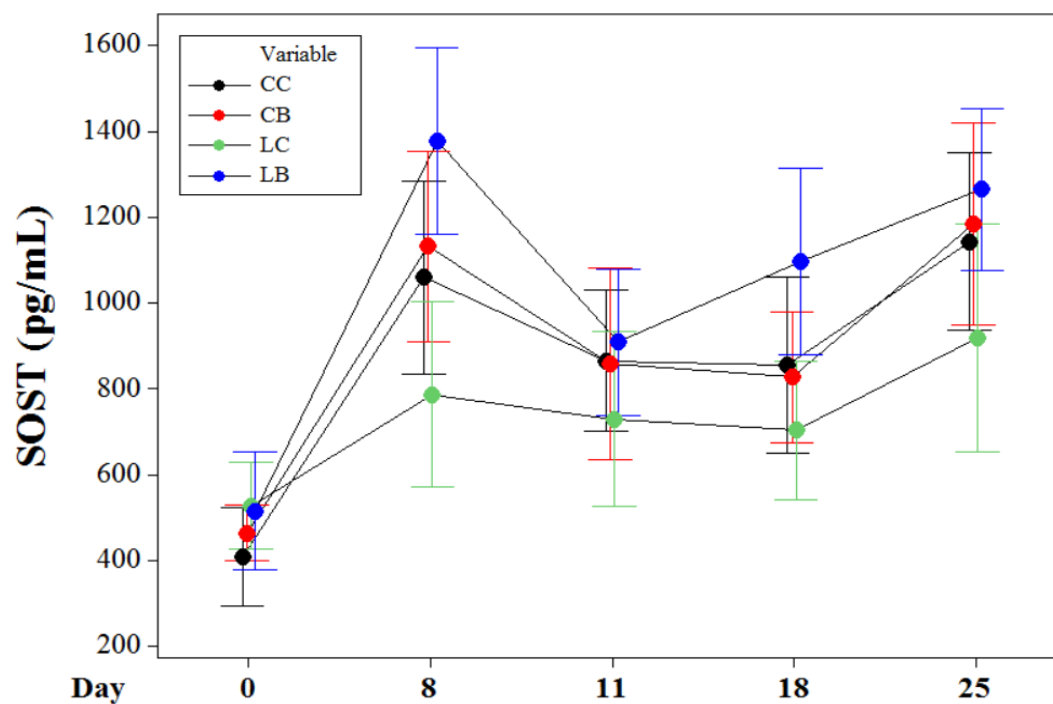
Figure 5.6 - SOST secretion for all treatment groups as measured at given time points. Error bars show 95% confidence interval for each time point.
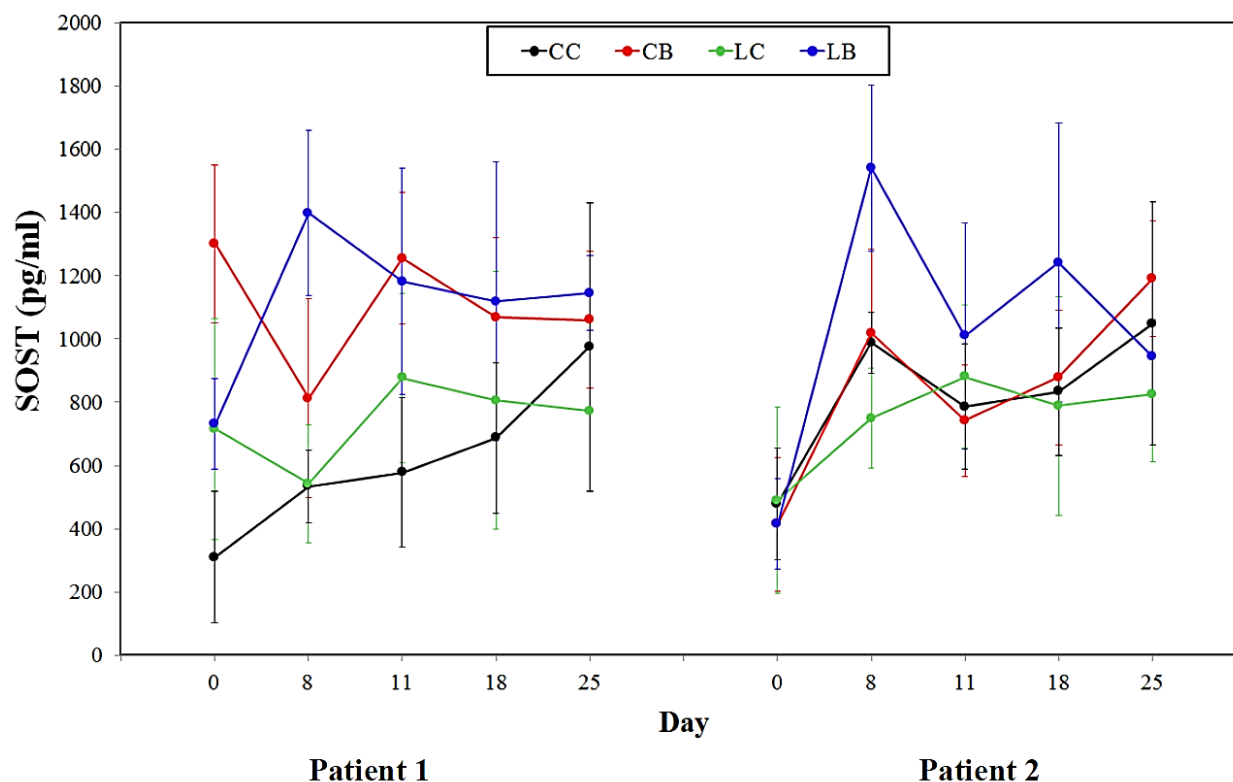
Figure 5.7 - SOST secretion for both patients in all treatment groups as measured at given time points. Error bars show 95% confidence interval for each time point.

Kruskal-Wallace tests found significant effects of treatment on IGF1 secretion on days 8 and 18 (p=0.0001, 0.00002). Wilcoxon tests found significant decreases from baseline in IGF1 secretion on days 8, 18 and 25 in the CC group (p=0.002, 0.000, 0.001). Secretion of IGF1 significantly decreased from baseline on days 8, 11, 18, and 25 in the CB group (p=0.001, 0.005, 0.005, 0.003) (Figure 5.8). Secretion of IGF1 was significantly lower than baseline on day 11 (p=0.003) and approaching significance on day 25 (p=0.052). Significant differences were also found on days 8, 18, and 25 between CC and LC groups (p=0.035, 0.024, 0.00007) and on days 8, 11, 18, and 25 between the LC and LB groups (p=0.00004, 0.0001, 0.043, 0.0005, 0.037). The patients were also examined separately, and no significant differences were found between patients in any group at any time point (Figure 5.9).
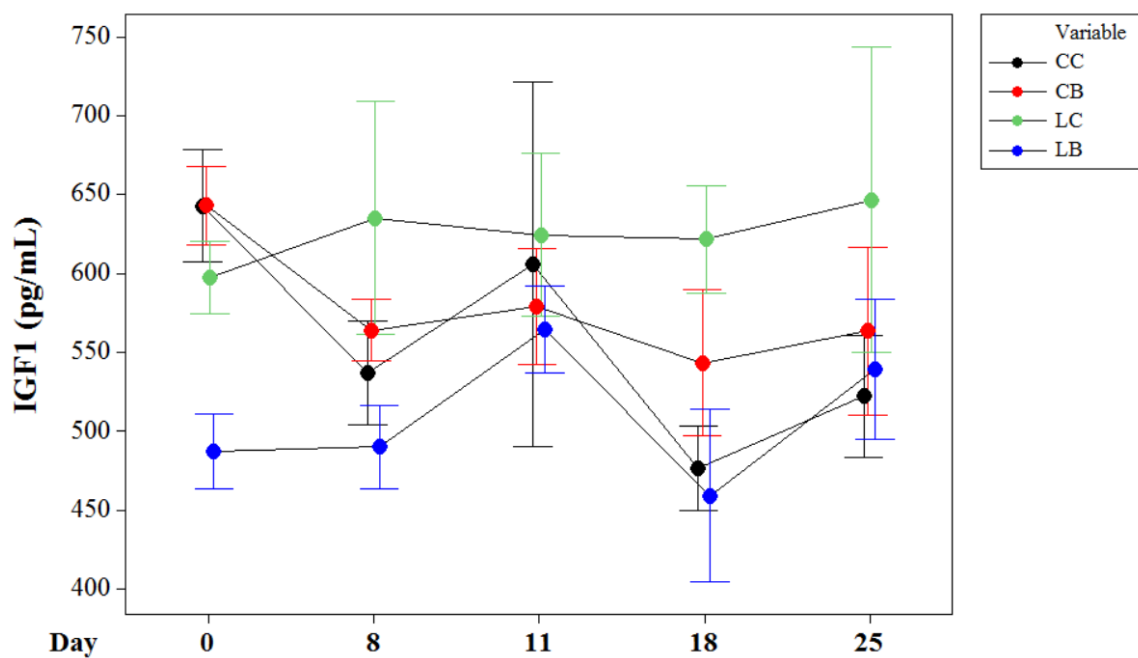
Figure 5.8 - IGF1 secretion in all treatment groups as measured at given time points. Error bars show 95% confidence interval for each time point.
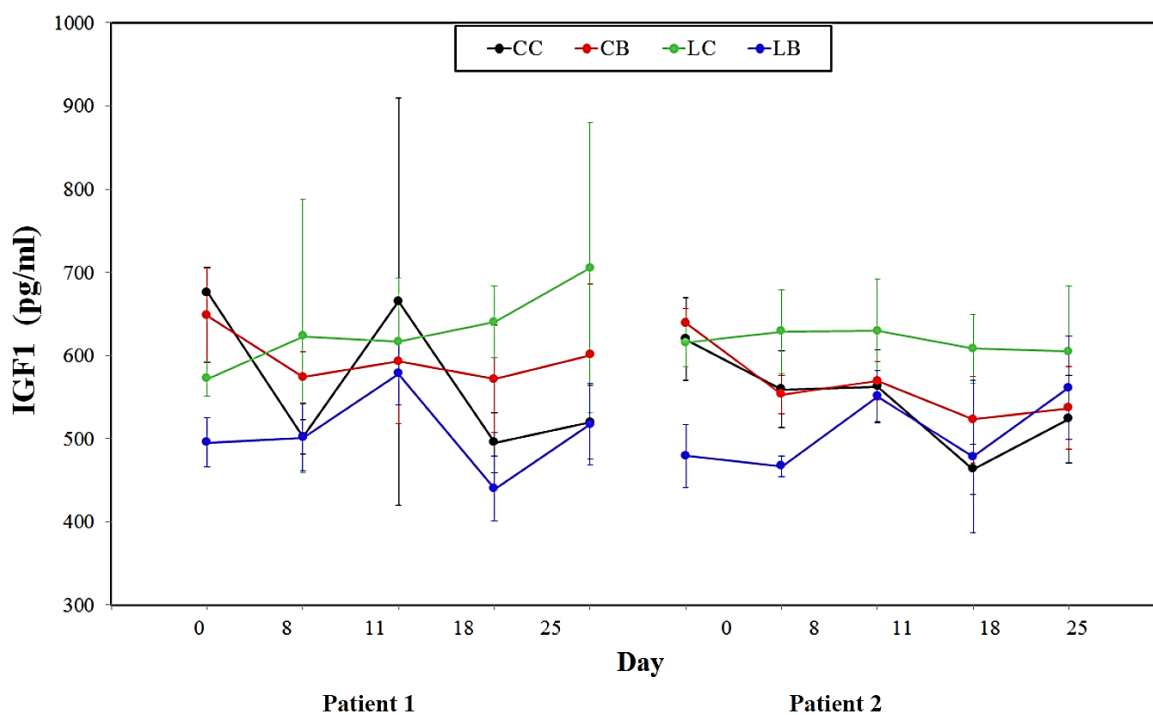
Figure 5.9 - IGF1 secretion for both patients in all treatment groups as measured at given time points. Error bars show 95% confidence interval for each time point.

Kruskal-Wallace tests found significant effects of treatment on DKK1 secretion on days 8 and 18 (p=0.0021, 0.006). Wilcoxon tests found significant increases from baseline in DKK1 secretion on days 8, 11 and 25 in the CB group (p=0.003, 0.001, 0.000). Secretion of DKK1 significantly increased from baseline on days 8 and 11 in the LB group (p=0.031, 0.042) (Figure 5.10). Significant differences were also found on days 8, 11, and 25 between CB and LC groups (p=0.040, 0.050, 0.015) and on days 8 and 18 between the LC and LB groups (p=0.028, 0.003). The patients were also examined separately, and no significant differences were found between patients in any group at any time point (Figure 5.11).
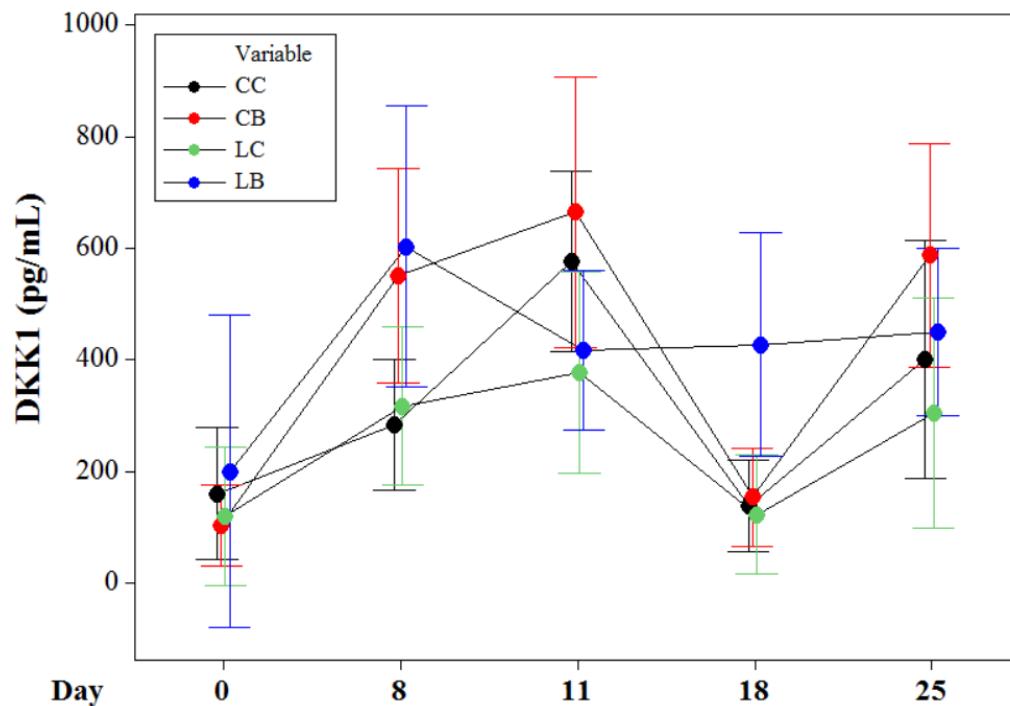
Figure 5.10 - DKK1 secretion in all treatment groups as measured at given time points. Error bars show 95% confidence interval for each time point.
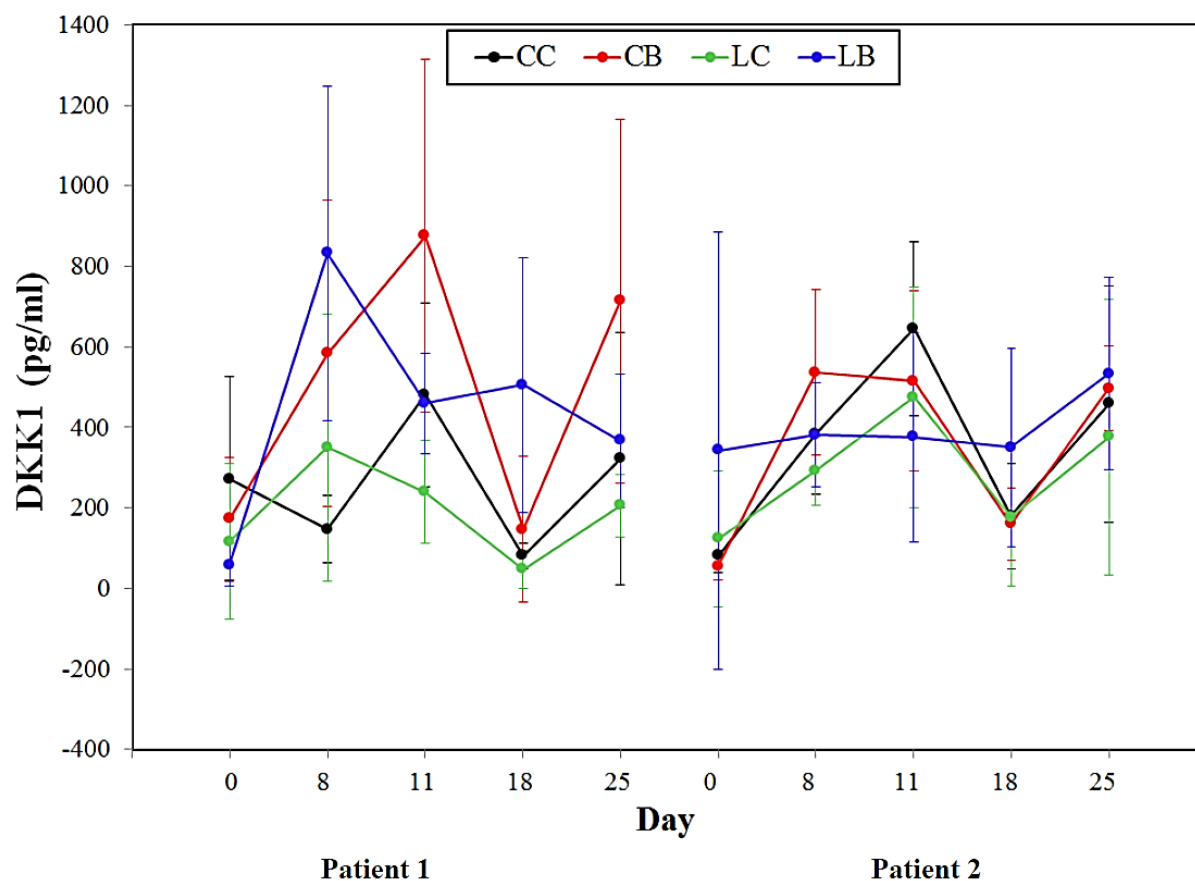
Figure 5.11 - DKK1 secretion for both patients in all treatment groups as measured at given time points. Error bars show 95% confidence interval for each time point.

Kruskal-Wallace tests found significant effects of treatment on PGE2 secretion on day 0 and day 8 (p=0.027, 0.0002). Wilcoxon tests found significant increases from baseline in PGE2 secretion on days 11, 18, and 25 in the CC group (p=0.007, 0.007, 0.0005) and LC group (p=0.016. 0.016, 0.0005). Secretion of PGE2 significantly increased from baseline on days 8 and 18, and 25 in the CB group (p=0.0005, 0.001, 0.0005) (Figure 5.12). Secretion of PGE2 was significantly higher than baseline on days 8 and 25 in the LB group (p=0.002, 0.005). Significant differences were also found on days 8 between the CC and CB groups (p=0.008), between the CC and LB groups (p= 0.000), and between the LC and LB groups (p=0.003). The patients were also examined separately, and no significant differences were found between patients in any group at any time point (Figure 5.13).
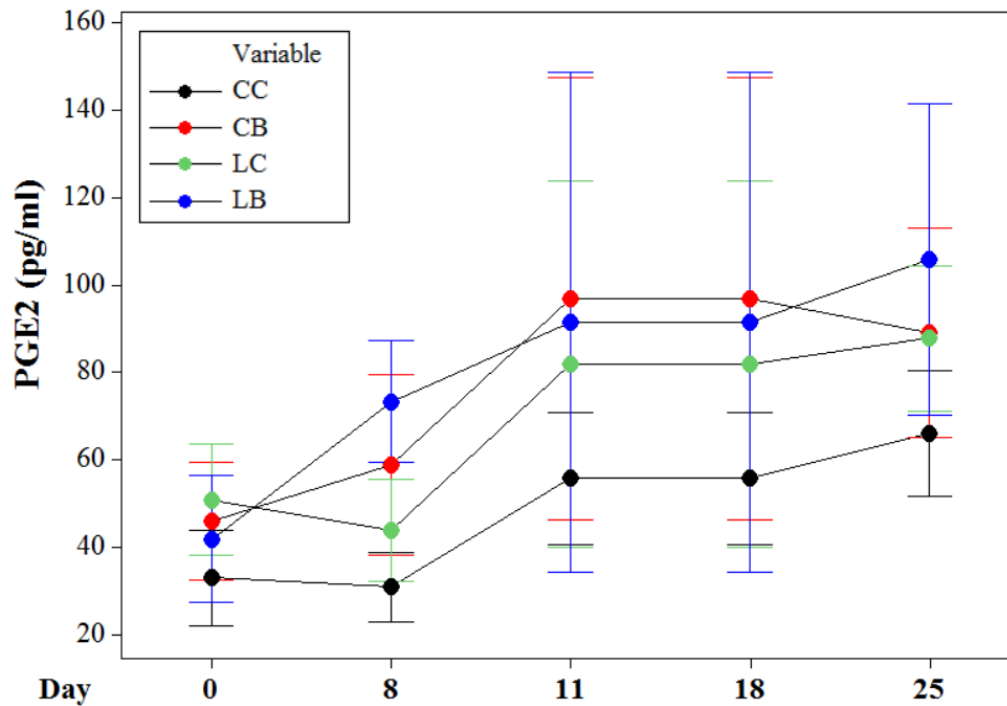
Figure 5.12 - PGE2 secretion for all treatment groups measured at given time points. Error bars show 95% confidence interval for each time point.
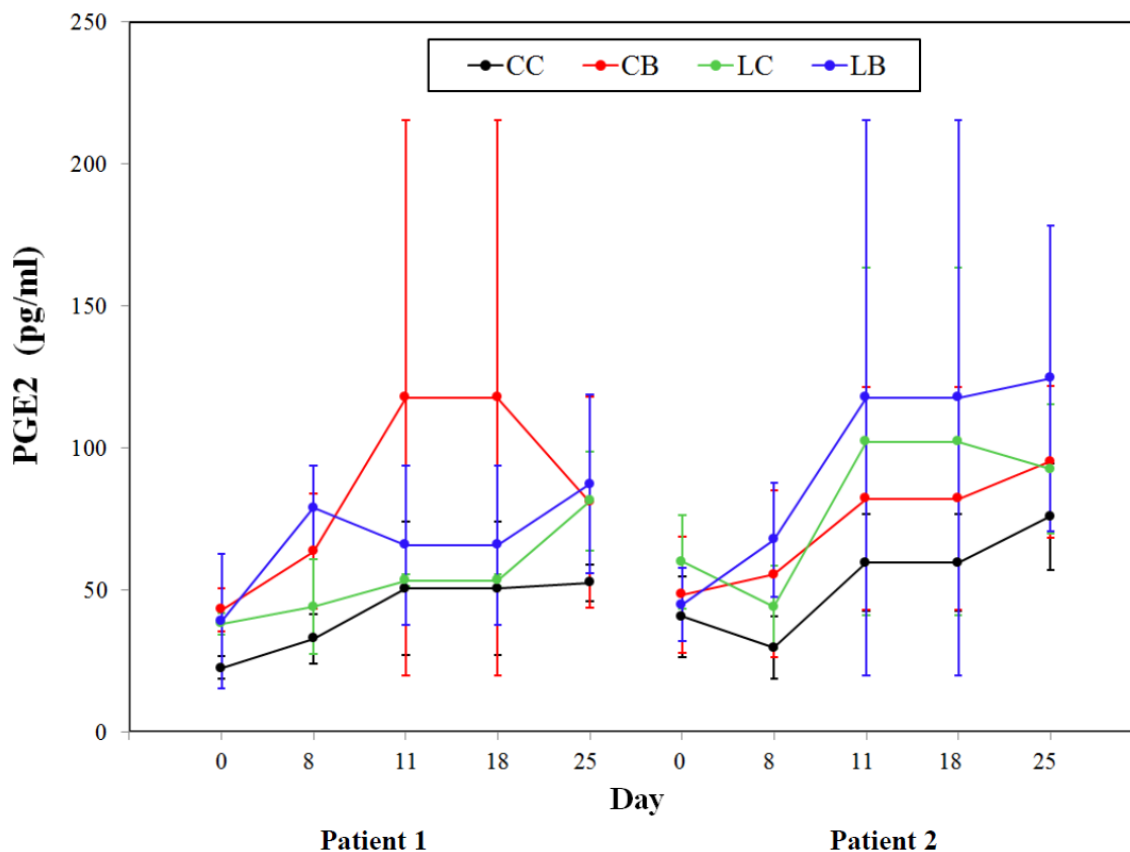
Figure 5.13 - PGE2 secretion for both patients in all treatment groups measured at given time points. Error bars show 95% confidence interval for each time point.

5.5 Discussion

Bone adaptation in response to mechanical stimulus is modulated by the synergistic interactions of stem cells, osteoblasts, osteocytes, and osteoclasts [12,102,103]. Bone adaptation has been successfully studied in a myriad of *ex vivo* studies, illustrating that the use of *ex vivo* organ culture systems is an effective method for investigating whole tissue without complications arising from systemic effects [9,46,48,80,82,83,107]. The ZETOS used in this study is an *ex vivo* organ culture system that has been used successfully in numerous previous studies to investigate bone adaptation [9,46,48,80,82]. These studies, in the same manner as the present study, have implemented both mechanical and biochemical assessments to evaluate bone (bovine, human, and ovine) response to an applied stimulus [9,46,48,80,82].

This is the first study to investigate the possible impact of ET1 blockade and mechanical stimulus on *ex vivo* human trabecular bone adaptation. Overall, the data imply that blockade of ET1 via BQ-123 impedes trabecular bone response to mechanical stimulus. Groups in which ET1 receptor A was antagonized (CB and LB) exhibited increased SOST secretion and decreased IGF1 secretion in response to the applied stimulus. In addition, the ET_A blocked groups also tended to exhibit lower ΔE_{app} compared to the control and load control groups (CC and LC). These results suggest that ET1 signaling is required for human trabecular bone response to mechanical stimulus and indicate that ET1 signaling interacts with pathways that respond to mechanical stimulus.

Overall, the biochemical results support the initial study hypothesis. Increases in secretion of WNT pathway inhibitors SOST and DKK1 in the CB and LB groups and decreases in SOST and DKK1 secretion in the LC group indicate that ET1 signaling interacts with pathways that respond to load. These observed changes in SOST secretion from baseline caused by the applied treatments are also in agreement with results observed *in vivo* [138]. Further, decreased secretion of WNT pathway facilitator IGF1 in groups treated with the ET_A antagonist indicate reduced bone formation and adaptation activity resulting from ET1 blockade. This effect is further demonstrated by higher IGF1 secretion in the CC group and much higher in the LC group compared to the CB and LB groups. Additionally, increased ET1 secretion in blocked groups implies the presence of a feedback loop within the signaling pathway.

While statistical significance was not achieved between treatment groups for the ΔE_{app} measurements, the observed trends supported the initial study hypothesis: ΔE_{app} was lowest in the CB and LB groups and highest in the LC group. Though previous studies with similar experimental setup and low sample sizes have reported statistically significant ΔE_{app} due to mechanical loading [88], the lack of statistical significance in the ΔE_{app} results from the present study could have been influenced by Type II error caused by small sample sizes, high variance, excision methods, and sampling from multiple human subjects with inherently different biology and pathology.

Although the applied dynamic loading regimen (-3000 µε) used for this study was well within the range of accepted and appropriate loads for mimicking physiological activity [19,130–132], the lack of bone tissue response as measured by statistical insignificance in ΔE_{app} could potentially result from mechanically loading the bone cores in a direction that was unaligned with the physiological loading axis pre-excision. *Ex vivo* experiments on bovine trabecular tissue subjected to dynamic loading with a maximum bulk strain of −4000 µε found an average ΔE_{app} of approximately 50% after 21 days [46]. A similar study using bovine trabecular tissue observed lower ΔE_{app} (17–19%) after 23 days [9]. The excision methods implemented for this study were largely designed to maximize the number of usable excised bone cores and not necessarily for machining cores that would share the same loading axis as the previous physiological loading axis in the human hip. This discrepancy could have contributed to the cores' lower than expected response to mechanical stimulus. Clarification of this potential source of error could be achieved through analysis of micro computed tomography scans of the bone cores and determining the degree of anisotropy and magnitude of the fabric tensors for each core.

Type II error could have potentially been exacerbated by the choice of statistical test. Non-parametric methods were chosen for analyses since the data sets including both subjects appeared to be non-normal; however, when the subjects were analyzed for normality individually it was difficult to determine if the data sets were normal or non-normal due to the small sample size. As such, it was impossible to know if non-parametric or parametric methods were the most appropriate when analyzing the samples individually. As stated previously, the Wilcoxon tests found no significant differences between treatment groups for either patient. Using a student t-test found statistical differences between the CC and CB (0.031), CC and LB (0.040), CB and LC (0.012), and LC and LB (0.018) groups for patient one. The discrepancy between results from implementing parametric versus non-parametric statistical methods highlights the inadequacy of normality tests for small data sets and, consequently, the impact of selecting an appropriate statistical method.

Variance in the study results can be attributed to the intrinsic variability in trabecular bone tissue, loss of connectivity caused by the excision process, and the biological and pathological differences between the two subjects from which the bone cores were sourced. In addition to differences in age and gender, the two subjects included in this *ex vivo* study were subject to different medications and other systemically altering medical treatments prior to THA; however, the patients' health history was not known prior to the start of the study and as such, neither subject was deemed unacceptable for inclusion in the *ex vivo* study. Differences in patient pathology and medications history would affect the magnitude of the observed responses of the excised trabecular bone cores to applied mechanical stimulus and ET_A blockade.

There were potential sources of error associated with compression testing of the trabecular bone cores including compliance of the loading machine, and end effects on the sample [99,126–128]. Multiple steps were taken to reduce error and sources of variance in the experimental procedures. The calibrated range for the ZETOS loading system was calibrated prior to the start of the *ex vivo* experiment and found to have a 3% accuracy in E_{app} within the range of 40-1500 MPa [99]. Additionally, the geometry and dimensions of the trabecular bone cores allowed for sustaining specimen viability and satisfied stipulations for continuum assumptions required for implementing Hooke's Law [128]. Although the 5 mm x 10 mm core dimensions and resulting 0.5 aspect ratio are advantageous for preserving specimen viability, it does introduce the possibility of exacerbated end effects; however, since minimal "toe" region was present in the force-displacement data collected during quasi-static testing, any potential end effects appear to be minimal.

5.6 Conclusion

This study successfully demonstrated that ET1 blockade through ETA antagonism inhibits osteogenesis in *ex vivo* human trabecular bone by interfering with signaling pathways responsible for mechanotransduction. This conclusion is supported by observed increases in WNT pathway inhibitors (SOST, DKK1), decreases in WNT pathway facilitators (IGF1), and lower ΔE_{app} in blocked groups

compared to non-blocked groups. The findings of this study will be used for further investigations of bone adaptation and the roles of factors within the WNT pathway on trabecular bone adaptation in response to mechanical stimulus.

Chapter 6

6. Using Morphological and Biochemical Factors to Predict Human Trabecular Bone Stiffness

[1]Department of Biomedical Engineering, University of Wisconsin – Madison,[2]Department of Medicine, University of Wisconsin – Madison, [3]Department of Population Health Sciences, University of Wisconsin – Madison, [4]University of Wisconsin Hospital and Clinics, [5]University of Wisconsin – Madison School of Medicine and Public Health, [6]Department of Mechanical Engineering, University of Wisconsin – Madison

6.1 Abstract

Understanding bone biomechanical behavior is necessary to identify the causes and improve treatment of osteoporosis and other structural and systemic diseases in bone. While it is well documented that mechanical loading promotes bone modeling and remodeling, the additional contributions from mechanotransduction pathways and tissue level morphology are less understood. The purpose of this study was to investigate the impact of biochemical factors on bone stiffness in cores donated by two hip arthroplasty patients. Twenty-four human trabecular bone cores (5 mm x 10 mm) were prepared from bone removed during two hip arthroplasties (48-year-old male, 68-year-old female). The bone cores were allocated to two groups using block randomization based on the donor and apparent elastic modulus (E_{app}) determined on day 0. One group was the control group ("Control") and the other ("Load") was subjected to daily mechanical loading (-3000 $\mu\varepsilon$, 120 cycles daily). The cores were maintained in individual bioreactors for 25 days. A quasi-static compression test of 4000 $\mu\varepsilon$ measured E_{app} on day 22. Culture medium from each sample was analysed for secretion of insulin-like growth factor (IGF1) and Dickkopf protein 1 (DKK1) on days 0, 8, 11, 18 and 25. At the end of the *ex vivo* study, the cores were imaged using a micro-CT scanner at a resolution of 10 μm to calculate the core volume, bone volume/total

volume (BV/TV), bone surface area (BSA), trabecular thickness (T.Th), trabecular spacing (T.Sp), connectivity, degree of anisotropy (Anisotropy) and the structural model index (SMI). The measured biochemical factors and the calculated morphological factors were then combined using principal components analysis to determine the predicting factors for E_{app}. Best general linear model with Akaike Information Criterion was used to determine the appropriate model. A best General Linear Model (GLM) approach was subsequently implemented to determine the factors that could best predict E_{app}. It was found that BV/TV was the best predictor of E_{app} (p=0.022) for both patients.

6.2 Introduction

At least half of women older than 50 years will sustain an osteoporotic fracture within their lifetime [139]. Osteoporosis is a systemic skeletal disease that causes deterioration of bone tissue [140]. Individuals who have sustained osteoporotic fractures have higher (1.3 to 3-fold) mortality risk compared to those who have not experienced fracture [3]. Understanding bone biomechanical behavior is imperative for identifying the causes and improving the treatment options for osteoporosis and other systemic, degenerative bone diseases.

Mechanical loading has been proven multitudinously to promote bone modeling and remodeling; however, the additional contributions from mechanotransduction pathways and tissue level morphology are less understood [74]. Previous studies (conducted by the authors and others) have investigated the effects of compression testing to -2000 µε and -4000 µε on *ex vivo* trabecular bone cores and found that mechanical loading causes bone adaptation, quantified by percent change in apparent elastic modulus (ΔE_{app}), biological markers of bone formation, and histological evidence of osteogenesis [9,46,48,80,82].

Bone adaptation is also largely affected by genetic factors. Specifically, cellular signaling pathways, such as the WNT pathway, and factors responsible for pathway modulation occupy a dominant role in controlling bone mechanotransduction where up- or down-regulation of key factors can cause bone

formation or resorption [40,86,92,133]. Monitoring the secretion of select WNT pathway factors can provide evidence of bone adaptive activity [133,141].

Bone mechanical properties can be used to assess bon health. Non-invasive methods for assessing bone mechanical properties, specifically bone stiffness, are often implemented for diagnosing and predicting the onset of degenerative bone diseases such as osteoporosis [60,61]. Previous studies have investigated the ability of computed tomography (CT) imaging to non-invasively determine the bone stiffness [60,61]. Using CT imaging, the macro- and micro-level structure of bone tissue can be characterized. Depending on the scanner resolution, metrics including bone volume, trabecular thickness, trabecular spacing, connectivity and degree of anisotropy can be measured. Unfortunately, CT imaging alone is often insufficient for accurately determining bone mechanical properties since metrics determined from CT imaging are not the sole contributors to bone mechanical properties and do not incorporate any pathological factors.

The purpose of this study was to determine which CT-based metric could best predict E_{app} in trabecular bone tissue that are subject to regular mechanical stimulus and bone tissue that is not regularly stimulated. In addition, the study aimed to investigate if CT-based prediction of bone stiffness could be enhanced with knowledge of biochemical factors. The study hypothesis was that prediction of bone stiffness using CT imaging could be improved by including biochemical factors.

6.3 Materials and Methods

The study hypothesis was tested by conducting an *ex vivo* investigation on human trabecular bone tissue excised from the femoral hip heads of two patients undergoing total hip arthroplasty (THA). Two human femoral heads were donated by one 48-year-old male and one 68-year-old female donor undergoing THA. The implemented protocol was approved by the Institutional Review Board at the University of Wisconsin – Madison and consent was obtained from both donating individuals. Twenty-four bone cores were excised from the two femoral heads and subsequently maintained in bioreactors for

25 days. The bone cores were allocated to two treatment groups: Control and Load. The cores in the Control group were maintained for the duration of the experiment without any applied mechanical stimulation. The cores in the Load group were mechanically loaded daily (-3000 µε, 120 cycles daily, "jump" waveform) using the ZETOS Bone Loading and Bioreactor System (ZETOS) to mimic trabecular bone tissue subjected to regular physiological activity [9,45,46,48,80,82]. Both groups were assembled such that both had approximately the same mean apparent elastic modulu1s (E_{app}) and number of cores from each donor hip. Modeling and remodeling of the bone cores was monitored through changes in E_{app} (ΔE_{app}), Dikkopf protein (DKK1), and insulin growth factor (IGF1).

6.3.1 Preparation and Culture of Bone Cores for Ex Vivo Study

Two femoral heads were donated by two THA patients (48-year-old male, 68-year-old female). Trabecular bone cores (5mm height, 10 mm diameter) were excised immediately upon receipt of the femoral heads which had been excised no longer than 30 minutes prior. The entire excision and machining process of the bone cores was executed under sterile conditions derived from the protocols developed by Smith and Jones [45]. Femurs were first sliced into parallel 7 mm sections using a diamond band saw (Exact, Norderstert, Germany). Cores measuring 10 mm in diameter were then excised from the femoral sections with a diamond-tipped coring bit and subsequently milled on both terminal axial ends to a final height of 5mm. Bone cores were washed with culture medium to eliminate debris remaining from excision and to reduce risk of infection. Cores were then placed into polycarbonate chambers and mechanically tested quasi-statically in compression to -4000 µε to ascertain the axial stiffness (K_{axial}) and, consequently, E_{app}. To promote bone core viability for the duration of the 25-day *ex vivo* portion of the study, culture medium (Dulbecco's Modified Eagle Medium) was constantly perfused through each bioreactor (6.6 ml/hr) using peristaltic pumps (Ismatec ISM939D, IDEX Health & Science SA, Glattburgg, Switzerland) and maintained at a pH of 7.2-7.3. The entire *ex vivo* culture was kept in a constant 37°C environment to mimic physiological conditions.

6.3.2 Ex Vivo Data Collection

The bone cores were rested for 48 hours post-excision before initiating mechanical stimulus treatments. Bone cores in the Load group were dynamically loaded on a daily basis using ZETOS. The loading protocol mimicked a "jump" waveform generated from normative human jump data and consisted of cyclic (120 cycles, 0.5 sec/cycle) compression to a maximum bulk strain of 3000 $\mu\varepsilon$ [78,82]. The E_{app} for each bone core in both the Control and Load groups was measured quasi-statically (maximum bulk strain = -4000 $\mu\varepsilon$) using the ZETOS system weekly (days 1, 8, 15, 22) and assuming Hooke's Law [102]. Bone core adaptation ton in response to mechanical stimulus (Load group) was quantified by calculating ΔE_{app}.

The culture medium from each bone core was changed daily and samples were collected on days 0, 8, 11, 18, and 25. Culture medium samples were analyzed with appropriate enzyme linked immunosorbent assays (ELISA) to determine secreted amounts of DKK1 and IGF1—a WNT signaling pathway inhibitor and promotor, respectively.

6.3.3 CT-Image Analysis of Bone Cores

At the conclusion of the *ex vivo* study, all bone cores were imaged with micro-CT (μCT) (Siemens microCATII, 34 μm, 80 kVp, 50 μA) (Figure 6.1). Scans were then analyzed using Mimics (Materialise, Leuven, Belgium) and BoneJ (ImageJ, National Institute of Health) to determine the bone core volume (BV), bone volume/total volume (BV/TV), bone surface area (BSA), trabecular thickness (T.Th), trabecular spacing (T.Sp), connectivity, degree of anisotropy (Anisotropy), structural model index (SMI), and fabric tensor direction (FabricTensor) [142].
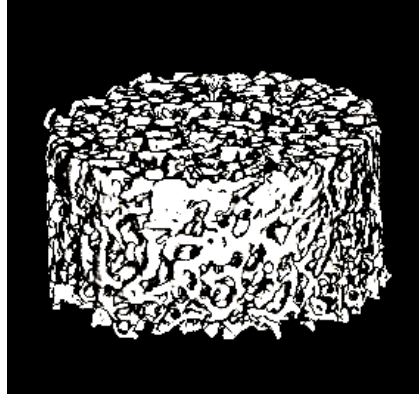
Figure 6.14 - Micro CT scan of human trabecular bone core. Scan taken at the end of the ex vivo study.

6.3.4 Statistical Analysis of Collected Data

The means and standard deviations for each measured or calculated parameter were determined. Values that were more than three standard deviations away from the mean were considered to be outliers and were omitted from statistical analysis. The combined mechanical, biochemical, and morphological data sets for both patients were found to be non-normal. The data sets for each individual patient contained too few samples to confirm normality or non-normality.

To determine potential correlations between factors (mechanical, biochemical, and morphological), Principal Component Analysis (PCA) was conducted on the data from the final day of the study (Day 22 for E_{app} and Day 25 for all other factors). Since PCA is sensitive to both the scale of each factor and the variance for each factor, all data sets were transformed using logarithmic functions and subsequently standardized using the mean and standard error.

A best Generalized Linear Model (GLM) analysis was conducted on a subset of the measured factors to determine the best model for predicting E_{app}. The best GLM analysis was conducted using results from the PCA analysis and including the five factors having the largest first principal component and eigen values greater than one. The three factors containing the largest principal component were used for a best GLM analysis on data sets for individual patients due to the smaller sample size. The models were compared by calculating the Akaike Information Criterion (AIC) for each model. The model with

the lowest AIC value was considered the best model. The goodness of fit for the model was determined using a Hosmer-Lemeshow test.

6.4 Results

The mean and standard error of E_{app} on day 22 for all 24 cores in both the Control and Load groups were $E_{app} = 499 \pm 86.4$ MPa. The mean and standard error of E_{app} on day 22 for the cores excised from patient 1 were $E_{app} = 260 \pm 30.7$ MPa. The mean and standard error of E_{app} on day 22 for the cores excised from patient 2 were $E_{app} = 671 \pm 130$ MPa (Figure 6.2). Wilcoxon tests found no significant differences in E_{app} on day 22 between patients (0.082), between treatment groups (0.072), or between patients within treatment groups (0.625). No statistical differences were found between patients, between treatment groups, or between patients within treatment groups for any of the calculated morphological factors (BV, SA, BSA/BV, BV/TV, T.Th, T.Sp, Connectivity, Anisotropy, SMI, or Fabric Tensor) (Figure 6.3). Secretion of IGF1 on day 25 was significantly different (p=0.018) between the Control and Load groups and nearly significant between patients in the Load group (p=0.063) (Figure 6.4). No significant differences in DKK1 secretion were found between patients, treatment groups, or between patients within treatment groups. The results from the *ex vivo* study, μCT scans, and post-scanning analysis are Table 6.1, 6.2, and 6.3, respectively.
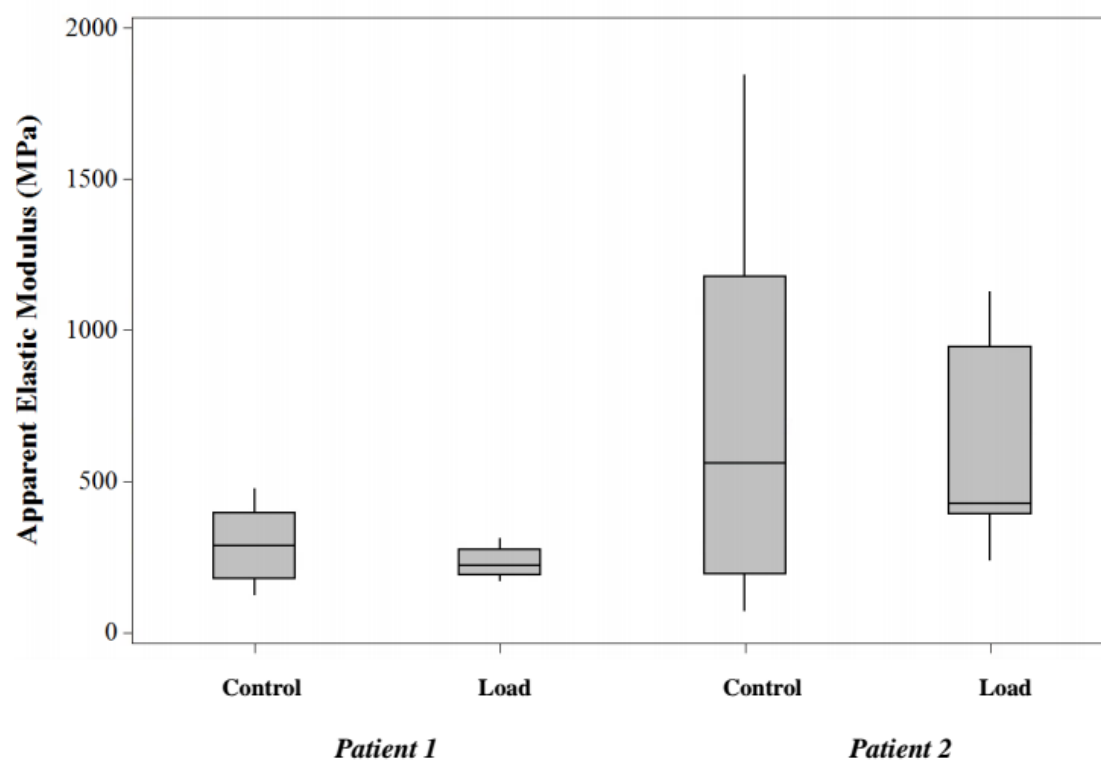
Figure 6.2 - Apparent elastic modulus for each patient in both treatment groups. Error bars show 95% confidence interval. Patient 1 and Patient 2 represent data from the female and male patients, respectively.
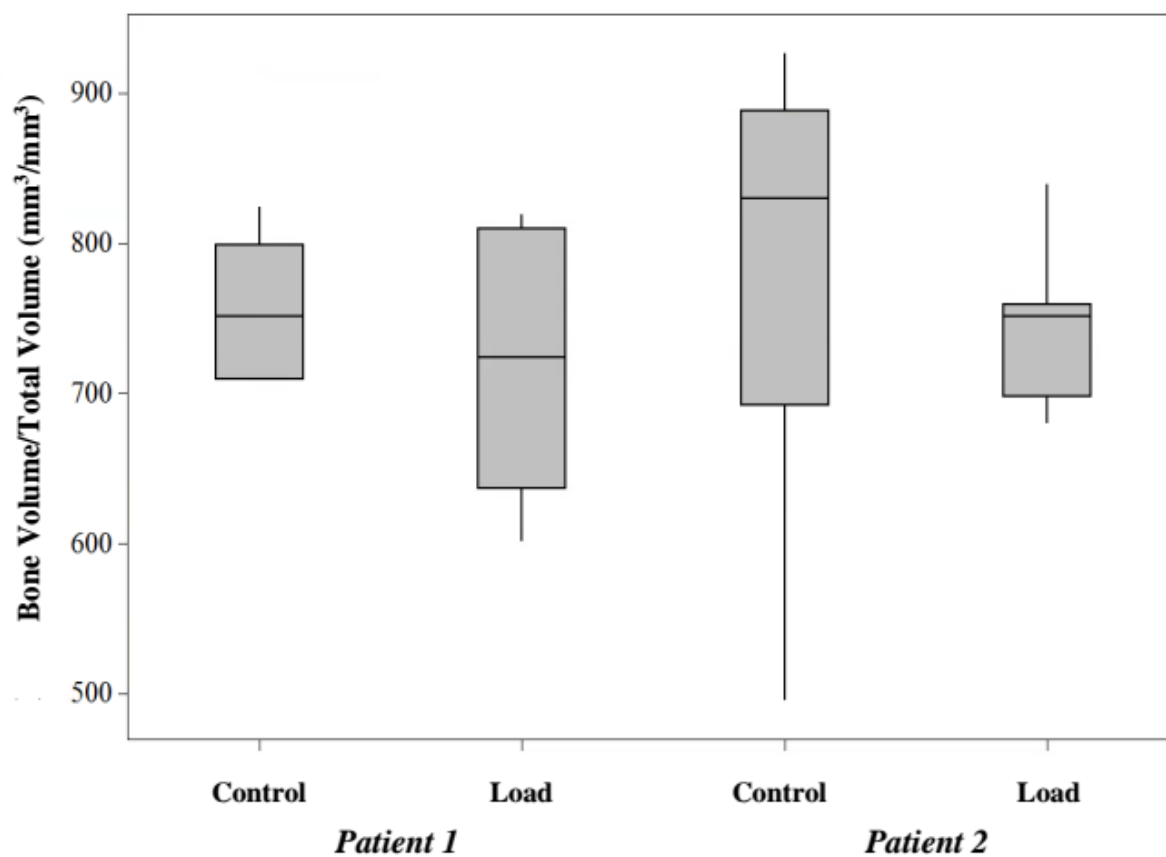
Figure 6.3 - Bone volume/Total volume for each patient in both treatment groups. Error bars show 95% confidence interval. Patient 1 and Patient 2 represent data from the female and male patients, respectively.
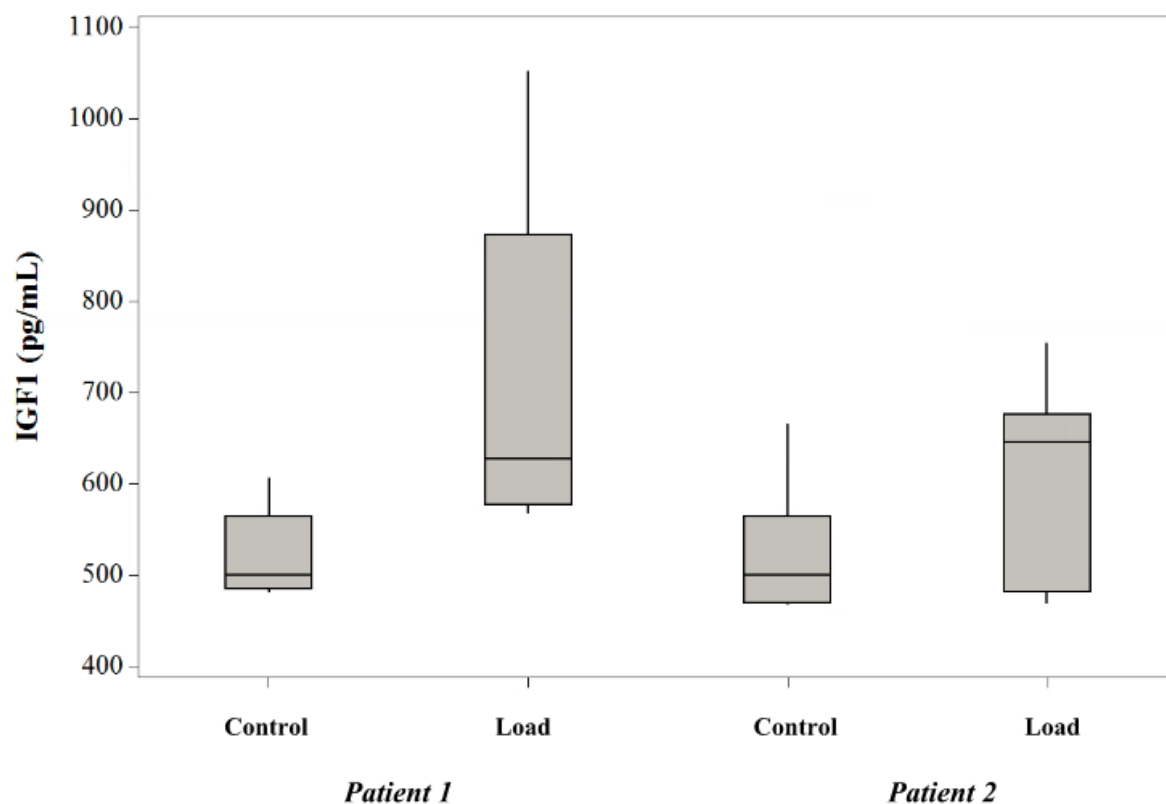
Figure 6.4 – IGF1 secretion for each patient in both treatment groups. Error bars show 95% confidence interval. Patient 1 and Patient 2 represent data from the female and male patients, respectively.

Table 6.1 - Summary of ex vivo study results. Means and standard error are shown for each parameter

		Final E_{app} (MPa)	ΔE_{app} (%)	IGF1 (pg/mL)	DKK1 (pg/mL)
Control	*Patient 1 (Female)*	288 ± 57.6	33.6 ± 12.8	520 ± 22.8	321 ± 160
	Patient 2 (Male)	703 ± 235	31.2 ± 9.20	524 ± 26.8	458 ± 150
Load	*Patient 1 (Female)*	231 ± 23.0	39.2 ± 11.8	706 ± 89.2	205 ± 39.5
	Patient 2 (Male)	639 ± 131	14.2 ± 4.30	605 ± 40.2	376 ± 175

Table 6.2 - Summary of bone core morphological properties as determined from µCT imaging. Means and standard error are shown for each parameter.

		Bone Volume (mm³)	Bone Surface Area (mm²)	Bone Surface Area /Bone Volume (mm²/mm³)	Bone Volume/ Total Volume (mm³/mm³)	Trabecular Thickness (µm)	Trabecular Spacing (µm)
Control	*Patient 1 (Female)*	1050 ± 74	1505 ± 49	1470 ± 129	0.847 ± 0.03	2284 ± 171	189 ± 16
	Patient 2 (Male)	942 ± 45	1535 ± 66	1483 ± 88	0.844 ± 0.02	2563 ± 169	176 ± 17
Load	*Patient 1 (Female)*	1053 ± 64	1420 ± 79	1529 ± 135	0.835 ± 0.02	2360 ± 153	203 ± 15
	Patient 2 (Male)	927 ± 42	1342 ± 70	1465 ± 92	0.848 ± 0.02	2085 ± 96.9	180 ± 14

Table 6.3 - Summary of bone core trabecular orientation properties as determined from μCT image analysis. Means and standard error are shown for each parameter.

		Connectivity (mm²)	Structural Model Index	Anisotropy	Fabric Tensor Alignment (Θ)
Control	*Patient 1 (Female)*	1.78 ± 0.35	-1.54 ± 1.5	0.54 ± 0.02	52.6 ± 2.0
	Patient 2 (Male)	1.48 ± 0.12	-2.26 ± 1.1	0.51 ± 0.04	53.7 ± 1.3
Load	*Patient 1 (Female)*	1.19 ± 0.08	-1.29 ± 1.2	0.60 ± 0.06	52.1 ± 4.0
	Patient 2 (Male)	1.58 ± 0.21	-2.33 ± 0.97	0.50 ± 0.02	50.9 ± 2.0
	Context	*Anisotropy: isotropic = 0, anisotropic = 1* *SMI: plate = 0, rod = 3, sphere = 4, concave < 0* *Fabric Tensor alignment: angle relative to preferential direction of loading*			

After collection of data, the values for each parameter on the last day of the study were individually compared to each other to determine potential correlations. Linear regressions were generated for each paired combination of factors. Figure 6.5 shows a summary of the results correlation coefficients for the parameters and Figure 6.6 shows the corresponding p-values for each correlation coefficient between parameters. P-values for each comparison were corrected using the Benjamini and Hochberg method to adjust for multiple comparisons. From the linear regressions, BV/TV, BSA/BV, Anisotropy, T.Sp, and Connectivity were the most highly correlated with bone core Final E_{app}, having correlation coefficients of -0.83 (p=0.00), 0.77 (p=0.00), 0.9 (p=0.00), 0.84 (p=0.00), and 0.8 (0.00), respectively. Biochemical factors had much lower and statistically insignificant correlation coefficients of -0.52 (p=0.1) and 0.25 (p=0.43) for IGF1 and DKK1, respectively.
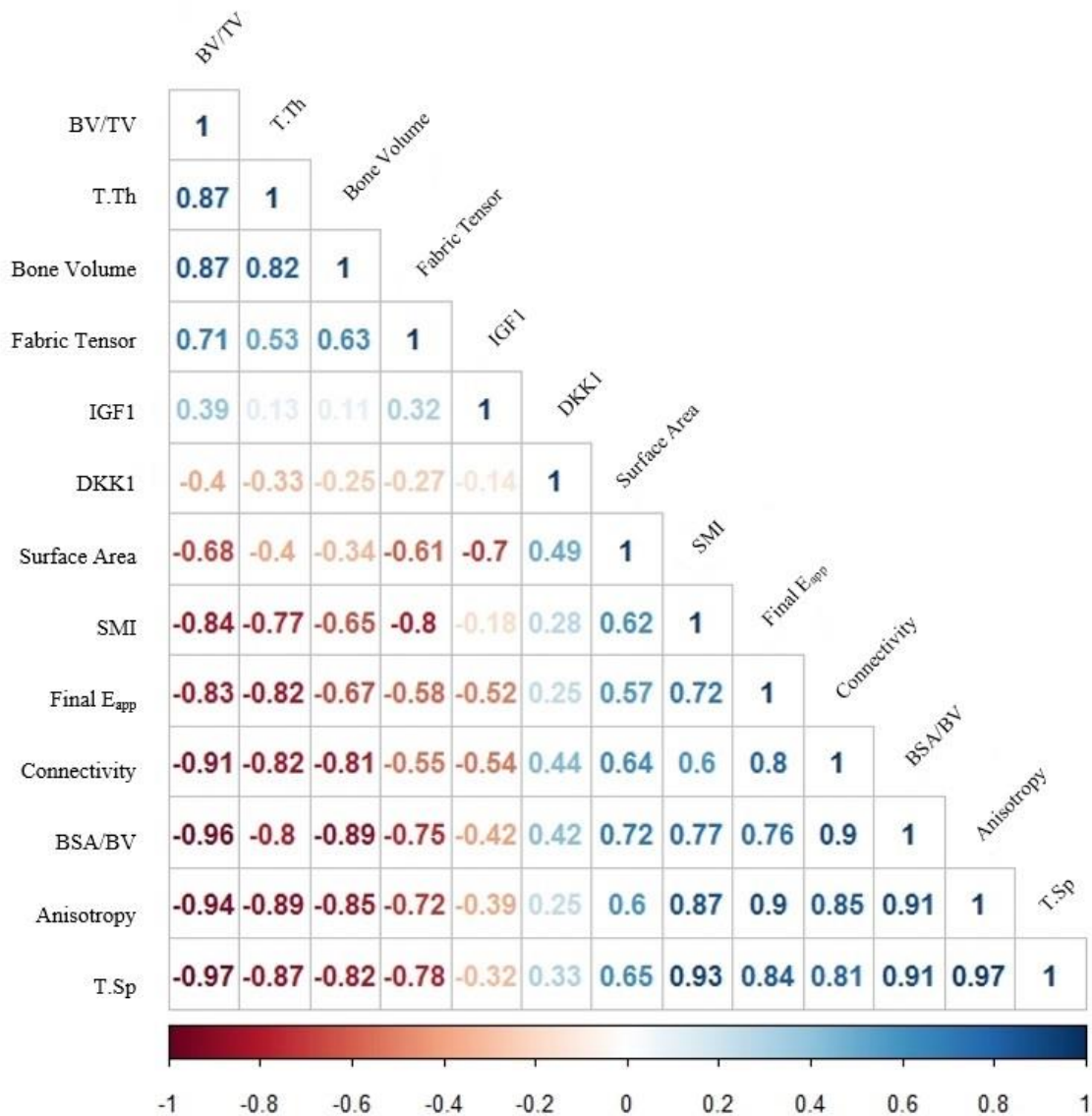
Figure 6.5 - Correlation plot for factors measured during ex vivo study and during µCT scanning of trabecular bone cores. Color scheme relates to the correlation coefficient and corresponds to the bottom x-axis of the plot. The values present in each cell indicate the correlation coefficient for each correlation between the two corresponding factors.
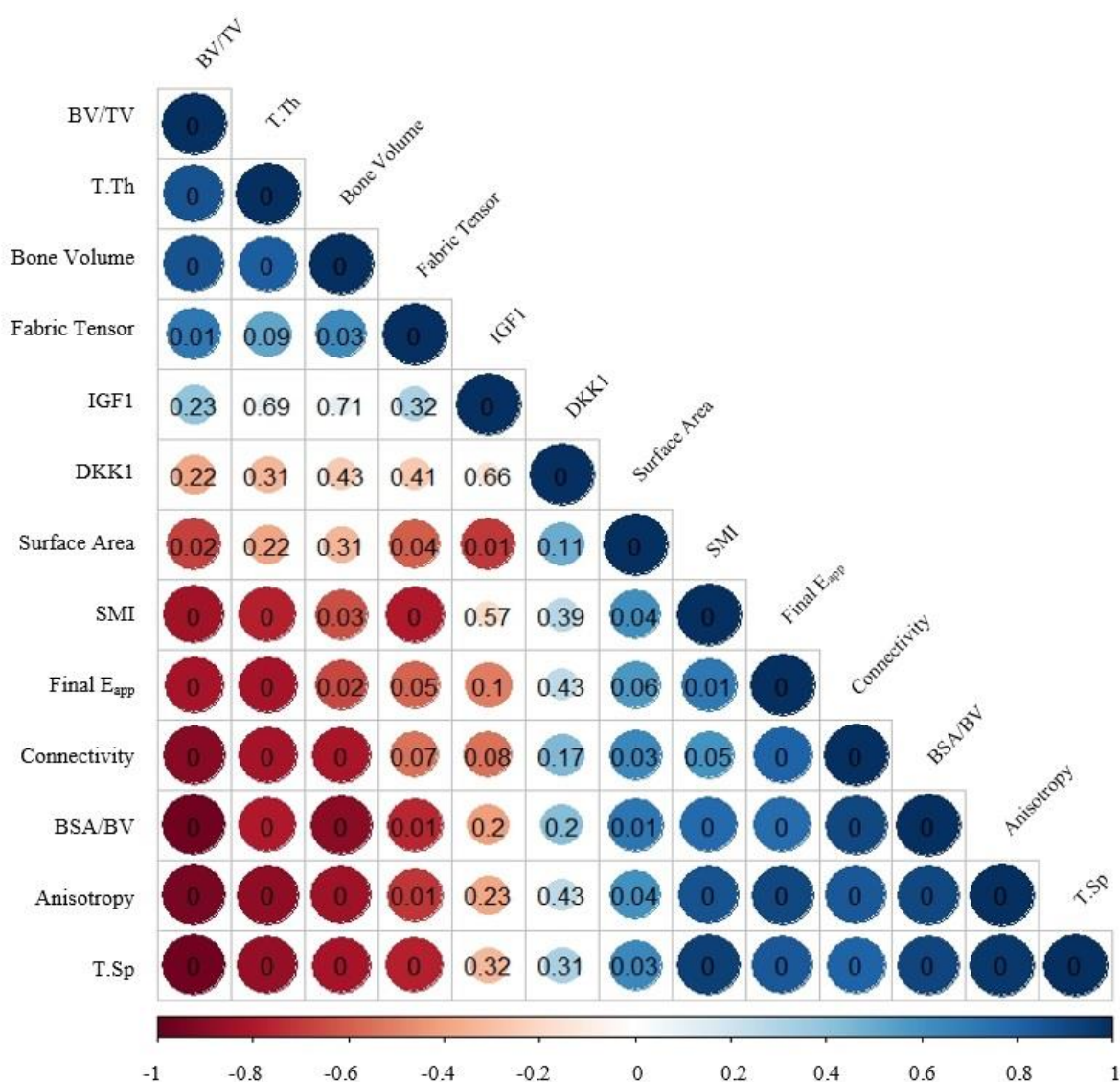
Figure 6.6 - Correlation plot for factors measured during ex vivo study and during μCT scanning of trabecular bone cores. Color scheme indicates the correlation coefficient and corresponds to the bottom x-axis of the plot. The values present in each cell indicate the adjusted p-value for each correlation between the two corresponding factors.

Principal Component Analysis was subsequently conducted to determine the contributions of measured parameters to the final apparent stiffness (E_{app}) of the trabecular bone cores. The complete list of factors and their first and second principal components are listed in Table 6.4. Figure 6.7 shows the loading plot for the PCA results.

Table 6.4 - Summary of principal components for factors contributing to trabecular bone core E_{app}. Factors above the dotted line indicate the five factors with the highest first principal component.

Factor	Principal Component	
	1st	2nd
Bone Volume/Total Volume	0.3919	0.0318
Trabecular Spacing	-0.3913	-0.0334
Bone Surface Area/Bone Volume	-0.3823	0.0503
Anisotropy	-0.3571	-0.0324
Connectivity	-0.3038	0.0698
Structural Model Index	-0.2907	0.0374
Bone Volume	0.2725	0.4561
Trabecular Thickness	0.2688	0.3215
Bone Surface Area	-0.2073	0.6129
Fabric Tensor	0.1878	0.0009
DKK1	-0.1061	0.2995
IGF1	0.0822	-0.4597
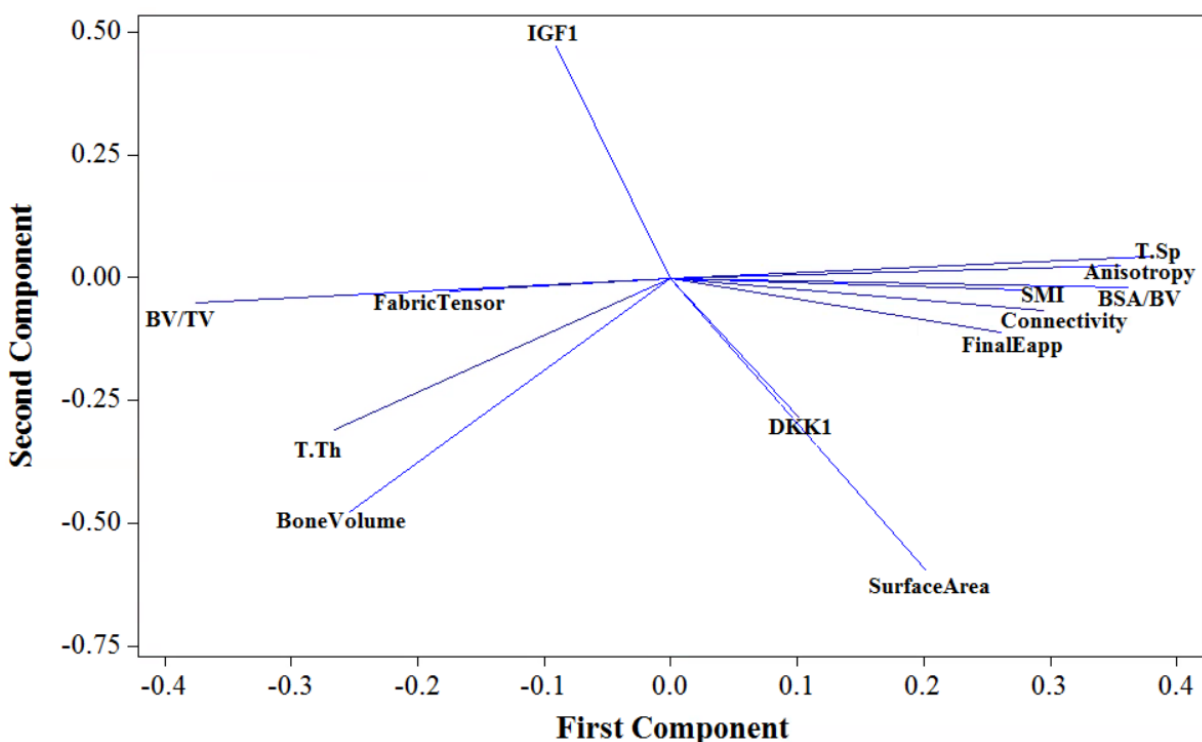
Figure 6.7 - Loading plot for factors contributing to trabecular bone core E_app. Labeled vectors illustrate the relative direction and magnitude of the first two principal components for each factor.

A best general linear model (GLM) analysis was conducted on the combined data set for both patients to determine the best linear model for predicting E_app using the five highest correlated factors identified with PCA. The model with the lowest Akaike information criterion (AIC) was selected as the best model. Best GLM results showed that a model using only Bone Volume to Total Volume ratio (BV/TV) had the best predictive capability with a correlation coefficient of -0.83 (p=0.022) (Equation 6.1, Figure 6.8). The Hoslem-Lemeshow test was used to determine goodness of fit (p=1). A model having only a marginally higher AIC included only T.Sp (correlation coefficient = -0.97, p=0.022) to predict E_app (Equation 6.2, Figure 6.9).

$$\textbf{Equation 6.1} \qquad \mathbf{E_{app,1,2} = -4069\, \frac{BV}{TV} + 3933}$$

$$\textbf{Equation 6.2} \qquad \mathbf{E_{app,1,2} = 5.247\, T.Sp - 474.6}$$
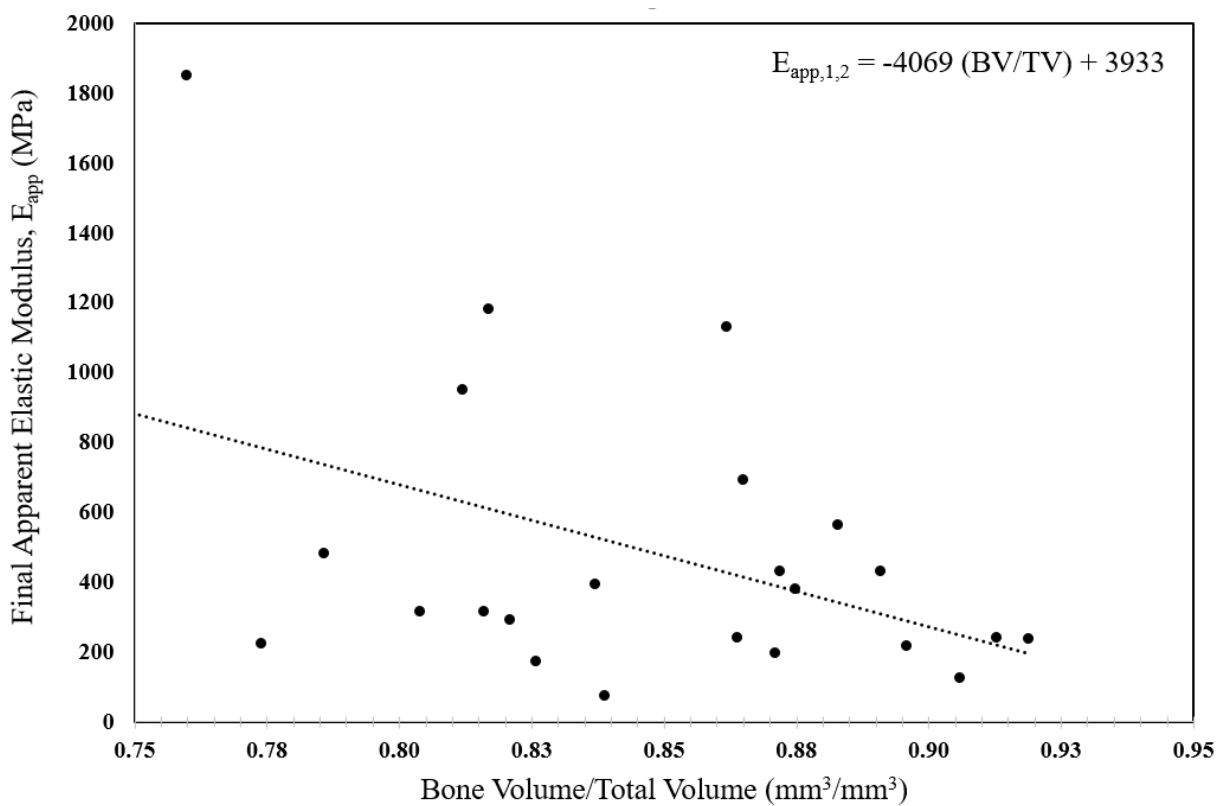
Figure 6.8 - Final E$_{app}$ versus Bone Volume/Total volume for both patients with best GLM shown

$$E_{app,1,2} = -4069\,(BV/TV) + 3933$$
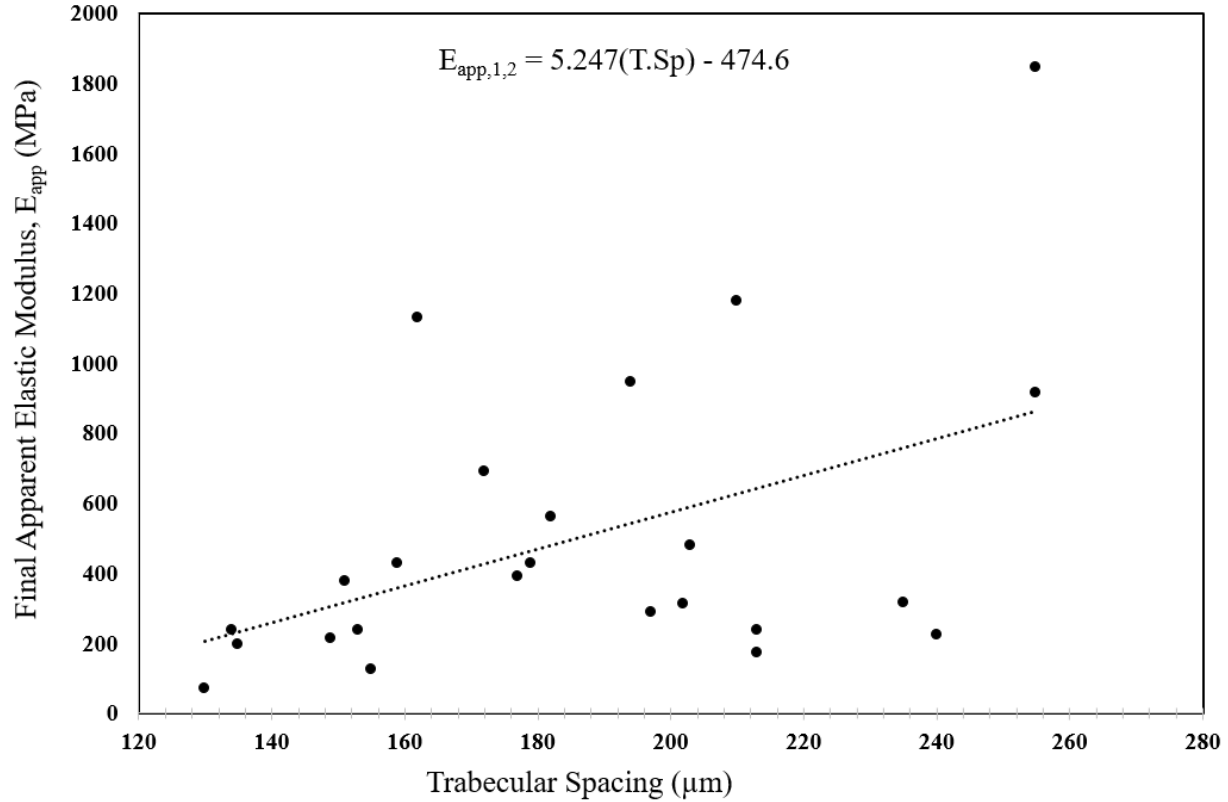
Figure 6.9 - Final E_{app} versus trabecular spacing for both patients with second best GLM shown

The best GLM approach was used to determine the best predictors for Eapp within each patient data set using the three highest correlated factors identified with PCA. Using data exclusively from patient 1 (female), the best model (with the lowest AIC) included both BSA/BV (p=0.0038) and BV/TV (0.0016) (Equation 6.3). The next best model for the female patient included T.Sp in addition to BSA/BV and BV/TV. Data exclusively from patient 2 (male) showed that the best model required only T.Sp (p=0.00046) (Equation 6.4). The next best model for the male patient included BSA/BV in addition to T.Sp. The best GLM models for the female and male patients both passed the Hosmer-Lemeshow goodness of fit test with p-values of 1.

$$\text{Equation 6.3} \qquad E_{app,p1} = -5938\,\frac{BV}{TV} - 0.9275\,\frac{BSA}{BV} + 6646$$

$$\text{Equation 6.4} \qquad E_{app,p2} = 9.845\,T.Sp - 1084$$

6.5 Discussion

Bone mechanical and material properties are dependent on both the tissue composition and tissue morphology [12,143]. The overarching goal of this study was to determine how to improve prediction of E_{app} using CT-based metrics and biochemical data. The primary aim of the study was to determine the most appropriate CT-based metric for predicting E_{app}. Furthermore, it was hypothesized that prediction of trabecular bone E_{app} could be improved by inclusion of biochemical factors related to WNT pathway signaling, and consequently, bone modeling, remodeling, and homeostasis.

Overall, the study showed that Bone Volume/Total Volume is the best CT-based parameter for predicting the apparent elastic modulus of human trabecular bone cores that are both mechanically stimulated and not stimulated. Principal component analysis showed that the morphological properties of the bone cores determined from µCT generally had the largest first principal component, indicating the biggest contribution to elastic modulus. The measured biochemical factors IGF1 and DKK1 generally had larger second principal components compared to the morphological factors indicative of a secondary role in contributing to the bone core E_{app}. Using the five parameters with the largest principal components, the best GLM approach demonstrated that the best predictor for E_{app} was solely BV/TV.

The PCA and subsequent best GLM analyses were for both patients individually and using three factors to adjust for the smaller sample size. Using the female patient data only, it was determined that the best prediction of E_{app} was only possible using both BV/TV and BSA/BV. PCA and linear regression analyses demonstrated strong correlations between factors descriptive of trabecular architecture and trabecular bone E_{app}. Although many of these morphological factors were not determined to provide best predictive capability for E_{app}, a few factors including Connectivity, Anisotropy, and T.Sp were identified as strongly correlating to E_{app}. The lack of statistical significance between many of the parameters describing trabecular bone morphology and trabecular bone E_{app} could have been largely influenced by small sample sizes, high variance among the measured parameters, and the method used for excising the

bone cores from the donated tissue. Moreover, variability and subsequent Type II error within the presented results could be attributed to excising trabecular bone cores from two patients with inherently different underlying biology and pathology and exacerbated further due to differences in age.

Additional variability could have been introduced during the process through which mechanical stimulus was applied during the *ex vivo* study or from loss of connectivity resulting from the bone core excision process. It is also possible that the µCT scanner or scanner settings used for determination of the trabecular bone core morphological parameters were not ideal for accurately capturing the necessary detail of the trabecular bone structure.

Although the study hypothesis was that inclusion of biochemical factors in addition to CT-based parameters would improve E_{app} prediction, the study results showed that the best predictors for trabecular bone core E_{app} did not include biochemical factors. While IGF1 and DKK1 were not found to be significantly correlated to E_{app}, PCA found that the second principal components of IGF1 and DKK1 were largest compared to the measured morphological parameters, indicating a secondary role in contributing to the mechanical properties of the trabecular bone tissue. Further biochemical contributions could potentially be observed if other factors were monitored. Although this study only monitored the secretions of IGF1 and DKK1 (WNT pathway promotor and inhibitor, respectively), it is possible that other related biochemical factors, especially those contributing to the WNT signaling pathway, play a greater role in the contributing to the mechanical properties of trabecular bone tissue.

While it is possible that presented results were influenced by the aforementioned sources of variability and consequent Type II error, the study showed that non-invasive, CT-based methods have high potential for accurately predicting trabecular bone mechanical properties. Given that one CT-based parameter, BV/TV, was statistically significantly correlated to E_{app} for trabecular bone cores in both the Control and Load groups, for the pooled groups with cores from both patients, and individually for each patient indicates that E_{app} prediction could be possible for a wide range of patient populations.

6.6 Conclusion

This study successfully demonstrated that human trabecular bone E_{app} can be predicted by Bone Volume/Total Volume as measured using μCT. The study also showed that biochemical factors affecting tissue signaling pathways have a secondary role in contributing to trabecular bone E_{app} but are not necessary for prediction of E_{app} given CT-based parameters. Further study should be conducted to validate the predictive models generated in the present study and to determine how predictive methods could be improved for specific patient populations.

Chapter 7

7. Macro-, Micro-, and Nano-level Mechanical Analysis of Injection Molded Beta Tricalcium Phosphate Bone Scaffolds

Collaborators on this project include JF Vivanco[1], J Slane[2], and H-L Ploeg[2]

[1]Facultad de Ingeniería y Ciencias, Universidad Adolfo Ibáñez – Chile, [2]Department of Mechanical Engineering, University of Wisconsin – Madison

7.1 Abstract

Voids in bone tissue can be repaired through the implantation of porous three-dimensional (3D) scaffolds that support and stimulate existing tissue. Tricalcium phosphate (TCP) is used extensively in clinical and research applications due to its biocompatibility and bioresorbability. Since the success of scaffolds is greatly dependent on their ability to osteointegrate, it is imperative to understand their mechanical behavior and appropriately select material to use for scaffolds that would mimic not only bone morphology, but also bone mechanical properties. Fifty TCP scaffolds were injection molded (approximate bulk dimensions: 5.4x5.4x4.2mm^3) and sintered at 950°C, 1050°C, and 1150°C. A finite element (FE) model was made using bulk dimensions of the scaffold. The model was compressively loaded in two orthogonal directions (Abaqus 6.11, Simulia) to mimic mechanical testing of the actual scaffold samples (quadratic tetrahedral elements, 0.2 mm). The E_{app} of the simulated scaffold was calculated from the maximum force and deflection, assuming Hookean behavior. The analysis was done using the micro-level elastic modulus (E_{micro}) and the nano-level elastic modulus (E_{nano}). The results of the FE model were compared to experimental data collected previously by authors. The FE analysis produced E_{app} values that were 1.5-2.8 times larger than experimental results using E_{nano} and E_{mico};, however, using E_{nano} produced results that were closer to experimental results by 5%, 8%, and 33% for the scaffolds sintered at 950 °C, 1050 °C, and 1150°C, respectively. Based on the results of the FE analysis, the bulk properties of the bone scaffold more closely matched the material properties of the TCP on the nano-

level. This implies that the bulk mechanical properties of the scaffold are more affected by the nano-level material and mechanical properties than on the micro-level. Therefore, manufacturing control variables for injection molded TCP scaffolds should be selected based on their effect on the nano-level mechanical and material properties of the intended scaffold design. Limiting factors include idealization of the scaffold geometry implemented in the FE model and lack of TCP porosity consideration. Future studies should include more representative scaffold geometry from micro computed tomography images, for use in the FE model and account for additional TCP material properties such as porosity.

7.2 Introduction

Approximately half of clinically reported injuries are musculoskeletal [1]. These injuries can arise from a multitude of causes, though many are the result of bone tissue fracture [1,144]. Bone fracture can be caused by an isolated traumatic incident or the result of gradual degradation of bone tissue [145]. More than 50% of adults older than 50 years suffer from osteoporosis, a systemic degenerative skeletal disease that causes low bone mass and microarchitectural deterioration of bone tissue [139,140]. Low bone mass and deterioration of bone microstructure results in increased bone fragility and, consequently, an increased susceptibility to fractures [145]. Treatment of bone tissue fractures incurs a substantial cost of medical care. Nearly $19 billion was spent in 2005 in the United States on fracture related medical expenses and the cost is expected to increase to $25 billion by the year 2025 [139,146]. In 2004, $34 billion was spent on total opportunity costs and the cost is projected to increase to $41 billion by 2025 [147].

There are a few existing methods to address and treat bone fractures resulting from degenerative diseases including osteoporosis. One of the most widely implemented methods for repairing bone fractures includes implantations. These implants include invasive joint replacements, as is the case with fractured hips, and bone plates to repair long bones. Implantation of non-biological material limits the surrounding bone tissue adaptation response to physiological conditions and loading, often resulting in

resorption due to stress shielding or re-operation due to failure of the implant [37,65,148]. Alternatively, a pharmaceutical approach is implemented for prevention or treatment of microarchitectural bone fractures. These methods include prescription of anti-resorptive medications and anabolic agents [140,149–153]. Anti-resorptive drugs and anabolic agents affect the signaling pathways that regulate bone modeling, remodeling, and adaptation and cause an increase in bone formation while inhibiting bone resorption [140,149]. The implementation of such drugs often has limited efficacy and frequently causes adverse side effects including increased fractures in peripheral bone tissue [140,149,150,154]. In addition, the optimal dosage and duration for use of many of the ant-resorptives and anabolic agents are unknown [154].

Implantation of bone scaffolds provides an alternative method for bone tissue repair. Bone scaffolds incorporate applied mechanical engineering principles in the context of tissue engineering to produce an implantable scaffold that can integrate with host bone architecture to regenerate tissue and, consequently, regain mechanical integrity [137,155–157]. Bone scaffolds, immediately upon implantation, provide temporary mechanical support to defective or injured bone. If designed appropriately, scaffolds can subsequently maintain biocompatibility and support tissue regeneration via mass transport to restore bone tissue [158–160].

In a previous study, Vivanco *et al.* partnered with Phillips Plastics (Hudson, WI) to manufacture fifty injection molded beta tricalcium phosphate (TCP). These rectangular scaffolds each had bulk dimensions of 5.4 x 5.4 x 4.2 mm^3 [155]. Each scaffold consisted of approximately six 500 µm^2 beams layered in alternating orthogonal directions [155]. The scaffolds were sintered at 950 ºC, 1050 ºC, and 1150 ºC. Subsets of the scaffolds were subsequently evaluated to determine the effect of sintering temperature on their architectural, material, and mechanical properties [155,156,161]. To determine the effect of sintering temperature on the scaffold dimensions, a subset of the scaffolds was evaluated using a stereo microscope and a scanning electron microscope (SEM) [155][161]. Additionally, dry and wet bulk weight and dimensions were measured using digital scales and calipers [155,156]. It was found that

increased sintering temperature decreased the scaffold volume, water absorption, and porosity [161]. A separate subset of the sintered scaffolds was evaluated using nano-indentation to determine the nano-level material properties [157]. It was found that the nano-level hardness (H_{nano}) and elastic modulus (E_{nano}) were significantly increased in scaffolds sintered at 1050 ℃ compared to 950 ℃, but E_{nano} was significantly decreased in scaffolds sintered at 1150 ℃ compared to 1050 ℃ [157]. An additional subset of scaffolds was evaluated using micro-indentation to determine the micro-level material properties [161]. Experimentation found that micro-level hardness (H_{micro}) and elastic modulus (E_{micro}) were significantly increased in scaffolds sintered at 1050 ℃ compared to 950 ℃ and E_{micro} was slightly decreased for scaffolds sintered at 1150 ℃ compared to 1050 ℃ [161]. Finally, a subgroup of the scaffolds was subjected to macro-level axial compression using the ZETOS Bone Loading and Bioreactor System (ZETOS) to determine the bulk mechanical properties ($E_{app,exp}$) [155,156]. A trend similar to those observed in nano- and micro-level testing was found where $E_{app,exp}$ was increased in scaffolds sintered at 1050 ℃ compared to 950 ℃ but decreased in scaffolds sintered at 1150 ℃ compared to 1050 ℃ [155,156]. The overall conclusions of this series of studies conducted by Vivanco *et al.* were that sintering temperature had a significant effect on the morphological, material, and mechanical properties of TCP scaffolds.

The purpose of the present study was to build upon previous research conducted by Vivanco *et al.* to evaluate the mechanical properties of three-dimensional (3D), injection molded beta TCP scaffolds sintered at different temperatures to design materials that would be biocompatible, bioresorbable, osteointegrate, and mimic the morphological and mechanical properties of bone tissue. Since the success of scaffold implantation as a tool for facilitating bone repair is dependent on scaffold's ability to osteointegrate, it is imperative to understand their mechanical behavior and appropriately select scaffold material that would not only mimic bone morphology, but also bone mechanical properties. The specific aim of the present study was to determine if the bulk mechanical properties of beta TCP scaffolds is more reflective of the nano- or micro-level material properties of the material.

7.3 Materials and Methods

Finite element (FE) models were generated using data from prior studies conducted by *et al*. Computer aided design (CAD) models were created using Solidworks 2013 (SolidWorks Corp., Dassault Systemes, Waltham, Massachusetts) using the average bulk dimensions (Table 7.1) and average strut thicknesses (Table 7.2) for scaffolds sintered at 950 ℃, 1050 ℃, and 1150 ℃ to simulate structures representative of scaffolds sintered at each temperature. Figure 7.1 shows a stereoscope image of a representative TCP scaffold.
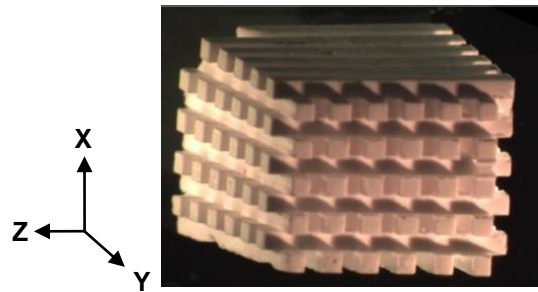
Figure 7.1 - Stereoscope image of a representative TCP scaffold [155]

Table 7.1 – Bulk dimensions for CAD models of TCP scaffolds taken from results from studies conducted by Vivanco et al [161]**.**

Sintering Temperature (°C)	Bulk Dimension (mm)		
	x-direction	*y-direction*	*z-direction*
950	6.11±0.021	6.11±0.024	4.66±0.018
1050	5.61±0.032	5.61±0.036	4.28±0.030
1150	5.45±0.033	5.46±0.149	4.17±0.030

Table 7.2 - Strut dimensions for CAD models of TCP scaffolds taken from results from studies conducted by Vivanco et al [161]**.**

Sintering Temperature (°C)	Strut Dimension (mm)		
	xy-plane	*xz-plane*	*y-z plane*
950	0.537±0.056	0.464±0.077	0.448±0.019
1050	0.498±0.066	0.440±0.008	0.439±0.007
1150	0.494±0.079	0.414±0.006	0.407±0.009

The CAD models were subsequently used to generate FE models in Abaqus (Simulia, Dassault Systemes, Waltham, Massachusetts) (Figure 7.2). The side of the scaffold directly opposing the direction of loading was pinned on all beam faces and one node near the center of the bottom face was fixed in all directions. The model was designed such that deformation of the scaffold was caused by displacement of a rigid platen (diameter = 8 mm, thickness = 0.5 mm, E =100,000,000 GPa) atop the scaffold along the x-axis (Figure 7.3). The model was designed to mimic the axial compression conducted during Vivanco's studies and thus implemented hard contact at the loading surface of the scaffold (Figure 7.3). The contact-pair was modeled as having a friction coefficient of 0.01. The scaffold was defined as being the "slave" and the loading platen was defined as the "master." The bottom surface of the platen was placed such that it was coincident with the top surface of the scaffold at the start of the simulation. The platen was subsequently displaced 10 µm in the negative direction along the x-axis. Quadratic tetrahedral elements

with global element length (GEL) of 0.125 mm were used for meshing on both the scaffold and loading platen (Figure 7.3).
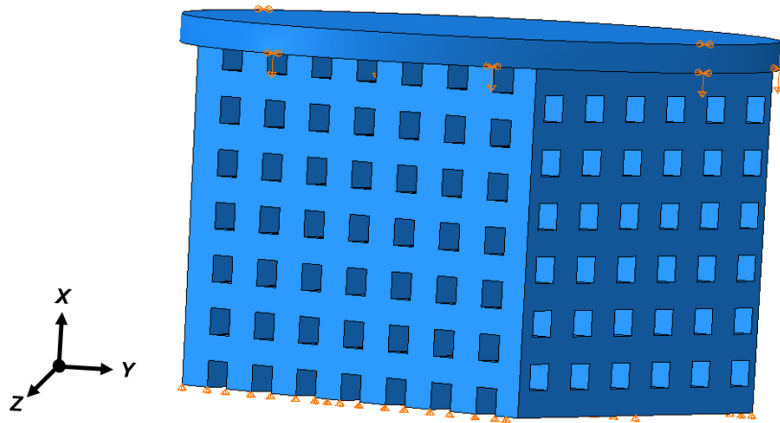
Figure 7.2 - Representative CAD model of TCP scaffold with axes shown
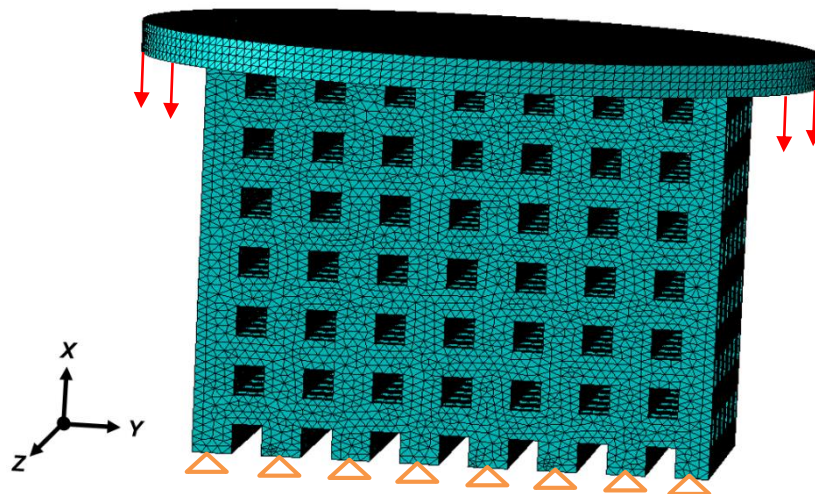
Figure 7.3 - Representative FE model of TCP scaffold with axes, boundary conditions, and applied displacement shown.

To determine how the bulk mechanical properties of the TCP scaffolds were affected by the nano- and micro-level material properties, the FE model was evaluated twice for each representative scaffold from each sintering temperature: first using the nano-level material properties for the scaffold and then again using the micro-level material properties for the scaffold. The values used for E_{nano} and E_{micro} were sourced from Vivanco *et al.* and are shown in Table 7.3. After the FE analyses were complete, the E_{app} from the model ($E_{app,FE}$) was calculated from the sum of the forces located at the platen (F), the initial length of the scaffold in the direction of loading (L_0), the bulk cross-sectional area of the scaffold (A), and the change in length of the scaffold dimension in the direction of loading (δ) (Equation 7.1). The scaffold material was assumed to be linearly elastic, isotropic, homogeneous, and have a Poisson's ratio (v) of 0.27.

Table 7.3 - Summary of material and mechanical properties of TCP scaffolds as determined from experiments conducted by Vivanco et al [155–157,161].

Sintering Temperature (°C)	Scaffold Property		
	E_{nano} (GPa)	E_{micro} (GPa)	$E_{app,exp}$ (GPa)
950	44.3±5.7	46.5±42	6.41±2.3
1050	87.8±7.6	104.5±2.5	11.1±0.76
1150	73.8±4.3	103.1±3.3	9.07±1.3

$$\text{Equation 7.1} \qquad E_{app,FE} = \frac{FL_0}{\delta A}$$

7.4 Results

The apparent elastic modulus calculated from the FE analyses ($E_{app,FE}$) for each of the three

scaffolds modeled with material properties reflecting E_{nano} and E_{micro} were compared to the corresponding

apparent elastic modulus values determined from axial compression tests ($E_{app,exp}$). Figure 7.4 shows the

displacement distribution for a representative scaffold FE model. A representative stress distribution in

the direction of the loading axis of the scaffold is shown in Figure 7.5. The maximum applied force for

the 950°C scaffold was 870 N and 914 N when $E_{app,nano}$ and $E_{app,micro}$ were used for the FE analysis,

respectively. The maximum applied force for the 1050 °C scaffold was 1628N and 1760 N when $E_{app,nano}$

and $E_{app,micro}$ were used for the FE analysis, respectively. The maximum applied force for the 1150 °C

scaffold was 1026 N and 1431 N when $E_{app,nano}$ and $E_{app,micro}$ were used for the FE analysis, respectively.
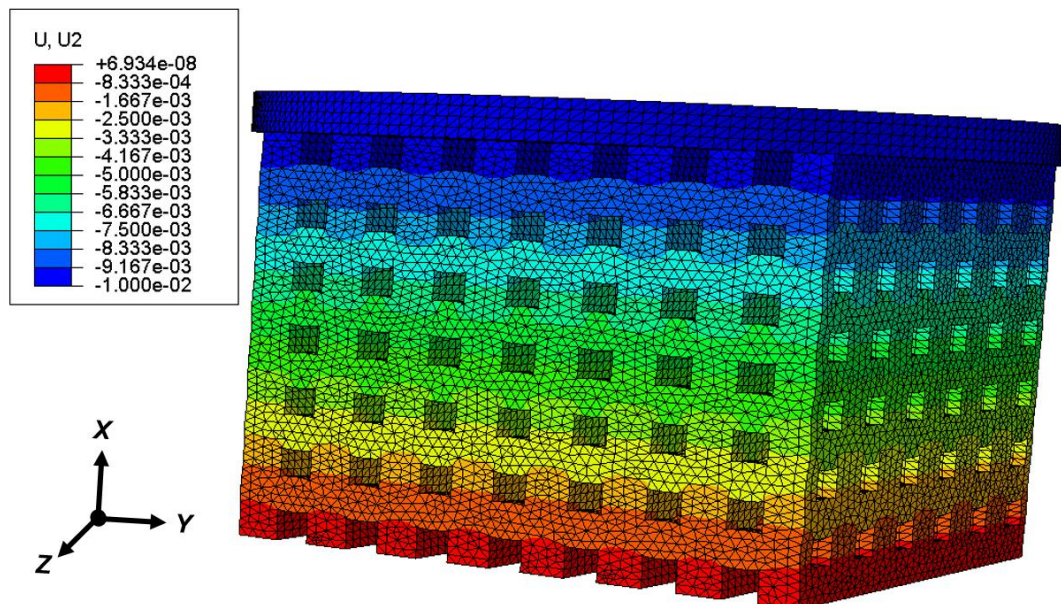
Figure 7.4 - Deformation distribution in the direction of displacement application for representative FEA of TCP scaffold. Units are in millimeters (mm).
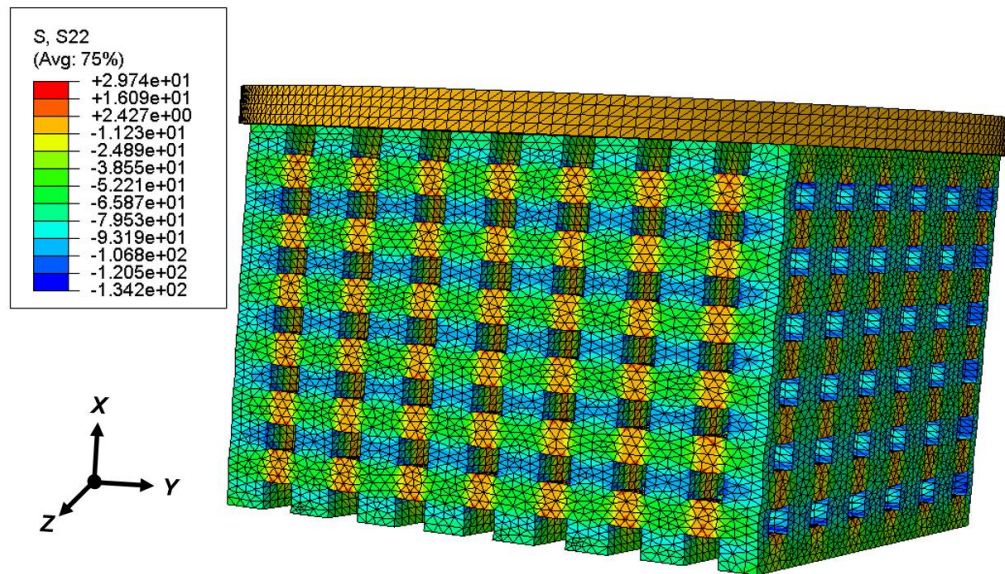
Figure 7.5 - Stress distribution in the direction of displacement application for representative FEA of TCP scaffold. Stresses are listed in units of MPa.

Overall, the FE analyses for all three scaffolds resulted in $E_{app,FE}$ values that generally followed similar trends observed by Vivanco *et al*. The FE analysis modeled with $E_{app,nano}$ for the TCP material properties showed increased E_{app} for the scaffold representative of the 1050 °C sintering group compared to the representative 950 °C scaffold (Figure 7.6). Modeling with $E_{app,nano}$ also showed decreased $E_{app,FE}$ for the scaffold representative of the 1150 °C compared to the 1050 °C scaffold (Figure 7.6). The FE analysis modeled with $E_{app,micro}$ for the TCP material properties showed increased E_{app} for the scaffold representative of the 1050 °C sintering group compared to the representative 950 °C scaffold (Figure 7.7). Modeling with $E_{app,nano}$ also showed decreased $E_{app,FE}$ for the scaffold representative of the 1150 °C compared to the 1050 °C scaffold (Figure 7.7). The calculated apparent elastic moduli ($E_{app,FE}$) from the

FE analyses were consistently two to three times larger than the E_{app} ($E_{app,exp}$) determined from axial compression testing of the TCP scaffolds. Table 7.4 shows a summary of the results. The $E_{app,FE}$ determined from the analysis using $E_{app,nano}$ showed 190%, 169%, and 170% error between the FE and experimental results for the scaffolds sintered at 950 °C, 1050 °C, and 1150 °C
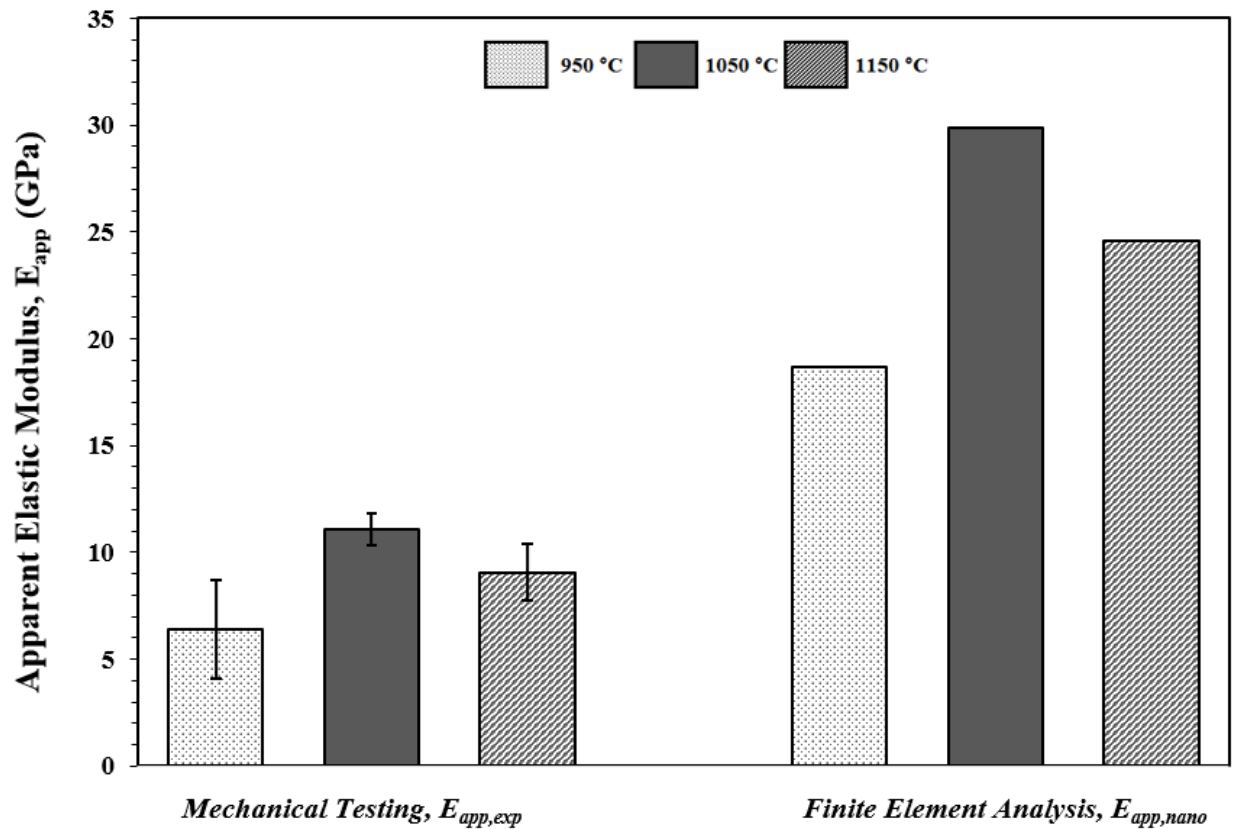
Figure 7.6 - Comparison of apparent elastic modulus determined from finite element analysis using nano-level material properties for TCP scaffolds compared to E_{app} determined from macro-level axial compression testing of TCP scaffolds. Error bars represent the standard error for $E_{app,exp}$
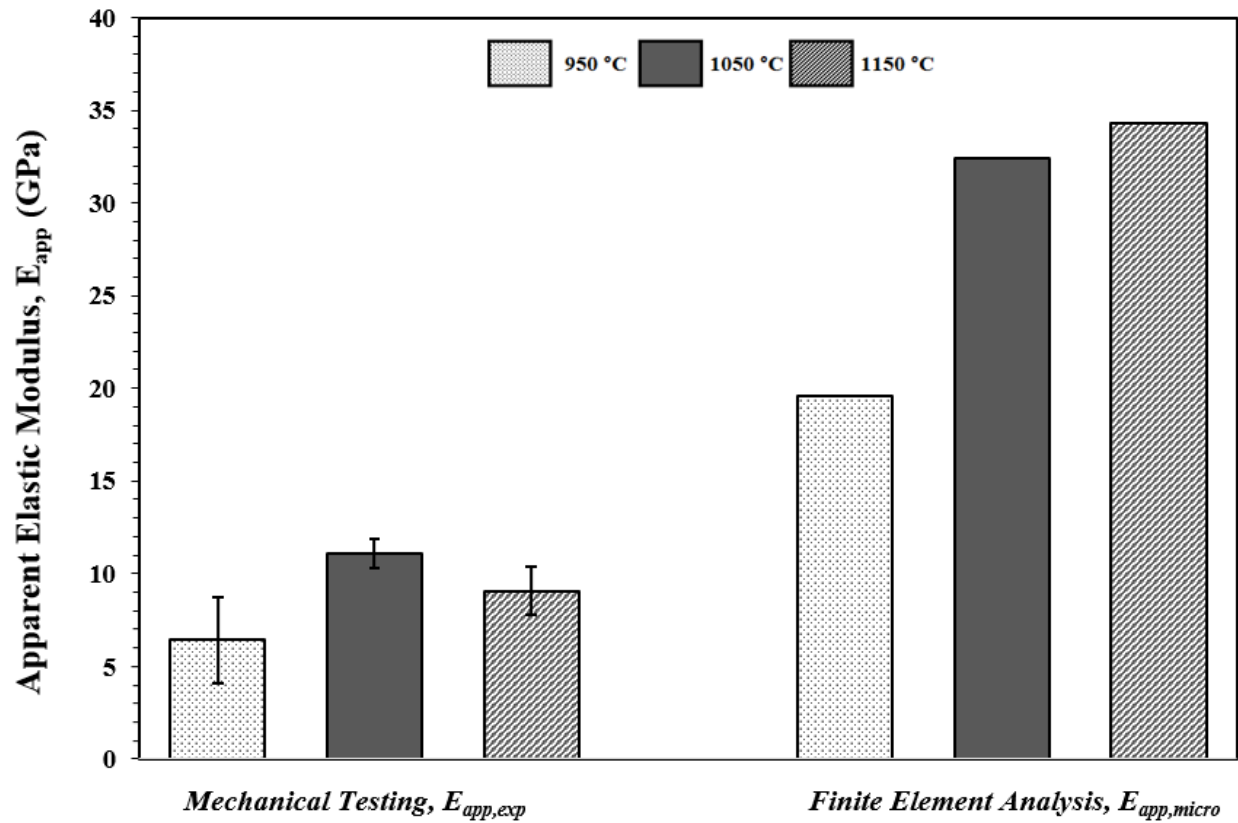
Figure 7.7 - Comparison of apparent elastic modulus determined from finite element analysis using micro-level material properties for TCP scaffolds compared to E_{app} determined from macro-level axial compression testing of TCP scaffolds. Error bars represent the standard error for $E_{app,exp}$.

Table 7.4 - Apparent elastic modulus values for TCP scaffolds sintered at 950 °C, 1050 °C, and 1150 °C determined from FEA and from experimental axial compression.

Sintering Temperature (°C)	FE Model Apparent Modulus		Experimental
	$E_{app,nano}$ (GPa)	$E_{app,micro}$ (GPa)	$E_{app,exp}$ (GPa)
950	18.7	19.6	6.41±2.3
1050	29.9	32.4	11.1±0.76
1150	24.6	34.3	9.07±1.3

7.5 Discussion

Overall, the present study was successful in illustrating the influences of sintering temperature and material properties on the overall bulk mechanical properties of beta-TCP scaffolds. The study showed that sintering temperature can substantially alter the observed mechanical properties of TCP scaffolds, largely due to geometric and morphologic changes resulting from the sintering process. Further, the study illustrated that the nano- and micro-level material properties influence the overall mechanical properties of TCP differently.

The study results from Vivanco *et al.* showed that nano-level evaluations of TCP material properties differed from micro-level evaluations [156,157,161]. Nano-indentation found that $E_{app,nano}$ was increased for scaffolds sintered at 1050 °C to 950 °C, but decreased from 1050 °C to 1150 °C. Micro-indentation found that $E_{app,micro}$ was also increased from 950 °C to 1050 °C, but there was no substantial difference between $E_{app,micro}$ for scaffolds sintered at 1150 °C compared to 1050 °C. While studies conducted by Vivanco *et al.* examined the effects of sintering temperature on the bulk elastic modulus of the TCP scaffolds, the effects were each investigated in separate studies to quantify geometry changes and material property differences between scaffolds. The present study was designed to investigate the effects of sintering temperature and multi-scale material properties simultaneously. Although the results of the FE analyses produced apparent elastic modulus values that were considerably larger than the E_{app} values determined from experimental axial compression, the observed trends remained the same. The results of the FEA presented in this study showed that $E_{app,FEA}$ determined when nano-level material properties were used demonstrated an increase from the representative 950 °C scaffold to the 1050 °C scaffold and decreased from the 1050 °C to the 1150 °C representative scaffold. Similarly, the FEA results showed that $E_{app,FEA}$ determined when micro-level material properties were used increased from the representative 950 °C scaffold to the 1050 °C scaffold; however, the FE model also showed a further increase in $E_{app,FEA}$ in the representative 1150 °C scaffold compared to the 1050 °C scaffold. Based on the results of the FEA,

and given the findings of Vivanco *et al.*, the nano-level material properties appear to be the best predictors of the bulk mechanical properties of TCP bone scaffolds.

The sizeable discrepancy between the experimental axial compression results and the FEA results can be attributed to a number of causes. First, the FE model in the present study implemented a single, idealized geometry that was designed using average dimensions from measurements obtained by Vivanco *et al.* for scaffolds sintered at each of the 950 °C, 1050 °C, and 1150 °C temperatures. The axial compression tests; however, were conducted on a multitude of scaffolds, each of which had a slightly different morphology—even within the same subgroup of scaffolds sintered at the same temperature. In addition, the exact architecture of each scaffold, determined from micro computed tomography images, varied with some scaffolds having more or less struts than others or having partial struts due to fractures resulting from handling. Furthermore, the FE model of the TCP scaffolds did not account for the porosity of the TCP material. Vivanco *et al.* reported significant differences in porosity, 24%, 6% and 0% [161] for scaffolds sintered at 950 °C, 1050 °C, and 1150 °C, respectively. The FEA did not include affects due to microstructure, connectivity, damage or porosity.

Despite the difference in magnitude between FE and experimental results, the findings still provide insight on the effect of the nano- versus micro-level material property contributions to the bulk mechanical properties. Using $E_{app,nano}$ in the FEA resulted in bulk E_{app} values that were 5%, 8%, and 33% closer to $E_{app,exp}$ resulting from axial compression tests compared to FEA results generated using $E_{app,micro}$ for the 950 °C, 1050 °C, and 1150 °C sintering temperatures, respectively . This implies that not only is the overall mechanical behavioral trend of TCP scaffolds better predicted by the nano-level material properties, but that the magnitude of the bulk mechanical properties is better predicted by the nano-level material properties.

7.6 Conclusion

Overall, the present study successfully demonstrated that geometric and morphological differences in beta-TCP bone scaffolds caused by sintering at 950 °C, 1050 °C, and 1150 °C can be

reflected using FEA. In addition, the study showed that E_{app} calculations using $E_{app,nano}$ within the TCP scaffold FE model were closer in magnitude to experimentally determined scaffold E_{app}. Furthermore, FE analyses conducted with nano-level TCP material properties exhibited the same trends in changes in mechanical properties with sintering temperature as determined from axial compression testing. The results of this study indicate that the bulk mechanical properties of beta-TCP scaffolds are better predicted by the nano-level material properties than micro-level material properties.

Chapter 8

8. Modeling of Human Trabecular Bone Mechanical Properties Using Finite Element Analysis

8.1 Abstract

Currently, about 55% of adults older than 50 years are affected by or at risk for osteoporosis—a systemic skeletal disease causing deterioration of bone tissue and associated with a high mortality risk. Understanding bone biomechanical behavior is imperative to promote bone health throughout aging, preventing fractures, and improving treatment options. In the present study, micro computed tomography (CT) images of a human trabecular bone core (height = 5 mm, diameter = 10 mm) were used to generate multiple finite element models of the bone core subject to axial compression in order to evaluate the feasibility of implementing traditional FE methods for the purpose of modeling the mechanical properties of trabecular bone. The first FE model simulated axial compression with hard contact of a geometric part reflecting the micro-level bone morphology with homogeneous material properties assumed. A second FE model was developed that simulated axial compression with hard contact of a simplified geometry with heterogeneous material properties assigned from bone mineral density determined from the CT images. A third FE model was generated that simulated axial compression without contact of a simplified geometry with heterogeneous material properties assigned from bone mineral density determined from the bone core CT images. The available computational resources during the study did not allow for convergence of the generated FE models due to complications with mesh generation. Future studies will investigate the use of voxel-based meshing to generate viable FE models of trabecular bone tissue.

8.2 Introduction

Fifty percent of women and twenty-five percent of men older than 50 years will sustain bone fracture caused by osteoporosis, increasing their risk of morbidity and mortality [139]. Osteoporosis is a

systemic skeletal disease that causes deterioration of bone tissue [140,145]. Medical costs associated with osteoporotic fractures and subsequent treatment reached $19 billion in 2005 and has been projected to exceed $25 billion by 2025 [139]. Of those costs, an estimated 57% was associated with inpatient care [7]. The economic burden of osteoporosis treatment is even more drastic when considering the total opportunity cost which reached $34 billion in 2004 and has been projected to increase to $41 billion by 2025 [147].

Understanding bone biomechanical behavior is imperative to identify the causes of, improve treatment options for, and prevent the onset of osteoporosis. It is well known that mechanical loading of bone tissue promotes modelling and remodeling [12,26,79,141,143]. Non-invasive methods exist for predicting bone mechanical properties, including the use of computed tomography-based metrics [49,56,60,162]. While CT-based metrics for bone tissue are generally accessible by clinicians and researchers, the accuracy of the predicted bone tissue mechanical properties is often lacking [60,163,164]. In addition, use of CT images alone does not provide insight on the stress and strain distributions within the bone tissue caused by an applied mechanical load. To understand how and where bone tissue is likely to adapt to an applied load through modeling or remodeling, it is necessary to understand its localized response to mechanical stimulus.

One method for evaluating the mechanical behavior of bone tissue is finite element analysis (FEA). FEA methods implement non-invasive modeling of the bone tissue and can simulate application of mechanical loading. Use of FEA to model bone tissue has been used by many a researcher to model bone structure and material properties to determine its bulk mechanical response [69,127,165–168]. The purpose of this study was to compare FEA methods for modeling human trabecular bone tissue and determine the system requirements and limitations associated with using traditional FEA to model human bone tissue.

8.3 Materials and Methods

A human trabecular bone core (approximate bulk dimensions: height = 5 mm, diameter = 10 mm) used in a previous study conducted by Meyer *et al.* was obtained [9]. The bone core was excised from the proximal femur of a 48-year-old male undergoing total hip arthroplasty. Micro-CT images (Siemens microCATII, 34 µm, 80 kVp, 50 µA) of the bone core were obtained and subsequently segmented using Mimics (Materialise, Leuven, Belgium) (Figure 8.1). Three separate finite element (FE) models were then generated in Abaqus (Simulia, Dassault Systemes, Waltham, Massachusetts) to simulate axial compression of the bone core similar to the methods presented in previous *ex vivo* studies conducted by Meyer *et al.* and others [9,46,48,80,82].

For the first model, the bone core was exported to 3-matic (Materialize, Leuven, Belgium), an FE pre-processor, for meshing. Due to the nature of the trabecular bone tissue, there were orphan pieces of tissue within the core. The floating pieces that were visible were removed using Boolean operations within 3-matic. A volume mesh was then created for the bone core using tetrahedral elements with a global edge length of 0.2 mm. The resulting volume mesh was then exported to Abaqus. A layer of nodes on the bottom of the bone core (along the y-axis) were fixed in the y-direction with 4 nodes fixed in all directions. A compressive displacement of 20 µm in the y-direction was then applied to the bone core through a rigid cylindrical platen ($E = 1 \times 10^9$ GPa, Poisson's ratio = 0.3). The model assumed "hard" contact with the platen acting as the "master" surface and the top surfaces of the bone core acting as the "slave" surfaces. The contact was modeled with a tangential friction coefficient of 0.01. This first model assumed linear elastic, homogeneous material properties for the bone core tissue and consequently an elastic modulus of 1 GPa and a Poisson's ratio of 0.3 were assumed from literature.

For the second model, the bone core volume was then exported to 3-matic (Materialize, Leuven, Belgium) where a cylindrical outline was superimposed upon the trabecular bone core. This operation was done to minimize error within the FE solver due to small or isoparametric elements caused by sharp geometries. A volume mesh was then created for the encasing cylinder using tetrahedral elements with a

global edge length of 0.2 mm. The bone core was assigned material properties within Mimics using known relationships between bone tissue density and Haunsfield units for human trabecular bone (HU) [169,170]. The HU calibration was done using air and water scans. The volume mesh was then assigned material properties based on the HU distribution within the volume (Figure 8.2). Twenty materials were used for the assignment and the Poisson's ratio was assumed to be 0.3. After material assignment was complete, the mesh was exported to Abaqus. A layer of nodes on the bottom of the cylinder (along the y-axis) were fixed in the y-direction with 4 nodes fixed in all directions. A compressive displacement of 20 µm in the y-direction was then applied to the cylinder through a rigid cylindrical platen (E = 1 x 10^9 GPa, Poisson's ratio = 0.3). The model assumed "hard" contact with the platen acting as the "master" surface and the top surfaces of the cylinder acting as the "slave" surfaces. The contact was modeled with a tangential friction coefficient of 0.01.

A third model was generated that mimicked the second FE model. The same steps were taken to generate a 3D geometry and assign volume mesh material properties based on CT-image HU distribution. To reduce computation time, load application was implemented by applying a compressive 20 µm to a layer of surface nodes on the top of the cylinder in the y-direction.
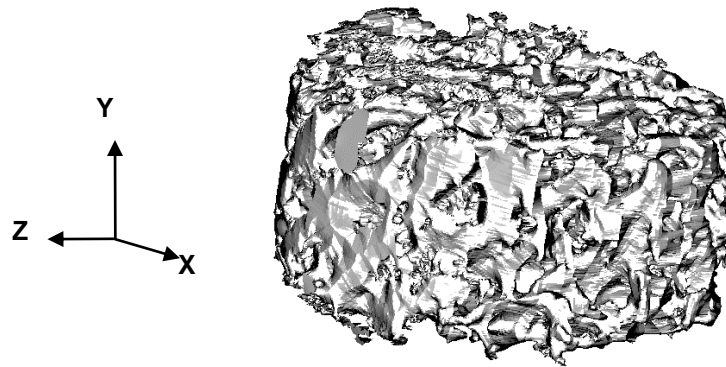
Figure 8.1 - Micro-CT scan of human trabecular bone core used for FE modeling
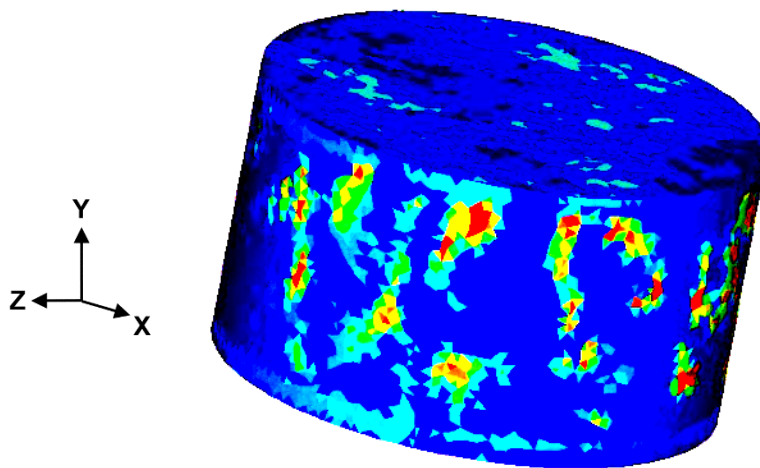
Figure 8.2 - Cylindrical model of trabecular bone core with heterogeneous material properties applied

8.4 Results

For all three FE models, the limiting factor was computational power. The first model (Figure 8.3), which used the trabecular bone core geometry from the CT image but a homogeneous material assignment, could not complete the calculations successfully. Multiple iterations were run with varied element sizes. While increasing the global element size (and thus reducing the number of elements and corresponding degrees of freedom) does aid in reducing the time required for the FEA to generate a

solution, the number of sharp edges within the trabecular bone structure and corresponding low-quality elements resulted in a non-convergence of the FE model. Reducing the global element length (increasing the number of elements within the model) reduced the number of low-quality elements, but there was insufficient available computational power to compete the FE calculations. The added computational requirements to model contact on the numerous irregular surfaces of the trabecular bone geometry likely also contributed to the lack of convergence.
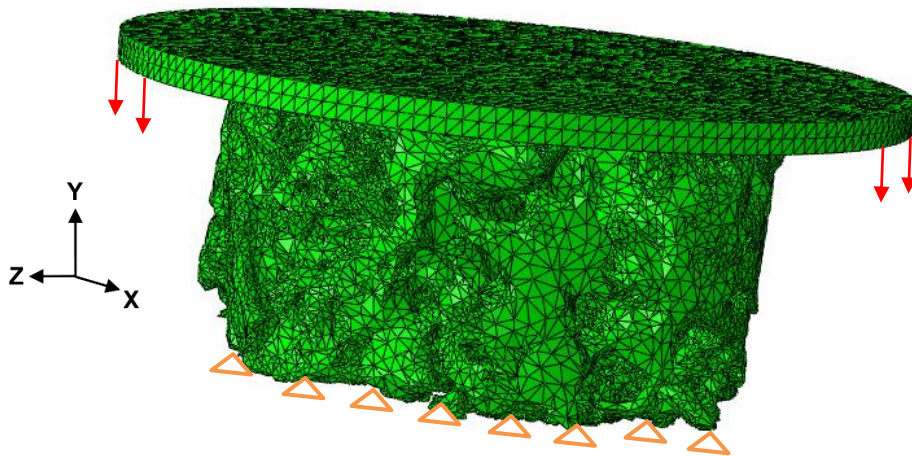
Figure 8.3 - FE model of trabecular bone geometry with applied load and boundary conditions shown.

The second model (Figure 8.4) which used the cylindrical geometry and material properties assigned from the CT image could not complete the calculations successfully. Multiple iterations were run with varied element sizes. While increasing the global element size (and thus reducing the number of elements and corresponding FE equations) does aid in reducing the time required for the FEA to generate a solution, the distribution of assigned material properties becomes increasingly coarse, leading to a non-convergence of the model. Increasing the number of elements exceeded the available computational power. This was likely only further exacerbated by the computations required for modeling surface-surface contact.
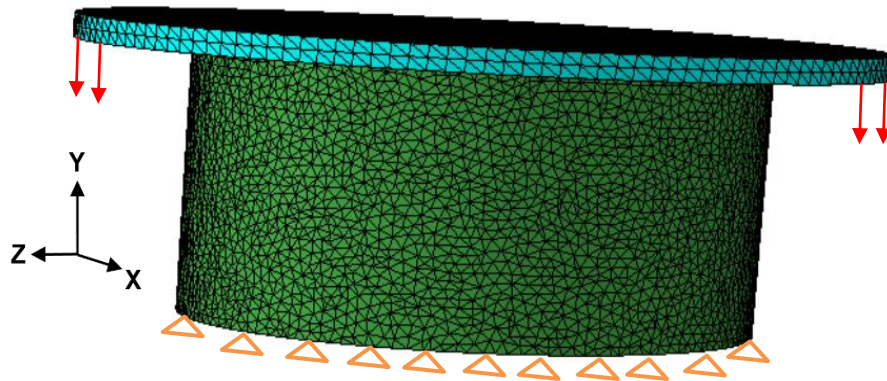
Figure 8.4 - FE model of cylindrical representation of trabecular bone core with heterogeneous material properties.

The third model (Figure 8.5) which used the cylindrical geometry and material properties assigned from the CT image could not complete the calculations successfully. Multiple iterations were run with varied element sizes. While increasing the global element size (and thus reducing the number of elements and corresponding FE equations) does aid in reducing the time required for the FEA to generate a solution, the distribution of assigned material properties becomes increasingly coarse. The non-contact model converged on a solution and the determined elastic modulus was 11 MPa. Mechanical testing of the modeled trabecular bone core *ex vivo* determined the elastic modulus to be 237 MPa. Figures 8.6 and 8.7 show the displacement distribution and von Mises stress distribution within the model, respectively. In addition, the deformed mesh shows uneven displacement throughout the model in addition to bulging elements along the outside border of the cylinder.
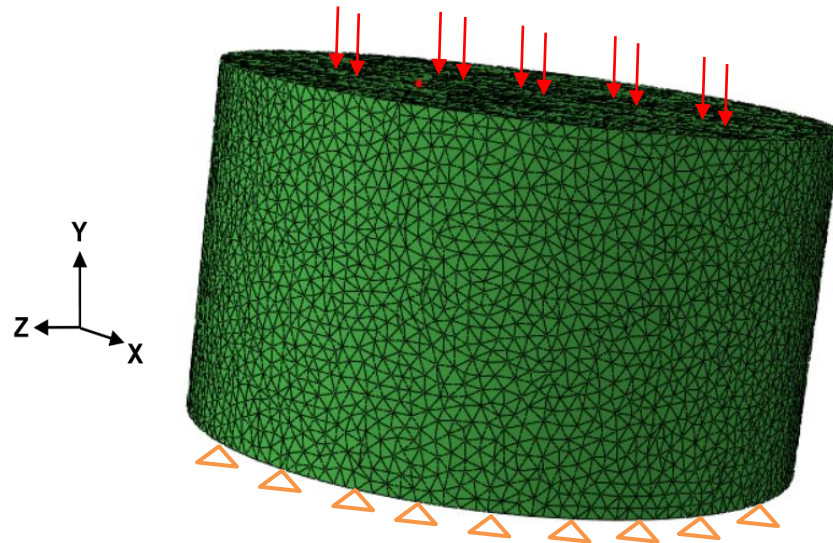
Figure 8.5 - Non- contact FE model of cylindrical representation of trabecular bone core with heterogeneous material properties.
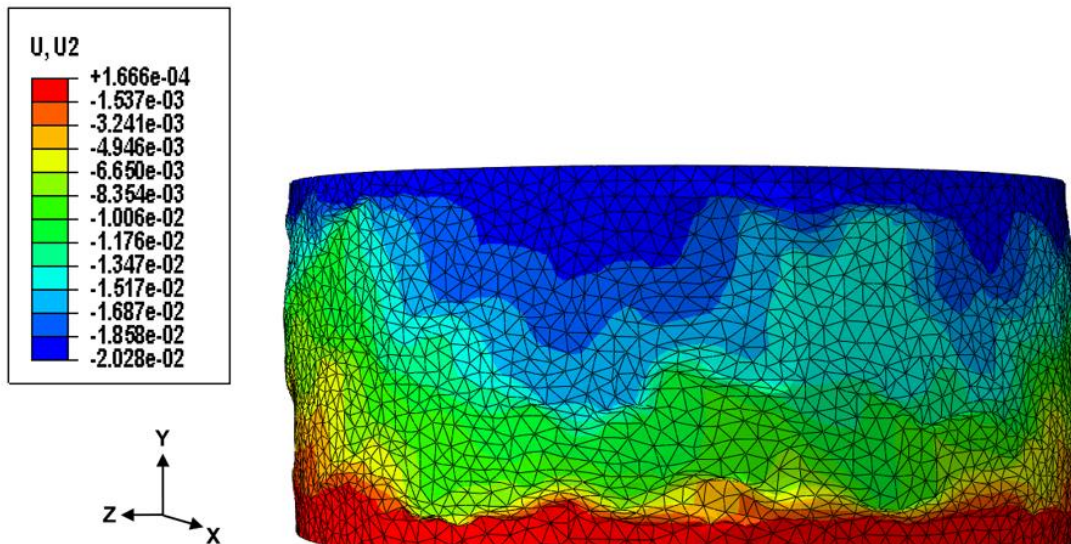
Figure 8.6 - Displacement distribution within the non-contact FE model of cylindrical representation of trabecular bone core with heterogeneous material properties
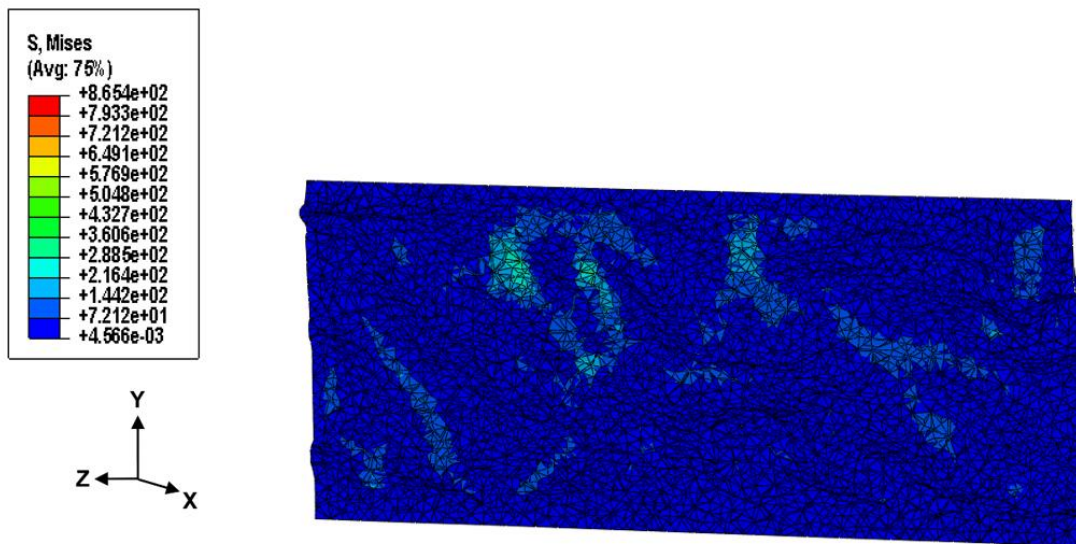
Figure 8.7 - von Mises stress distribution within the non-contact FE model of cylindrical representation of trabecular bone core with heterogeneous material properties

8.5 Discussion

Overall, the study was successful in demonstrating the enormous computational cost of conducting FEA on models with complex micro-scale geometries or with varying material properties. The findings of the study indicate that use of traditional FEA to model and predict bone mechanical properties on the micro-scale is not feasible for widespread practical applications.

Besides the computational requirements for generating a tetrahedral volume mesh for a complex structure, added complications arise from the presence of low-quality elements within the native mesh resulting in a low-quality mesh. Low-quality elements include elements that are distorted, which, for tetrahedral elements, includes elements that have isoparametric angles outside of the suggested limits and have exceedingly sharp vertices. Mesh quality could potentially be improved through the use of different FE pre-processors. The software used for this study, 3-matic, is designed largely for the purpose of generating surface meshes from CT-images so that the resulting mesh can be used for three-dimensional (3D) printing or similar applications. Various existing software packages are designed more specifically

for generating volume meshes to be used within FE models. It is possible that using a higher quality mesh generated with an alternate FE pre-processor could have led to convergence of the FE models presented in this study.

Previous studies have demonstrated that the FE method itself can be successful on whole bone analyses and provide useful information about the bulk mechanical properties of the skeleton; however, van Rietbergen *et al.* and others have repeatedly reported numerous complications associated with using traditional FE methods to model bone tissue on the micro level [171–173]. In several of his published works, van Rietbergen has listed reasons for avoiding traditional FEA of bone tissue microstructure, often attributing convergence failures of µFE models to excessive computational cost, further highlighting its limited accessibility as a modeling method. Many research studies interested in reducing computation time for FE models of bone tissue implement voxel-based meshes [162,169]. Muller *et al.* have reported success with voxel-based meshing methods in modeling bone tissue mechanics [171]. This meshing technique is convenient for solvers since it uses the native voxel size of the CT images to generate elements. The method loses effectiveness with decreased image resolution, however, for the CT images used in this study with a voxel size of 34 µm, a voxel-based mesh would be comparable with the quality of the mesh generated through 3-matic.

8.6 Conclusion

Overall the study illustrated that using traditional FEA techniques for modeling trabecular bone tissue mechanics has substantial limitations that reduce its accessibility and feasibility. Future studies should investigate alternative meshing methods including voxel-based meshing.

Chapter 9

9. Algorithm for Simulating Human Cortical Bone Remodeling

Additional contributing authors include CJ Collins[1], K Suresh[1], and H-L Ploeg[1]

[1]Department of Mechanical Engineering, University of Wisconsin – Madison

9.1 Abstract

More than half of adults over the age of 50 years is affected by or at risk for osteoporosis—a systemic skeletal disease causing deterioration of bone tissue and associated with a high mortality risk. Understanding bone biomechanical behavior is imperative to promote bone health throughout aging, preventing fractures, and improving treatment options. The goal of the current study was to develop an algorithm that could simulate human cortical bone adaptation on a simple two-dimensional (2D) geometric model, in real time. The inputs for biochemical factors (RANK, RANKL, OPG, PTH, and TGF-β) cell concentrations, initial bone porosity (5%), and isotropic mechanical properties were assumed from literature (elastic modulus=10 GPa, Poisson's ratio=0.3) and were assigned to a simple 2D geometry under 500 N compressive uniaxial loading and a finite element analysis (FEA) with 4000 linear quadrahedral elements was performed. Calculated strain energy density (SED) and assumed biological factors were used to minimize the SED in load bearing tissue by changing the porosity in relevant areas. Doses of PTH ($1\text{-}50\text{x}10^4$ pM), PTH production rate ($2.5\text{-}20\text{x}10^2$ pM/day), and PTH deactivation rate ($4.3\text{-}17.2$ day^{-1}) were varied. Each time, the algorithm was repeated for 5, 10, and 20 time steps to simulate bone adaptation with time. Von mises stress increased by approximately 11% and the maximum porosity in the bone decreased by approximately 30% with a consistent 3% difference between the maximum and minimum porosity values. The SED was decreased by nearly 100%. Variation of PTH dose minimally affected the changes in stress, porosity and SED during the iterations, however changing PTH activation and deactivation altered the rates of stress increase and porosity decrease by approximately 5%. The algorithm shows promise in that the results were consistent with known physiological bone remodeling

patterns. Incorporation of additional contributing biochemical factors is necessary to fully mimic physiological bone remodeling. Furthermore, the algorithm will be tested on additional 2D structures more representative of bone

9.2 Introduction

Approximately 55% of adults older than 50 years are affected by or at risk for osteoporosis—a systemic skeletal disease that is characterized by reduced bone mass and subsequent bone fragility [52,139]. An estimated 75 million individuals are affected by osteoporosis in Europe, the United States, and Japan [174]. Deterioration of bone tissue resulting from osteoporosis increases risk of bone fracture and is associated with a high mortality risk [3,175]. Cost of treating osteoporotic fractures and osteoporosis related medical complications accounted for nearly $20 billion in 2005—a figure which is projected to exceed $25 billion by the year 2025 [139]. Many osteoporosis treatments include anti-resorptive drugs and anabolic agents to inhibit the bone resorption process or to increase bone formation activity, respectively [152–154]. These available treatments for osteoporosis are woefully inadequate and often cause adverse side effects [150]. In addition, the methods for diagnosis and prevention of osteoporosis is imperfect, with many patients remaining undiagnosed until bone deterioration is irreversible with current medical advances [52,176,177]. Understanding bone biomechanical behavior is imperative to promoting bone health throughout aging, preventing fractures, and improving treatment options of widespread systemic skeletal disorders such as osteoporosis.

Bone adaptation to mechanical and biochemical stimulus occurs through modeling, remodeling, and homeostasis. The bone adaptation process is modulated by osteoclasts, osteoblasts, and osteocyte activity which are responsible for bone resorption, bone formation, and bone maintenance, respectively [12,18,143,178,179]. The interactions of these bone-native cell types are governed by signaling pathways, including the WNT signaling pathway [84,89,180,181]. These signaling pathways are influenced by key biochemical factors, including parathyroid hormone (PTH), transforming growth factor beta 1 (TGF-β),

osteoprotegerin (OPG), and receptor activator of nuclear factor kappa-B and the corresponding ligand (RANK and RANKL, respectively) [71,87,92,179,182,134,183,184].

Recently, Scheiner *et al.* implemented one-dimensional (1D) analytical stress analysis, and system's biology in tandem to develop mathematical models to predict the morphological changes in bone resulting from mechanical and biochemical stimuli [71]. The purpose of Scheiner's model was to estimate tissue level adaptation to mechanical stimulus, quantified by changes in porosity, by simulating interactions between relevant bone-native cells and biochemical factors. To predict changes in bone porosity, a single mechanical stimulus was mathematically applied in the form of strain energy density (SED). In the model, each cell type and biochemical factor was associated with a set of governing equations that dictated their activation and deactivation within the bone tissue. In the case of osteoclasts and osteoblasts, there were additional mathematical relationships to account for the progenitor and precursor activity, in addition to equations governing cell apoptosis. Upon "load application" to bone cells, subsequent calculations were carried out separately for each bone cell type (osteoclasts, osteoblasts, and osteocytes)—influenced by concentrations and activity of relevant biochemical factors. Finally, the new activity level and concentration of bone-native cells was related to density and porosity of the overall bone tissue.

The goal of the current study was to build upon the work of Scheiner *et al.* to simulate cortical bone adaptation on a simple two-dimensional (2D) geometric model, in real time.

9.3 Materials and Methods

An algorithm (detailed in Appendix E) to predict cortical bone adaptation on a simple 2D geometric model was developed in MATLAB (version R2013a, MathWorks, Simulink, Natick, MA) by modifying the analytical models determined by Scheiner *et al.* for bone cell interactions to interface with a 2D finite element (FE) solver. The algorithm was designed to have four distinct sections (Figure 9.1). The first section of the algorithm initialized the predictive process by inputting starting bone cell

concentrations, biochemical factor concentrations, defining the model geometry, and applying the mechanical stimulus. The second section of the algorithm implemented the FE method for determining the stresses, strains, and SED throughout the geometric model. In the third section, the outputs from the FE analysis were then used as further inputs into the cell population models adapted from Scheiner's previous work. Finally, the changes in cell populations and biochemical factors determined from the cell population models were related to porosity and density of the model material in the fourth and final portion of the code. The algorithm then iterates through segments two to four to simulate bone remodeling.
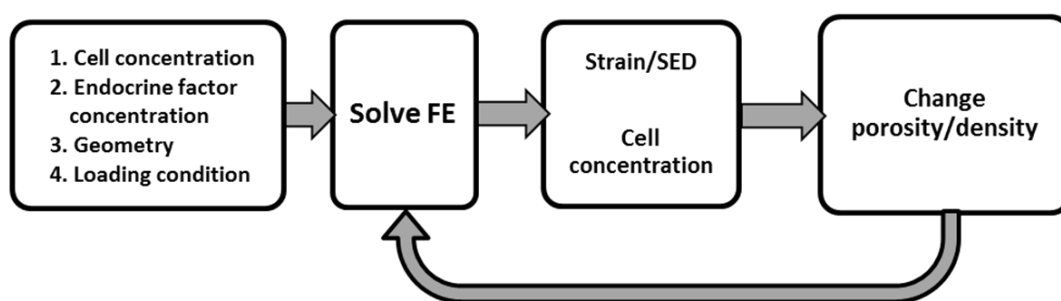
Figure 9.1 - Schematic illustrating the structure of the presented bone remodeling algorithm

To initialize the algorithm, the inputs for biochemical factors (RANK, RANKL, OPG, PTH, and TGF-β), bone-native cell concentrations, and initial bone porosity (5%) were assumed from literature [70,71]. For each of the biochemical factors, a corresponding activator equilibrium constant, repressor equilibrium constant, and degradation rate was needed. For each of the bone cell populations, corresponding cell precursors, cell progenitors, cell differentiation rate, and cell apoptosis rate were required. Figure 9.2 shows a schematic of the bone cell population model implemented within the algorithm. Due to the complexity of the cell population models, not all factors implemented within Scheiner's 1D work were accounted for within the 2D algorithm. Table 9.1 shows the initial

concentrations of bone cell populations for the computational model. Table 9.2 outlines the differentiation and apoptosis rates used for osteoblasts and osteoclasts in the computational model. Table 9.3 shows the initial concentrations, and activator and repressor equilibrium coefficients for the biochemical factors included within the algorithm.
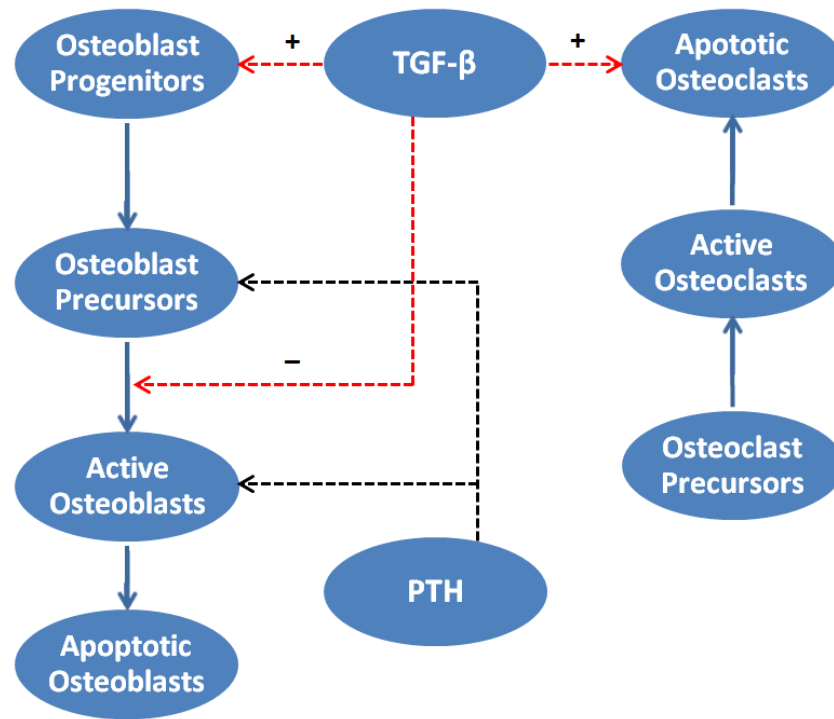
Figure 9.2 - Schematic of bone cell population model for remodeling

Table 9.1 - Initial concentrations of bone cell populations within the computational model.

Cell Type		Initial Concentration (pM)
Osteoblast precursors	$C_{OB,P0}$	0.001
Active Osteoblasts	$C_{OB,A0}$	0.005
Osteoclast precursors	$C_{OC,P0}$	0.001
Active Osteoclasts	$C_{OC,A0}$	0.0001

Table 9.2- Apoptosis and differentiation rates for osteoblast and osteoclast populations within the computational model.

Factor		*Initial Concentration* (d^{-1})
Osteoblast apoptosis rate	A_{OBa}	2.111×10^{-1}
Osteoblast differentiation rate	D_{OBp}	1.657×10^{-1}
Osteoclast apoptosis rate	A_{OCa}	5.649×10^{-4}
Osteoclast differentiation rate	D_{OCp}	2.100×10^{0}

Table 9.3 - Initial concentrations, activator equilibrium constants, and repressor equilibrium constants for biochemical factors included within the computational model.

.*Factor*		*Initial Concentration* (pM)
PTH dosage	$P_{PTH,d}$	5.000×10^{4}
PTH activator equilibrium constant	$K_{PTH,Act,Ob}$	1.500×10^{2}
PTH repressor equilibrium constant	$K_{PTH,Rep,Ob}$	2.226×10^{-1}
TGF-β dosage	$P_{TGF,d}$	5.000×10^{4}
TGF-β activator equilibrium constant	$K_{TGF,Act,Ob}$	5.633×10^{-4}
TGF-β repressor equilibrium constant	$K_{TGF,Rep,Ob}$	1.754×10^{-4}

After initializing the algorithm, the finite element problem was defined and solved. To avoid additional complications associated with using a complex geometry, a simple rectangular model (1600 mm width, 600 mm height) with a central hole (100 mm radius) was used for this study (Figure 9.3). Isotropic mechanical properties were assumed from literature (elastic modulus=10 GPa, Poisson's ratio=0.3). These properties were assigned to the 2D rectangular geometry under 500 N compressive uniaxial loading and a finite element analysis (FEA) with 4000 linear quadrahedral elements was performed (Figure 9.4). The algorithm, using the initial biological factors detailed previously and the calculated strain energy density (SED) from the FE analysis, repeated to minimize the SED in load bearing tissue by changing the porosity in relevant areas. The porosity was used to calculate the bone volume and subsequently the bone density (ρ). Changes in stiffness of the bone were assumed to be related to ρ^3. The algorithm was repeated for 5, 10, and 20 time steps to simulate bone adaptation with time.
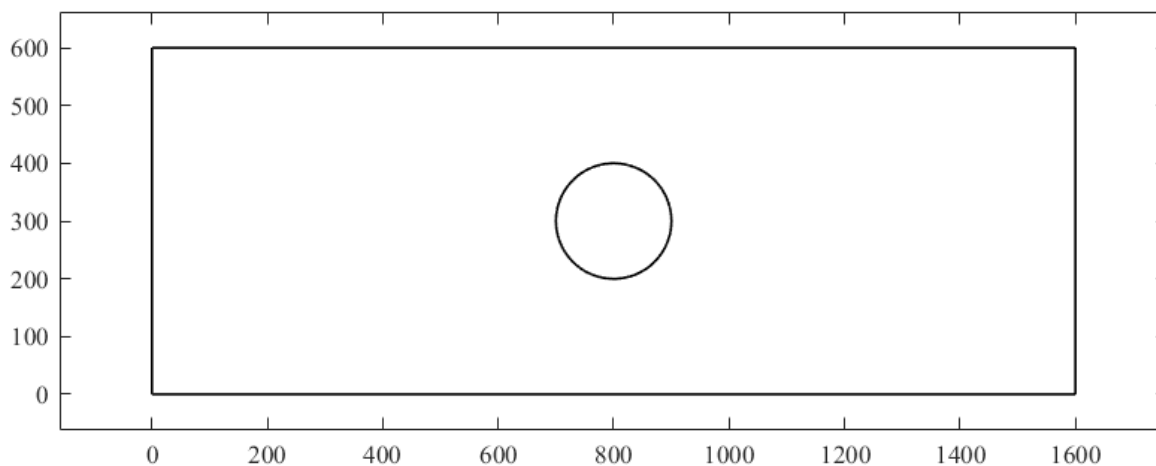
Figure 9.3 - Schematic of 2D geometry used for algorithm
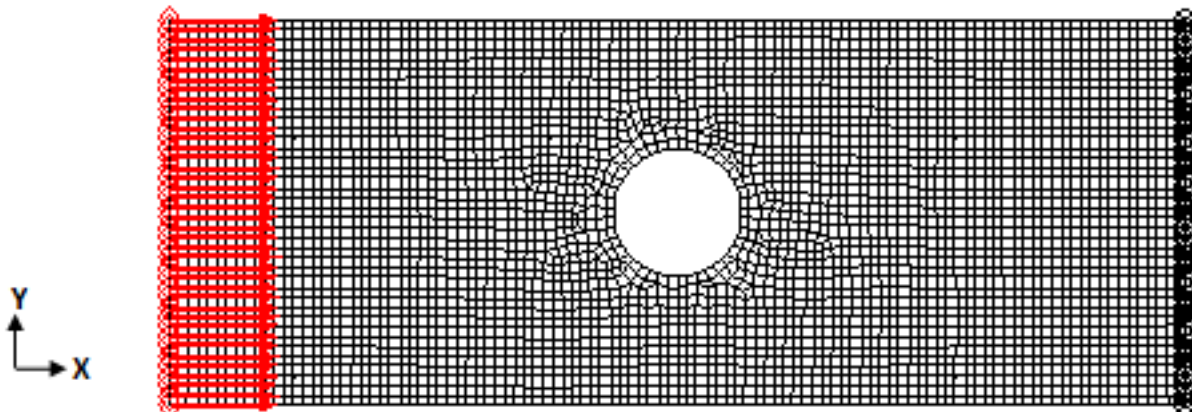
Figure 9.4 - Schematic of 2D finite element model with boundary conditions and applied load shown

9.4 Results

Overall, the algorithm results showed evidence of osteoblast and osteoclast coupling with active changes in the bone cell populations with every iteration. Concentrations of biochemical factors TGF-β and PTH were also changed regularly with each iteration. It was found, however, that changing the initial dose of PTH resulted in minimal differences ($< 5\%$) in the activation and deactivation of bone cell populations.

As expected, the simulation found the maximum Von mises stress located in the stress concentration caused by the hole (Figure 9.5). After 20 iterations, the maximum Von mises stress increased by 11% whereas the SED was decreased by nearly 100%. The maximum porosity within the modeled bone, initially 5%, decreased by 30% with a 3% difference between the maximum and minimum porosity values. During the 20 iterations, the model tried to reduce porosity in the regions with the highest SED. At the end of the simulation, the maximum porosity within the model was 3.48% and the minimum porosity was 3.39%.

Changing the initial dose of PTH was found to minimally affect the changes in stress, porosity and SED during the iterations, however changing PTH activation and deactivation constants altered the

rates of stress increase and porosity decrease by approximately 5%. and bone material adapted to reduce porosity at that location (Figure 9.5).
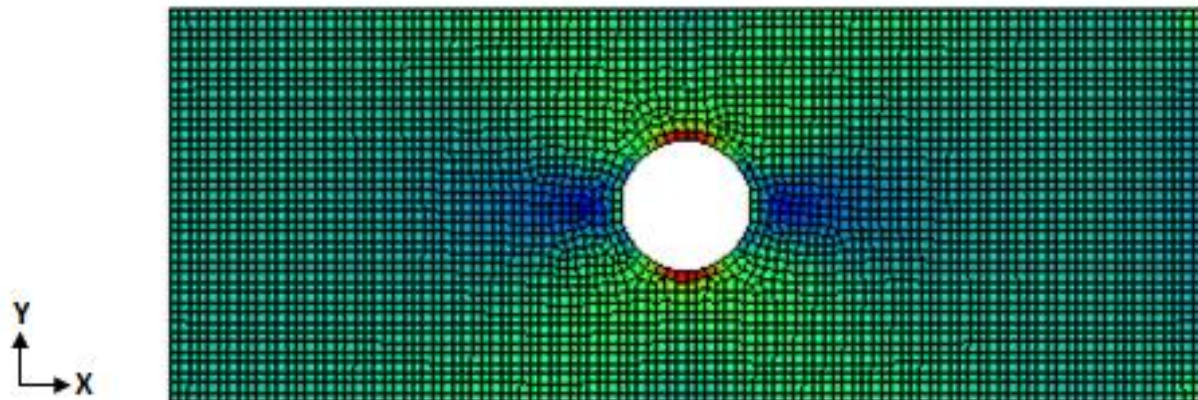
Figure 9.5 - Von mises stress distribution throughout rectangular model after 20 iterations.
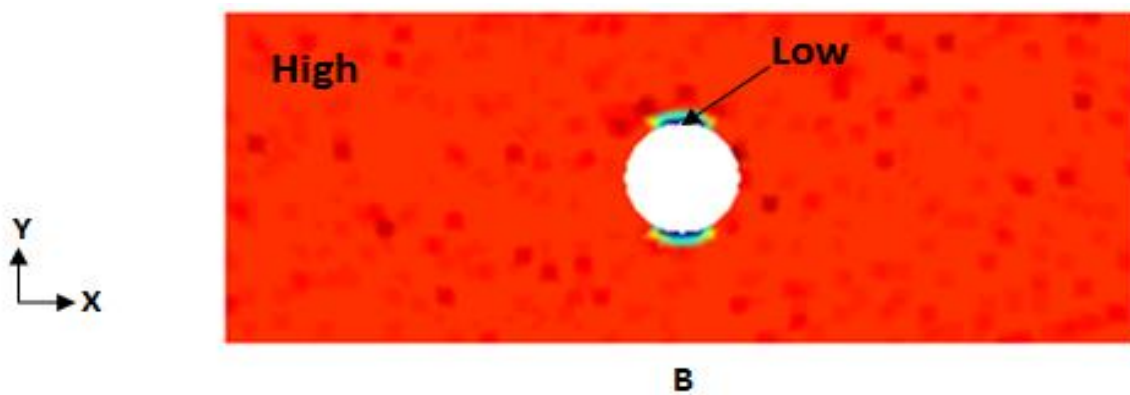
Figure 9.6 - Predicted porosity distribution across hole after 20 iterations

9.5 Discussion

Overall, the algorithm developed in the present study successfully mimicked bone remodeling in two dimensions with a simplified geometry. The intent of the current research was to expand Scheiner's algorithm from 1D analytical stress analysis and show remodeling of simulated bone in response to initial concentrations of biochemical factors, porosities, and mechanical stimuli.

There were a few limitations associated with the generation of the presented computational model. First and foremost, the developed algorithm does not include all biochemical factors needed to accurately model bone adaptation to mechanical stimulus. Some of the factors present in Scheiner's initial 1D models, including OPG, RANK, and RANKL were excluded due to the added complexity associated with the inclusion of these added factors and the corresponding equations governing their activity within the simulated bone tissue. Including only PTH and TGF-β without the appropriate factors to interact with likely contributed to the majority bone formation response of the simulated bone tissue, evidenced by exclusive porosity decrease in areas with high SED but no simultaneous porosity increase in areas with comparatively lower SED. An added limitation of the presented model is associated with the geometry used to simulate bone remodeling. While the rectangular geometry used in the present study allows for quantitative verification of the FE method and qualitative verification of the observed remodeling trends, it was not representative of bone tissue on any level. The simplistic nature of the geometric model in addition to the uniformity of the applied load could have contributed to the lack of porosity distribution throughout the model. Since the algorithm is not designed to accommodate a specific geometry, future work could be done to adapt more complex geometries to model bone adaptation. A study conducted by Mercuri et al. adapted the bone population models developed by Scheiner *et al.* and applied them to generic a 2D femoral geometry without microstructural detail [185]. While Mercuri *et al.* were able to demonstrate the bone cell population models on a 2D geometry, the FE model could not be validated.

The current algorithm was limited in the time scale of the simulated remodeling process. Scheiner *et al*. did not include time as a factor within the developed bone cell population models. Given the omission of time within the models, the only parameter to illustrate advancement of the bone remodeling process was the number of iterations to run the algorithm. Since it was assumed that one iteration of the algorithm encompassed a full activation and deactivation cycle for both osteoblasts and osteoclasts, the resolution of the simulated remodeling process was very low. From a biological standpoint, one full bone

remodeling cycle is completed over the course of 6-8 weeks. Future work is required to adapt the present algorithm to predict bone turnover within a shorter time period.

Finally, the present model implemented the global SED present in the geometric model as an input for the bone cell population models so that Scheiner's bone population models could be readily adapted; however, it is yet unknown if SED is the most appropriate FE-based mechanical stimulus for inducing bone remodeling. Future work is needed to investigate the use of localized stress and strain in addition to SED for implementation into the presented algorithm.

9.6 Conclusion

The algorithm shows promise in that the results were consistent with known physiological bone remodeling patterns. Incorporation of additional contributing biochemical factors is necessary to fully mimic physiological bone remodeling. Furthermore, the algorithm should be tested on additional 2D structures more representative of bone. Finally, the algorithm will be expanded to three dimensions to model whole bone.

Chapter 10

10. Conclusions and Future Work

10.1 Conclusions

. Overall, the studies presented within this document represented multiple facets of biomechanics research. The objectives driving the research presented in this document were 1) Assess bone tissue adaptation and its contributing factors using an *ex vivo* testing environment and 2) Model structural, material, and biochemical properties of the bulk tissue and of its constituents to simulate and predict bone tissue response and adaptation to applied stimulus.

The studies presented in Chapters 4-6 successfully demonstrated the utility of *ex vivo* organ culture for studying the effects of specific factors contributing to bone tissue biomechanical properties and bone modeling and remodeling. The *ex vivo* culture environment is a valuable tool for evaluating the response of bone tissue and observing its real time changes in mechanical and material properties. Though traditional engineering methods can provide some information about the mechanical and material properties of bone tissue, the results are often lacking since bone physical properties are dynamic and adapt in response to applied stimuli. Through the use of *ex vivo* culture, it is possible to simulate a physiological environment where systemic effects can be eliminated and observed changes within the maintained bone tissue can be attributed to isolated factors. This unique capability of *ex vivo* testing was evidenced in both Chapters 4 and 5, wherein it was determined that the endocrine/paracrine signaling molecule big endothelin-1 (ET1) and its receptors play a key role in the ability of bone to adapt to an applied mechanical stimulus. It was found that introduction of ET1 increased the rate of bone formation and increased the overall apparent elastic modulus of bovine trabecular bone cores. In the follow-up study presented within Chapter 5, it was determined that inhibition of ET1 signaling receptors significantly reduced the ability of human trabecular bone cores to adapt to an applied load.

Even after the conclusion of the *ex vivo* study, it was possible to evaluate changes within the bone tissue using a variety of methods that would have been less useful if alternative live culture testing had been conducted. In addition to being able to determine the bulk mechanical properties of the bone tissue and surveying the changes in biochemical activity through culture medium, it was possible to assess the micro level adaptations within the bone tissue in response to applied stimulus. This was accomplished through the use of histomorphometry whereby bone tissue was sectioned and analyzed to quantify the changes in tissue formation, mineralization, and cellular activity. In addition, morphological properties of the bone tissue could be analyzed and subsequently related to *ex vivo*-determined parameters. Analysis of the bone morphology found that bulk mechanical properties of trabecular bone tissue can be predicted by CT-based metrics. Moreover, these findings indicate that bone tissue mechanical properties are dependent on geometry in addition to the material properties of the underlying tissue.

Modeling of bone tissue is a valuable method for understanding contributions of multi-scale material and mechanical properties to the overall bulk tissue mechanical properties. Within the presented research, finite element (FE) analyses were successfully conducted on beta tricalcium phosphate (TCP) bone scaffolds—materials designed to mimic bone architecture and mechanical properties. By generating FE models that implemented the micro-level and nano-level material properties of the TCP scaffolds, it was possible to determine how the overall bulk mechanical properties were influenced by the properties of the framework material. This FE modeling was taken a step further to model human trabecular bone. Although computational limitations prevented quantitative modeling of trabecular bone, areas for model improvement were identified. Consistent with observations reported within literature, it was determined that using traditional FEA for modeling bone microstructure is not a broadly feasible method due to complications associated with mesh generation. A literature review found that generating a voxel-based mesh prior to conducting FEA would reduce computational requirements and improve determined results.

Finally, within the presented research, it was determined that bone modeling and remodeling can be simulated by implementing an iterative process that accounts for both mechanical stimulus and cellular

interactions within the tissue. An algorithm was generated that could successfully mimic bone remodeling by accounting for bone-native cell populations, relevant endocrine factors contributing to bone cell signaling, and an applied mechanical stimulus determined from FEA. While the developed algorithm did not include all necessary factors to fully represent a physiological environment accurately, the results suggest that future improvements to the model could have potential to predict human bone remodeling in real time.

10.2 Future Work

There are multiple areas for improvement and future research opportunities to follow the presented studies within this thesis. While *ex vivo* organ culture is an extremely useful tool for investigating the effects of mechanical and biochemical stimulus on the adaptation of bone tissue, there are a few limitations associated with the methods presented within this thesis. First and foremost, the axial loading apparatus used within the *ex vivo* culture system lacks mechanisms that would allow for control of strain rate and exact displacement application since the load applicator is voltage controlled. Future research should be focused on the development of an improved axial loading apparatus that would provide consistent displacement application across bone tissue samples, regardless of their bulk elastic modulus. Within the *ex vivo* culture system, improvements could be made to the experimental setup. The ZETOS *ex vivo* culture system used for the studies presented in Chapters 4-6 was limited by the lack of modularity and portability. Due to the inability to move any portion of the *ex vivo* system, acquiring micro-CT images of trabecular tissue prior to the start of the live testing was impossible and as such, determining changes in morphology resulting from the treatments administered during the study was not feasible.

With regards to the data collected during the *ex vivo* study process, there are also potential areas for further research. Besides acquiring micro-CT images of bone cores at the start of the study, it would be beneficial to acquire images throughout the course of live testing. This would allow for non-invasive (compared to histological methods) tracking of trabecular bone microstructure adaptations to applied

mechanical and biochemical stimulus. In addition, dual energy micro CT scans could be obtained for the bone cores. This would allow for increased ability to distinguish between phases of bone tissue and permit measurement of osteoid content. The capability for tracking osteoid content within trabecular bone samples would provide invaluable insight into the localized regions where bone formation is being initiated. In addition, implementing CT-based methods for evaluating microstructural changes within bone tissue would likely prove more cost-effective and allow for increased data collection to characterize the dynamic changes within bone tissue compared to traditional histomorphometric methods. This would subsequently increase the sensitivity of time-related bone remodeling analyses.

Within additional capability to survey the microstructural adaptations of trabecular bone tissue using CT-based methods comes an increased capability for validating FEA results. Future work should focus on correlating localized stresses, strains, and SED determined from FEA to the areas of highest mineral apposition or osteoid formation. The combination of FEA modeling with CT-based monitoring of live trabecular tissue could subsequently lead to comparison and evaluation of the underlying mechanisms regulating bone modeling and remodeling in response to mechanical loading.

Presented finite element methods used to model trabecular bone tissue could be improved through the use of CT-based voxel meshes. As stated in literature and as determined through the studies presented within this thesis, traditional FEA meshing is often too computationally expensive to model trabecular bone microstructure. A much more practical method would use the voxel size and position from bone CT scans to define mesh size and node positions. The resulting mesh could then be assigned uniform material properties or material density determined from the CT images could be used to assign a heterogeneous material model.

Finally, there are future research directions worth pursuing with regards to the developed bone remodeling algorithm presented in Chapter 9. First and foremost, the finite element method implemented could be improved such that geometric inputs would more closely reflect that of trabecular bone tissue. Ideally, the algorithm would be compatible with CT images so that the aforementioned voxel-based

meshing methods could be used for assigning initial material properties and for improved mesh quality within the FE solver. Since the ideal FE-based mechanical stimulus is yet unknown, the algorithm should be designed such that both strain and stress could be investigated as mechanical inputs in addition to the currently used strain energy density. The current model simulates bone as being linearly elastic and homogeneous. Given the non-linear, viscoelastic, and heterogeneous nature of bone, the current model is inadequate. Scheiner *et al.* has continued work in the area of analytical modeling and prediction of bone remodeling and has, in his most recent work, incorporated poroelasticity within the framework of the developed predictive models [71,186–188]. Future work should be driven towards expanding the current algorithm to reflect Scheiner's advancements and accommodate a more accurate simulation of bone's mechanical properties and remodeling response.

In addition, the algorithm should be expanded to three dimensions (3D) to accurately model bone geometrical adaptations. It is possible that this expansion into 3D will require a shift in the methods used to relate apparent elastic modulus and density of the simulated bone tissue. The current two-dimensional algorithm implements density-based stiffness relationships whereby the elastic modulus is related directly to the density cubed. Expanding this to 3D has the potential to cause discontinuities within the volume. Alternative methods, including topology optimization, should be investigated for further development of the predictive algorithm. Lastly, detailed validation of the bone remodeling algorithm is impossible if the factors included within the model to not match the factors measured and investigated within *ex vivo* studies. Future research should focus on designing *ex vivo* studies that investigate biochemical factors and mechanical loading schemes that are simulated within the bone remodeling algorithm or contrariwise.

References

[1]   L. Lidgren, The bone and joint decade 2000-2010., Bull. World Health Organ. 81 (2003) 629. http://www.ncbi.nlm.nih.gov/pubmed/19251065.

[2]   O. Johnell, J.A. Kanis, An estimate of the worldwide prevalence and disability associated with osteoporotic fractures, Osteoporos. Int. 17 (2006) 1726–1733. doi:10.1007/s00198-006-0172-4.

[3]   J.R. Bliuc D, Nguyen N.D., Milch, V.E. Nguyen, T.V., Eisman, J.A., Center, Mortality risk associated with low-trauma osteoporotic fracture and subsequent fracture in men and women, JAMA J. Am. Med. Assoc. 301 (2009) 513–521. doi:10.1001/jama.2009.50.

[4]   N.O. Foundation, Clinician's Guide to Prevention and Treatment of Osteoporosis, Natl. Osteoporos. Found. (2010) 1–36.

[5]   B. Abrahamsen, T. van Staa, R. Ariely, M. Olson, C. Cooper, Excess mortality following hip fracture: a systematic epidemiological review, Osteoporos Int. 20 (2009) 1633–1650. doi:10.1007/s00198-009-0920-3.

[6]   J.R. Center, T. V Nguyen, D. Schneider, P.N. Sambrook, J.A. Eisman, Mortality after all major types of osteoporotic fracture in men and women: an observational study, The Lancet . 353 (1999) 878–882. http://linkinghub.elsevier.com/retrieve/pii/S0140673698090758.

[7]   S.W. Blume, J.R. Curtis, Medical costs of osteoporosis in the elderly Medicare population, Osteoporos Int. 22 (2011) 1835–1844. doi:10.1007/s00198-010-1419-7.

[8]   R. Lakes, Viscoelastic Materials, Cambridge University Press, New York, New York, 2009. http://books.google.com/books?id=GYtZu5ta80AC.

[9]   L.A. Meyer, M.G. Johnson, D.M. Cullen, J.F. Vivanco, R.D. Blank, H.-L. Ploeg, E.L. Smith, Combined exposure to big endothelin-1 and mechanical loading in bovine sternal cores promotes osteogenesis., Bone. 85 (2016) 115–122. doi:10.1016/j.bone.2016.02.001.

[10]   T.M. Keaveny, E.F. Morgan, G.L. Niebur, O.C. Yeh, Biomechanics of Trabecular Bone, Annu. Rev. Biomed. Eng. 3 (2001) 307–333. doi:10.1146/annurev.bioeng.3.1.307.

[11]   R.B. Martin, D.B. Burr, N.A. Sharkey, Skeletal Tissue Mechanics, Illustrate, Springer, 2010.

http://books.google.com/books?id=hAgV2r4I-bYC.

[12]   J.D. Currey, Bones: Structure and Mechanics, 2nd ed., Princeton University Press, Princeton, New Jersey, 2002. http://books.google.com/books?id=2jYsJhxiNWQC.

[13]   S.M. Rabiee, S.M.J. Mortazavi, F. Moztarzadeh, D. Sharifi, S. Sharifi, M. Solati-Hashjin, H. Salimi-Kenari, D. Bizari, Mechanical behavior of a new biphasic calcium phosphate bone graft, Biotechnol. Bioprocess Eng. 13 (2008) 204–209. doi:10.1007/s12257-007-0163-0.

[14]   I.P. Herman, Physics of the Human Body, Illustrate, Springer, New York, New York, 2008. http://books.google.com/books?id=vtubxNaSAdAC.

[15]   M. Doblaré, J.M. García, M.J. Gómez, Modelling bone tissue fracture and healing: a review, Eng. Fract. Mech. 71 (2004) 1809–1840. doi:10.1016/j.engfracmech.2003.08.003.

[16]   B.K. Hall, Bones and Cartilage: Developmental and Evolutionary Skeletal Biology, Elsevier Academic Press, 2005. http://books.google.com/books?id=y-RWPGDONlIC.

[17]   J.P. Stains, R. Civitelli, Cell-to-cell interactions in bone., Biochem. Biophys. Res. Commun. 328 (2005) 721–7. doi:10.1016/j.bbrc.2004.11.078.

[18]   V. Mann, C. Huber, G. Kogianni, D. Jones, B. Noble, The influence of mechanical stimulation on osteocyte apoptosis and bone viability in human trabecular bone., J. Musculoskelet. Neuronal Interact. 6 (2006) 408–17. http://www.pubmedcentral.nih.gov/articlerender.fcgi?artid=1847464&tool=pmcentrez&rendertype=abstract (accessed August 13, 2012).

[19]   C.T. Rubin, L.E. Lanyon, D. Ph, Regulation of bone formation by applied dynamic loads, J Bone Jt. Surg Am. 66 (1984) 397–402.

[20]   C. Rubin, Skeletal strain and the functional significance of bone architecture, Calcif. Tissue Int. 36 (1984) S11–S18. doi:10.1007/BF02406128.

[21]   C.H. Turner, D.B. Burr, Basic biomechanical measurements of bone: A tutorial, Bone. 14 (1993) 595–608. http://www.sciencedirect.com/science/article/pii/875632829390081K.

[22]   S. Dudley-Javoroski, R.K. Shields, Asymmetric bone adaptations to soleus mechanical loading

after spinal cord injury., J. Musculoskelet. Neuronal Interact. 8 (2008) 227–238. http://www.ncbi.nlm.nih.gov/pubmed/18799855.

[23]   Y.C. Fung, Biomechanics: Mechanical Properties of Living Tissues, Springer, 1993. http://books.google.com/books?id=4HaMStTGOHwC.

[24]   J. Wolff, P. Maquet, R. Furlong, The law of bone remodelling, Springer-Verlag, 1986. http://books.google.com/books?id=XolsAAAAMAAJ.

[25]   H.M. Frost, Skeletal structural adaptations to mechanical usage (SATMU): 1. Redefining Wolff's law: the bone modeling problem., Anat. Rec. 226 (1990) 403–413. http://www.ncbi.nlm.nih.gov/pubmed/2184695.

[26]   H.M. Frost, The mechanostat: a proposed pathogenic mechanism of osteoporoses and the bone mass effects of mechanical and nonmechanical agents., Bone Miner. 2 (1987) 73–85. http://europepmc.org/abstract/MED/3333019.

[27]   P. Weinkamer, R, Fratzl, Mechanical adaptation of biological materials – The examples of bone and wood, Mater. Sci. Eng. 31 (2011) 1164–1173.

[28]   G.T. Aarnes, H. Steen, P. Ludvigsen, L.P.Å.L. Kristiansen, O. Reikerås, High frequency distraction improves tissue adaptation during leg lengthening in humans., J. Orthop. Res. 20 (2002) 789–92. doi:10.1016/S0736-0266(01)00175-9.

[29]   M. Liebschner, B. Bucklen, M. Wettergreen, Mechanical Aspects of Tissue Engineering, Semin. Plast. Surg. 19 (2005) 217–228.

[30]   V.J. Vigorita, Orthopaedic Pathology, Lippincott Williams & Wilkins, 2007. http://books.google.com/books?id=ehaH8sEq1zEC.

[31]   M.R. Forwood, C.H. Turner, Skeletal adaptations to mechanical usage: results from tibial loading studies in rats, Bone. 17 (1995) S197–S205. doi:10.1016/8756-3282(95)00292-L.

[32]   H.M. Frost, Skeletal structural adaptations to mechanical usage (SATMU): 3. The hyaline cartilage modeling problem., Anat. Rec. 226 (1990) 423–432. http://www.ncbi.nlm.nih.gov/pubmed/1691901.

[33]   C. Rubin, A.S. Turner, C. Mallinckrodt, C. Jerome, K. McLeod, S. Bain, Mechanical strain, induced noninvasively in the high-frequency domain, is anabolic to cancellous bone, but not cortical bone, Bone. 30 (2002) 445–452. doi:10.1016/s8756-3282(01)00689-5.

[34]   E. Seeman, Bone modeling and remodeling, Crit Rev Eukaryot Gene Expr. 19 (2009) 219–233.

[35]   B.C. Herman, L. Cardoso, R.J. Majeska, K.J. Jepsen, M.B. Schaffler, Activation of bone remodeling after fatigue: Differential response to linear microcracks and diffuse damage, Bone. 47 (2010) 766–772. http://www.sciencedirect.com/science/article/pii/S8756328210013499.

[36]   N. Marquis, M.E., Lord, E., Bergeron, E., Drevele, O., Park, H., caban, F., Senta, H., Faucheux, Bone Cells-Biomaterials Interactions, Front. Biosci. 14 (2009) 1023–1067.

[37]   T.A. Burgers, J. Mason, G. Niebur, H.L. Ploeg, Compressive properties of trabecular bone in the distal femur., J. Biomech. 41 (2008) 1077–85. doi:10.1016/j.jbiomech.2007.11.018.

[38]   V. David, L.D. Quarles, ASARM mineralization hypothesis: a bridge too far?, J. Bone Miner. Res. 25 (2010) 692–4. doi:10.1002/jbmr.69.

[39]   T.S. Gross, K.J. McLeod, C.T. Rubin, Characterizing bone strain distributions in vivo using three triple rosette strain gages, J. Biomech. 25 (1992) 1081–1087. http://www.sciencedirect.com/science/article/pii/0021929092900442.

[40]   a G. Robling, C.H. Turner, Mechanotransduction in bone: genetic effects on mechanosensitivity in mice., Bone. 31 (2002) 562–9. http://www.ncbi.nlm.nih.gov/pubmed/12477569.

[41]   T.E. Wenzel, M.B. Schaffler, D.P. Fyhrie, In vivo trabecular microcracks in human vertebral bone, Bone. 19 (1996) 89–95. http://www.sciencedirect.com/science/article/pii/8756328296888715.

[42]   D.B. Burr, R.B. Martin, M.B. Schaffler, E.L. Radin, Bone remodeling in response to in vivo fatigue microdamage, J. Biomech. 18 (1985) 189–200. http://www.sciencedirect.com/science/article/pii/0021929085902040.

[43]   W.L. Hylander, In vivo bone strain in the mandible of Galago crassicaudatus, Am. J. Phys. Anthropol. 46 (1977) 309–326. http://dx.doi.org/10.1002/ajpa.1330460212.

[44]   S.P. Fritton, K. J. McLeod, C.T. Rubin, Quantifying the strain history of bone: spatial uniformity

and self-similarity of low-magnitude strains, J. Biomech. 33 (2000) 317–325. http://www.sciencedirect.com/science/article/pii/S0021929099002109.

[45]   E.L. Jones, D.B., Broeckmann, E., Pohl, T. Smith, Development of a Mechanical Testing and Loading System for Trabecular Bone Studies for Long Term Culture, Eur. Cells Mater. 5 (2003) 48–60.

[46]   E. Vivanco, J, Garcia, S, Ploeg, H-L, Alvarez, G, Cullen, D, Smith, Apparent Elastic Modulus of Ex Vivo Trabecular Bovine Bone Increases with Dynamic Loading, J. Eng. Med. 227 (2013) 904–912.

[47]   A.K. Aiyangar, J. Vivanco, A.G. Au, P.A. Anderson, E.L. Smith, H.-L. Ploeg, Dependence of Anisotropy of Human Lumbar Vertebral Trabecular Bone on Quantitative Computed Tomography-Based Apparent Density, J. Biomech. Eng. 136 (2014) 91003. http://dx.doi.org/10.1115/1.4027663.

[48]   V. David, D. Ph, A. Guignandon, A. Martin, A. Rattner, V.A.L. Mann, B. Noble, D.B. Jones, L. Vico, D.E.T. Al, L. Malaval, M.-H. Lafage-Proust, Ex Vivo bone formation in bovine trabecular bone cultured in a dynamic 3D bioreactor is enhanced by compressive mechanical strain., Tissue Eng. Part A. 14 (2008) 117–126. doi:10.1089/ten.a.2007.0051.

[49]   J.A. Kanis, P. Delmas, P. Burckhardt, C. Cooper, D. Torgerson, Guidelines for diagnosis and management of osteoporosis, Osteoporos. Int. 7 (1997) 390–406. doi:10.1007/BF01623782.

[50]   S. Vasikaran, R. Eastell, O. Bruyère, A.J. Foldes, P. Garnero, A. Griesmacher, M. McClung, H.A. Morris, S. Silverman, T. Trenti, D.A. Wahl, C. Cooper, J.A. Kanis, Markers of bone turnover for the prediction of fracture risk and monitoring of osteoporosis treatment: a need for international reference standards, Osteoporos. Int. 22 (2011) 391–420. doi:10.1007/s00198-010-1501-1.

[51]   T. V. Nguyen, J.R. Center, J.A. Eisman, Osteoporosis: Underrated, underdiagnosed and undertreated, Med. J. Aust. (2004). doi:papers://82E9EA27-E255-4A82-9E40-6DAC45A310F4/Paper/p492.

[52]   L.S. Lim, L.J. Hoeksema, K. Sherin, Screening for osteoporosis in the adult U.S. population: ACPM position statement on preventive practice., Am. J. Prev. Med. 36 (2009) 366–75. doi:10.1016/j.amepre.2009.01.013.

[53]   R.P. van Hove, P.A. Nolte, A. Vatsa, C.M. Semeins, P.L. Salmon, T.H. Smit, J. Klein-Nulend, Osteocyte morphology in human tibiae of different bone pathologies with different bone mineral

density--is there a role for mechanosensing?, Bone. 45 (2009) 321–9. doi:10.1016/j.bone.2009.04.238.

[54] L. Humbert, J. Hazrati Marangalou, L.M. del Río Barquero, G.H. van Lenthe, B. van Rietbergen, Technical Note: Cortical thickness and density estimation from clinical CT using a prior thickness-density relationship, Med. Phys. 43 (2016) 1945–1954. doi:10.1118/1.4944501.

[55] M.I. Fanuscu, T.-L. Chang, Three-dimensional morphometric analysis of human cadaver bone: microstructural data from maxilla and mandible, Clin. Oral Implants Res. 15 (2004) 213–218. http://dx.doi.org/10.1111/j.1600-0501.2004.00969.x.

[56] D. Ulrich, B. van Rietbergen, A. Laib, P. Ŗuegsegger, The ability of three-dimensional structural indices to reflect mechanical aspects of trabecular bone, Bone. 25 (1999) 55–60. doi:10.1016/S8756-3282(99)00098-8.

[57] L.W. Goldman, Principles of CT and CT technology., J. Nucl. Med. Technol. 35 (2007) 115–28; quiz 129–30. doi:10.2967/jnmt.107.042978.

[58] J. Damilakis, J.E. Adams, G. Guglielmi, T.M. Link, Radiation exposure in X-ray-based imaging techniques used in osteoporosis., Eur. Radiol. 20 (2010) 2707–14. doi:10.1007/s00330-010-1845-0.

[59] A.C. Langheinrich, M. Kampschulte, C. Crössmann, R. Moritz, W.S. Rau, R.M. Bohle, E.L. Ritman, Role of computed tomography voxel size in detection and discrimination of calcium and iron deposits in atherosclerotic human coronary artery specimens., J. Comput. Assist. Tomogr. 33 517–22. doi:10.1097/RCT.0b013e318194c0a2.

[60] T.L. Mueller, M. Stauber, T. Kohler, F. Eckstein, R. Müller, G.H. van Lenthe, Non-invasive bone competence analysis by high-resolution pQCT: an in vitro reproducibility study on structural and mechanical properties at the human radius., Bone. 44 (2009) 364–71. doi:10.1016/j.bone.2008.10.045.

[61] N. Dalzell, S. Kaptoge, N. Morris, A. Berthier, B. Koller, L. Braak, B. van Rietbergen, J. Reeve, Bone micro-architecture and determinants of strength in the radius and tibia: age-related changes in a population-based study of normal adults measured with high-resolution pQCT., Osteoporos. Int. 20 (2009) 1683–94. doi:10.1007/s00198-008-0833-6.

[62] R. Cook, RD, Malkus, DS, Plesha, ME, Witt, Concepts and Applications of Finite Element Analysis, 4th ed., Wiley, New York, New York, 2001.

[63]   T.M. Turner, D.R. Sumner, R.M. Urban, D.P. Rivero, J.O. Galante, A comparative study of porous coatings in a weight-bearing total hip-arthroplasty model., J. Bone Joint Surg. Am. 68 (1986) 1396–409. http://jbjs.org/content/68/9/1396.abstract (accessed November 12, 2014).

[64]   C.K. McCarthy, G.G. Steinberg, M. Agren, D. Leahey, E. Wyman, D.T. Baran, Quantifying bone loss from the proximal femur after total hip arthroplasty, J. Bone Jt. Surgery, Br. Vol. 73-B (1991) 774–778. http://www.bjj.boneandjoint.org.uk/content/73-B/5/774.abstract.

[65]   B. Huiskes, R, Weinans, H, van Rietbergen, The Relationship Between Stress Shielding and Bone Resorption Around Total Hip Stems and the Effects of Flexible Materials, Clin. Orthop. Relat. Res. 274 (1992) 124–134.

[66]   R.P. Crawford, C.E. Cann, T.M. Keaveny, Finite element models predict in vitro vertebral body compressive strength better than quantitative computed tomography, Bone. 33 (2003) 744–750. doi:10.1016/S8756-3282(03)00210-2.

[67]   J. Schmitt, J. Meiforth, M. Lengsfeld, Development of a hybrid finite element model for individual simulation of intertrochanteric osteotomies, Med. Eng. Phys. 23 (2001) 529–539. doi:10.1016/S1350-4533(01)00085-6.

[68]   S. Boutroy, B. Van Rietbergen, E. Sornay-Rendu, F. Munoz, M.L. Bouxsein, P.D. Delmas, Finite element analysis based on in vivo HR-pQCT images of the distal radius is associated with wrist fracture in postmenopausal women., J. Bone Miner. Res. 23 (2008) 392–9. doi:10.1359/jbmr.071108.

[69]   S.P. Kotha, Y.-F. Hsieh, R.M. Strigel, R. Müller, M.J. Silva, Experimental and finite element analysis of the rat ulnar loading model-correlations between strain and bone formation following fatigue loading., J. Biomech. 37 (2004) 541–8. doi:10.1016/j.jbiomech.2003.08.009.

[70]   P. Pivonka, S. V Komarova, Mathematical modeling in bone biology: from intracellular signaling to tissue mechanics., Bone. 47 (2010) 181–9. doi:10.1016/j.bone.2010.04.601.

[71]   S. Scheiner, P. Pivonka, C. Hellmich, Coupling systems biology with multiscale mechanics, for computer simulations of bone remodeling, Comput. Methods Appl. Mech. Eng. 254 (2013) 181–196. doi:10.1016/j.cma.2012.10.015.

[72]   A. Fritsch, C. Hellmich, L. Dormieux, Ductile sliding between mineral crystals followed by rupture of collagen crosslinks: experimentally supported micromechanical explanation of bone strength., J. Theor. Biol. 260 (2009) 230–52. doi:10.1016/j.jtbi.2009.05.021.

[73]   C.T. Rubin, L.E. Lanyon, Regulation of bone mass by mechanical strain magnitude, Calcif. Tissue Int. 37 (1985) 411–417. doi:10.1007/BF02553711.

[74]   J. Klein-Nulend, A.D. Bakker, R.G. Bacabac, A. Vatsa, S. Weinbaum, Mechanosensation and transduction in osteocytes., Bone. 54 (2013) 182–90. doi:10.1016/j.bone.2012.10.013.

[75]   D.M. Raab, T.D. Crenshaw, D.B. Kimmel, E.L. Smith, A histomorphometric study of cortical bone activity during increased weight-bearing exercise., J. Bone Miner. Res. 6 (1991) 741–9. doi:10.1002/jbmr.5650060712.

[76]   D.M. Raab-Cullen, M.P. Akhter, D.B. Kimmel, R.R. Recker, Periosteal bone formation stimulated by externally induced bending strains., J. Bone Miner. Res. 9 (1994) 1143–52. doi:10.1002/jbmr.5650090803.

[77]   S. Srinivasan, D.A. Weimer, S.C. Agans, S.D. Bain, T.S. Gross, Low-Magnitude Mechanical Loading Becomes Osteogenic When Rest Is Inserted Between Each Load Cycle, J. Bone Miner. Res. 17 (2002) 1613–1620. doi:10.1359/jbmr.2002.17.9.1613.

[78]   H.M. Frost, Bone "mass" and the "mechanostat": a proposal., Anat. Rec. 219 (1987) 1–9. doi:10.1002/ar.1092190104.

[79]   H.M. Frost, Bone's mechanostat: a 2003 update., Anat. Rec. A. Discov. Mol. Cell. Evol. Biol. 275 (2003) 1081–101. doi:10.1002/ar.a.10119.

[80]   V. David, A. Martin, M.-H. Lafage-Proust, L. Malaval, S. Peyroche, D.B. Jones, L. Vico, A. Guignandon, Mechanical loading down-regulates peroxisome proliferator-activated receptor gamma in bone marrow stromal cells and favors osteoblastogenesis at the expense of adipogenesis., Endocrinology. 148 (2007) 2553–62. doi:10.1210/en.2006-1704.

[81]   C.M. Davies, D.B. Jones, M.J. Stoddart, K. Koller, E. Smith, C.W. Archer, R.G. Richards, Mechanically loaded ex vivo bone culture system "Zetos": systems and culture preparation., Eur. Cell. Mater. 11 (2006) 57–75; discussion 75. http://www.ncbi.nlm.nih.gov/pubmed/16612792.

[82]   D. Endres, S, Kratz, M, Wunsch, S, Jones, Zetos: A culture loading system for trabecular bone. Investation of different loading signal intensities on bovine bone cylinders, J. Musculoskelet. Neuronal Interact. 9 (2009) 173–183.

[83]   E. Birmingham, T.C. Kreipke, E.B. Dolan, T.R. Coughlin, P. Owens, L.M. McNamara, G.L.

Niebur, P.E. McHugh, Mechanical Stimulation of Bone Marrow In Situ Induces Bone Formation in Trabecular Explants, Ann. Biomed. Eng. (2014) 1–15. doi:10.1007/s10439-014-1135-0.

[84]   P.J. Niziolek, T.L. Farmer, Y. Cui, C.H. Turner, M.L. Warman, A.G. Robling, High-bone-mass-producing mutations in the Wnt signaling pathway result in distinct skeletal phenotypes., Bone. 49 (2011) 1010–9. doi:10.1016/j.bone.2011.07.034.

[85]   M.P. Akhter, D.J. Wells, S.J. Short, D.M. Cullen, M.L. Johnson, G.R. Haynatzki, P. Babij, K.M. Allen, P.J. Yaworsky, F. Bex, R.R. Recker, Bone biomechanical properties in LRP5 mutant mice., Bone. 35 (2004) 162–9. doi:10.1016/j.bone.2004.02.018.

[86]   K. Sawakami, A.G. Robling, M. Ai, N.D. Pitner, D. Liu, S.J. Warden, J. Li, P. Maye, D.W. Rowe, R.L. Duncan, M.L. Warman, C.H. Turner, The Wnt co-receptor LRP5 is essential for skeletal mechanotransduction but not for the anabolic bone response to parathyroid hormone treatment., J. Biol. Chem. 281 (2006) 23698–711. doi:10.1074/jbc.M601000200.

[87]   K.S. Kang, A.G. Robling, New Insights into Wnt-Lrp5/6-β-Catenin Signaling in Mechanotransduction., Front. Endocrinol. (Lausanne). 5 (2014) 246. doi:10.3389/fendo.2014.00246.

[88]   A.G. Robling, P.J. Niziolek, L.A. Baldridge, K.W. Condon, M.R. Allen, I. Alam, S.M. Mantila, J. Gluhak-Heinrich, T.M. Bellido, S.E. Harris, C.H. Turner, Mechanical stimulation of bone in vivo reduces osteocyte expression of Sost/sclerostin., J. Biol. Chem. 283 (2008) 5866–75. doi:10.1074/jbc.M705092200.

[89]   L.F. Bonewald, M.L. Johnson, Osteocytes, mechanosensing and Wnt signaling., Bone. 42 (2008) 606–15. doi:10.1016/j.bone.2007.12.224.

[90]   J. Rubin, C. Rubin, C.R. Jacobs, Molecular pathways mediating mechanical signaling in bone., Gene. 367 (2006) 1–16. doi:10.1016/j.gene.2005.10.028.

[91]   D.C. Genetos, C.E. Yellowley, G.G. Loots, Prostaglandin E2 signals through PTGER2 to regulate sclerostin expression., PLoS One. 6 (2011) e17772. doi:10.1371/journal.pone.0017772.

[92]   H. Keller, M. Kneissel, SOST is a target gene for PTH in bone., Bone. 37 (2005) 148–58. doi:10.1016/j.bone.2005.03.018.

[93]   M.G. Johnson, J. Kristianto, B. Yuan, K. Konicke, R. Blank, Big endothelin changes the cellular

miRNA environment in TMOb osteoblasts and increases mineralization., Connect. Tissue Res. 55 Suppl 1 (2014) 113–6. doi:10.3109/03008207.2014.923866.

[94] A.G. Robling, J. Li, K.L. Shultz, W.G. Beamer, C.H. Turner, Evidence for a skeletal mechanosensitivity gene on mouse chromosome 4., FASEB J. 17 (2003) 324–6. doi:10.1096/fj.02-0393fje.

[95] N. Saless, G.E. Lopez Franco, S. Litscher, R.S. Kattappuram, M.J. Houlihan, R. Vanderby, P. Demant, R.D. Blank, Linkage mapping of femoral material properties in a reciprocal intercross of HcB-8 and HcB-23 recombinant mouse strains., Bone. 46 (2010) 1251–9. doi:10.1016/j.bone.2010.01.375.

[96] N. Saless, S.J. Litscher, G.E. Lopez Franco, M.J. Houlihan, S. Sudhakaran, K.A. Raheem, T.K. O'Neil, R. Vanderby, P. Demant, R.D. Blank, Quantitative trait loci for biomechanical performance and femoral geometry in an intercross of recombinant congenic mice: restriction of the Bmd7 candidate interval., FASEB J. 23 (2009) 2142–54. doi:10.1096/fj.08-118679.

[97] N. Saless, S.J. Litscher, M.J. Houlihan, I.K. Han, D. Wilson, P. Demant, R.D. Blank, Comprehensive skeletal phenotyping and linkage mapping in an intercross of recombinant congenic mouse strains HcB-8 and HcB-23., Cells. Tissues. Organs. 194 (2011) 244–8. doi:10.1159/000324774.

[98] H.. von Schroeder, C.. Veillette, J. Payandeh, A. Qureshi, J.N.. Heersche, Endothelin-1 promotes osteoprogenitor proliferation and differentiation in fetal rat calvarial cell cultures, Bone. 33 (2003) 673–684. doi:10.1016/S8756-3282(03)00215-1.

[99] S. García-Rodríguez, E.L. Smith, H.-L. Ploeg, A Calibration Procedure for a Bone Loading System, J. Med. Device. 2 (2008) 11006. http://dx.doi.org/10.1115/1.2889059.

[100] P.J. McNair, H. Prapavessis, Normative data of vertical ground reaction forces during landing from a jump, J. Sci. Med. Sport. 2 (1999) 86–88. doi:10.1016/S1440-2440(99)80187-X.

[101] Y.H. An, R.A. Draughn, Mechanical testing of bone and the bone-implant interface, CRC press, 1999.

[102] S.C. Cowin, Bone biomechanics handbook, (2001).

[103] R.B. Bach, D. Burr, N.A. Sharkey, Skeletal Tissue Mechanics, Springer Science & Business

Media, 2013.

[104] R.R. Recker, D.B. Kimmel, D. Dempster, R.S. Weinstein, T.J. Wronski, D.B. Burr, Issues in modern bone histomorphometry., Bone. 49 (2011) 955–64. doi:10.1016/j.bone.2011.07.017.

[105] M.M. Saunders, Biomimetics in Bone Cell Mechanotransduction: Understanding Bone's Response to Mechanical Loading, INTECH Open Access Publisher, 2011.

[106] A.A. Pitsillides, S.C.F. Rawlinson, Using cell and organ culture models to analyze responses of bone cells to mechanical stimulation., Methods Mol. Biol. 816 (2012) 593–619. doi:10.1007/978-1-61779-415-5_37.

[107] A.B. Yeatts, J.P. Fisher, Bone tissue engineering bioreactors: dynamic culture and the influence of shear stress., Bone. 48 (2011) 171–81. doi:10.1016/j.bone.2010.09.138.

[108] M. Yanagisawa, H. Kurihara, S. Kimura, Y. Tomobe, M. Kobayashi, Y. Mitsui, Y. Yazaki, K. Goto, T. Masaki, A novel potent vasoconstrictor peptide produced by vascular endothelial cells, Nature. 332 (1988) 411–415.

[109] D. Xu, N. Emoto, A. Giaid, C. Slaughter, S. Kaw, D. deWit, M. Yanagisawa, ECE-1: A membrane-bound metalloprotease that catalyzes the proteolytic activation of big endothelin-1, Cell. 78 (1994) 473–485. doi:10.1016/0092-8674(94)90425-1.

[110] M. Barton, M. Yanagisawa, Endothelin: 20 years from discovery to therapyThis article is one of a selection of papers published in the special issue (part 2 of 2) on Forefronts in Endothelin., Can. J. Physiol. Pharmacol. (2008). http://www.nrcresearchpress.com.ezproxy.library.wisc.edu/doi/abs/10.1139/Y08-059#.VyE8ikfl9n0 (accessed April 27, 2016).

[111] T. Käsbauer, P. Towb, O. Alexandrova, C.N. David, E. Dall'Armi, A. Staudigl, B. Stiening, A. Böttger, The Notch signaling pathway in the cnidarian Hydra, Dev. Biol. 303 (2007) 376–390.

[112] K. Kaloulis, Molecular Basis of Morphogenetic Events in Hydra: Study of the CREB and Hedgehog Pathways during Budding and Regeneration., (2000).

[113] B. Hobmayer, F. Rentzsch, K. Kuhn, C.M. Happel, C.C. von Laue, P. Snyder, U. Rothbächer, T.W. Holstein, WNT signalling molecules act in axis formation in the diploblastic metazoan Hydra., Nature. 407 (2000) 186–9. doi:10.1038/35025063.

[114] J. Zhang, A. Leontovich, M.P. Sarras, Molecular and functional evidence for early divergence of an endothelin-like system during metazoan evolution: analysis of the Cnidarian, hydra, Development. 128 (2001) 1607–1615.

[115] D. Clouthier, K. Hosoda, J. Richardson, S. Williams, H. Yanagisawa, T. Kuwaki, M. Kumada, R. Hammer, M. Yanagisawa, Cranial and cardiac neural crest defects in endothelin-A receptor-deficient mice, Development. 125 (1998) 813–824. http://dev.biologists.org.ezproxy.library.wisc.edu/content/125/5/813.short (accessed April 28, 2016).

[116] K. Hosoda, R.E. Hammer, J.A. Richardson, A.G. Baynash, J.C. Cheung, A. Giaid, M. Yanagisawa, Targeted and natural (piebald-lethal) mutations of endothelin-B receptor gene produce megacolon associated with spotted coat color in mice, Cell. 79 (1994) 1267–1276. doi:10.1016/0092-8674(94)90017-5.

[117] H. Yanagisawa, M. Yanagisawa, R. Kapur, J. Richardson, S. Williams, D. Clouthier, D. de Wit, N. Emoto, R. Hammer, Dual genetic pathways of endothelin-mediated intercellular signaling revealed by targeted disruption of endothelin converting enzyme-1 gene, Development. 125 (1998) 825–836. http://dev.biologists.org.ezproxy.library.wisc.edu/content/125/5/825.short (accessed April 27, 2016).

[118] G.A. Clines, K.S. Mohammad, J.M. Grunda, K.L. Clines, M. Niewolna, C.R. McKenna, C.R. McKibbin, M. Yanagisawa, L.J. Suva, J.M. Chirgwin, T.A. Guise, Regulation of postnatal trabecular bone formation by the osteoblast endothelin A receptor., J. Bone Miner. Res. 26 (2011) 2523–36. doi:10.1002/jbmr.450.

[119] T.A. Guise, W.M. Kozlow, A. Heras-Herzig, S.S. Padalecki, J.J. Yin, J.M. Chirgwin, Molecular Mechanisms of Breast Cancer Metastases to Bone, Clin. Breast Cancer. 5 (2005) S46–S53. doi:10.3816/CBC.2005.s.004.

[120] K.S. Mohammad, T.A. Guise, Mechanisms of osteoblastic metastases: role of endothelin-1., Clin. Orthop. Relat. Res. 415 (2003) S67–S74.

[121] S. Harris, J.R. Wu-Wong, J.L. Wessale, J.J. Yin, K.S. Mohammad, S.M. Ka, R.J. Padley, I.R. Garrett, J.M. Chirgwin, T.A. Guise, S.M. Käkönen, S. Harris, J.R. Wu-Wong, J.L. Wessale, R.J. Padley, I.R. Garrett, J.M. Chirgwin, T.A. Guise, A causal role for endothelin-1 in the pathogenesis of osteoblastic bone metastases., Proc. Natl. Acad. Sci. U. S. A. 100 (2003) 10954–9. doi:10.1073/pnas.1830978100.

[122] S. Dekel, G. Lenthall, M. Francis, Release of prostaglandins from bone and muscle after tibial

fracture. An experimental study in rabbits, J Bone Jt. Surg Br. 63-B (1981) 185–189.
http://www.bjj.boneandjoint.org.uk.ezproxy.library.wisc.edu/content/63-B/2/185.short (accessed
April 27, 2016).

[123] K. Thorsen, A.O. Kristoffersson, U.H. Lerner, R.P. Lorentzon, In situ microdialysis in bone tissue.
Stimulation of prostaglandin E2 release by weight-bearing mechanical loading., J. Clin. Invest. 98
(1996) 2446–9. doi:10.1172/JCI119061.

[124] J. Klein-Nulend, E.H. Burger, C.M. Semeins, L.G. Raisz, C.C. Pilbeam, Pulsating fluid flow
stimulates prostaglandin release and inducible prostaglandin G/H synthase mRNA expression in
primary mouse bone cells., J. Bone Miner. Res. 12 (1997) 45–51. doi:10.1359/jbmr.1997.12.1.45.

[125] J. Klein-Nulend, J. Roelofsen, J.G. Sterck, C.M. Semeins, E.H. Burger, Mechanical loading
stimulates the release of transforming growth factor-beta activity by cultured mouse calvariae and
periosteal cells., J. Cell. Physiol. 163 (1995) 115–9. doi:10.1002/jcp.1041630113.

[126] T.M. Keaveny, T.P. Pinilla, R.P. Crawford, D.L. Kopperdahl, A. Lou, Systematic and random
errors in compression testing of trabecular bone., J. Orthop. Res. 15 (1997) 101–10.
doi:10.1002/jor.1100150115.

[127] W.B. Lievers, A.C. Petryshyn, A.S. Poljsak, S.D. Waldman, A.K. Pilkey, Specimen diameter and
"side artifacts" in cancellous bone evaluated using end-constrained elastic tension., Bone. 47
(2010) 371–7. doi:10.1016/j.bone.2010.03.024.

[128] T.P. Harrigan, M. Jasty, R.W. Mann, W.H. Harris, Limitations of the continuum assumption in
cancellous bone, J. Biomech. 21 (1988) 269–275. doi:10.1016/0021-9290(88)90257-6.

[129] R.R. Recker, D.B. Kimmel, M.A. Parfitt, M.K. Davies, N. Keshawarz, S. Hinders, Static and
tetracycline-based bone histomorphometric data from 34 normal postmenopausal females, J. Bone
Miner. Res. 3 (1988) 133–144. doi:10.1002/jbmr.5650030203.

[130] S.P. Fritton, C.T. Rubin, In vivo measurement of bone deformations using strain gauges, Bone
Mech. Handb. (2001) 1–8.

[131] D.B. Burr, C. Milgrom, D. Fyhrie, M. Forwood, M. Nyska, A. Finestone, S. Hoshaw, E. Saiag, A.
Simkin, In vivo measurement of human tibial strains during vigorous activity, Bone. 18 (1996)
405–410. doi:10.1016/8756-3282(96)00028-2.

[132] H.M.S. Davies, R.N. McCarthy, L.B. Jeffcott, Surface Strain on the Dorsal Metacarpus of Thoroughbreds at Different Speeds and Gaits, Cells Tissues Organs. 146 (1993) 148–153. doi:10.1159/000147437.

[133] A.G. Robling, C.H. Turner, Mechanical signaling for bone modeling and remodeling., Crit. Rev. Eukaryot. Gene Expr. 19 (2009) 319–38. http://www.pubmedcentral.nih.gov/articlerender.fcgi?artid=3743123&tool=pmcentrez&rendertype=abstract (accessed March 5, 2016).

[134] G.A. Clines, K.S. Mohammad, Y. Bao, O.W. Stephens, L.J. Suva, J.D. Shaughnessy, J.W. Fox, J.M. Chirgwin, T.A. Guise, Dickkopf homolog 1 mediates endothelin-1-stimulated new bone formation., Mol. Endocrinol. 21 (2007) 486–98. doi:10.1210/me.2006-0346.

[135] M.P. Akhter, D.M. Cullen, E.A. Pedersen, D.B. Kimmel, R.R. Recker, Bone Response to In Vivo Mechanical Loading in Two Breeds of Mice, Calcif. Tissue Int. 63 (1998) 442–449. doi:10.1007/s002239900554.

[136] K. Ishikawa, T. Fukami, T. Nagase, K. Fujita, T. Hayama, K. Niiyama, T. Mase, M. Ihara, M. Yano, Cyclic pentapeptide endothelin antagonists with high ETA selectivity. Potency- and solubility-enhancing modifications, J. Med. Chem. 35 (1992) 2139–2142. doi:10.1021/jm00089a028.

[137] J. Slane, J. Vivanco, J. Meyer, H.-L. Ploeg, M. Squire, Modification of acrylic bone cement with mesoporous silica nanoparticles: effects on mechanical, fatigue and absorption properties., J. Mech. Behav. Biomed. Mater. 29 (2014) 451–61. doi:10.1016/j.jmbbm.2013.10.008.

[138] robling niziolek baldrige condon - Google Scholar, (n.d.). https://scholar-google-com.ezproxy.library.wisc.edu/scholar?q=robling+niziolek+baldrige+condon&btnG=&hl=en&as_sdt=0%2C50 (accessed April 27, 2016).

[139] National Osteoporosis Foundation, What is Osteoporosis and What Causes It?, 2013. https://www.nof.org/patients/what-is-osteoporosis/ (accessed April 28, 2016).

[140] J.Y. Reginster, A. Neuprez, C. Beaudart, M.P. Lecart, N. Sarlet, D. Bernard, S. Disteche, O. Bruyere, Antiresorptive Drugs Beyond Bisphosphonates and Selective Oestrogen Receptor Modulators for the Management of Postmenopausal Osteoporosis, Drugs Aging. 31 (2014) 413–424. doi:10.1007/s40266-014-0179-z.

[141] C.H. Turner, S.J. Warden, T. Bellido, L.I. Plotkin, N. Kumar, I. Jasiuk, J. Danzig, A.G. Robling,

Mechanobiology of the skeleton., Sci. Signal. 2 (2009) pt3. doi:10.1126/scisignal.268pt3.

[142] M. Doube, M.M. Kłosowski, I. Arganda-Carreras, F.P. Cordelières, R.P. Dougherty, J.S. Jackson, B. Schmid, J.R. Hutchinson, S.J. Shefelbine, BoneJ: Free and extensible bone image analysis in ImageJ., Bone. 47 (2010) 1076–9. doi:10.1016/j.bone.2010.08.023.

[143] R.B. Martin, D.B. Burr, N.A. Sharkey, D.P. Fyhrie, Skeletal Tissue Mechanics, Springer New York, New York, NY, 2015. doi:10.1007/978-1-4939-3002-9.

[144] O. Johnell, J.A. Kanis, An estimate of the worldwide prevalence and disability associated with osteoporotic fractures, Osteoporos. Int. 17 (2006) 1726–1733. doi:10.1007/s00198-006-0172-4.

[145] C.M. Klotzbuecher, P.D. Ross, P.B. Landsman, T.A. Abbott, M. Berger, Patients with prior fractures have an increased risk of future fractures: a summary of the literature and statistical synthesis., J. Bone Miner. Res. 15 (2000) 721–39. doi:10.1359/jbmr.2000.15.4.721.

[146] R. Burge, B. Dawson-Hughes, D.H. Solomon, J.B. Wong, A. King, A. Tosteson, Incidence and Economic Burden of Osteoporosis-Related Fractures in the United States, 2005–2025, J. Bone Miner. Res. 22 (2007) 465–475. doi:10.1359/jbmr.061113.

[147] D.J. Vanness, A.N.A. Tosteson, Estimating the opportunity costs of osteoporosis in the United States., Top. Geriatr. Rehabil. 21 (2005) 4–16. http://search.ebscohost.com/login.aspx?direct=true&AuthType=ip,uid&db=rzh&AN=2005083952 &site=ehost-live&scope=site.

[148] S.J. Hoshaw, D.P. Fyhrie, Y. Takano, D.B. Burr, C. Milgrom, A method suitable for in vivo measurement of bone strain in humans, J. Biomech. 30 (1997) 521–524. doi:10.1016/S0021-9290(96)00176-5.

[149] S.L. Ruggiero, S.J. Drew, Osteonecrosis of the Jaws and Bisphosphonate Therapy, J. Dent. Res. 86 (2007) 1013–1021. doi:10.1177/154405910708601101.

[150] D.K. Wysowski, P. Greene, Trends in osteoporosis treatment with oral and intravenous bisphosphonates in the United States, 2002-2012., Bone. 57 (2013) 423–8. doi:10.1016/j.bone.2013.09.008.

[151] S.L. Silverman, K. Nasser, Teriparitide update., Rheum. Dis. Clin. North Am. 37 (2011) 471–7, vii. doi:10.1016/j.rdc.2011.08.002.

[152] M.R. McClung, A. Grauer, S. Boonen, M.A. Bolognese, J.P. Brown, A. Diez-Perez, B.L. Langdahl, J.-Y. Reginster, J.R. Zanchetta, S.M. Wasserman, L. Katz, J. Maddox, Y.-C. Yang, C. Libanati, H.G. Bone, Romosozumab in postmenopausal women with low bone mineral density., N. Engl. J. Med. 370 (2014) 412–20. doi:10.1056/NEJMoa1305224.

[153] J.S. McCombs, P. Thiebaud, C. McLaughlin-Miley, J. Shi, Compliance with drug therapies for the treatment and prevention of osteoporosis, Maturitas. 48 (2004) 271–287. doi:10.1016/j.maturitas.2004.02.005.

[154] B.S. Komm, D. Morgenstern, L. A Yamamoto, S.N. Jenkins, The safety and tolerability profile of therapies for the prevention and treatment of osteoporosis in postmenopausal women., Expert Rev. Clin. Pharmacol. 8 (2015) 769–84. doi:10.1586/17512433.2015.1099432.

[155] J. Vivanco, S. García-Rodríguez, E.L. Smith, H.-L. Ploeg, Material and Mechanical Properties of Tricalcium Phosphate-Based (TCP) Scaffolds, in: ASME 2009 Summer Bioeng. Conf. Parts A B, ASME, 2009: p. 879. doi:10.1115/SBC2009-204934.

[156] J. Vivanco, J. Slane, R. Nay, A. Simpson, H.-L. Ploeg, The effect of sintering temperature on the microstructure and mechanical properties of a bioceramic bone scaffold., J. Mech. Behav. Biomed. Mater. 4 (2011) 2150–60. doi:10.1016/j.jmbbm.2011.07.015.

[157] J. Vivanco, J. Slane, H. Ploeg, Nano-Mechanical Properties of Bioceramic Bone Scaffolds Fabricated at Three Sintering Temperatures, in: ASME 2011 Summer Bioeng. Conf. Parts A B, ASME, 2011: p. 1307. doi:10.1115/SBC2011-53734.

[158] J. Vivanco, J.E. Jakes, J. Slane, H.L. Ploeg, Accounting for structural compliance in nanoindentation measurements of bioceramic bone scaffolds, Ceram. Int. 40 (2014) 12485–12492. doi:10.1016/j.ceramint.2014.04.103.

[159] D.W. Hutmacher, Scaffolds in tissue engineering bone and cartilage, Biomaterials. 21 (2000) 2529–2543. http://www.sciencedirect.com/science/article/pii/S0142961200001216.

[160] J.R. Mauney, S. Sjostorm, J. Blumberg, R. Horan, J.P. O'Leary, G. Vunjak-Novakovic, V. Volloch, D.L. Kaplan, Mechanical stimulation promotes osteogenic differentiation of human bone marrow stromal cells on 3-D partially demineralized bone scaffolds in vitro., Calcif. Tissue Int. 74 (2004) 458–68. doi:10.1007/s00223-003-0104-7.

[161] H.-L. Vivanco, J., Araneda , A., Ploeg, Effect of Sintering Temperature on Microstructural Properties of Bioceramic Bone Scaffolds, in: S.B. and A.B. R. Narayan (Ed.), Biomater. Sci.

Process. Prop. Appl. II Ceram. Trans., Volume 237, John Wiley & Sons, Inc., Hoboken, NJ, USA, 2012.

[162] B. Van Rietbergen, S. Majumdar, W. Pistoia, D.C. Newitt, M. Kothari, A. Laib, P. Rüegsegger, Assessment of cancellous bone mechanical properties from micro-FE models based on micro-CT, pQCT and MR images, Technol. Heal. Care. 6 (1998) 413–420.

[163] J.. Waarsing, J.. Day, J.. van der Linden, A.. Ederveen, C. Spanjers, N. De Clerck, A. Sasov, J.A.. Verhaar, H. Weinans, Detecting and tracking local changes in the tibiae of individual rats: a novel method to analyse longitudinal in vivo micro-CT data, Bone. 34 (2004) 163–169. doi:10.1016/j.bone.2003.08.012.

[164] I.S. Tamminen, H. Isaksson, A.S. Aula, E. Honkanen, J.S. Jurvelin, H. Kröger, Reproducibility and agreement of micro-CT and histomorphometry in human trabecular bone with different metabolic status., J. Bone Miner. Metab. 29 (2011) 442–8. doi:10.1007/s00774-010-0236-6.

[165] K. Brixen, R. Chapurlat, A.M. Cheung, T.M. Keaveny, T. Fuerst, K. Engelke, R. Recker, B. Dardzinski, N. Verbruggen, S. Ather, E. Rosenberg, A.E. de Papp, Bone density, turnover, and estimated strength in postmenopausal women treated with odanacatib: a randomized trial., J. Clin. Endocrinol. Metab. 98 (2013) 571–80. doi:10.1210/jc.2012-2972.

[166] T.M. Keaveny, D.W. Donley, P.F. Hoffmann, B.H. Mitlak, E. V Glass, J.A. San Martin, Effects of Teriparatide and Alendronate on Vertebral Strength as Assessed by Finite Element Modeling of QCT Scans in Women With Osteoporosis, J. Bone Miner. Res. 22 (2007) 149–157. doi:10.1359/jbmr.061011.

[167] S. Boutroy, B. Van Rietbergen, E. Sornay-Rendu, F. Munoz, M.L. Bouxsein, P.D. Delmas, Finite Element Analysis Based on In Vivo HR-pQCT Images of the Distal Radius Is Associated With Wrist Fracture in Postmenopausal Women, J. Bone Miner. Res. 23 (2008) 392–399. doi:10.1359/jbmr.071108.

[168] R.I.K. HUISKES, H. WEINANS, B.V.A.N. RIETBERGEN, B. Huiskes, RIK, Weinans, H, van Rietbergen, B. Huiskes, R, Weinans, H, van Rietbergen, The Relationship Between Stress Shielding and Bone Resorption Around Total Hip Stems and the Effects of Flexible Materials, Clin. Orthop. Relat. Res. 274 (1992) 124–134. http://journals.lww.com/corr/Fulltext/1992/01000/The_Relationship_Between_Stress_Shielding_and_Bone.14.aspx.

[169] E.F. Morgan, H.H. Bayraktar, T.M. Keaveny, Trabecular bone modulus–density relationships depend on anatomic site, J. Biomech. 36 (2003) 897–904. doi:10.1016/S0021-9290(03)00071-X.

[170] B. Helgason, E. Perilli, E. Schileo, F. Taddei, S. Brynjólfsson, M. Viceconti, Mathematical relationships between bone density and mechanical properties: a literature review., Clin. Biomech. (Bristol, Avon). 23 (2008) 135–46. doi:10.1016/j.clinbiomech.2007.08.024.

[171] R. Müller, P. Rüegsegger, Three-dimensional finite element modelling of non-invasively assessed trabecular bone structures, Med. Eng. Phys. 17 (1995) 126–133. doi:10.1016/1350-4533(95)91884-J.

[172] B. van Rietbergen, Micro-FE Analyses of Bone: State of the Art, in: Springer US, 2001: pp. 21–30. doi:10.1007/978-1-4615-0651-5_3.

[173] B. van Rietbergen, H. Weinans, R. Huiskes, A. Odgaard, A new method to determine trabecular bone elastic properties and loading using micromechanical finite-element models, J. Biomech. 28 (1995) 69–81. doi:10.1016/0021-9290(95)80008-5.

[174] R. Lindsay, C. Christiansen, T.A. Einhorn, D.M. Hart, S. Ljunghall, C.A. Mautalen, P.J. Meunier, H. Morii, G.R. Mundy, A. Rapado, Who are candidates for prevention and treatment for osteoporosis?, Osteoporos. Int. 7 (1997) 1–6.

[175] S.R. Cummings, L.J. Melton, Epidemiology and outcomes of osteoporotic fractures., Lancet. 359 (2002) 1761–7. doi:10.1016/S0140-6736(02)08657-9.

[176] J. Vestbo, S.S. Hurd, R. Rodriguez-Roisin, The 2011 revision of the global strategy for the diagnosis, management and prevention of COPD (GOLD) – why and what?, Clin. Respir. J. 6 (2012) 208–214. doi:10.1111/crj.12002.

[177] J.S. Gregory, J.H. Waarsing, J. Day, H.A. Pols, M. Reijman, H. Weinans, R.M. Aspden, Early identification of radiographic osteoarthritis of the hip using an active shape model to quantify changes in bone morphometric features: can hip shape tell us anything about the progression of osteoarthritis?, Arthritis Rheum. 56 (2007) 3634–43. doi:10.1002/art.22982.

[178] D.R. Carter, G.S. Beaupré, Skeletal Function and Form: Mechanobiology of Skeletal Development, Aging, and Regeneration, 1st ed., Cambridge University Press, 2007. http://books.google.com/books?id=iW3sERfsGQoC.

[179] E.F. Eriksen, Cellular mechanisms of bone remodeling., Rev. Endocr. Metab. Disord. 11 (2010) 219–27. doi:10.1007/s11154-010-9153-1.

[180] L.H. Hoeppner, F.J. Secreto, J.J. Westendorf, Wnt signaling as a therapeutic target for bone diseases, Expert Opin. Ther. Targets. (2009). http://www.tandfonline.com.ezproxy.library.wisc.edu/doi/abs/10.1517/14728220902841961 (accessed March 25, 2016).

[181] V. Krishnan, Regulation of bone mass by Wnt signaling, J. Clin. Invest. 116 (2006) 1202–1209. doi:10.1172/JCI28551.

[182] S.J. Warden, Extreme skeletal adaptation to mechanical loading., 2010. http://www.springerlink.com/index/10.1007/s12018-008-9010-x.

[183] D. Smith, EL, Martens, F, Koller, K, Clark, W, Jones, E.L. Smith, F. Martens, K. Koller, W. Clark, D.B. Jones, The effects of 20 days of mechanical loading plus PTH on the E-modulus of cow trabecular bone, in: Am. Soc. Bone Miner. Res. 22nd Annu. Meet., AMER SOC BONE & MINERAL RES 2025 M ST, NW, STE 800, WASHINGTON, DC 20036-3309 USA, Toronto, Canada, 2000: p. s247.

[184] A.E. Simpson, M.J. Stoddart, C.M. Davies, K. Jähn, P.I. Furlong, J.A. Gasser, D.B. Jones, B.S. Noble, R.G. Richards, TGFβ3 and loading increases osteocyte survival in human cancellous bone cultured ex vivo, Cell Biochem. Funct. 27 (2009) 23–29. doi:10.1002/cbf.1529.

[185] E.G.F. Mercuri, A.L. Daniel, R.D. Machado, M.B. Hecke, Application of a Multi-Scale Mechanobiological Model for Bone Remodeling, J. Med. Imaging Heal. Informatics. 4 (2014) 142–146. doi:10.1166/jmihi.2014.1229.

[186] S. Scheiner, P. Pivonka, C. Hellmich, Poromicromechanics reveals that physiological bone strains induce osteocyte-stimulating lacunar pressure., Biomech. Model. Mechanobiol. 15 (2016) 9–28. doi:10.1007/s10237-015-0704-y.

[187] C. Lerebours, P.R. Buenzli, S. Scheiner, P. Pivonka, A multiscale mechanobiological model of bone remodelling predicts site-specific bone loss in the femur during osteoporosis and mechanical disuse., Biomech. Model. Mechanobiol. 15 (2016) 43–67. doi:10.1007/s10237-015-0705-x.

[188] T. Abdalrahman, S. Scheiner, C. Hellmich, Is trabecular bone permeability governed by molecular ordering-induced fluid viscosity gain? Arguments from re-evaluation of experimental data in the framework of homogenization theory., J. Theor. Biol. 365 (2015) 433–44. doi:10.1016/j.jtbi.2014.10.011.

Appendix A

A.   List of Terms and Abbreviations

A	cross-sectional area, mm^2
BFR/BS	bone formation rate, μm^3/ μm^2/year
big ET1	Big endothelin
BS	bone surface, μm
BV/TV	bone volume, %
δ	axial deformation, mm
ΔE_{app}	percent change in apparent elastic modulus
E_{app}	apparent elastic modulus
Ece1	endothelin converting enzyme 1
ET1	Endothelin-1
ET_A	endothelin receptor type A
ET_B	endothelin receptor type B
F	axial force, N
K_{axial}	axial stiffness, N/mm
L	length, mm
LRP5	lipoprotein receptor-related protein 5
MAR	mineral apposition rate, μm/day
MS/BS	mineralizing surface, %
PGE2	prostaglandin E2
PTH	parathyroid hormone
SOST	sclerostin

ZETOS	ZETOS Bone Loading and Bioreactor System
IGF1	Insulin-like growth factor 1
DKK1	Dickkopf protein 1
GLM	general linear model
THA	total hip arthroplasty
BV	bone volume, mm^3
BV/TV	bone volume/total volume, mm^3/mm^3
BSA	bone surface area, mm^2
BSA/TV	bone surface area/total volume, mm^2/mm^3
T.Th	trabecular thickness, µm
T.Sp	trabecular spacing, µm
Anisotropy	degree of anisotropy
SMI	structural model index
FabricTensor	fabric tensor direction, θ
PCA	principal component analysis
AIC	Akaike information criterion
ν	Poisson's ratio
TCP	tricalcium phosphate
CAD	computer aided design
E_{nano}	elastic modulus of a material at the nano-level
E_{micro}	elastic modulus of a material at the micro-level
$E_{app,exp}$	apparent elastic modulus of macro-level structure determine experimentally
$E_{app,FE}$	apparent elastic modulus of macro-level structure determine using FE
$E_{app,nano}$	calculated apparent elastic modulus of macro-level structure using E_{nano}
$E_{app,micro}$	calculated apparent elastic modulus of macro-level structure using E_{micro}

SED	strain energy density
TGF-β	transforming growth factor beta
OPG	osteoprotegerin
RANK	receptor activator of nuclear factor kappa-B
RANKL	receptor activator of nuclear factor kapp-B ligand
$C_{OB,P0}$	osteoblast precursor concentration, pM
$C_{OB,A0}$	active osteoblast concentration, pM
$C_{OC,P0}$	osteoclast precursor concentration, pM
$C_{OC,A0}$	active osteoclast concentration, pM
A_{OBa}	osteoblast apoptosis rate, d^{-1}
D_{OBp}	osteoblast differentiation rate, d^{-1}
A_{OCa}	osteoclast apoptosis rate, d^{-1}
D_{OCp}	osteoclast differentiation rate, d^{-1}
$P_{PTH,d}$	PTH dosage, pM
$K_{PTH,Act,Ob}$	PTH activator equilibrium constant, pM
$K_{PTH,Rep,Ob}$	PTH repressor equilibrium constant, pM
$P_{TGF,d}$	TGF-β dosage, pM
$K_{TGF,Act,Ob}$	TGF- β activator equilibrium constant, pM
$K_{TGF,Rep,Ob}$	TGF- β repressor equilibrium constant, pM

Appendix B

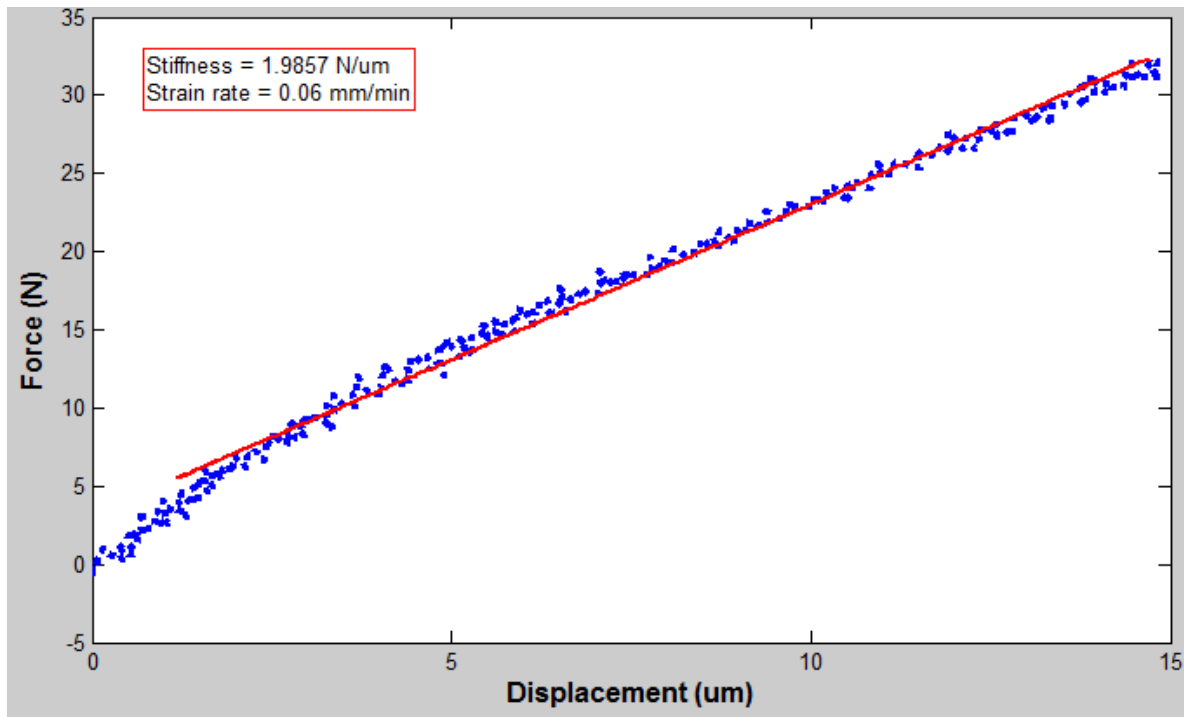## B. Force versus Displacement plots for Bovine Specimens, Chapter 4

Figure B.1 - Force vs. displacement plot of bovine sample 1 on day 23 of live bone study. Linear fit shown to determine bulk stiffness.
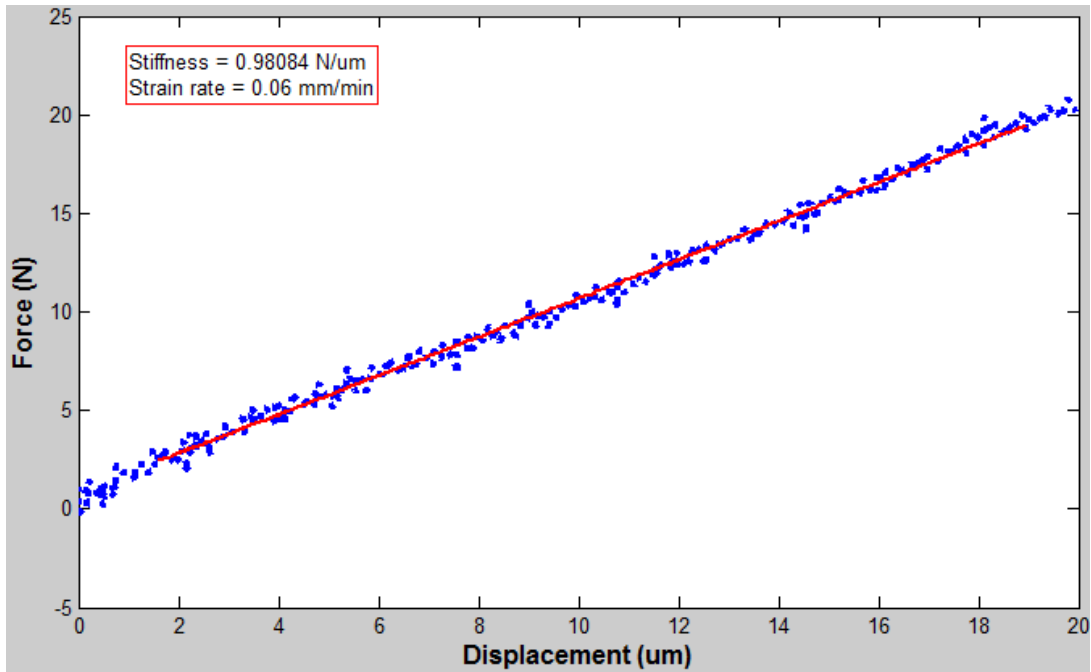
Figure B.2 - Force vs. displacement plot of bovine sample 2 on day 23 of live bone study. Linear fit shown to determine bulk stiffness.

Figure B.3 - Force vs. displacement plot of bovine sample 3 on day 23 of live bone study. Linear fit shown to determine bulk stiffness.

Figure B.4 - Force vs. displacement plot of bovine sample 4 on day 23 of live bone study. Linear fit shown to determine bulk stiffness.
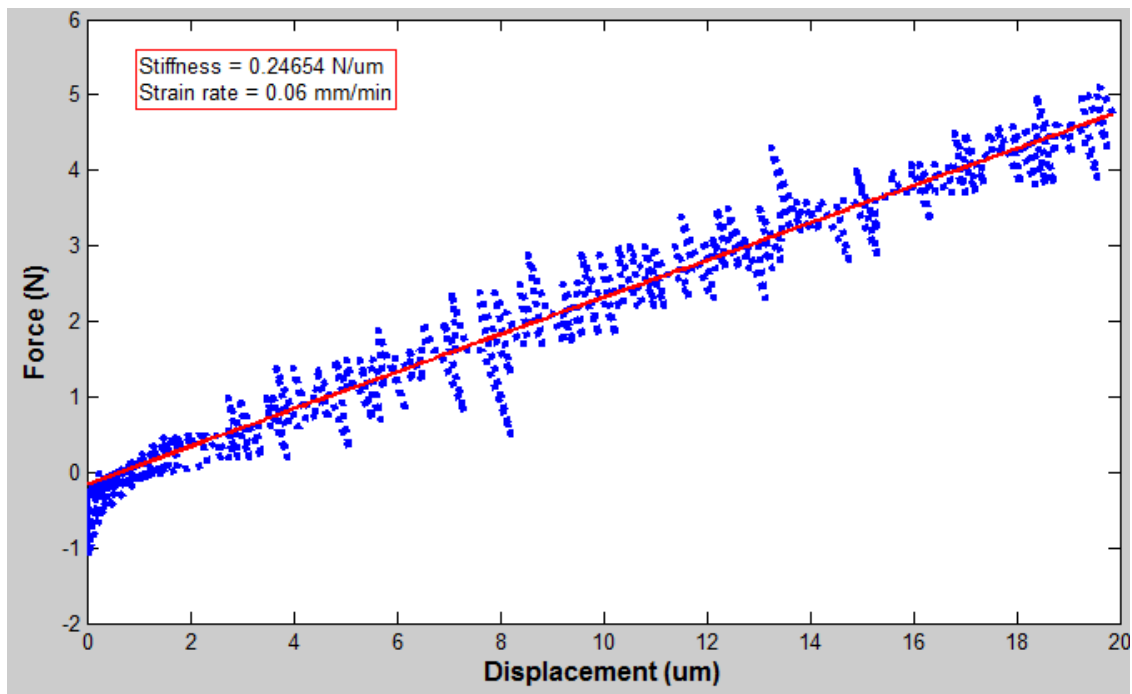

Figure B.5 - Force vs. displacement plot of bovine sample 5 on day 23 of live bone study. Linear fit shown to determine bulk stiffness.

Figure B.6 - Force vs. displacement plot of bovine sample 6 on day 23 of live bone study. Linear fit shown to determine bulk stiffness.

Figure B.7 - Force vs. displacement plot of bovine sample 7 on day 23 of live bone study. Linear fit shown to determine bulk stiffness.
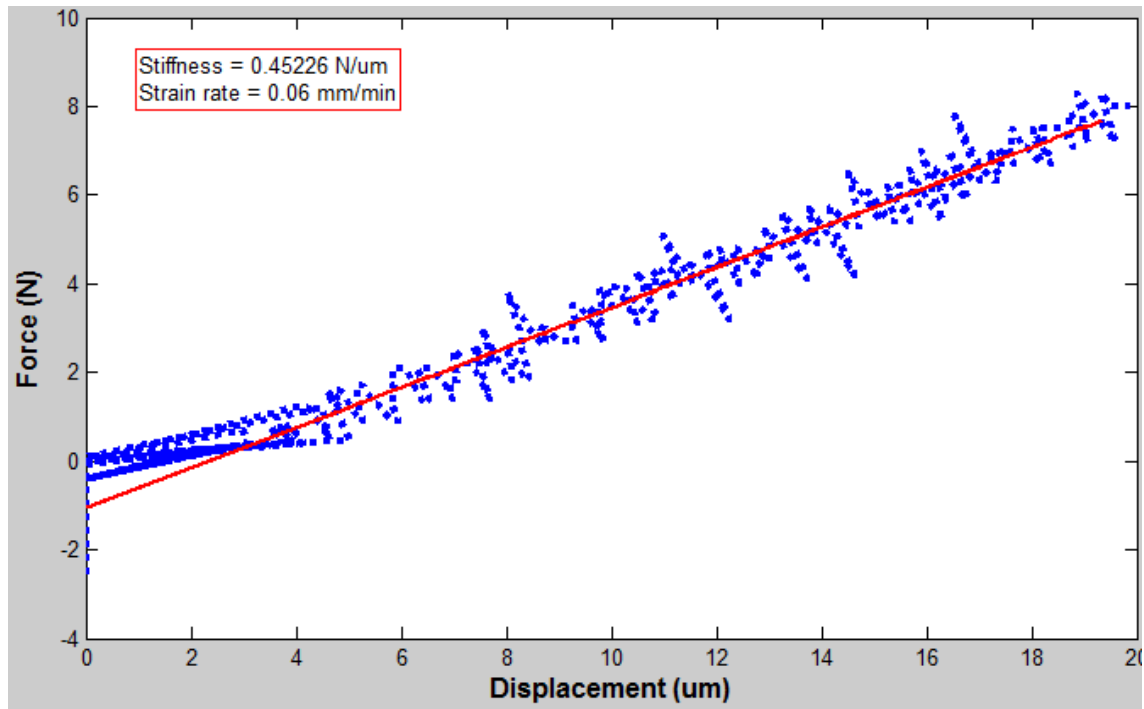
Figure B.8 - Force vs. displacement plot of bovine sample 8 on day 23 of live bone study. Linear fit shown to determine bulk stiffness.
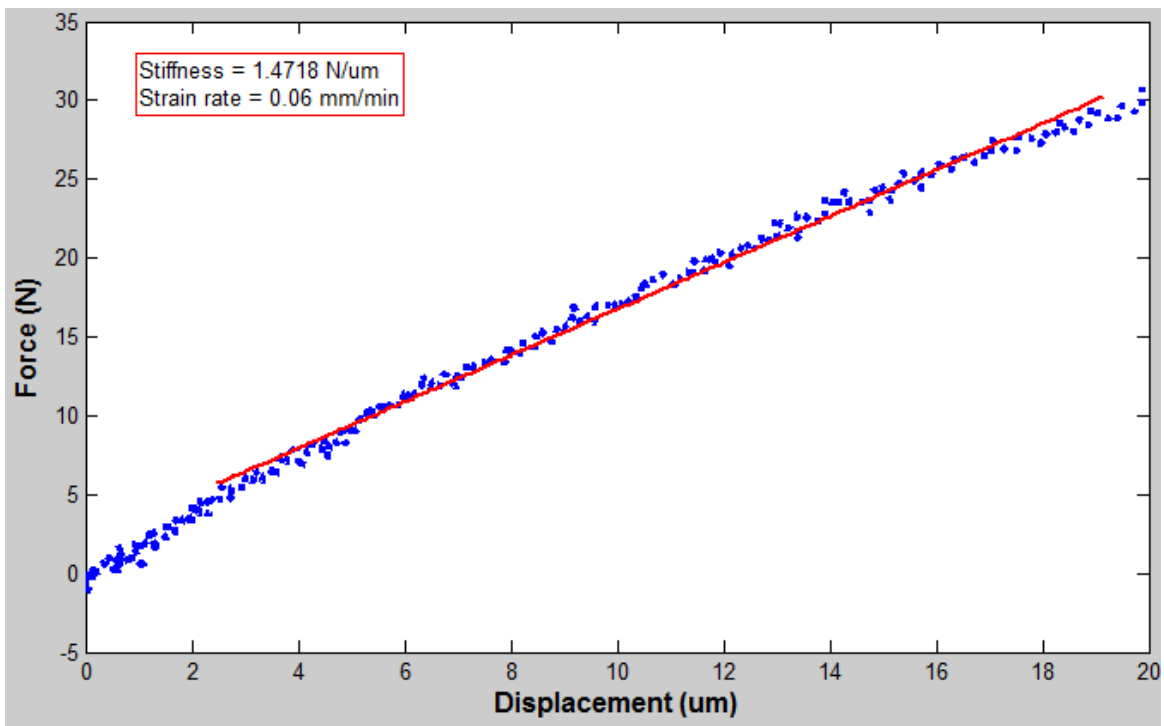

Figure B.9 - Force vs. displacement plot of bovine sample 9 on day 23 of live bone study. Linear fit shown to determine bulk stiffness.
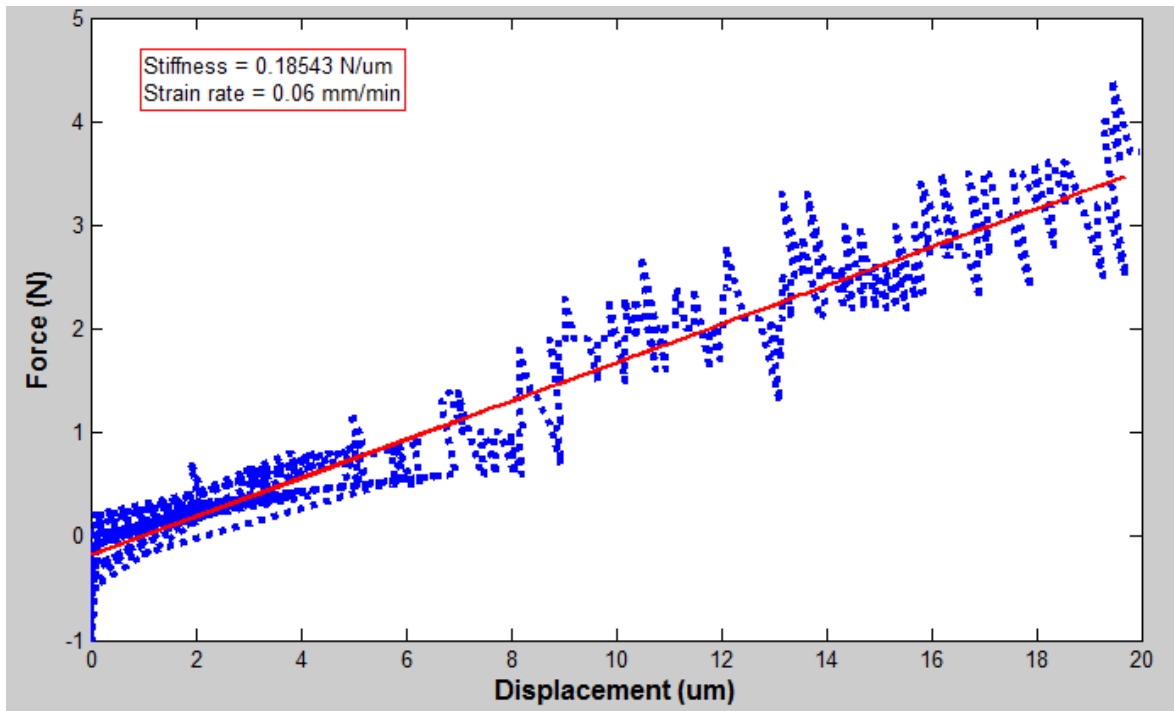
Figure B.10 - Force vs. displacement plot of bovine sample 10 on day 23 of live bone study. Linear fit shown to determine bulk stiffness.

Figure B.11 - Force vs. displacement plot of bovine sample 11 on day 23 of live bone study. Linear fit shown to determine bulk stiffness.
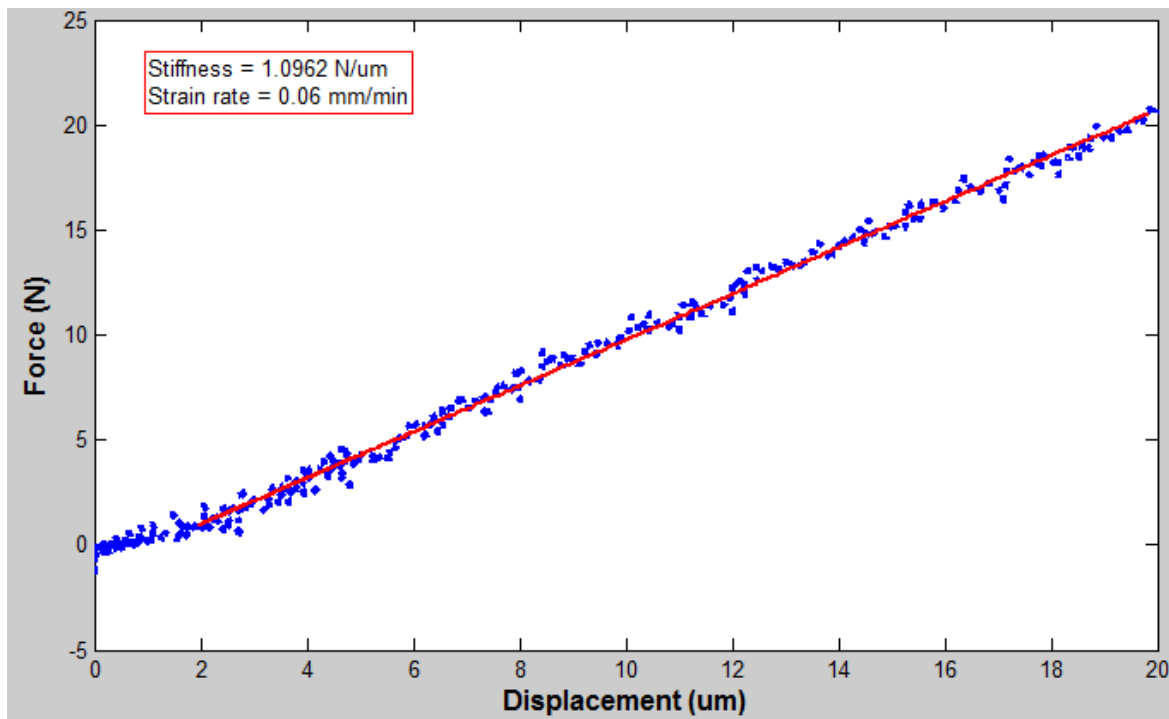
Figure B.12 - Force vs. displacement plot of bovine sample 12 on day 23 of live bone study. Linear fit shown to determine bulk stiffness.

Figure B.13 - Force vs. displacement plot of bovine sample 13 on day 23 of live bone study. Linear fit shown to determine bulk stiffness.
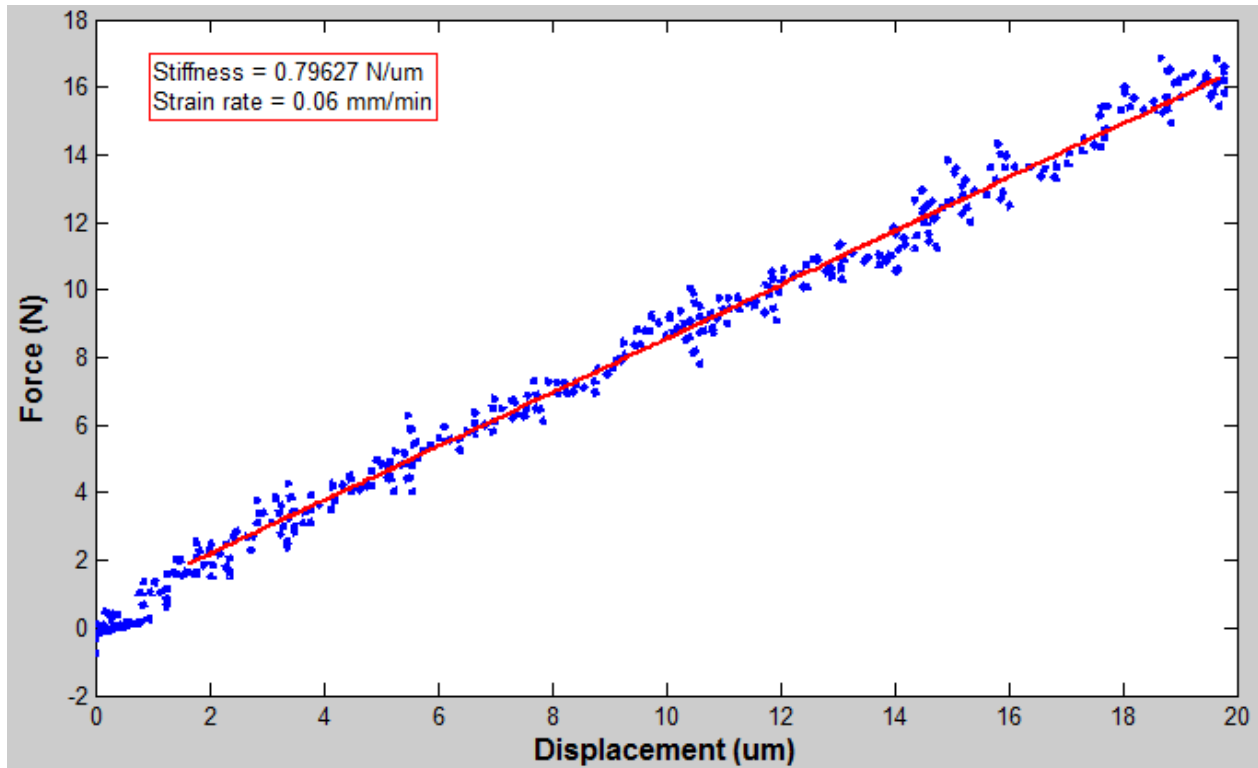
Figure B.14 - Force vs. displacement plot of bovine sample 14 on day 23 of live bone study. Linear fit shown to determine bulk stiffness.

Figure B.15 - Force vs. displacement plot of bovine sample 15 on day 23 of live bone study. Linear fit shown to determine bulk stiffness.

Figure B.16 - Force vs. displacement plot of bovine sample 16 on day 23 of live bone study. Linear fit shown to determine bulk stiffness.
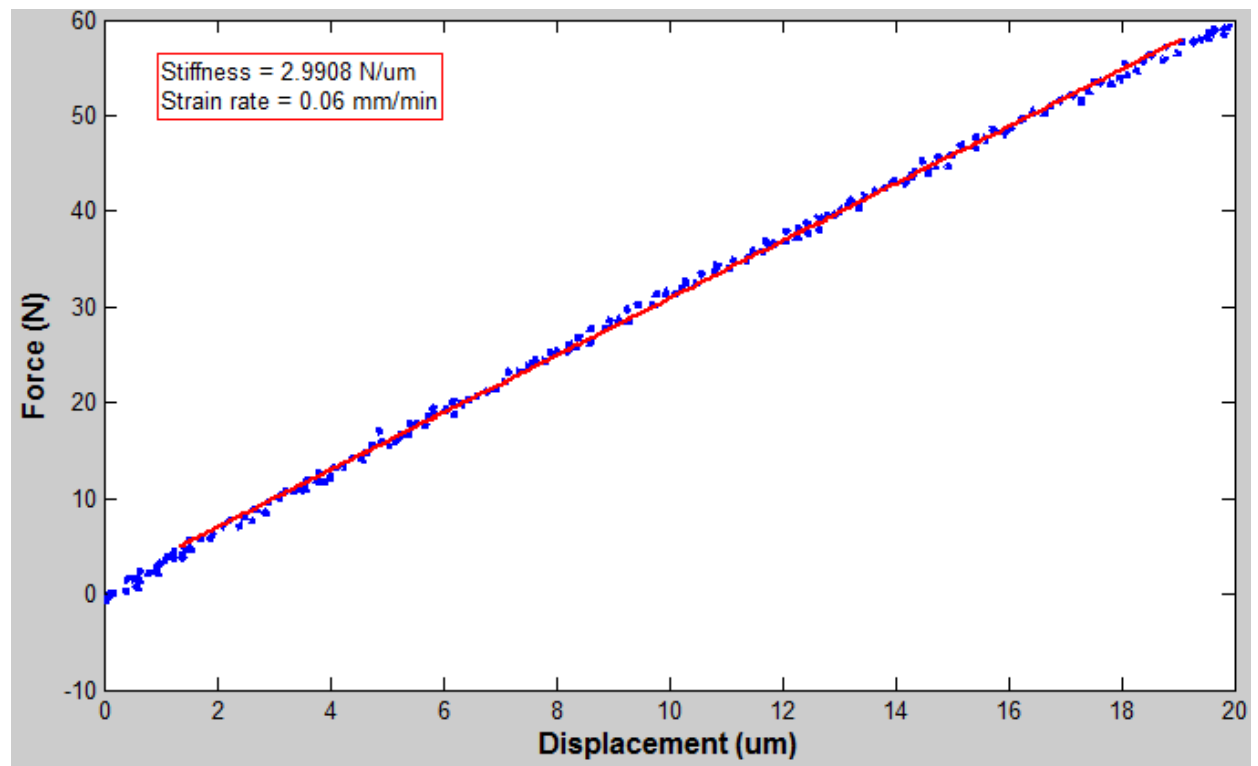

Figure B.17 - Force vs. displacement plot of bovine sample 17 on day 23 of live bone study. Linear fit shown to determine bulk stiffness.

Figure B.18 - Force vs. displacement plot of bovine sample 18 on day 23 of live bone study. Linear fit shown to determine bulk stiffness.

Figure B.19 - Force vs. displacement plot of bovine sample 19 on day 23 of live bone study. Linear fit shown to determine bulk stiffness.
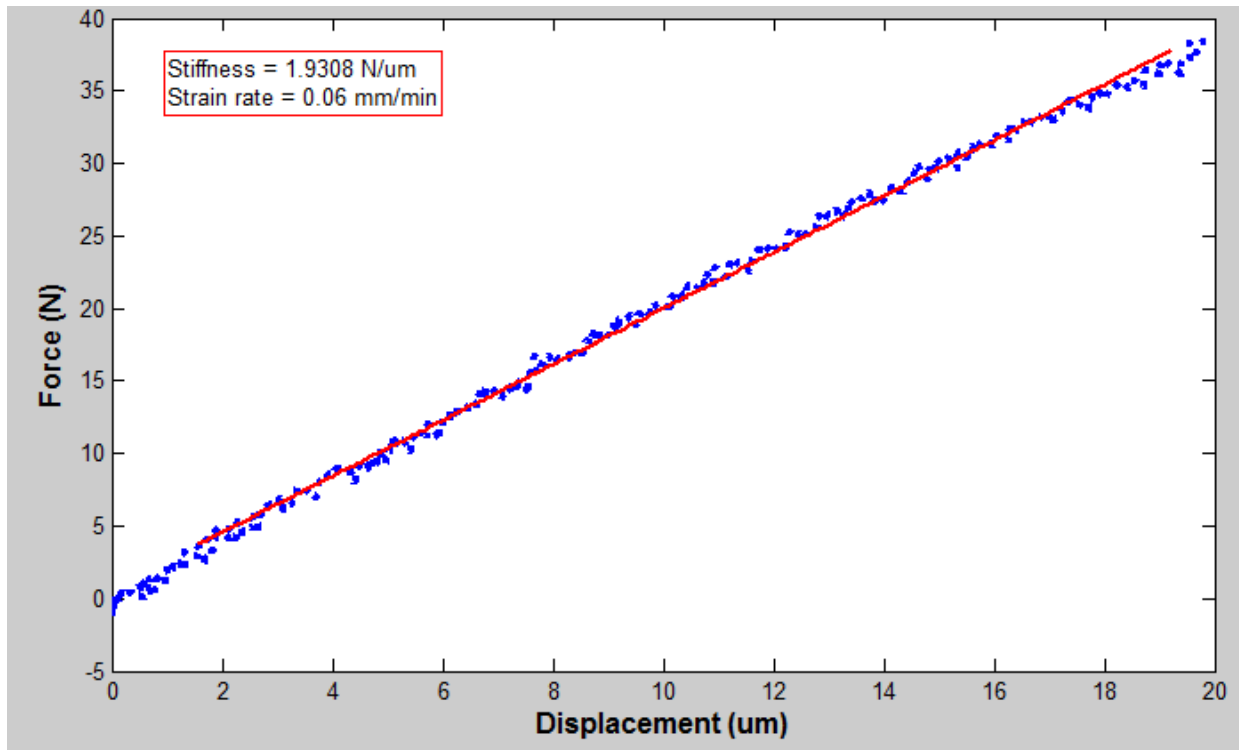
Figure B.20 - Force vs. displacement plot of bovine sample 20 on day 23 of live bone study. Linear fit shown to determine bulk stiffness.
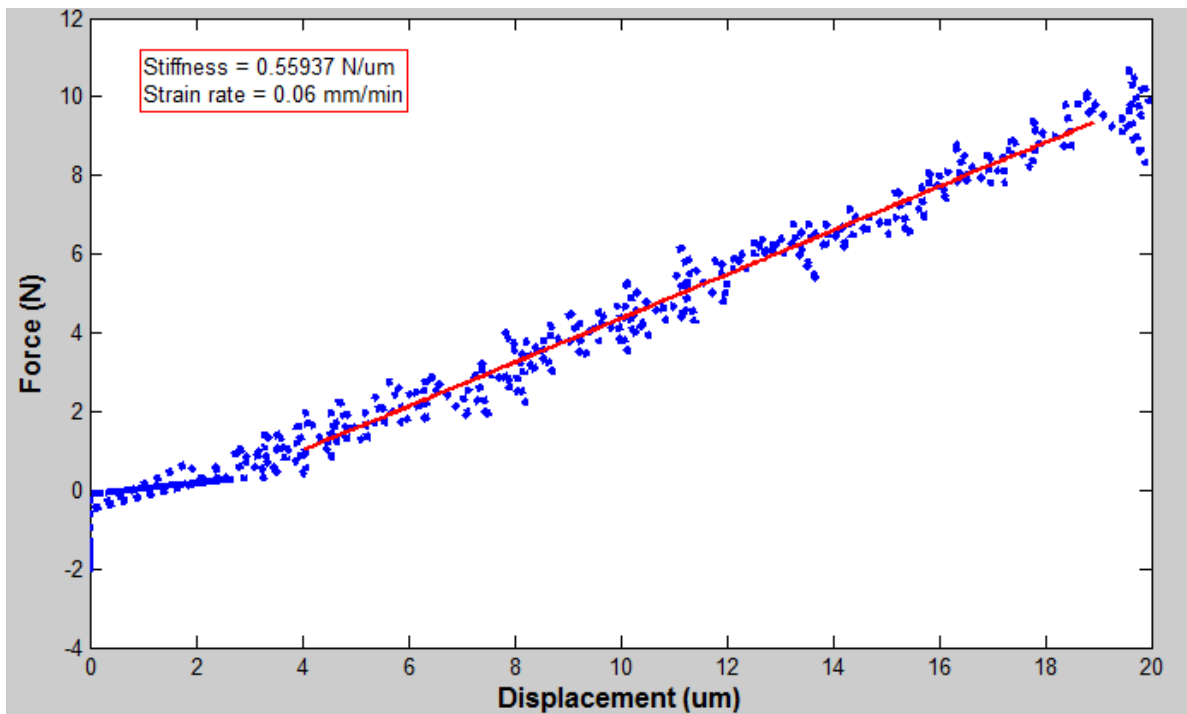

Figure B.21 - Force vs. displacement plot of bovine sample 21 on day 23 of live bone study. Linear fit shown to determine bulk stiffness.
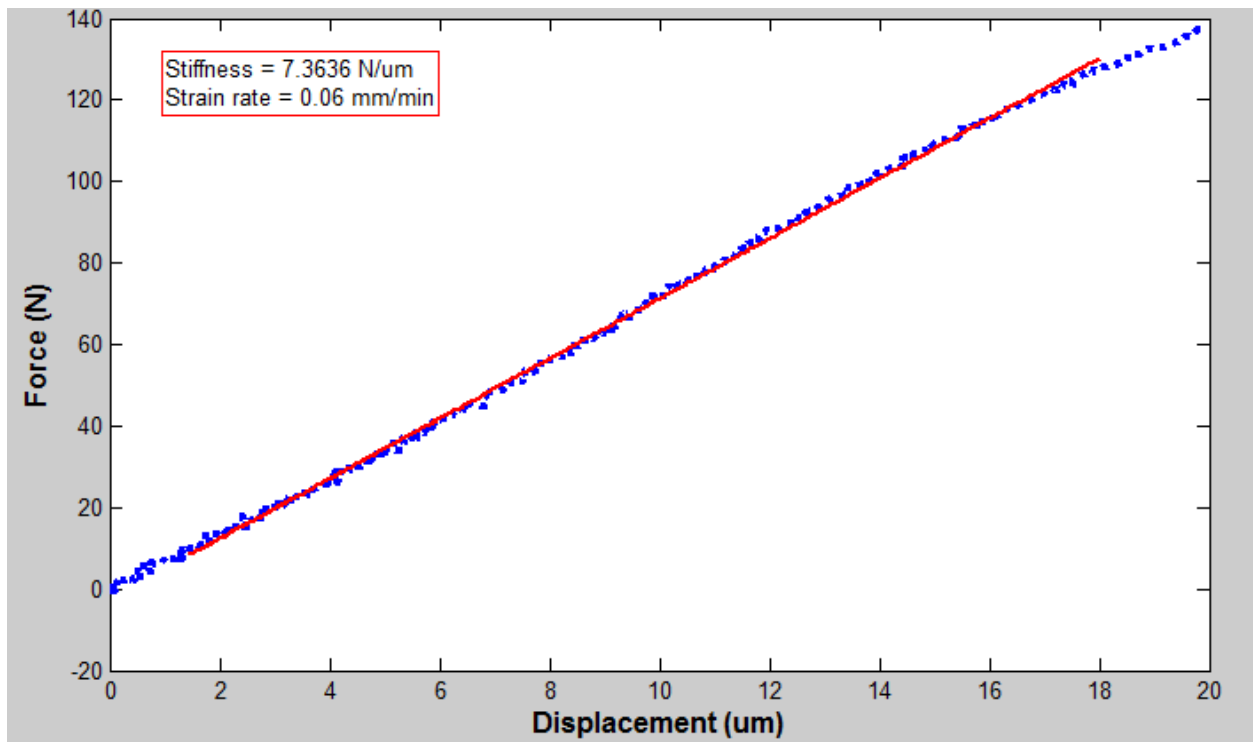
Figure B.22 - Force vs. displacement plot of bovine sample 22 on day 23 of live bone study. Linear fit shown to determine bulk stiffness.

Figure B.23 - Force vs. displacement plot of bovine sample 23 on day 23 of live bone study. Linear fit shown to determine bulk stiffness.

Figure B.24 - Force vs. displacement plot of bovine sample 24 on day 23 of live bone study. Linear fit shown to determine bulk stiffness.
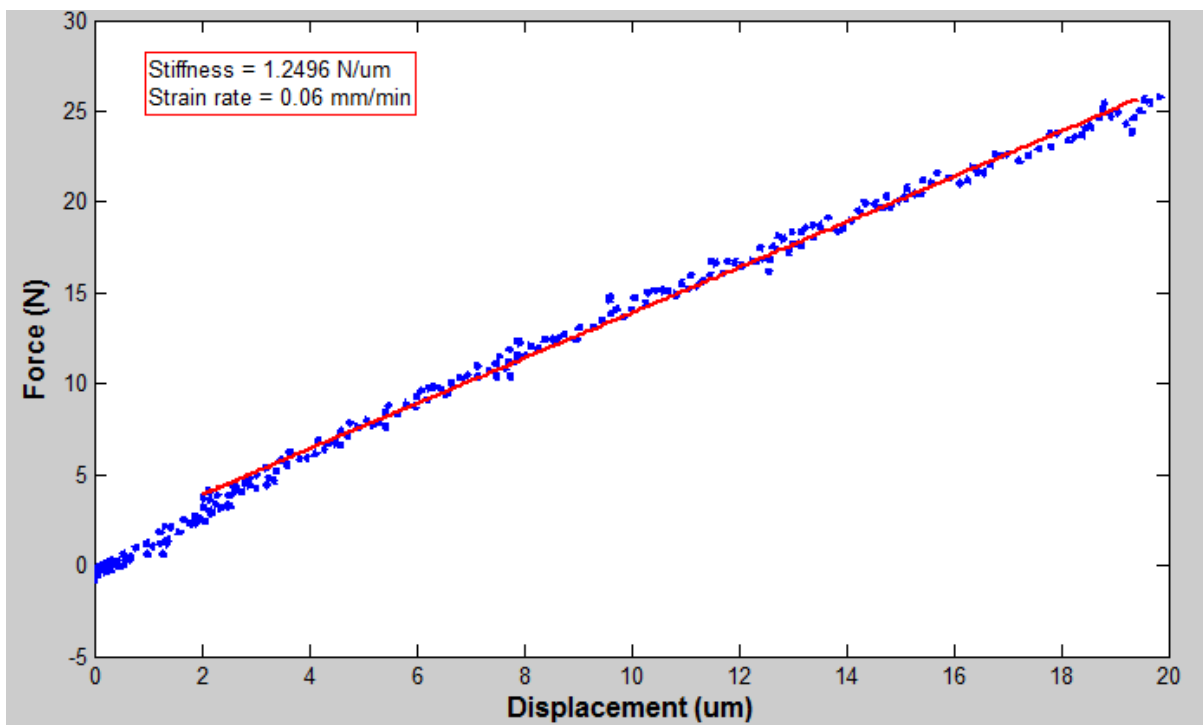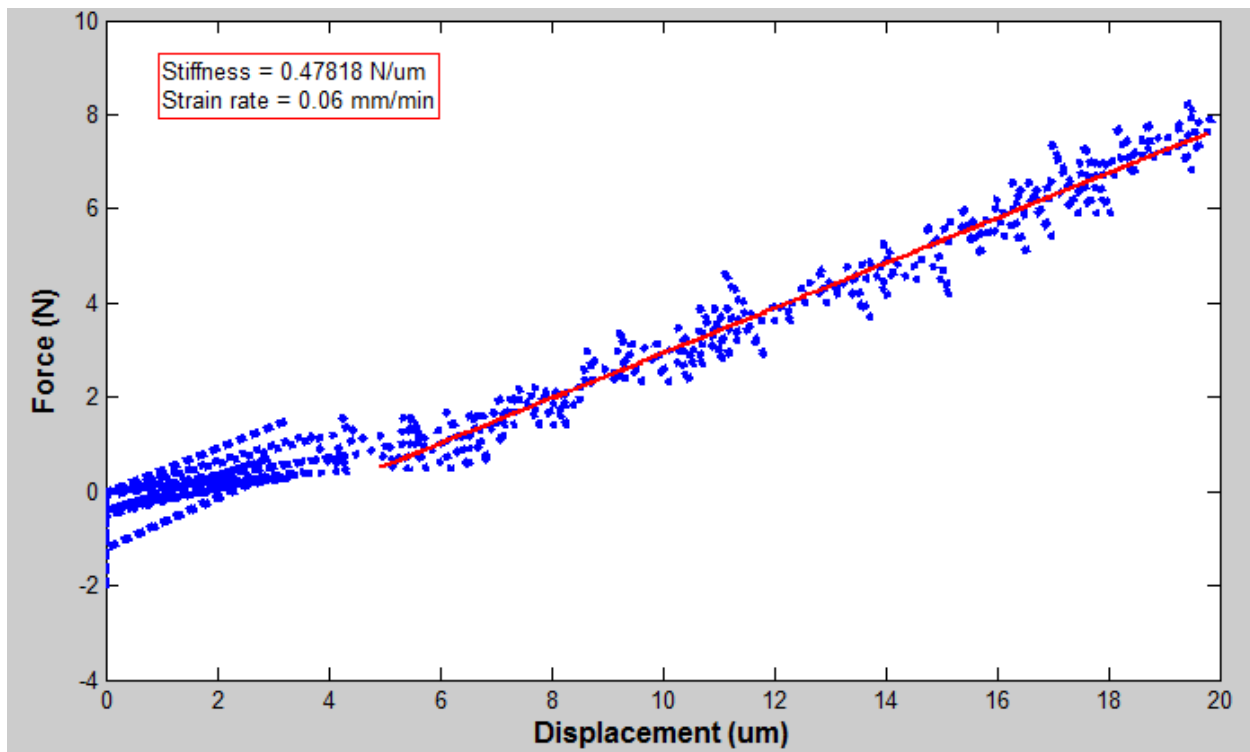

Figure B.25 - Force vs. displacement plot of bovine sample 25 on day 23 of live bone study. Linear fit shown to determine bulk stiffness.

Figure B.26 - Force vs. displacement plot of bovine sample 26 on day 23 of live bone study. Linear fit shown to determine bulk stiffness.
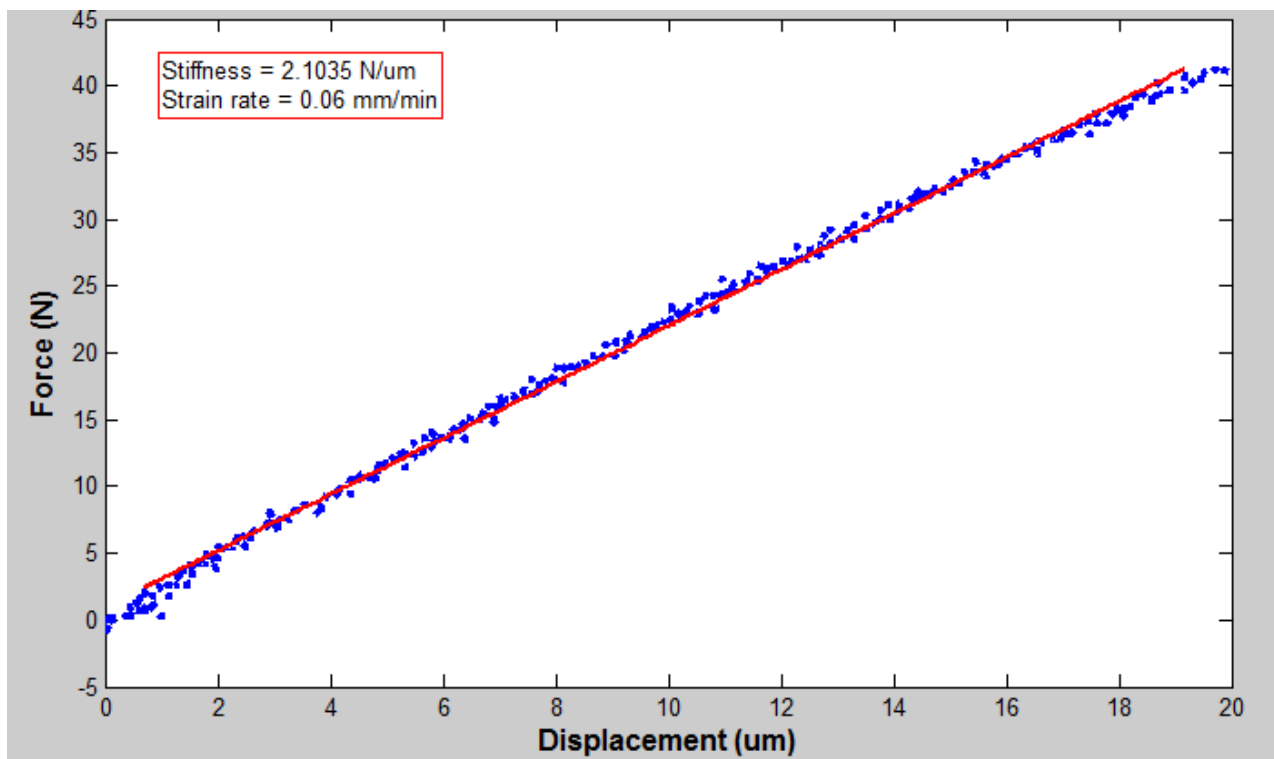

Figure B.27 - Force vs. displacement plot of bovine sample 27 on day 23 of live bone study. Linear fit shown to determine bulk stiffness.
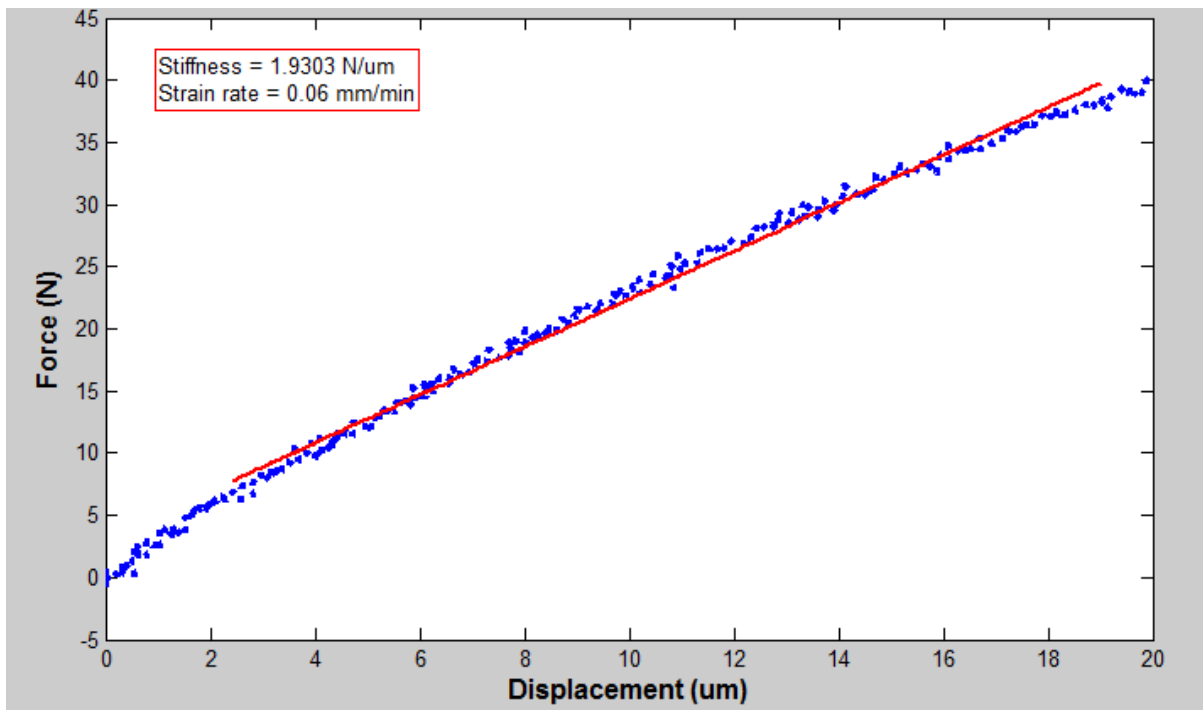
Figure B.28 - Force vs. displacement plot of bovine sample 28 on day 23 of live bone study. Linear fit shown to determine bulk stiffness.
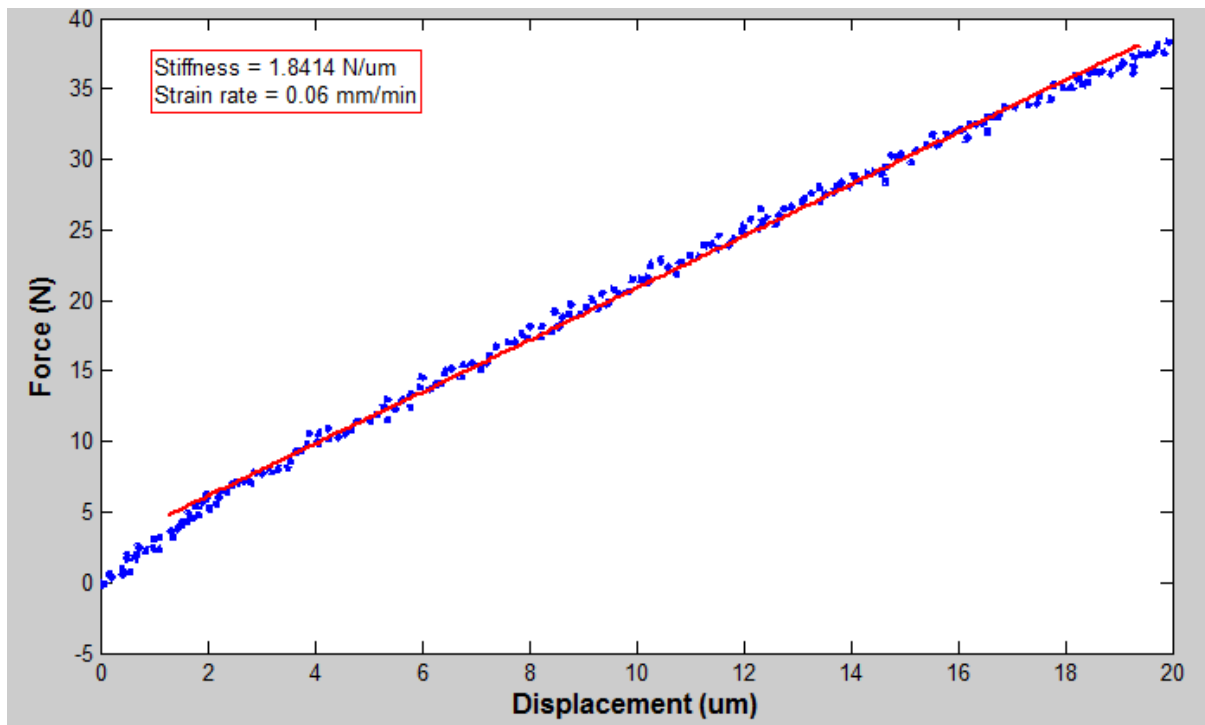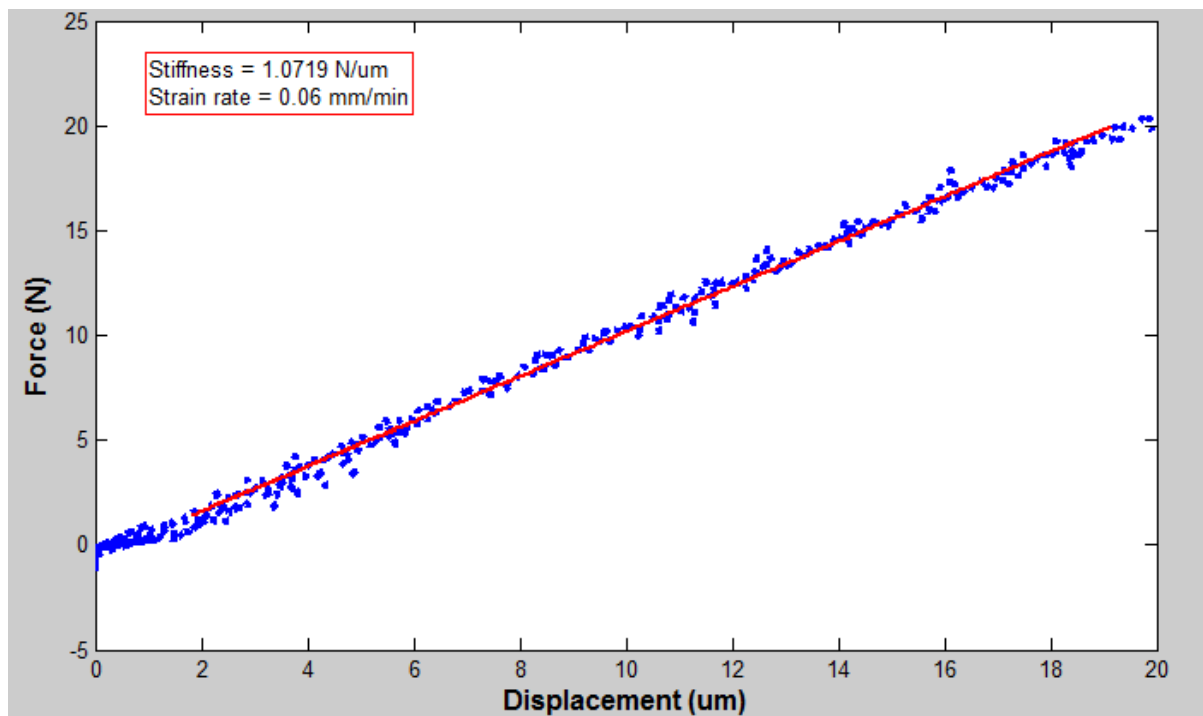

Figure B.29 - Force vs. displacement plot of bovine sample 29 on day 23 of live bone study. Linear fit shown to determine bulk stiffness.
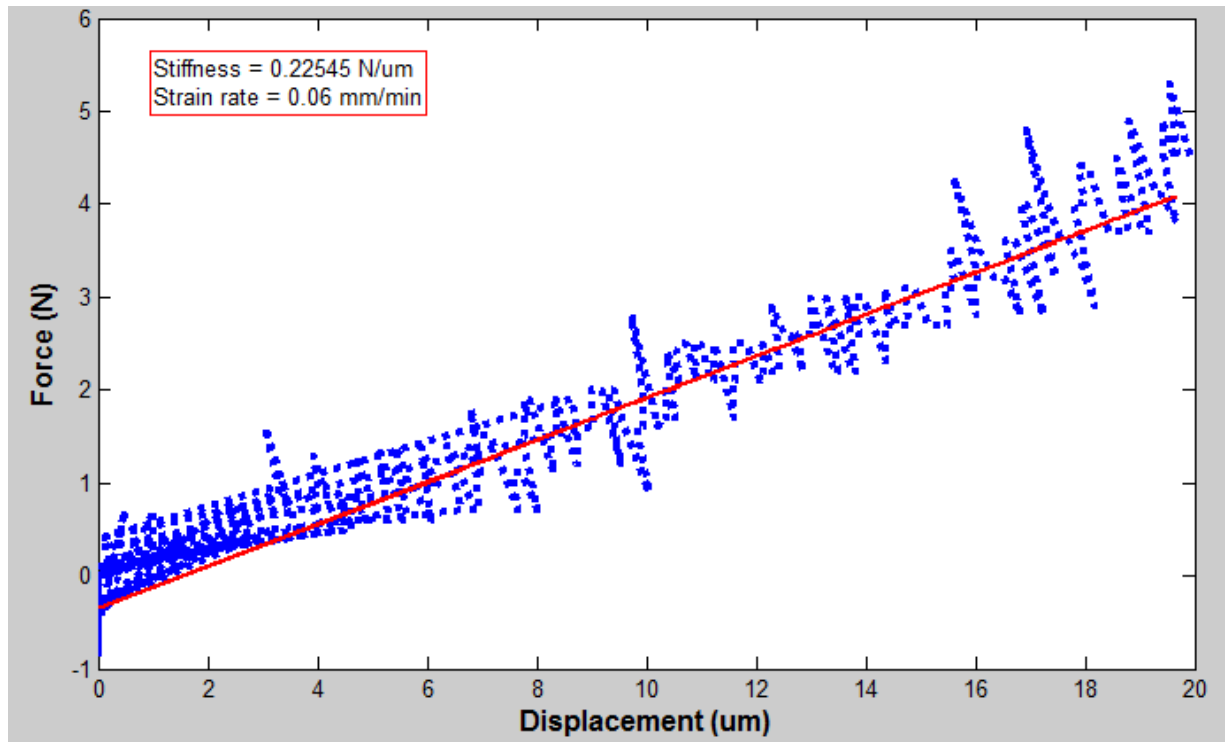
Figure B.30 - Force vs. displacement plot of bovine sample 30 on day 23 of live bone study. Linear fit shown to determine bulk stiffness.
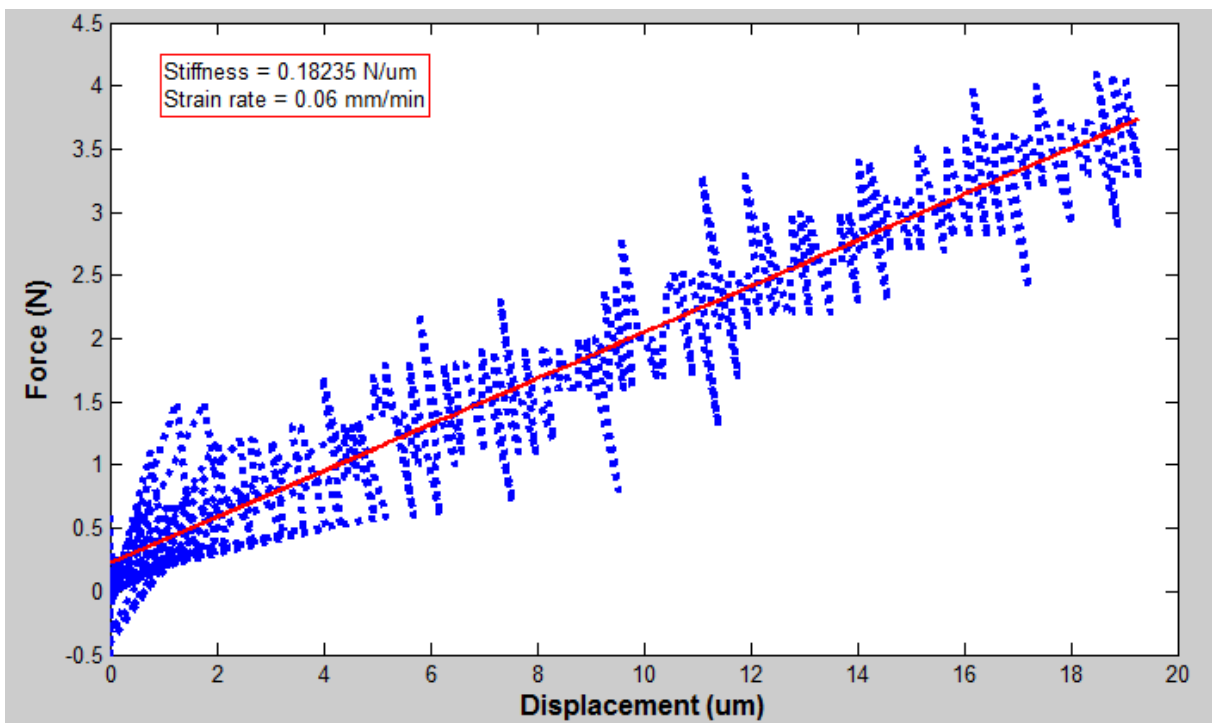
Figure B.31 - Force vs. displacement plot of bovine sample 31 on day 23 of live bone study. Linear fit shown to determine bulk stiffness.
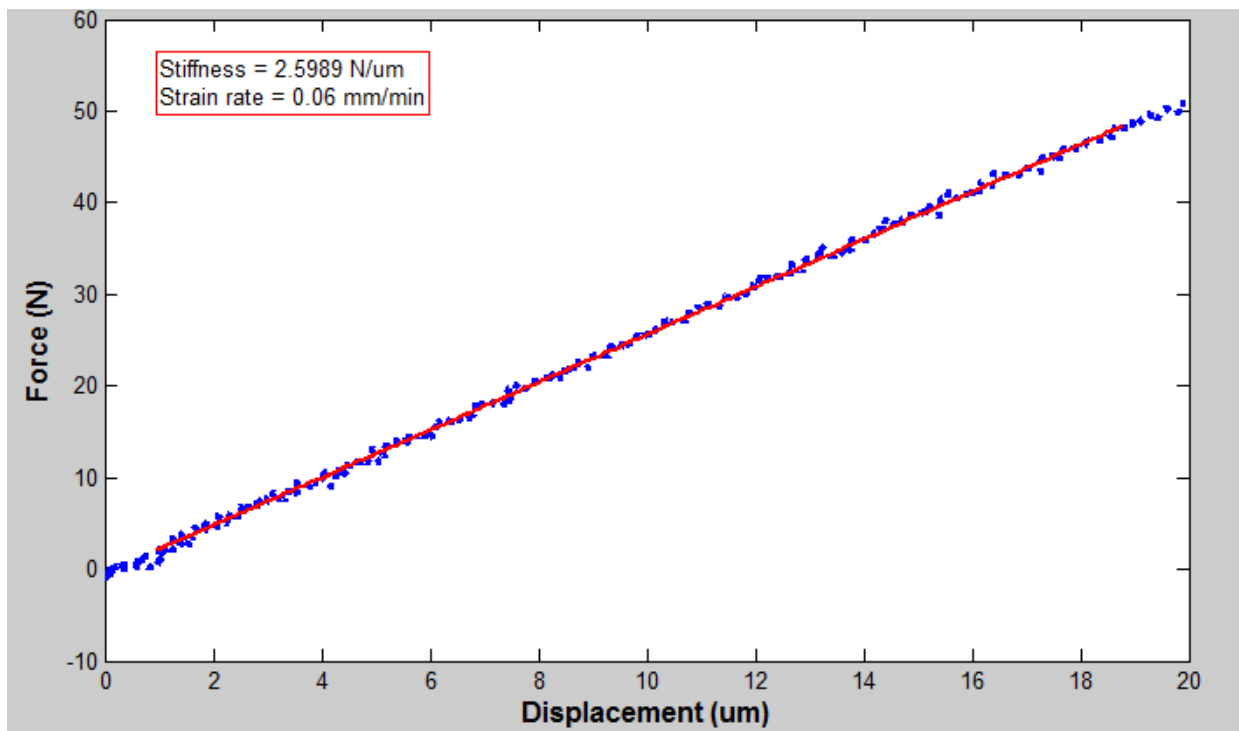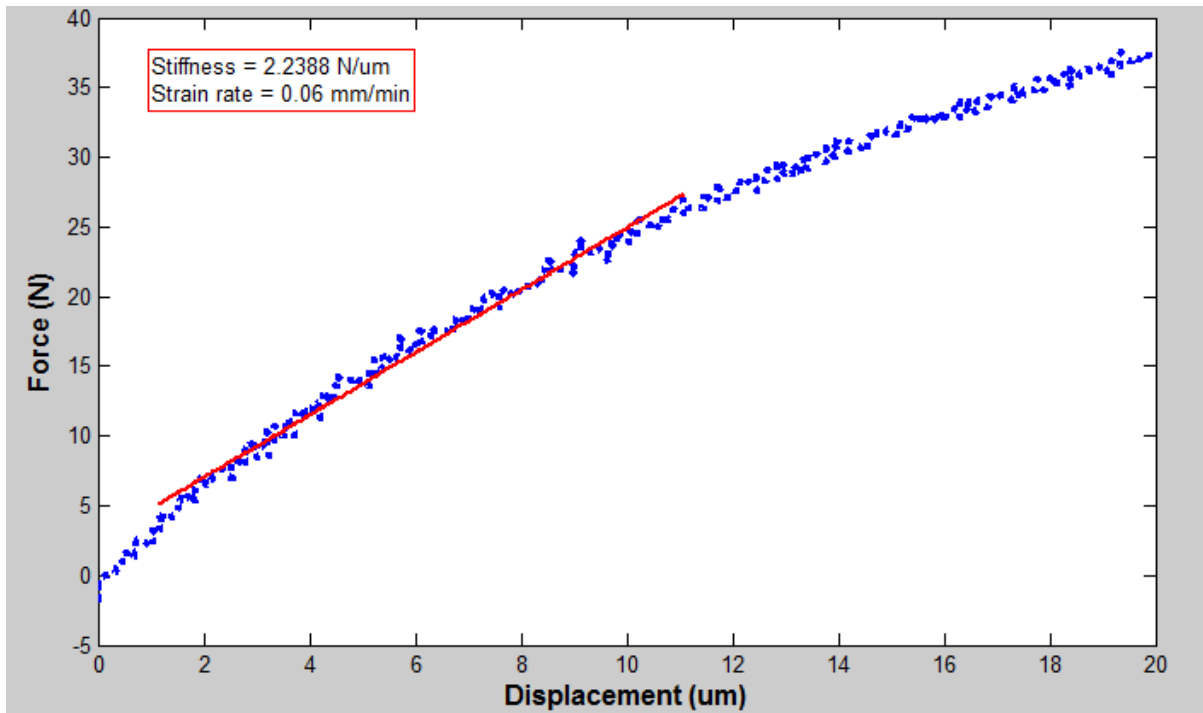
Figure B.32 - Force vs. displacement plot of bovine sample 32 on day 23 of live bone study. Linear fit shown to determine bulk stiffness.
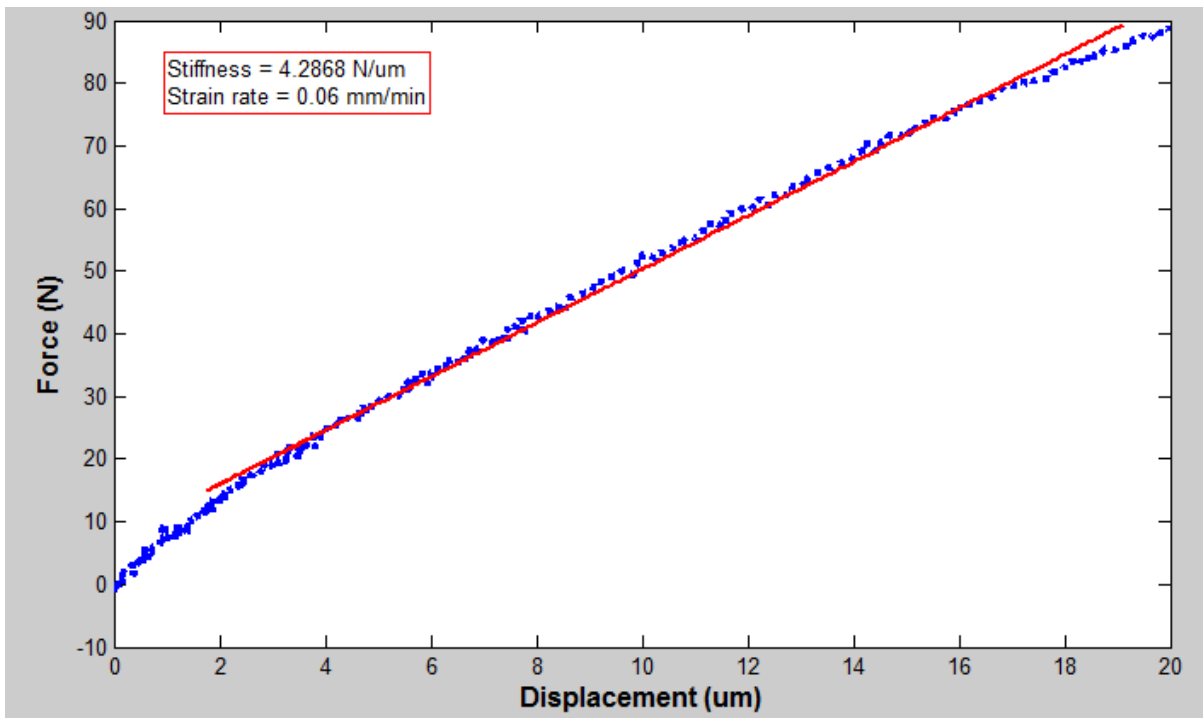
Figure B.33 - Force vs. displacement plot of bovine sample 33 on day 23 of live bone study. Linear fit shown to determine bulk stiffness.
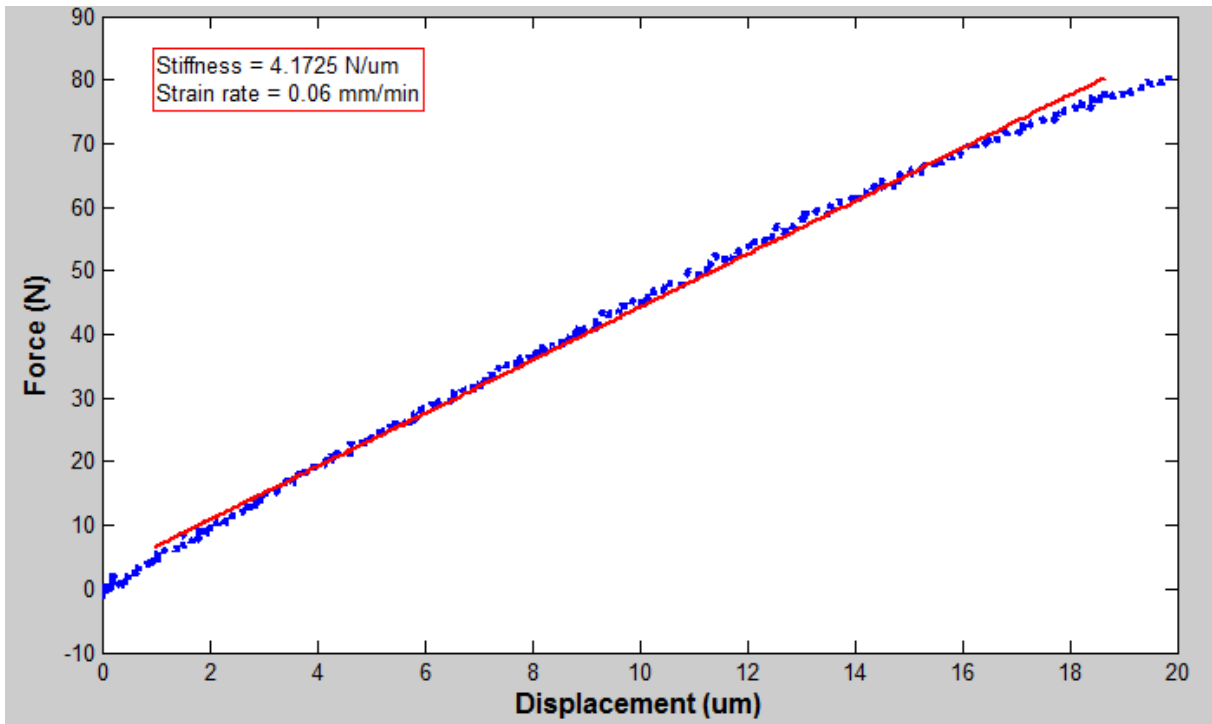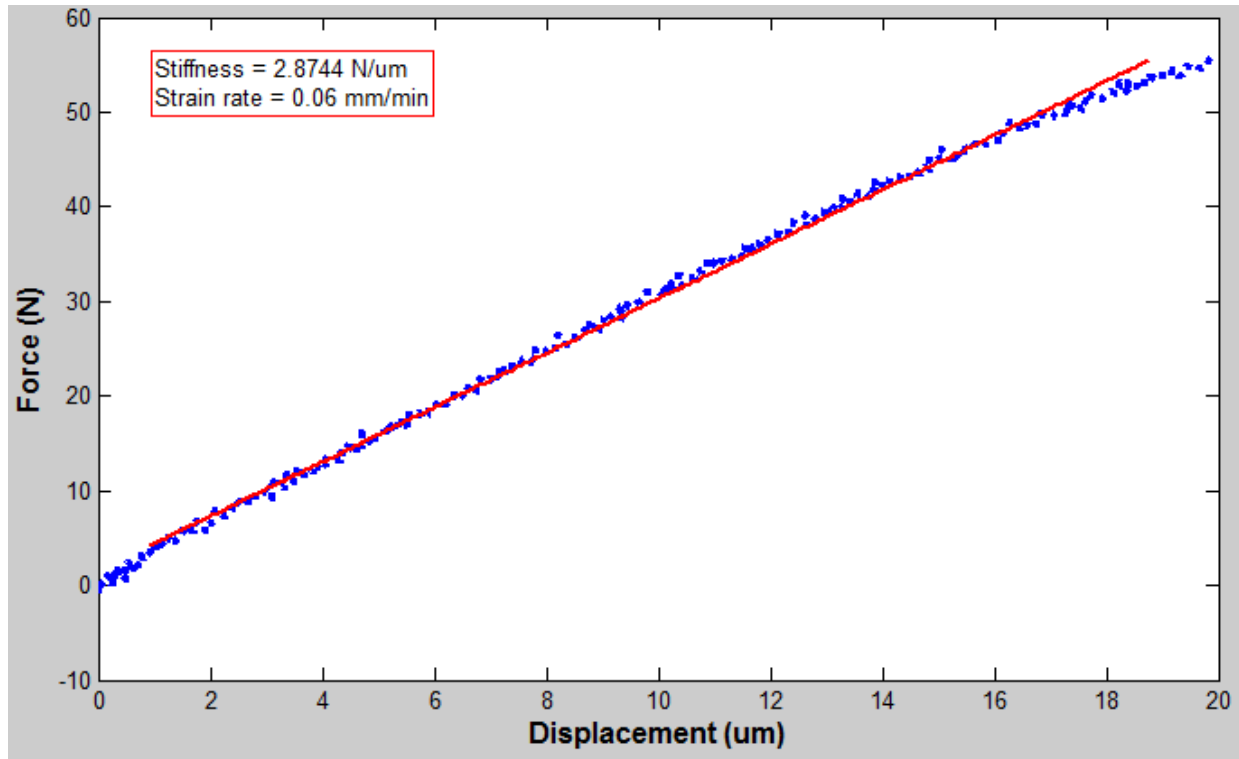
Figure B.34 - Force vs. displacement plot of bovine sample 34 on day 23 of live bone study. Linear fit shown to determine bulk stiffness.
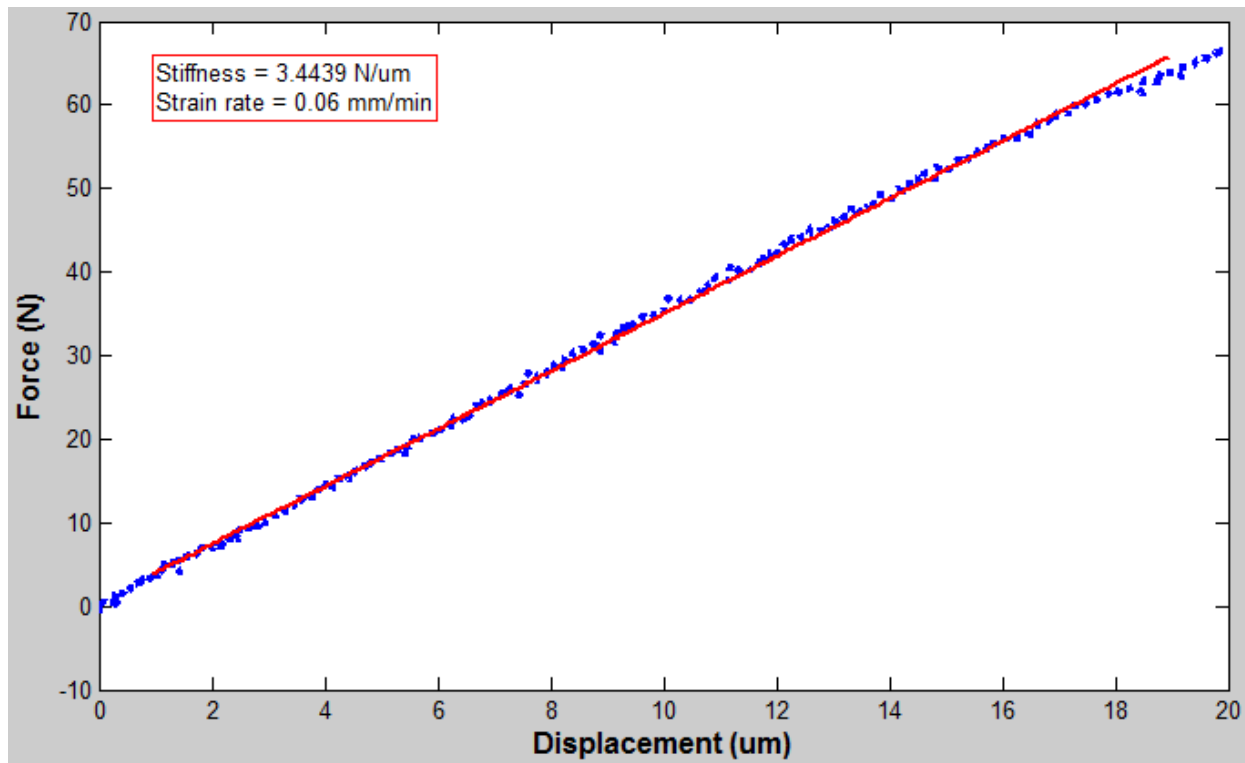
Figure B.35 - Force vs. displacement plot of bovine sample 35 on day 23 of live bone study. Linear fit shown to determine bulk stiffness.
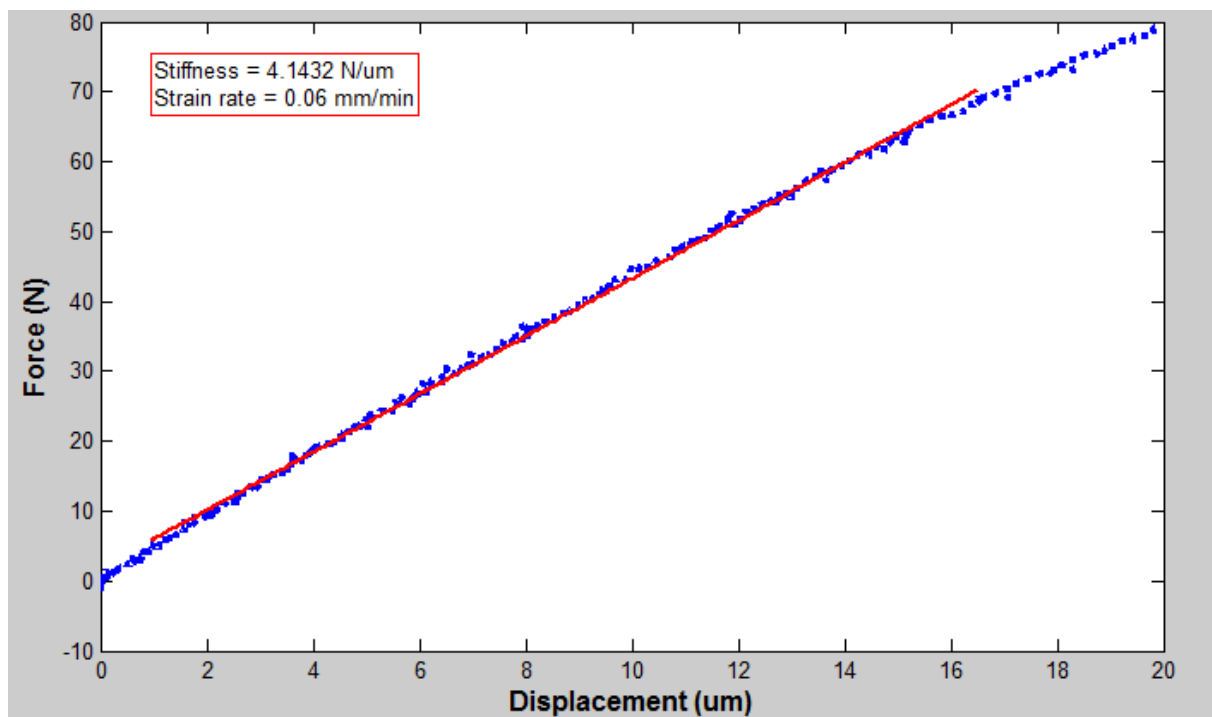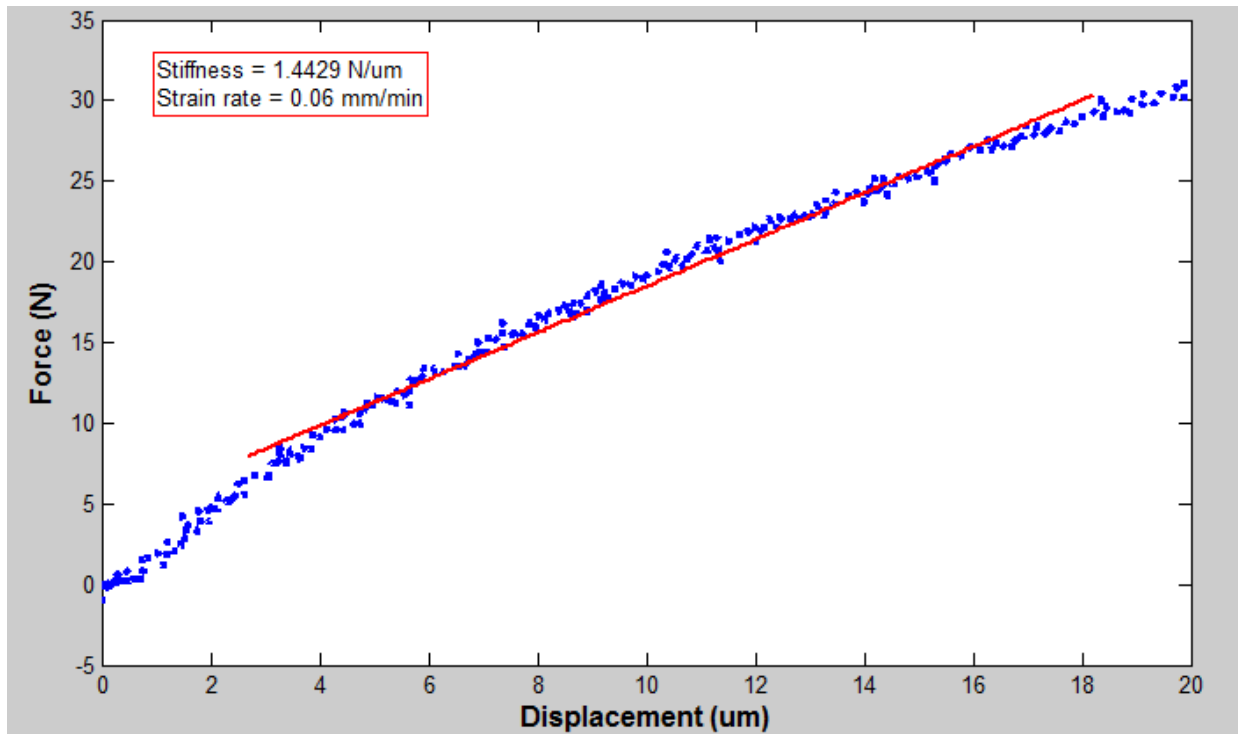
Figure B.36 - Force vs. displacement plot of bovine sample 36 on day 23 of live bone study. Linear fit shown to determine bulk stiffness.
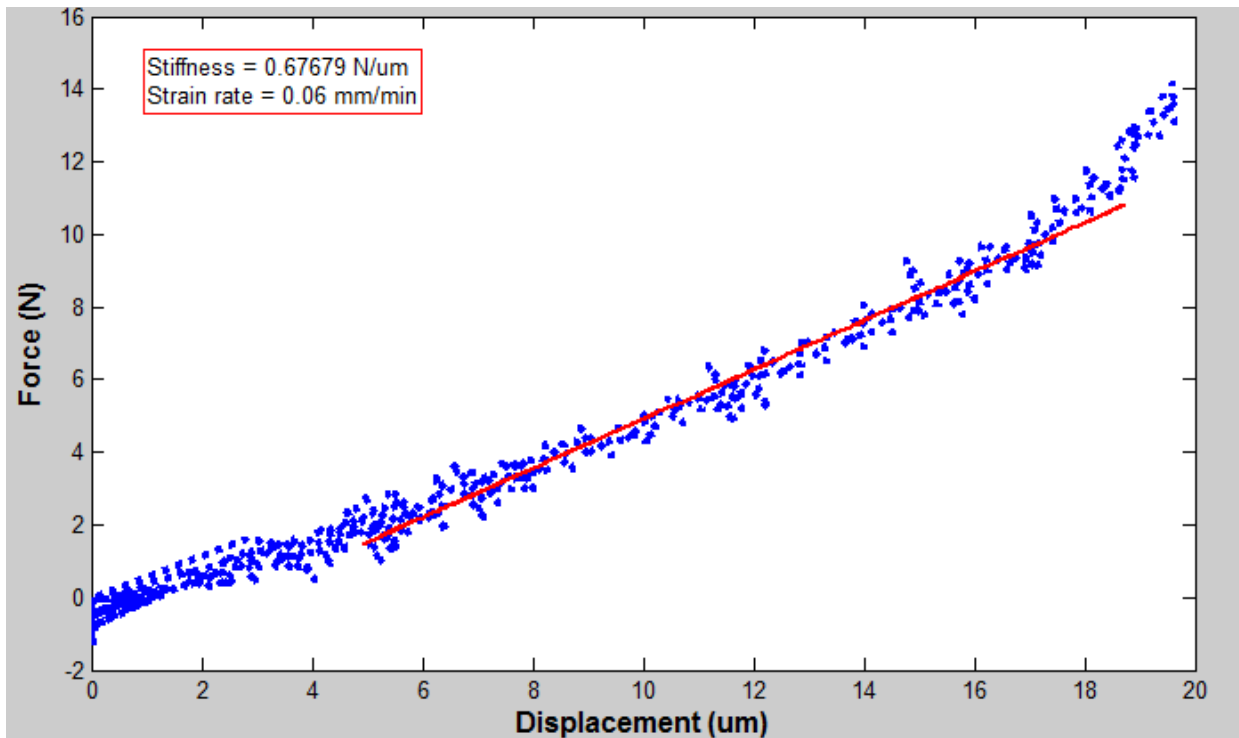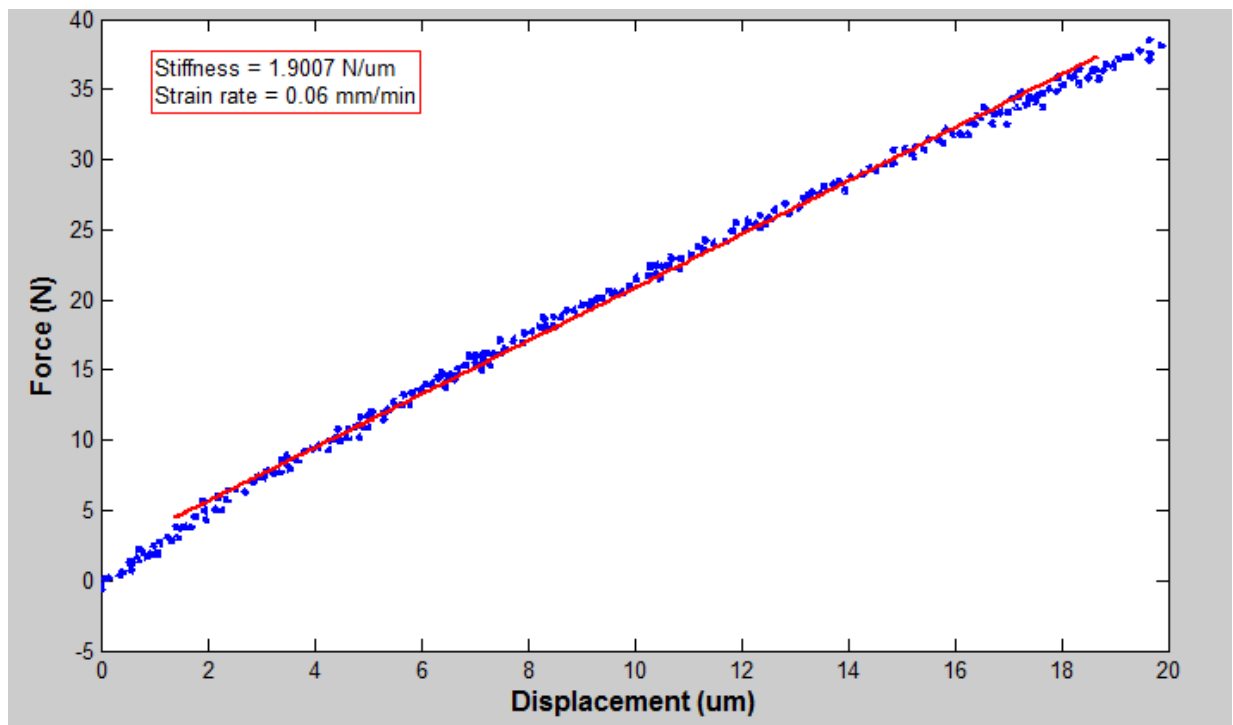

Figure B.37 - Force vs. displacement plot of bovine sample 37 on day 23 of live bone study. Linear fit shown to determine bulk stiffness.
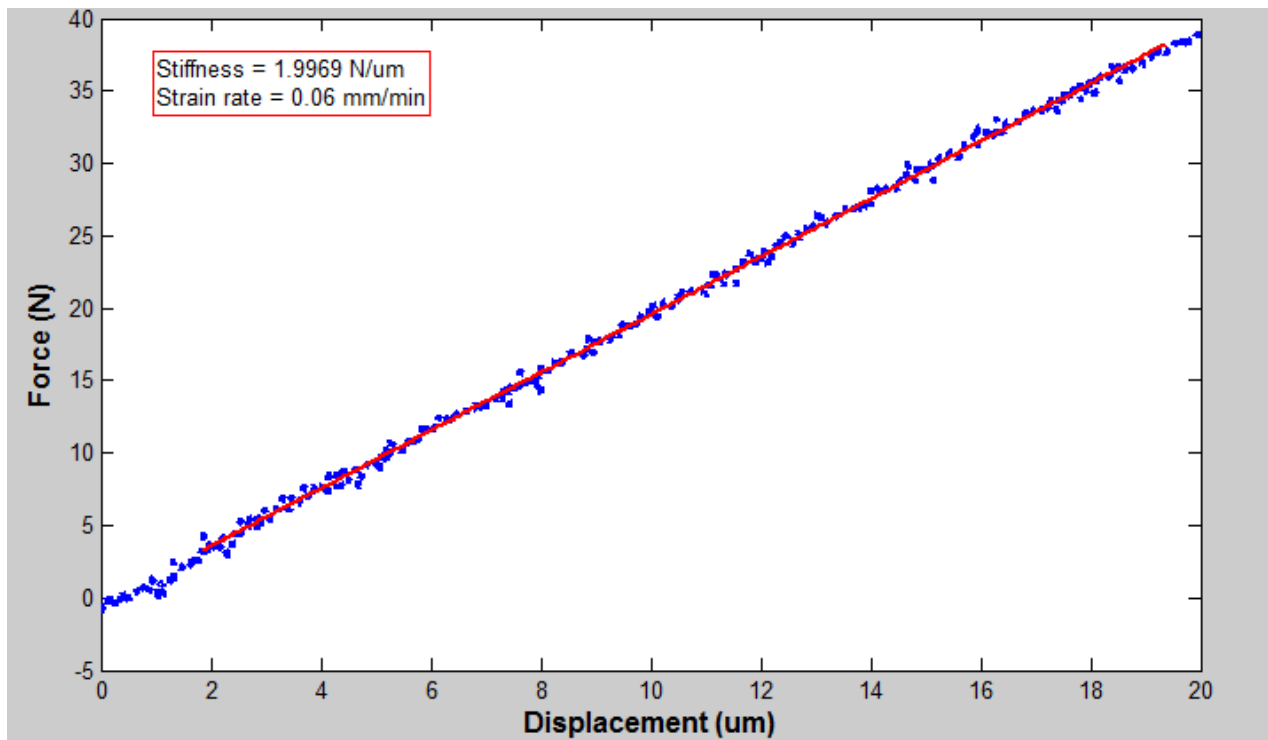
Figure B.38 - Force vs. displacement plot of bovine sample 38 on day 23 of live bone study. Linear fit shown to determine bulk stiffness.
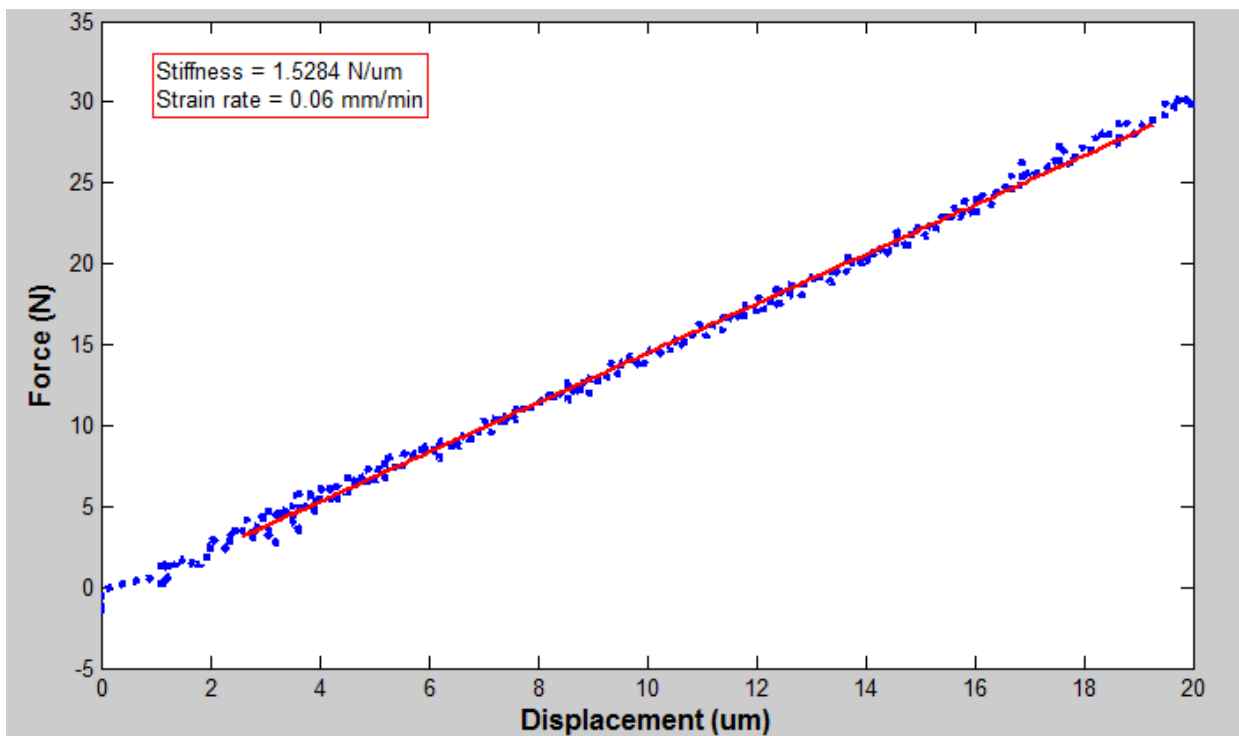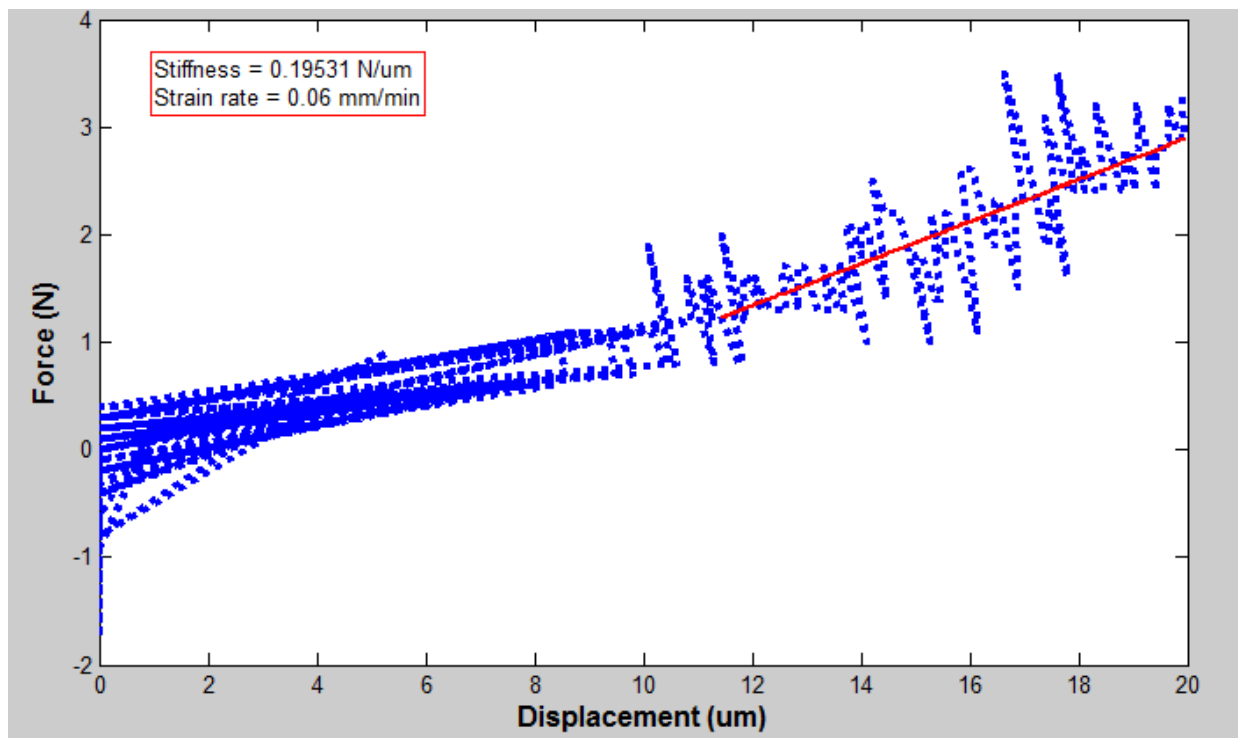

Figure B.39 - Force vs. displacement plot of bovine sample 39 on day 23 of live bone study. Linear fit shown to determine bulk stiffness.
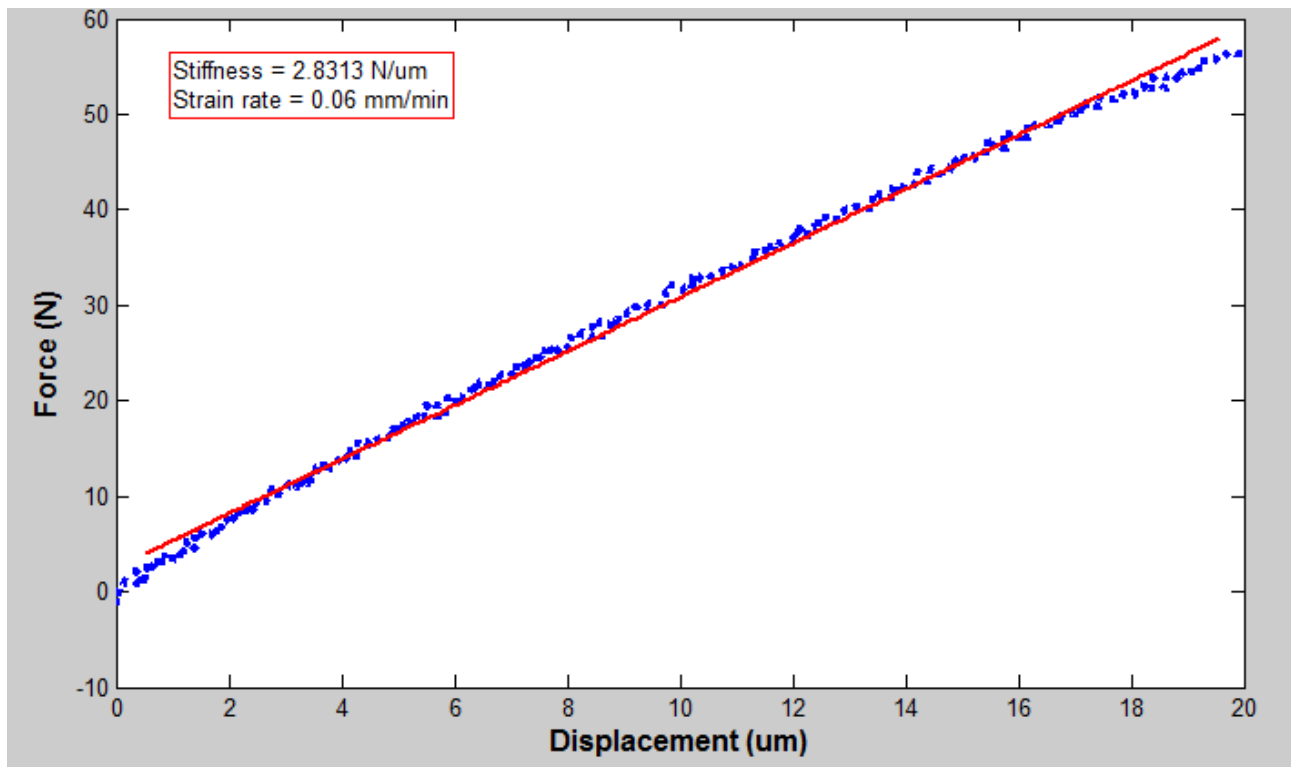
Figure B.40 - Force vs. displacement plot of bovine sample 40 on day 23 of live bone study. Linear fit shown to determine bulk stiffness.
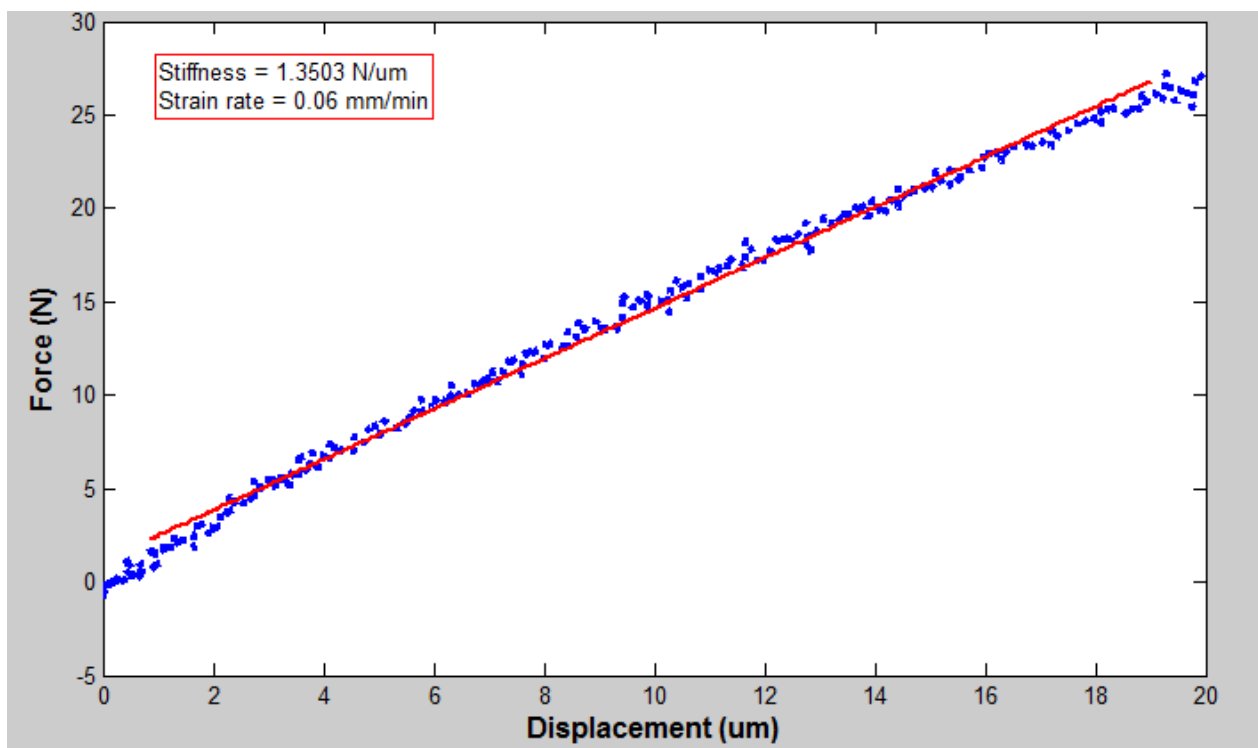
Figure B.41 - Force vs. displacement plot of bovine sample 41 on day 23 of live bone study. Linear fit shown to determine bulk stiffness.
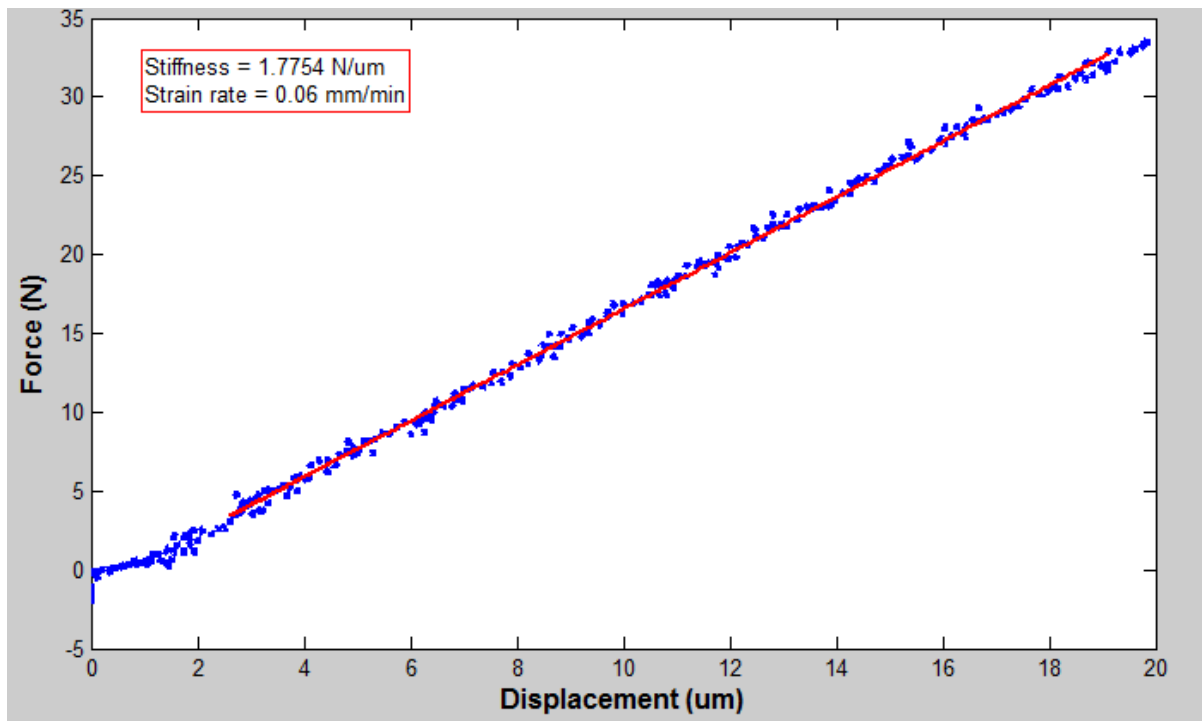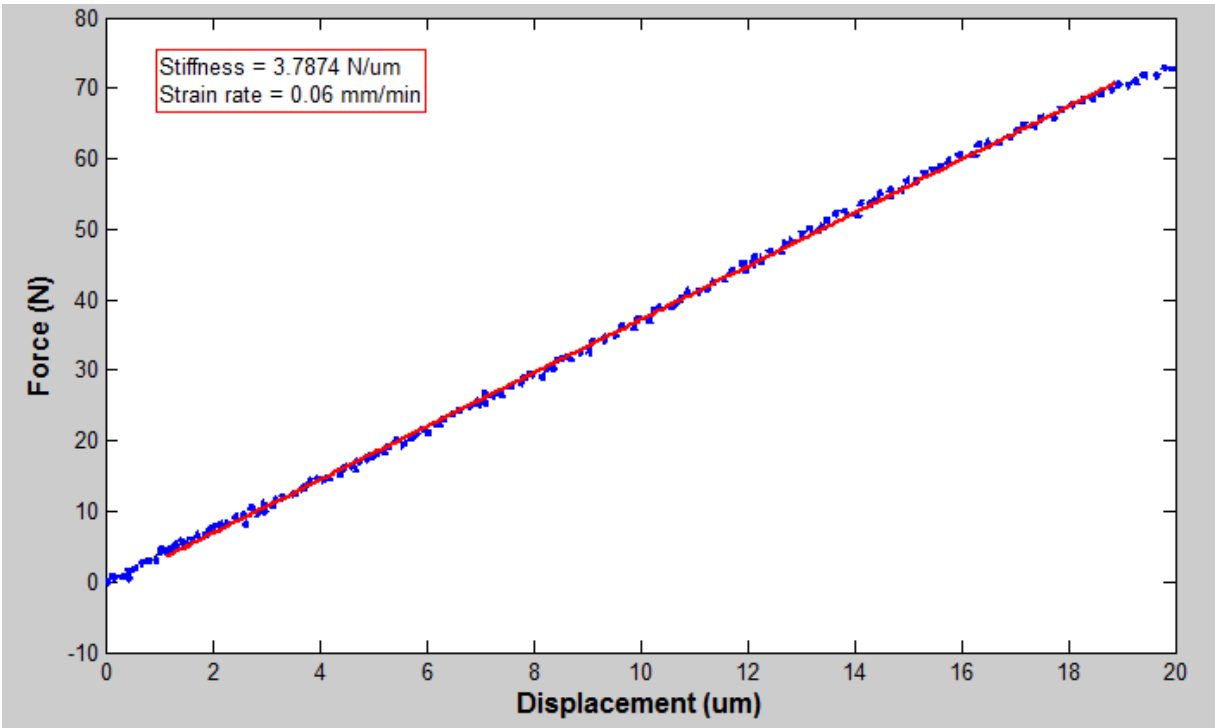
Figure B.42 - Force vs. displacement plot of bovine sample 42 on day 23 of live bone study. Linear fit shown to determine bulk stiffness.
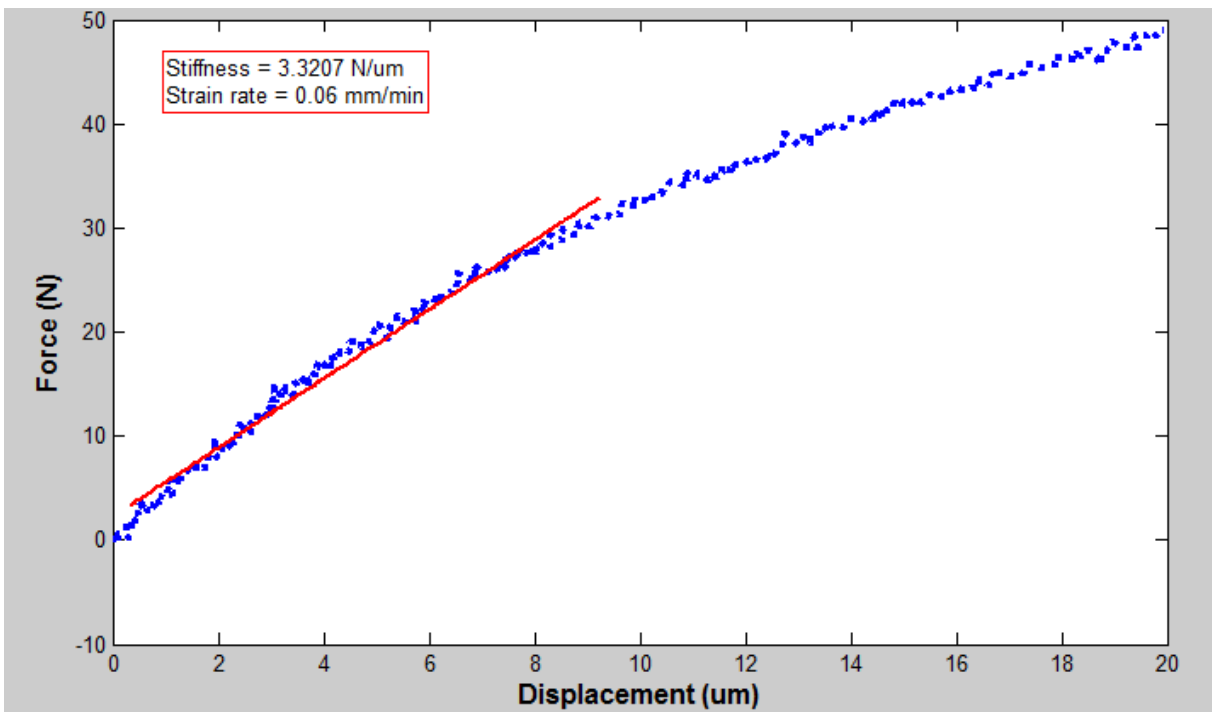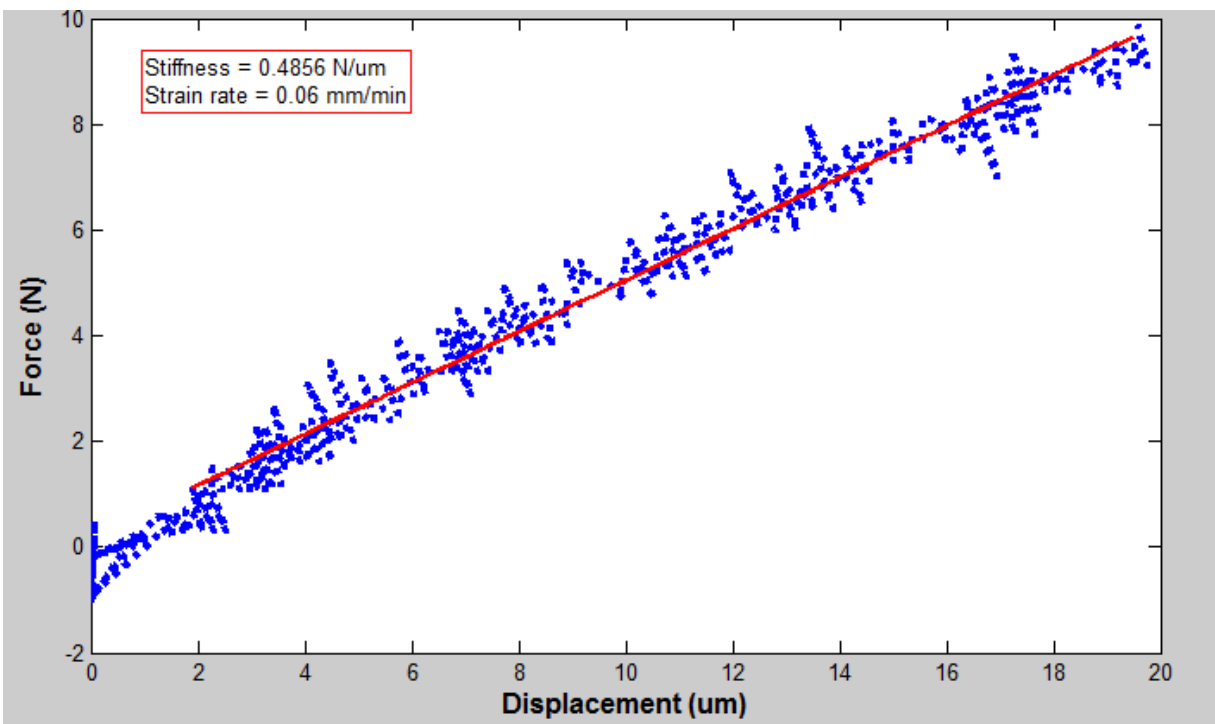

Figure B.43 - Force vs. displacement plot of bovine sample 43 on day 23 of live bone study. Linear fit shown to determine bulk stiffness.
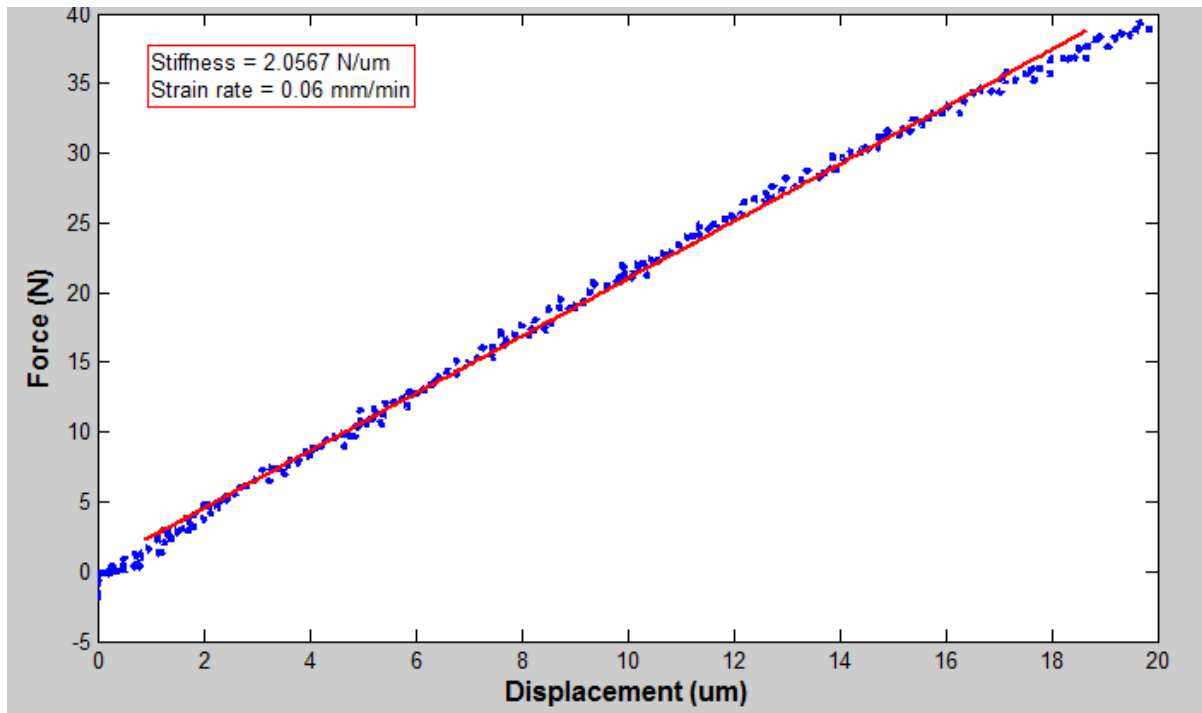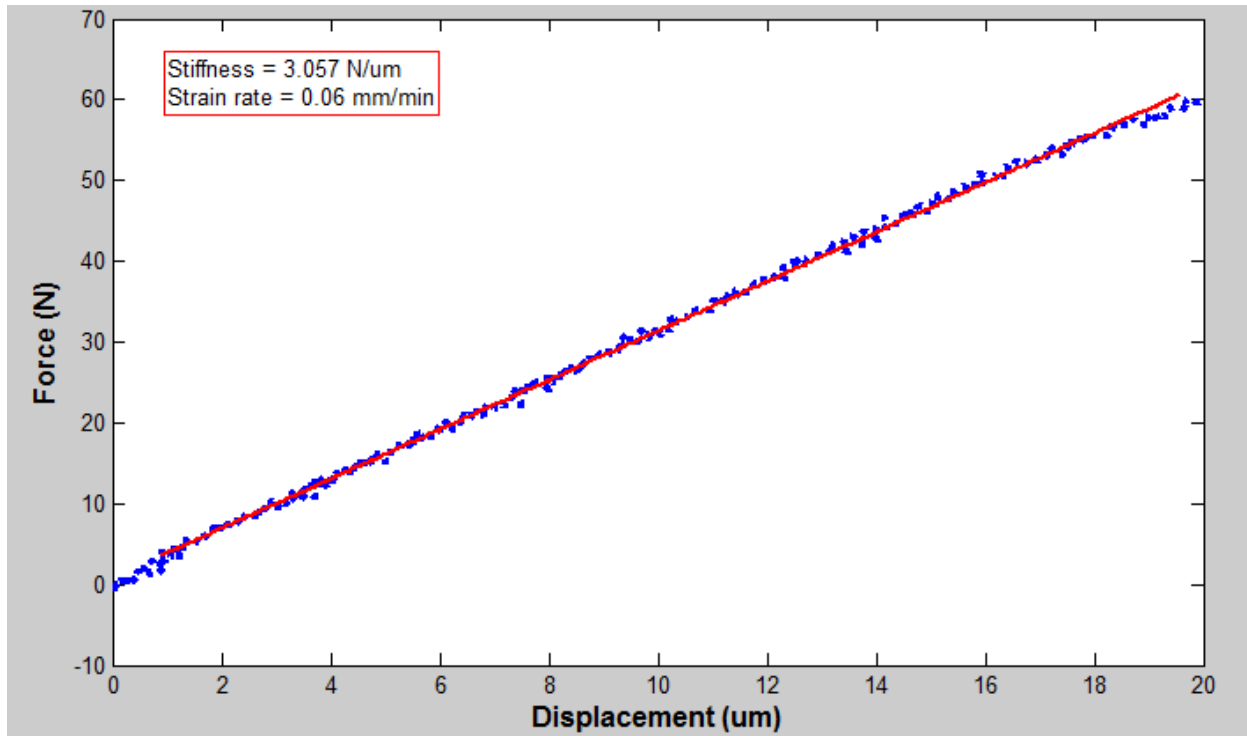
Figure B.44 - Force vs. displacement plot of bovine sample 44 on day 23 of live bone study. Linear fit shown to determine bulk stiffness.
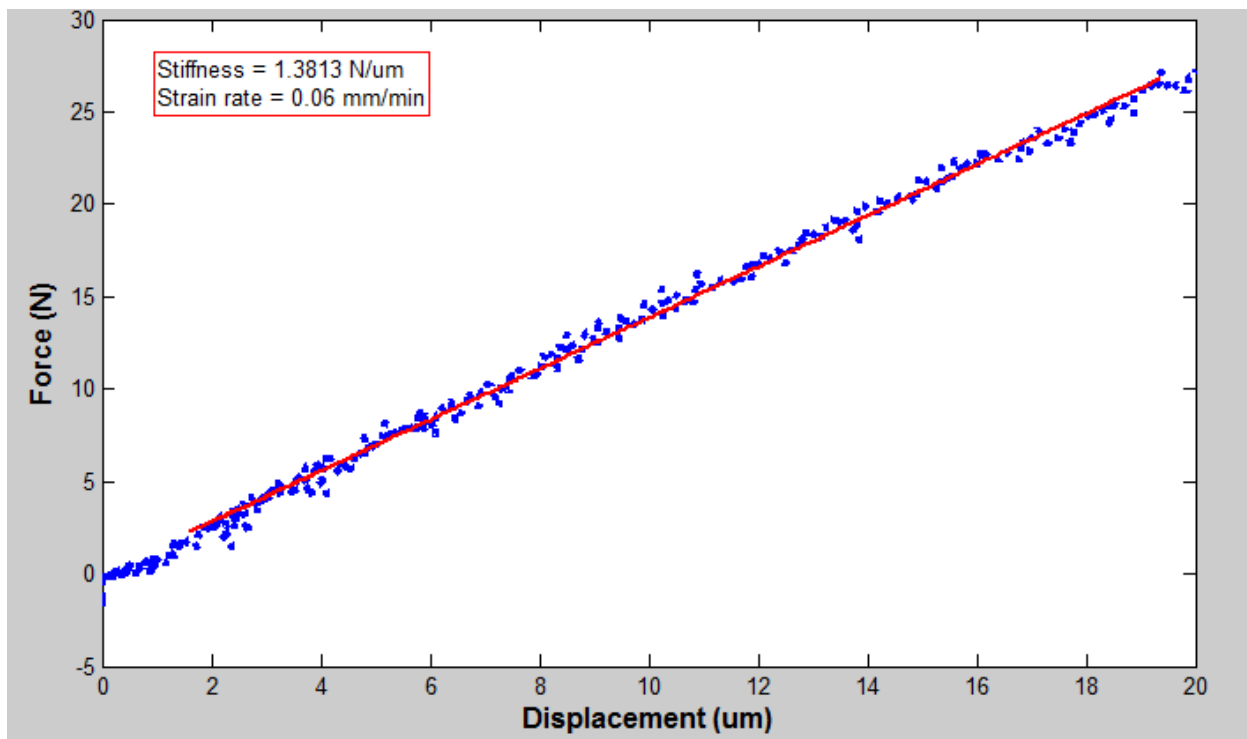
Figure B.45 - Force vs. displacement plot of bovine sample 45 on day 23 of live bone study. Linear fit shown to determine bulk stiffness.
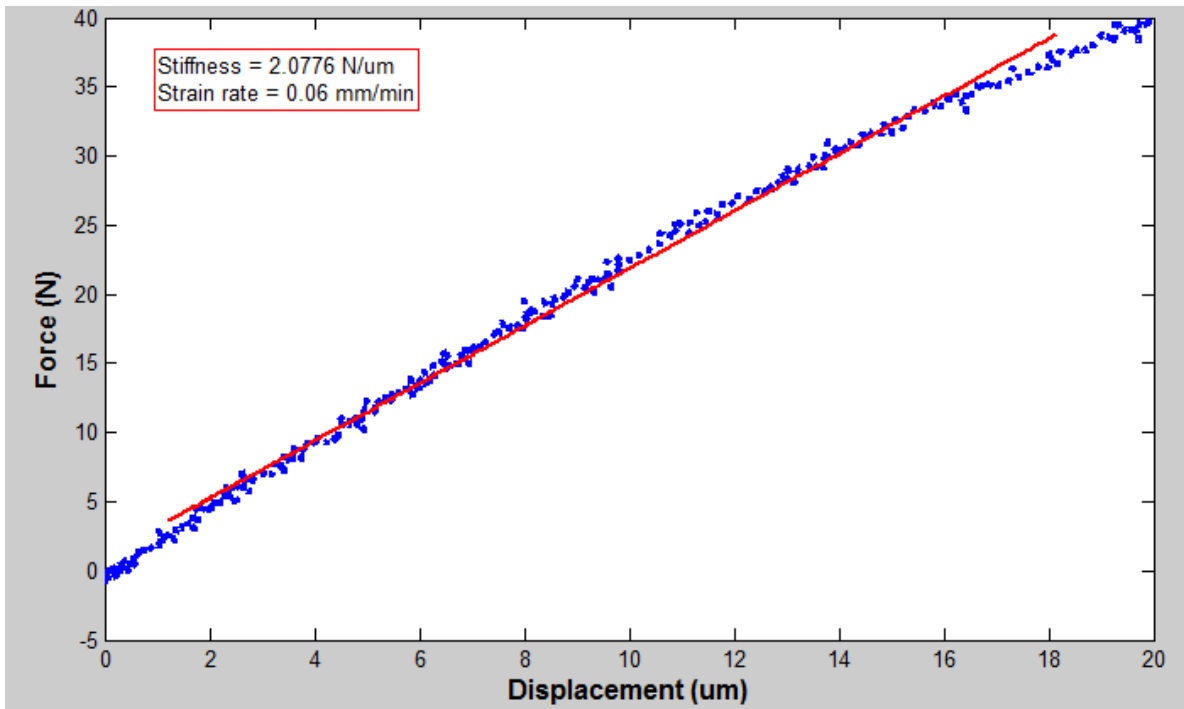
Figure B.46 - Force vs. displacement plot of bovine sample 46 on day 23 of live bone study. Linear fit shown to determine bulk stiffness.
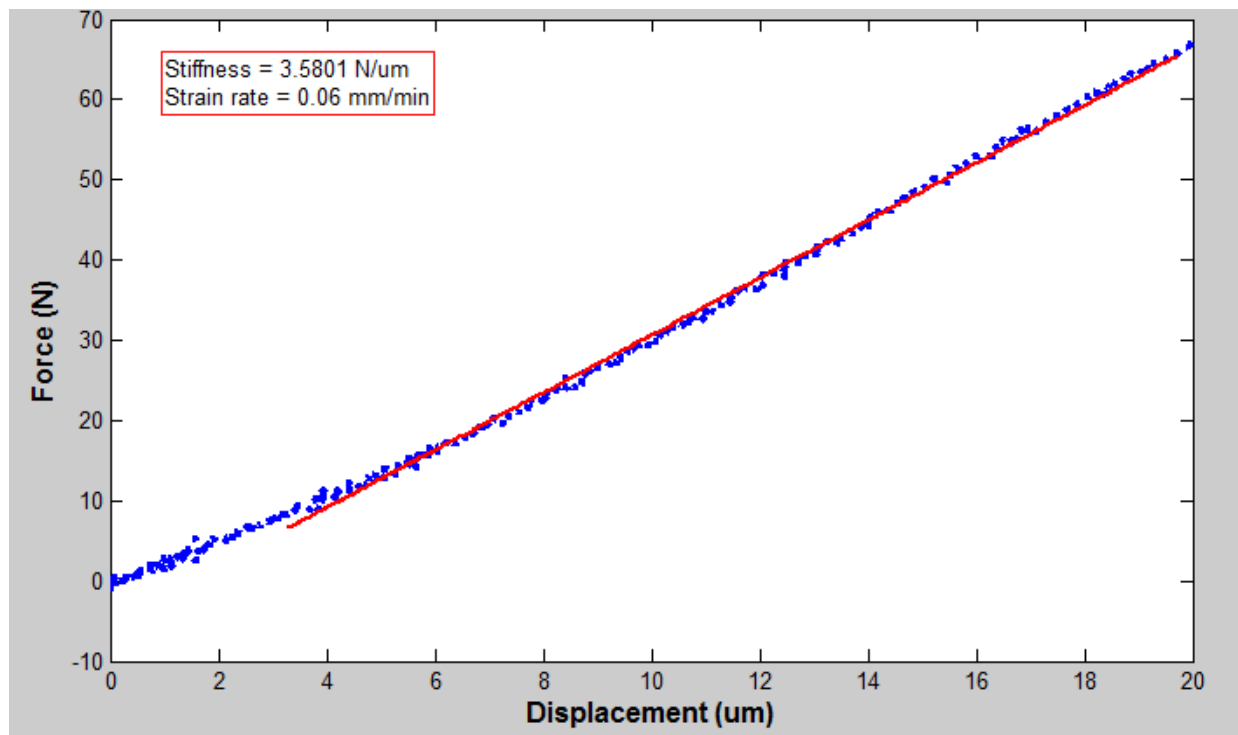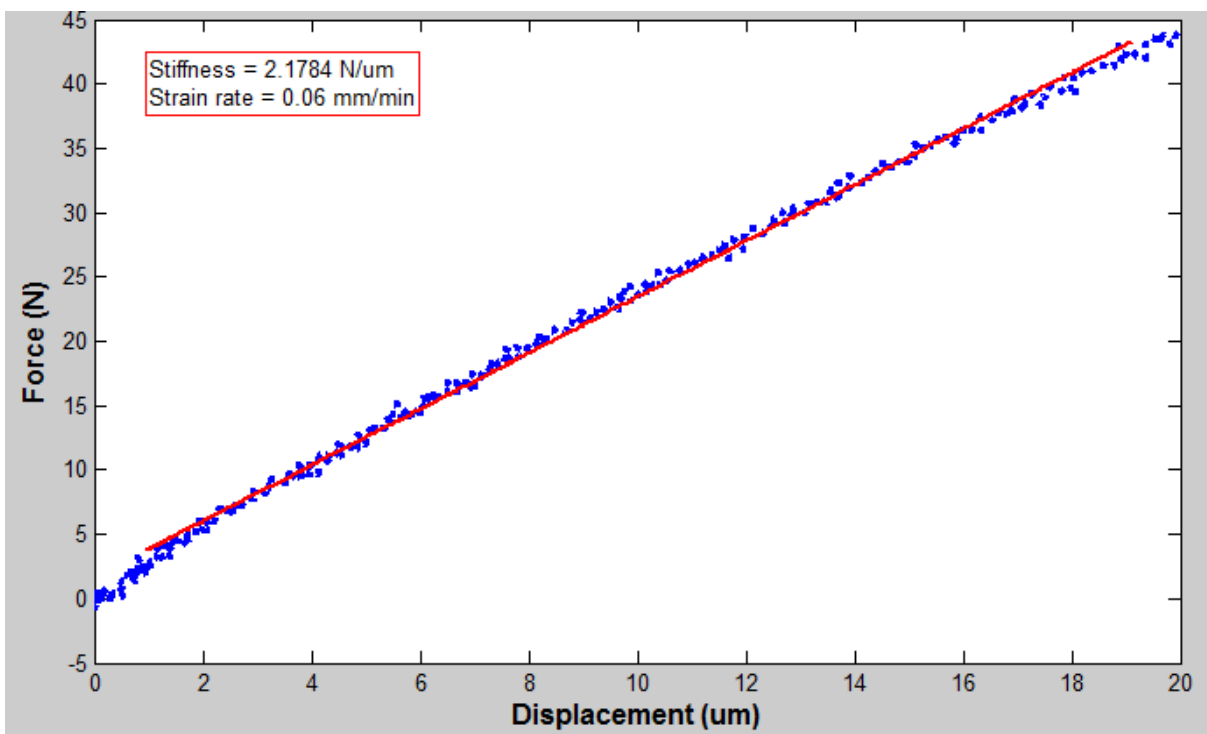

Figure B.47 - Force vs. displacement plot of bovine sample 47 on day 23 of live bone study. Linear fit shown to determine bulk stiffness.
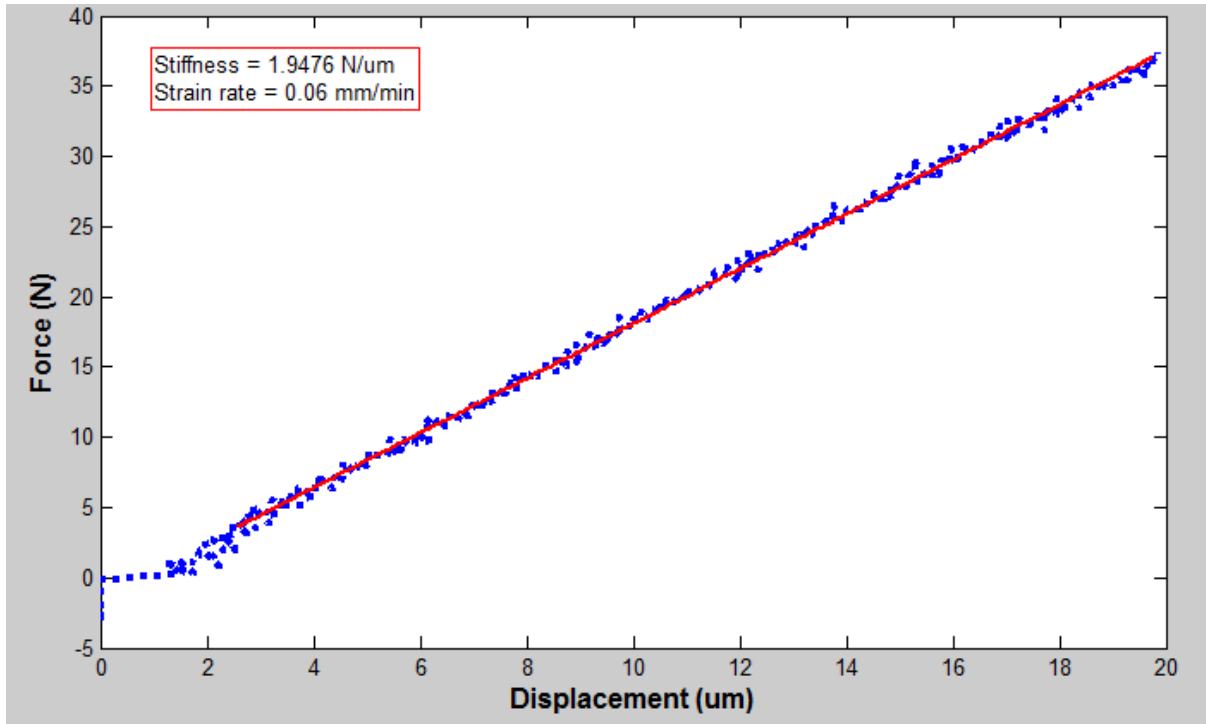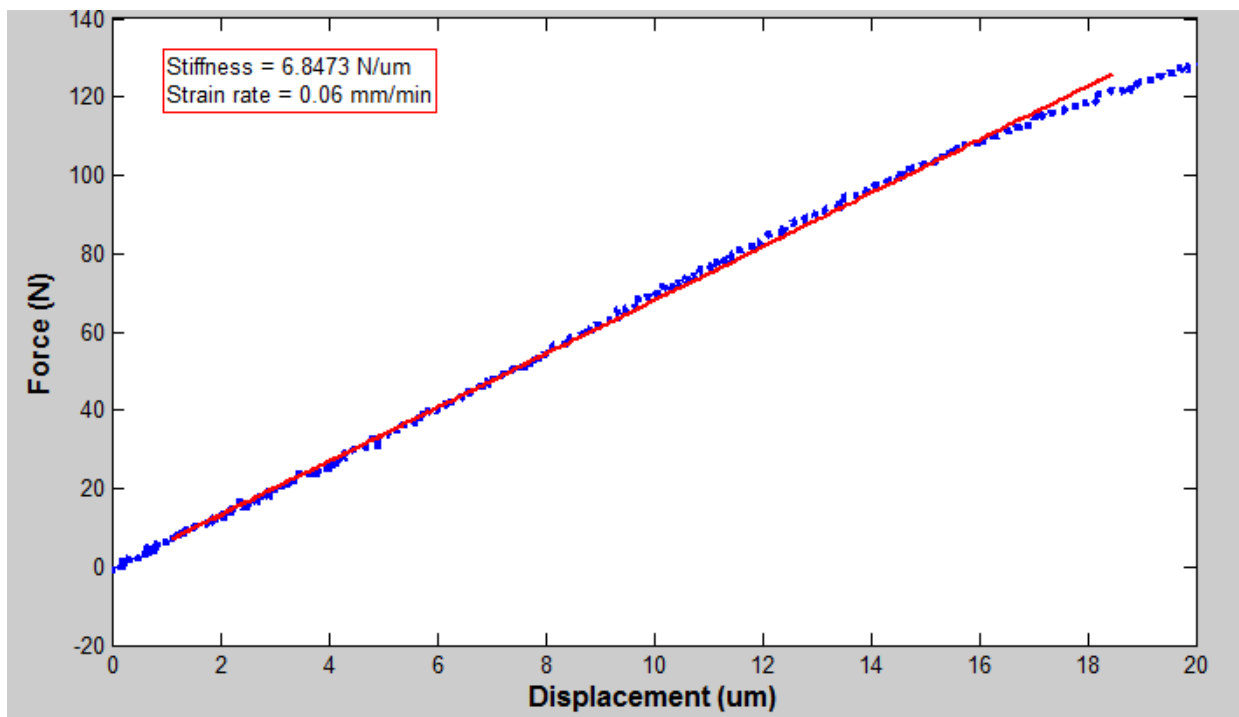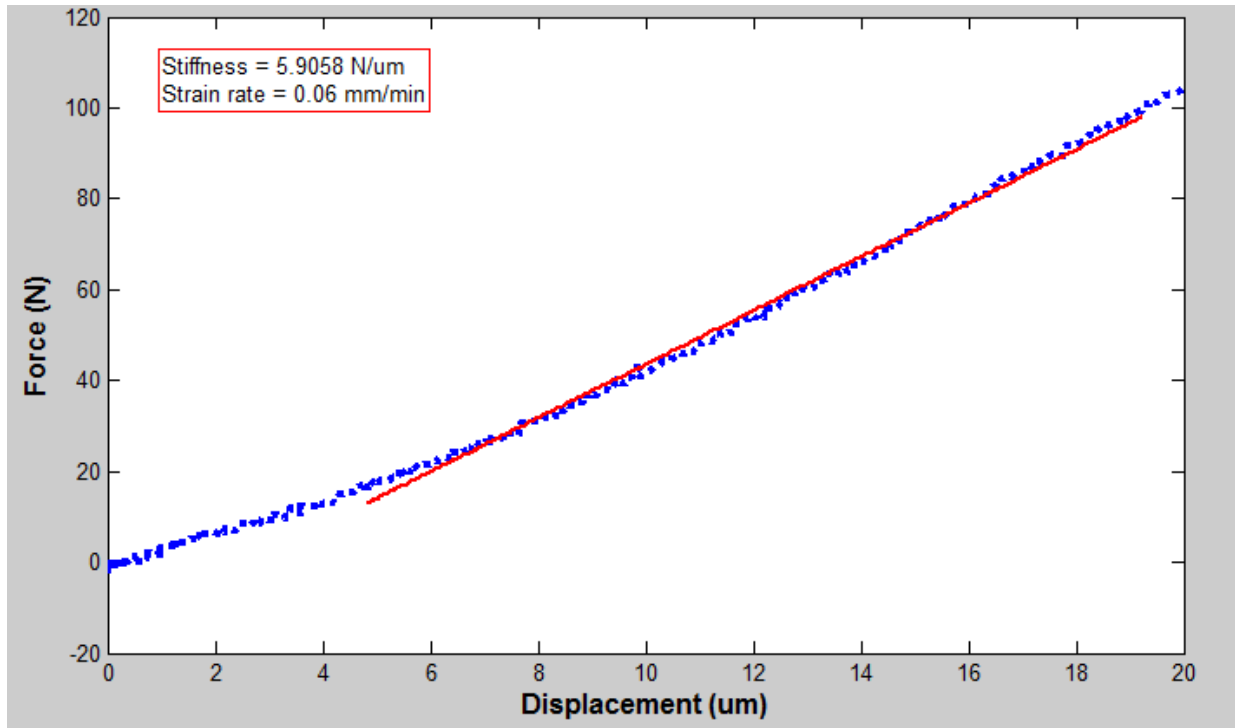
Figure B.48 - Force vs. displacement plot of bovine sample 48 on day 23 of live bone study. Linear fit shown to determine bulk stiffness.

Appendix C

C. Force versus Displacement plots for Human Hip Specimens, Chapter 5

Figure C.1 – Representative force vs. displacement plot of human sample 1 during live bone study. Linear fit shown to determine bulk stiffness

Figure C.2 - Representative force vs. displacement plot of human sample 2 during live bone study. Linear fit shown to determine bulk stiffness

Figure C.3 - Representative force vs. displacement plot of human sample 3 during live bone study. Linear fit shown to determine bulk stiffness

Figure C.4 - Representative force vs. displacement plot of human sample 4 during live bone study. Linear fit shown to determine bulk stiffness.

Figure C.5 - Representative force vs. displacement plot of human sample 5 during live bone study. Linear fit shown to determine bulk stiffness.

Figure C.6 - Representative force vs. displacement plot of human sample 6 during live bone study. Linear fit shown to determine bulk stiffness

Figure C.7 - Representative force vs. displacement plot of human sample 7 during live bone study. Linear fit shown to determine bulk stiffness

Figure C.8 - Representative force vs. displacement plot of human sample 8 during live bone study. Linear fit shown to determine bulk stiffness
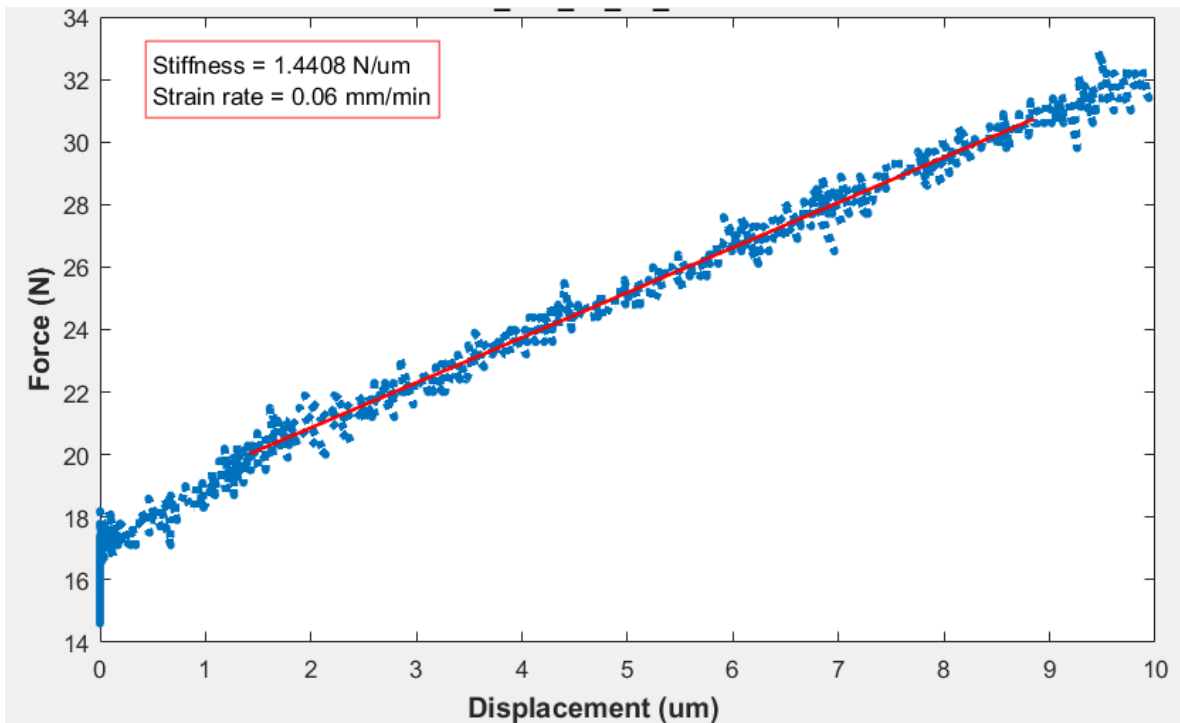
Figure C.9 - Representative force vs. displacement plot of human sample 9 during live bone study. Linear fit shown to determine bulk stiffness
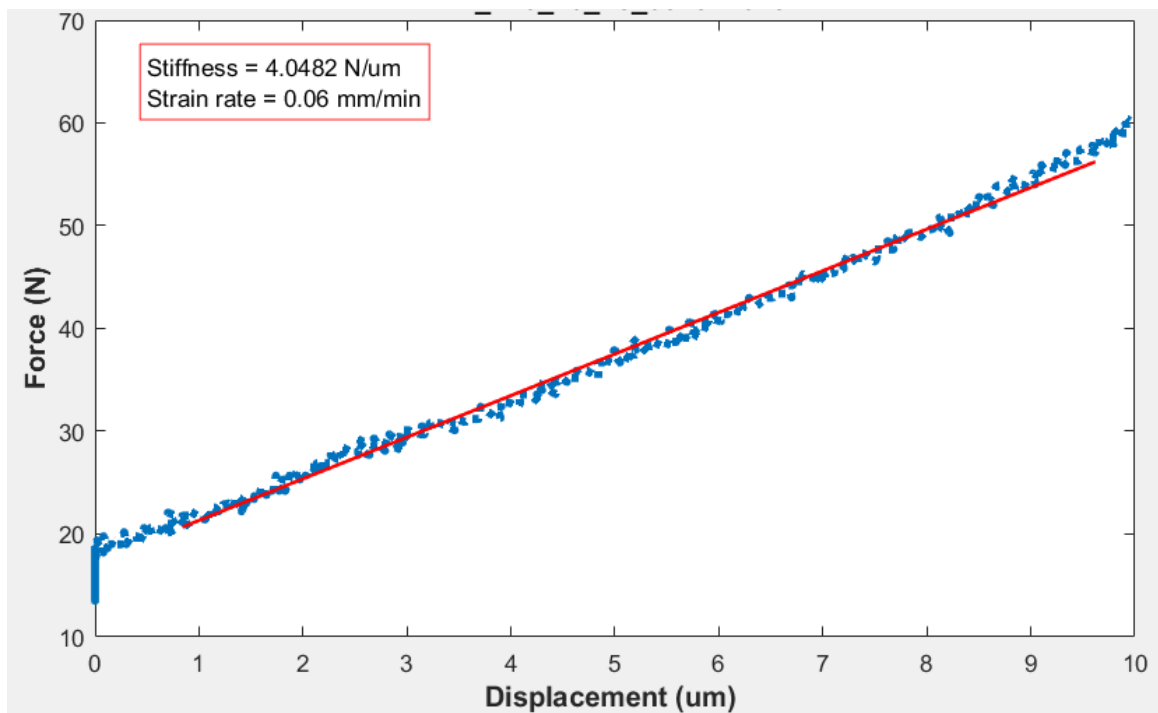
Figure C.10 - Representative force vs. displacement plot of human sample 10 during live bone study. Linear fit shown to determine bulk stiffness
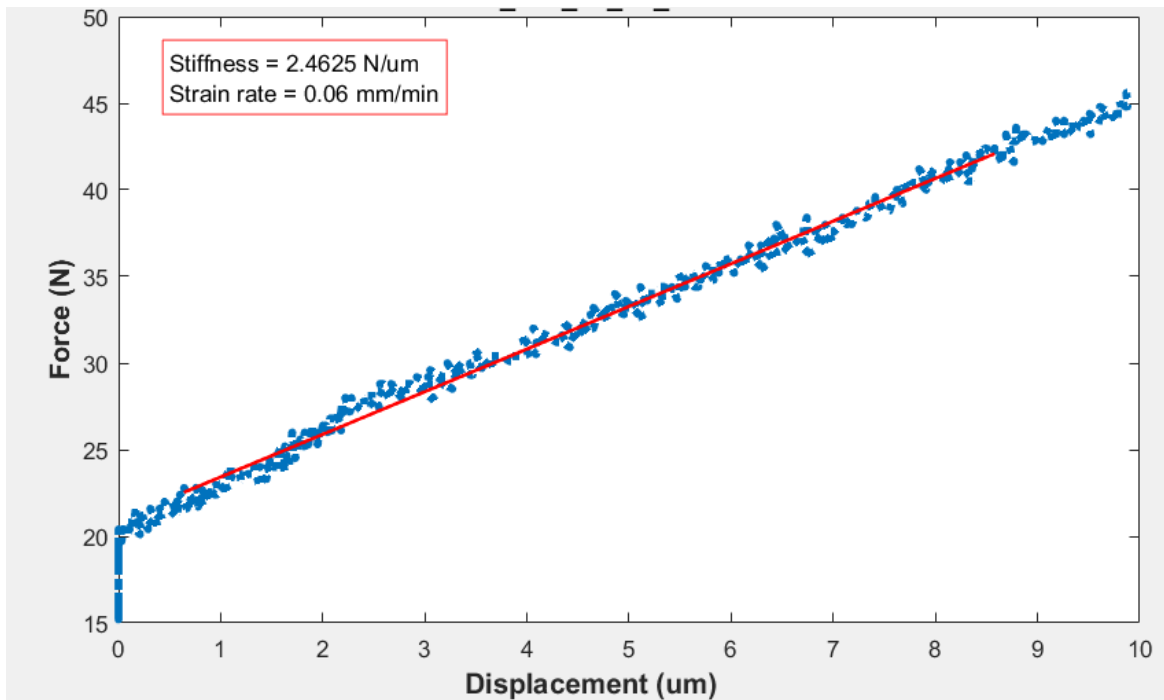
Figure C.11 - Representative force vs. displacement plot of human sample 11 during live bone study. Linear fit shown to determine bulk stiffness
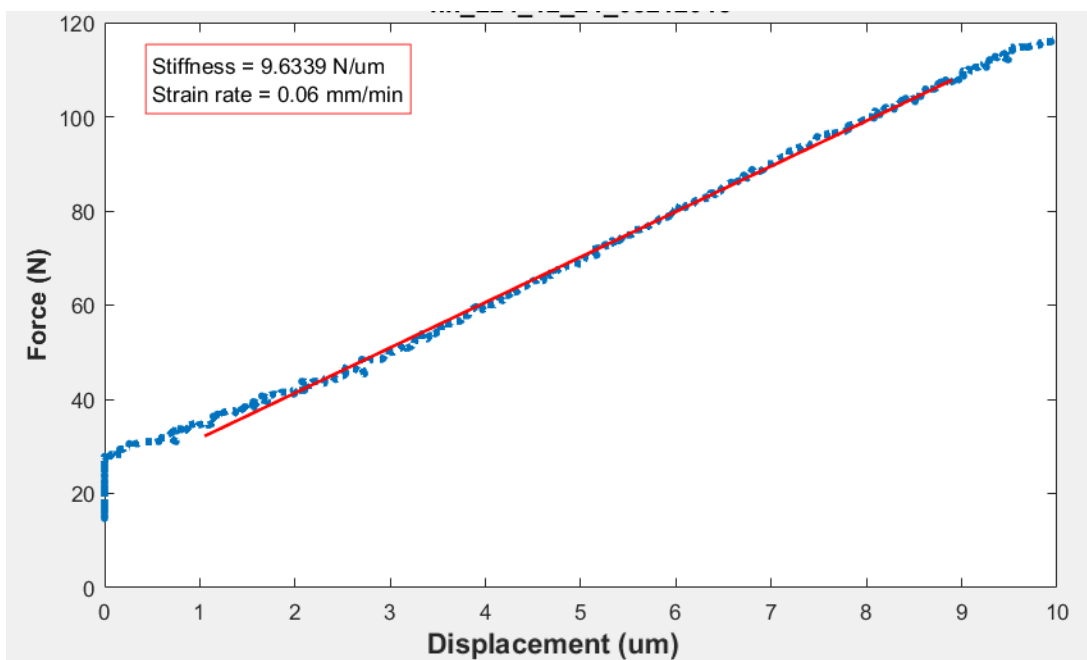
Figure C.12 - Representative force vs. displacement plot of human sample 12 during live bone study. Linear fit shown to determine bulk stiffness
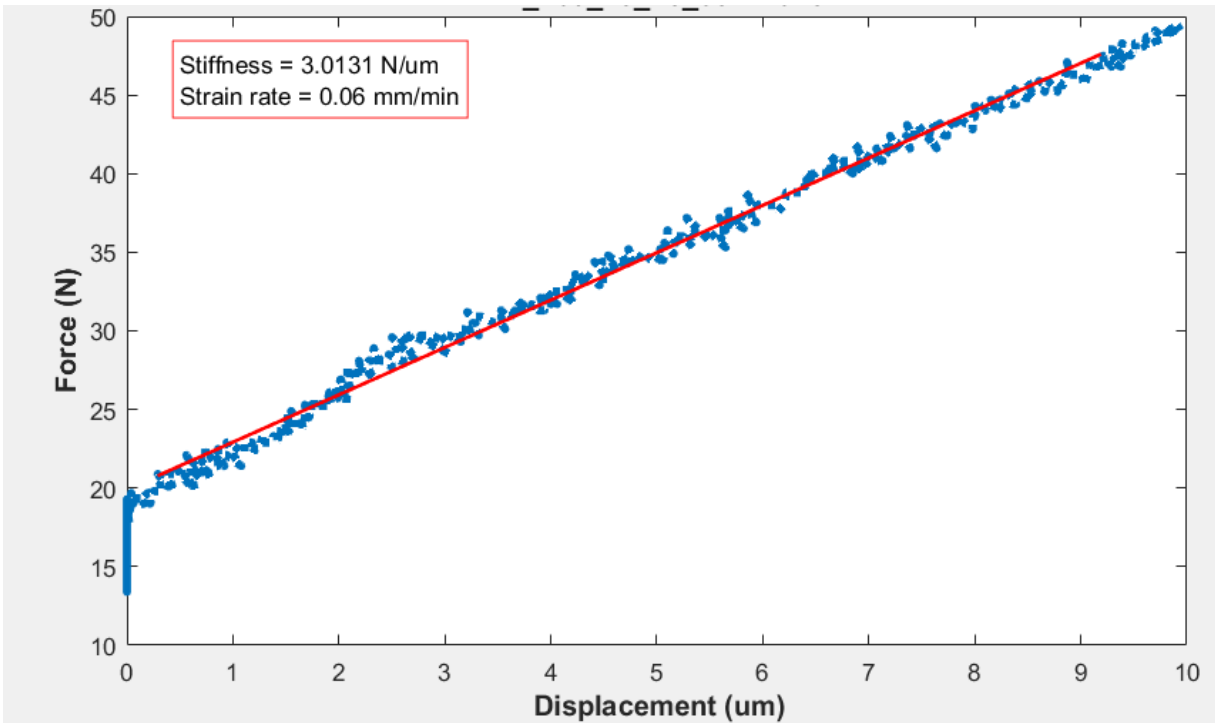
Figure C.13 - Representative force vs. displacement plot of human sample 13 during live bone study. Linear fit shown to determine bulk stiffness
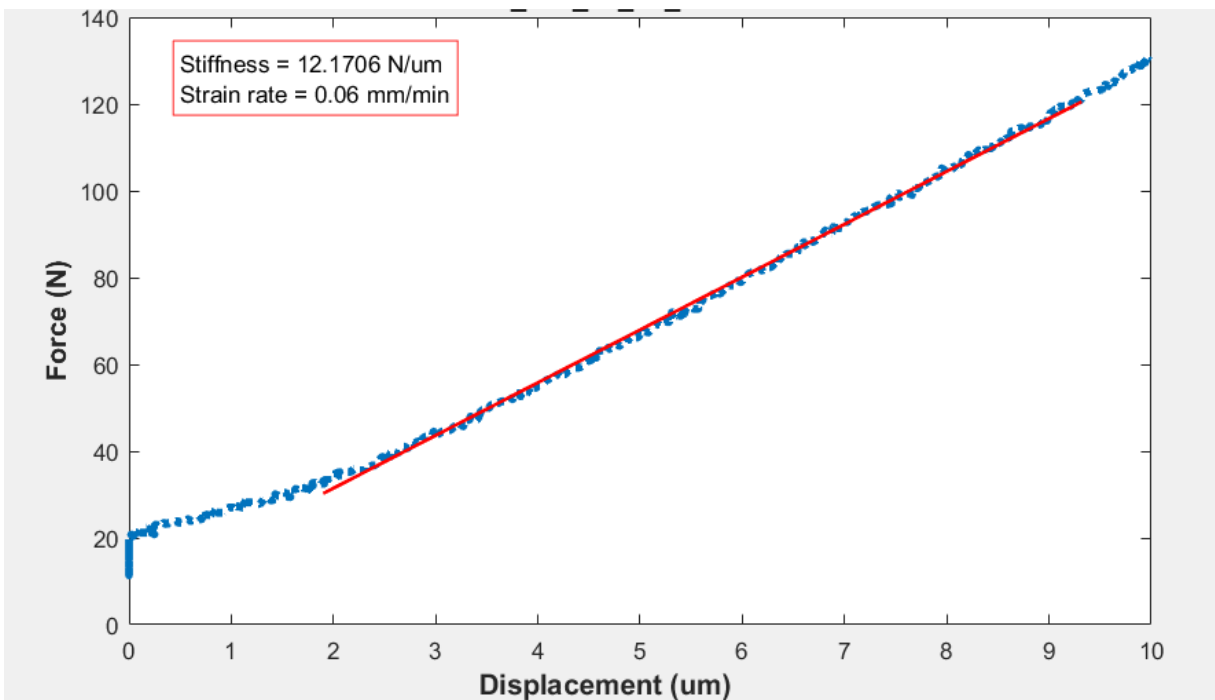
Figure C.14 - Representative force vs. displacement plot of human sample 14 during live bone study. Linear fit shown to determine bulk stiffness
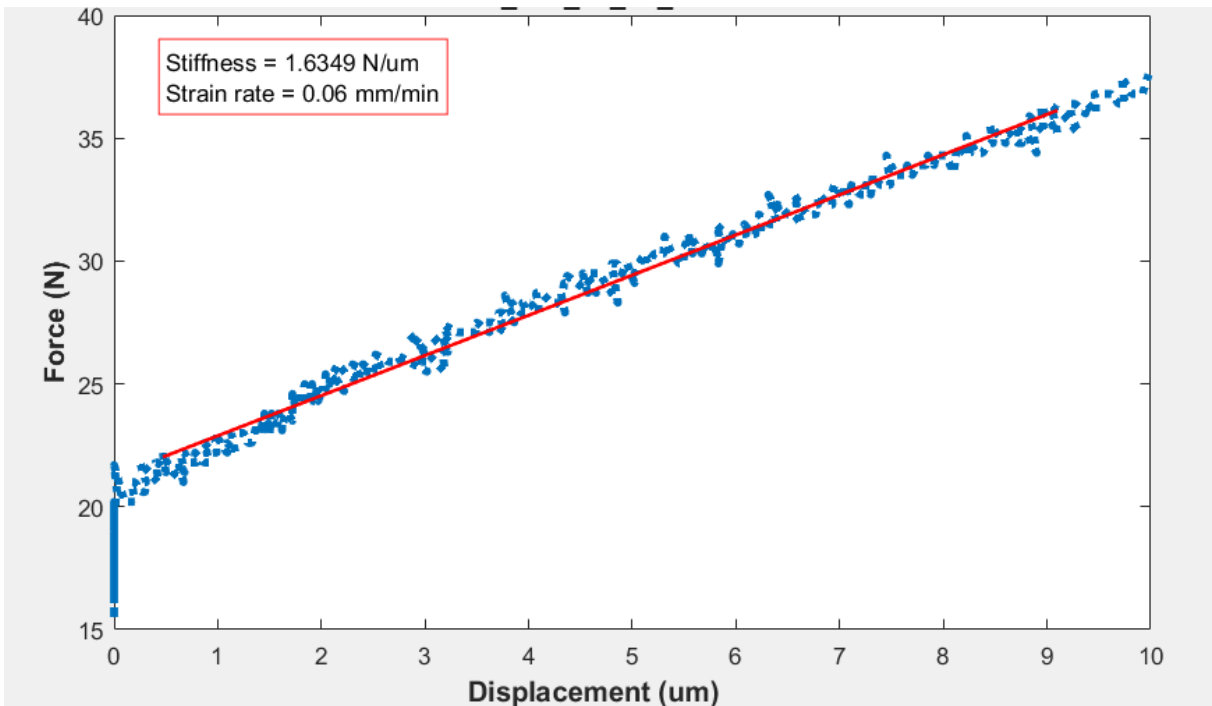
Figure C.15 - Representative force vs. displacement plot of human sample 15 during live bone study. Linear fit shown to determine bulk stiffness
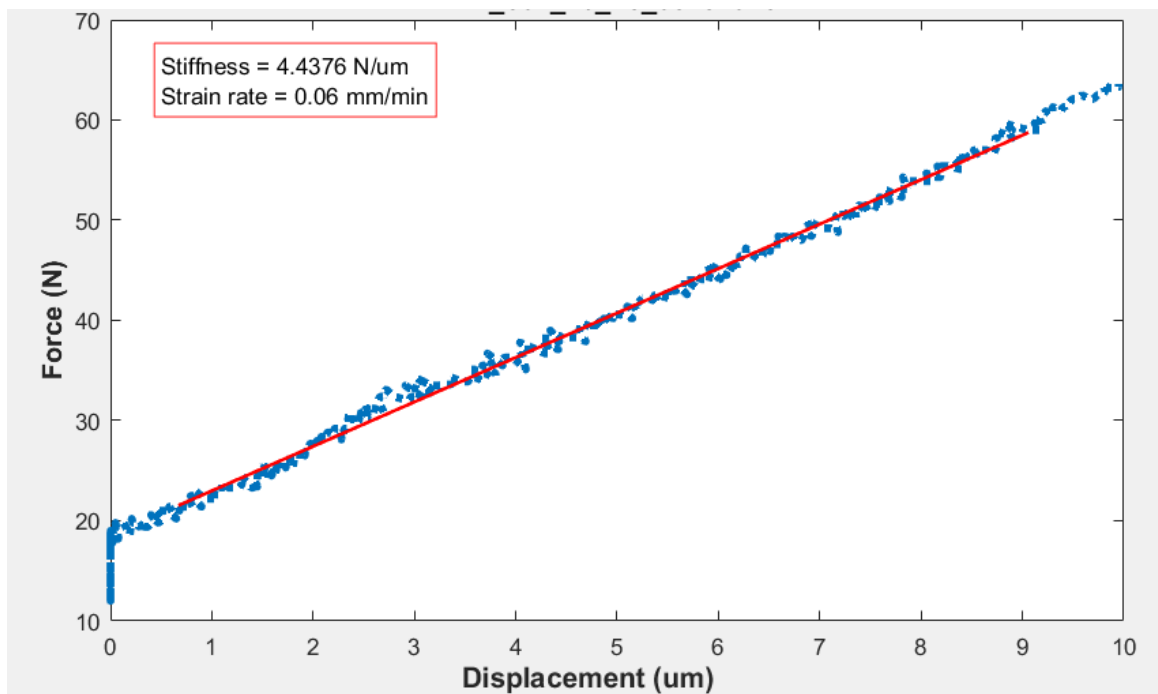
Figure C.16 - Representative force vs. displacement plot of human sample 16 during live bone study. Linear fit shown to determine bulk stiffness
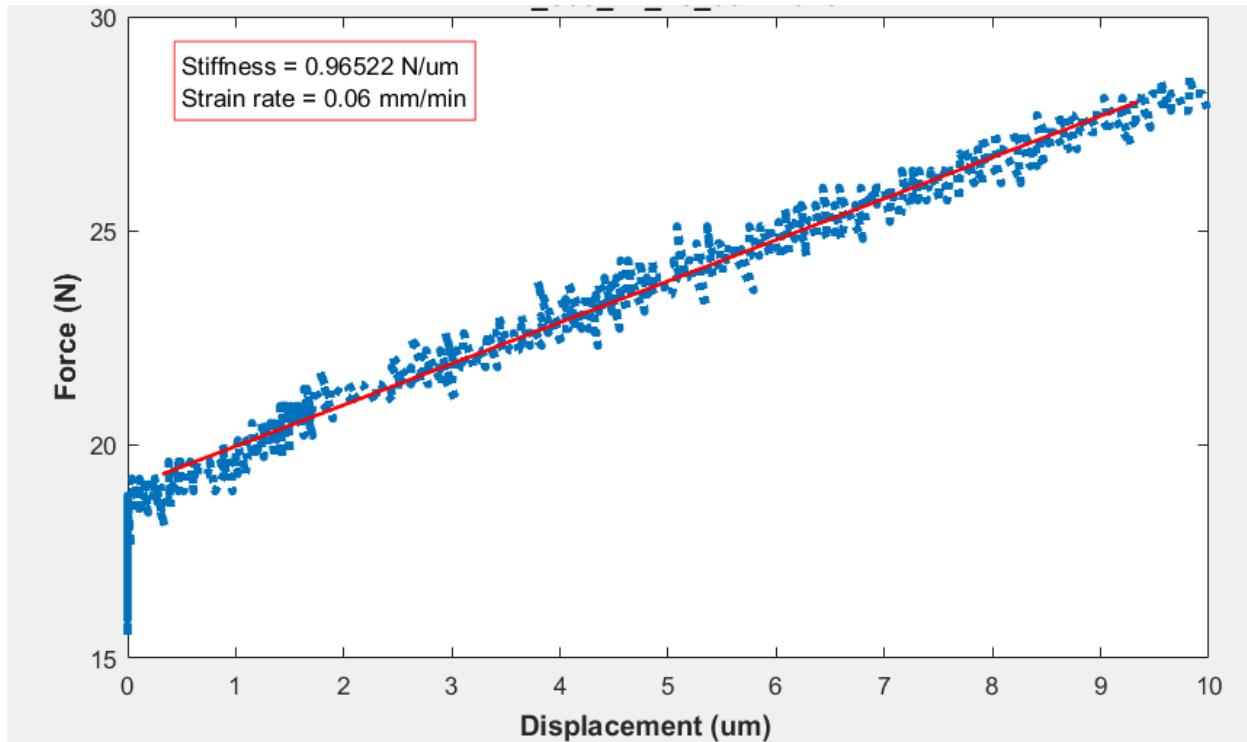
Figure C.17 - Representative force vs. displacement plot of human sample 17 during live bone study. Linear fit shown to determine bulk stiffness
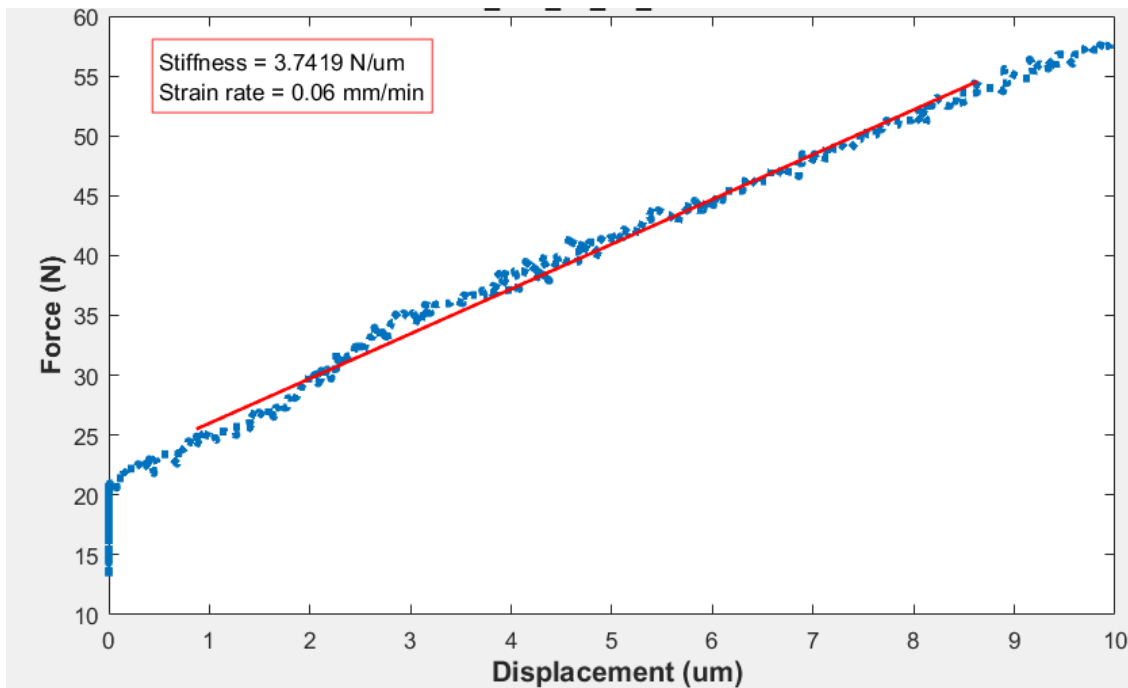
Figure C.18 - Representative force vs. displacement plot of human sample 18 during live bone study. Linear fit shown to determine bulk stiffness
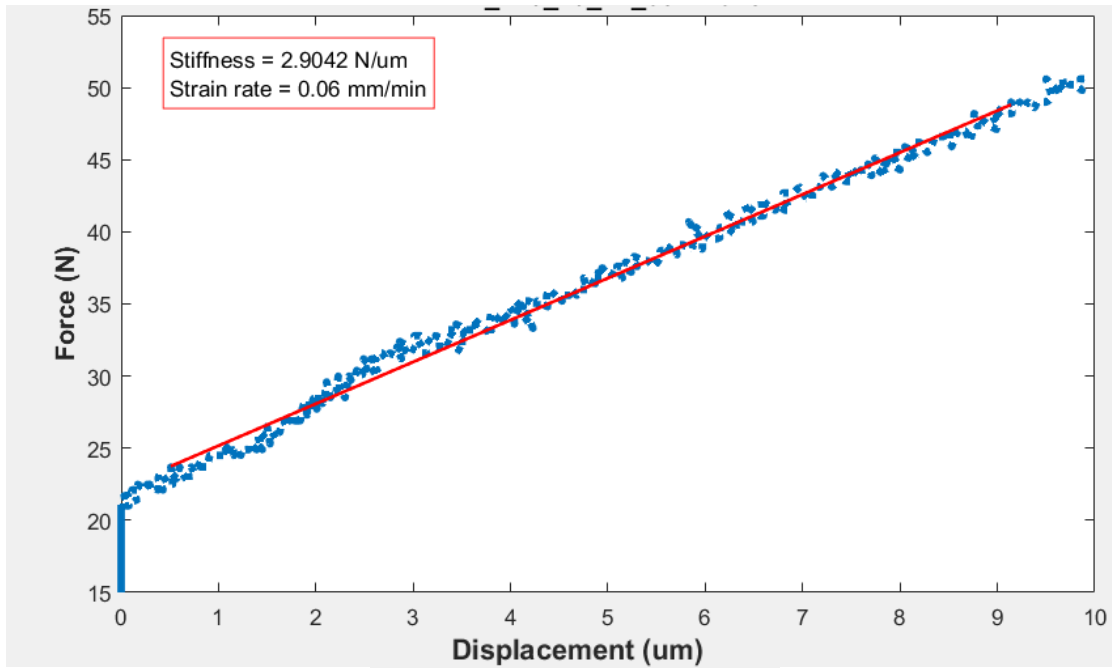
Figure C.19 - Representative force vs. displacement plot of human sample 19 during live bone study. Linear fit shown to determine bulk stiffness
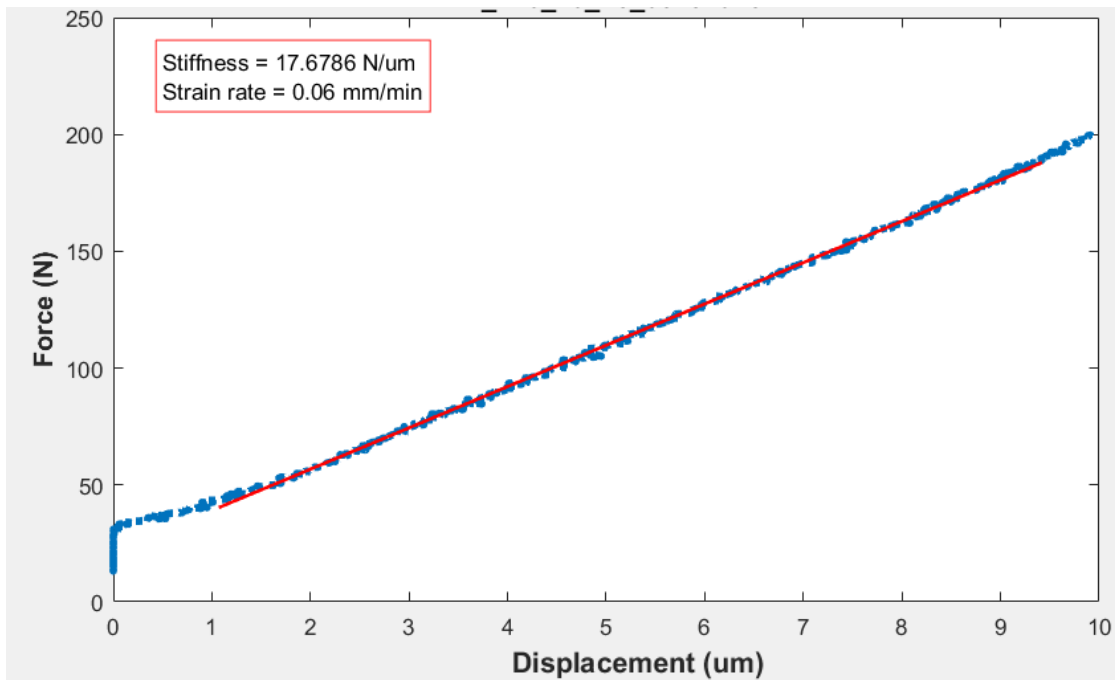
Figure C.20 - Representative force vs. displacement plot of human sample 20 during live bone study. Linear fit shown to determine bulk stiffness
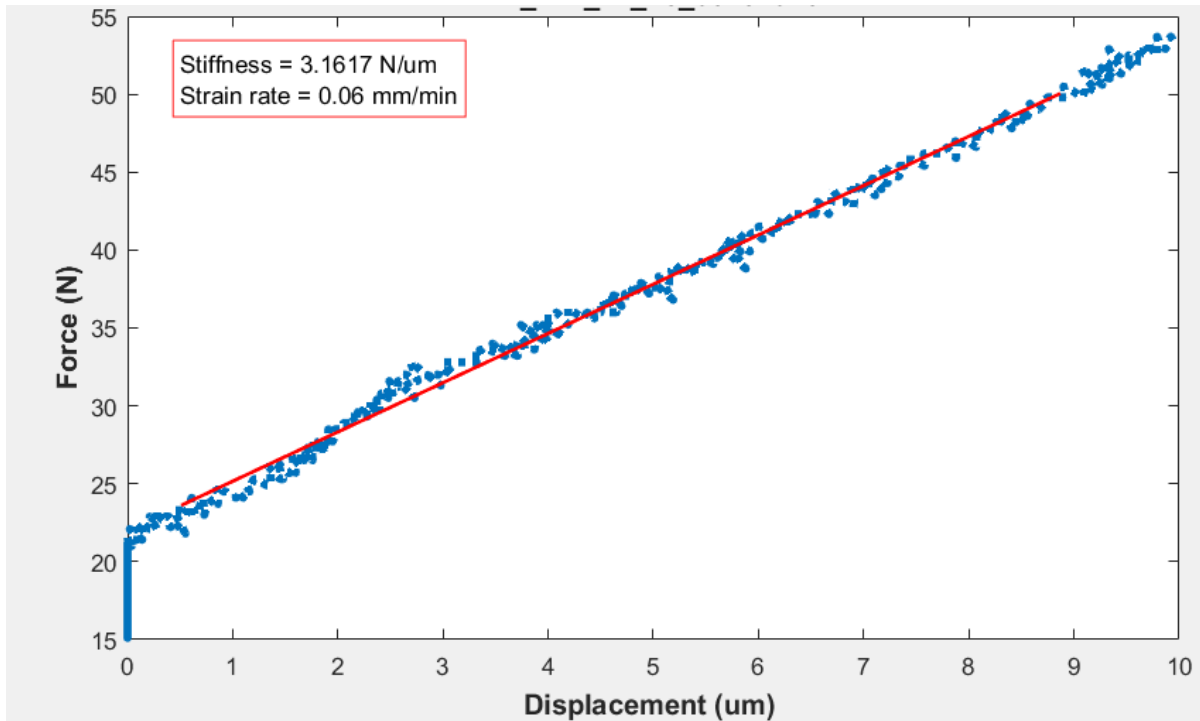
Figure C.21 - Representative force vs. displacement plot of human sample 21 during live bone study. Linear fit shown to determine bulk stiffness
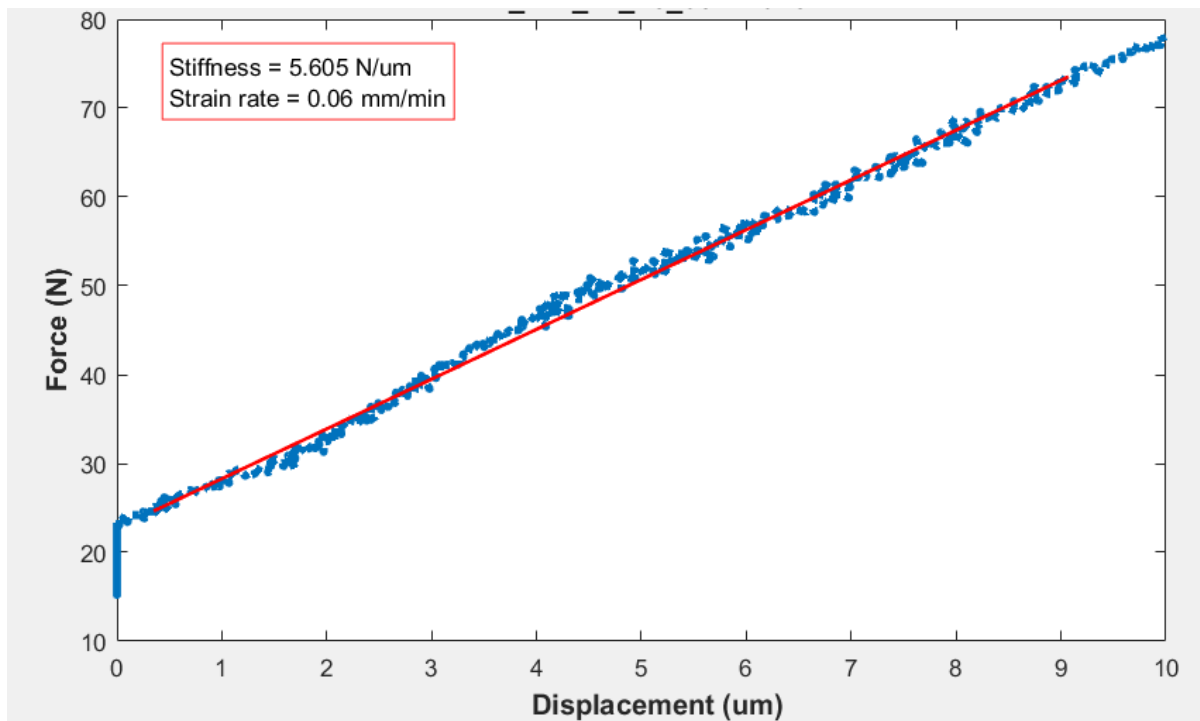
Figure C.22 - Representative force vs. displacement plot of human sample 22 during live bone study. Linear fit shown to determine bulk stiffness
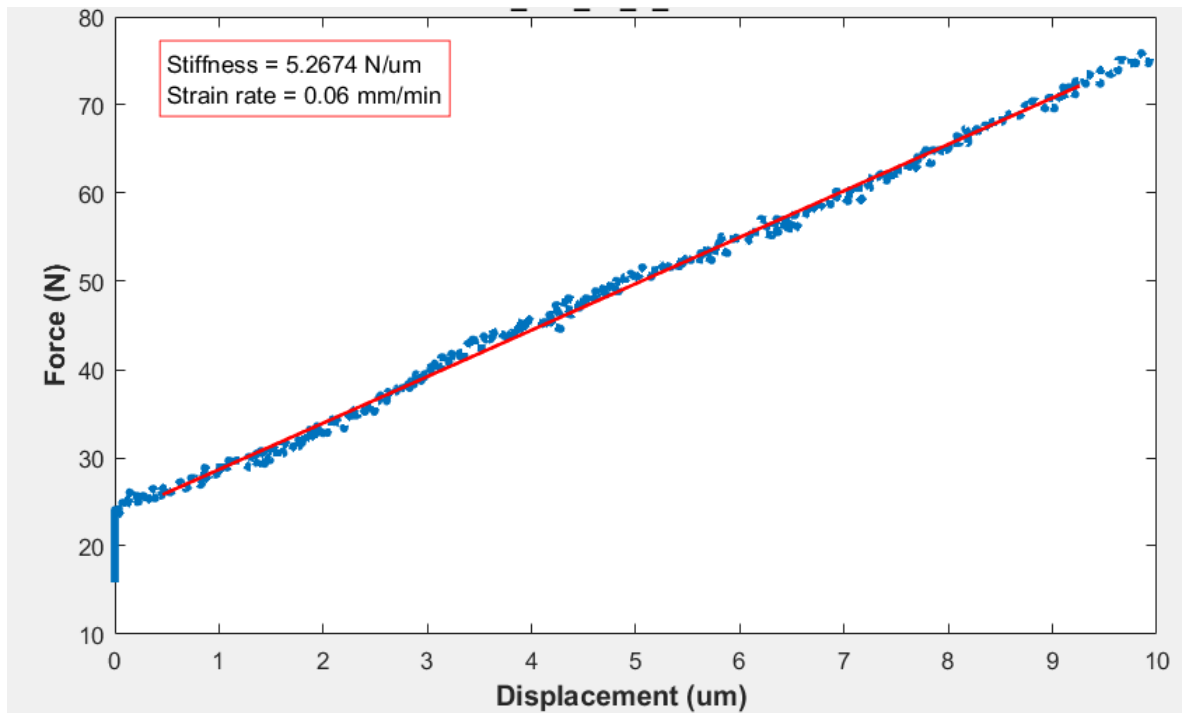
Figure C.23 - Representative force vs. displacement plot of human sample 23 during live bone study. Linear fit shown to determine bulk stiffness
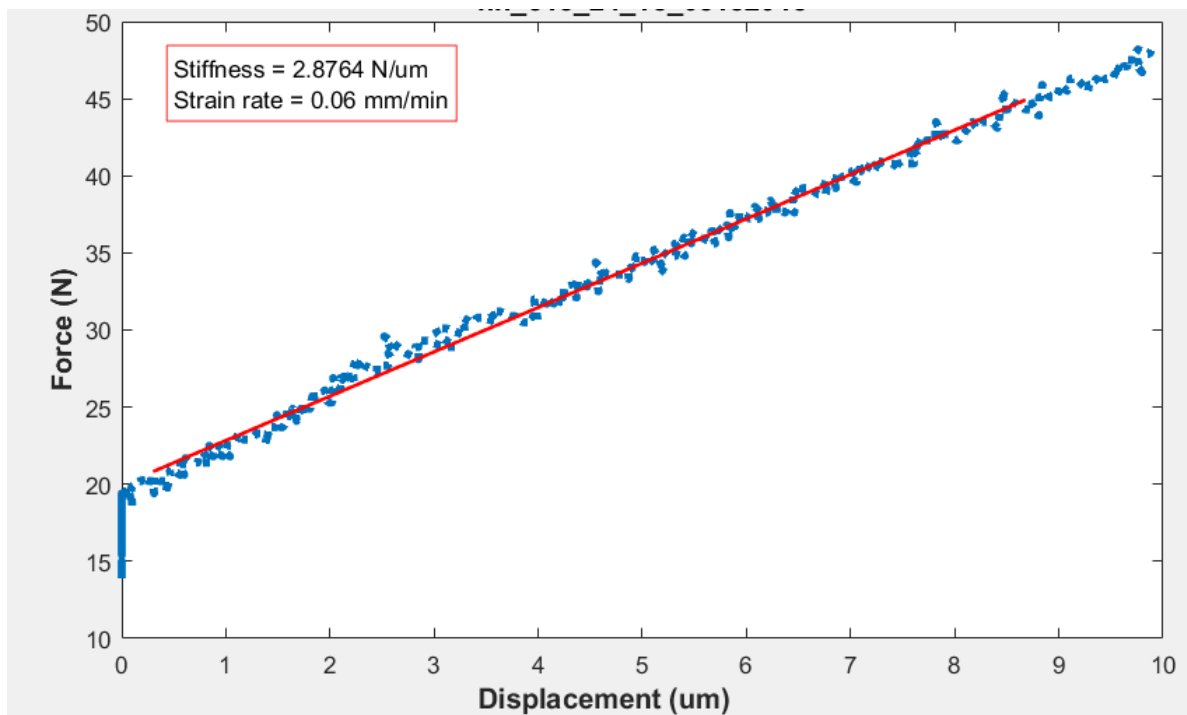
Figure C.24 - Representative force vs. displacement plot of human sample 24 during live bone study. Linear fit shown to determine bulk stiffness
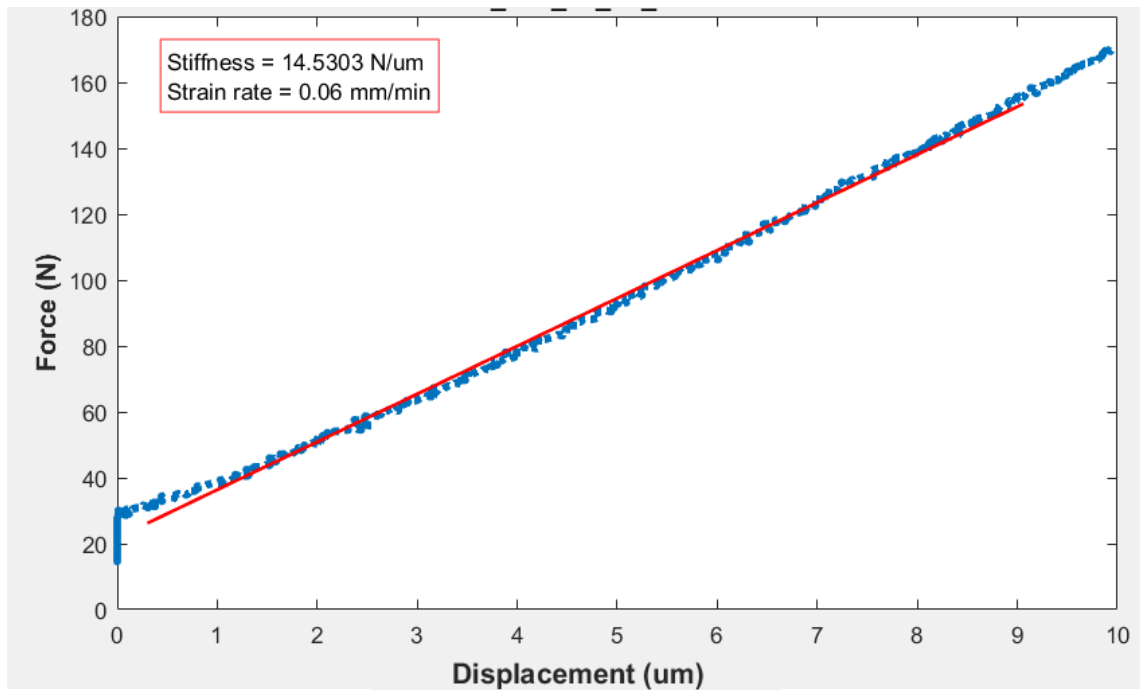
Figure C.25 - Representative force vs. displacement plot of human sample 25 during live bone study. Linear fit shown to determine bulk stiffness
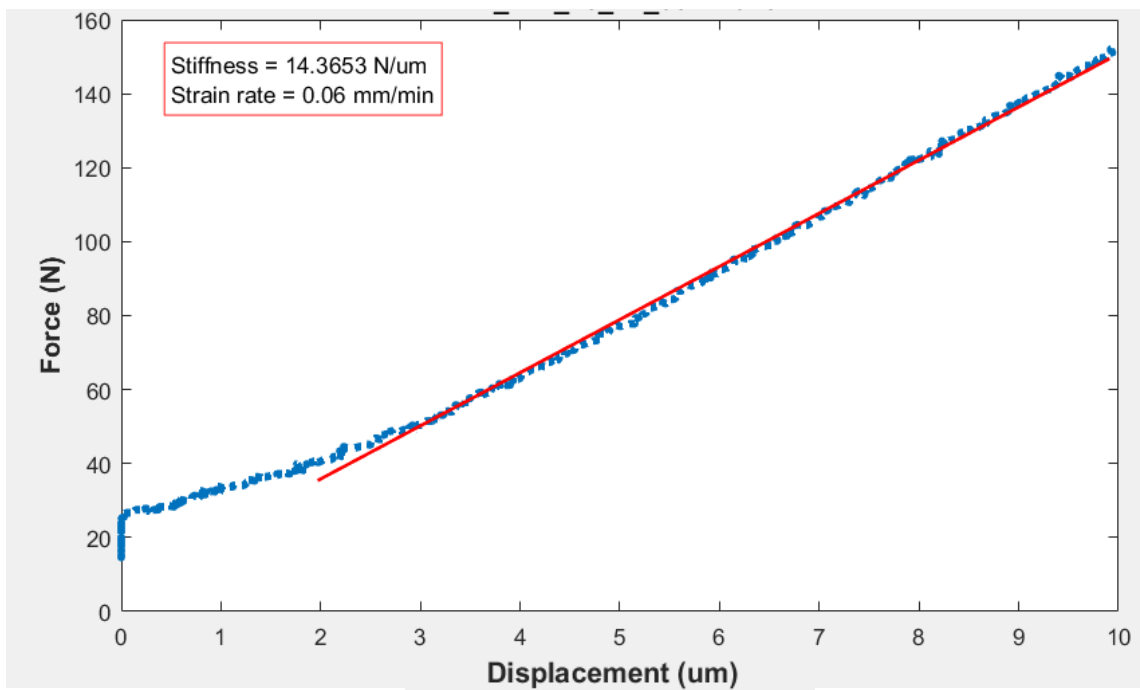
Figure C.26 - Representative force vs. displacement plot of human sample 26 during live bone study. Linear fit shown to determine bulk stiffness
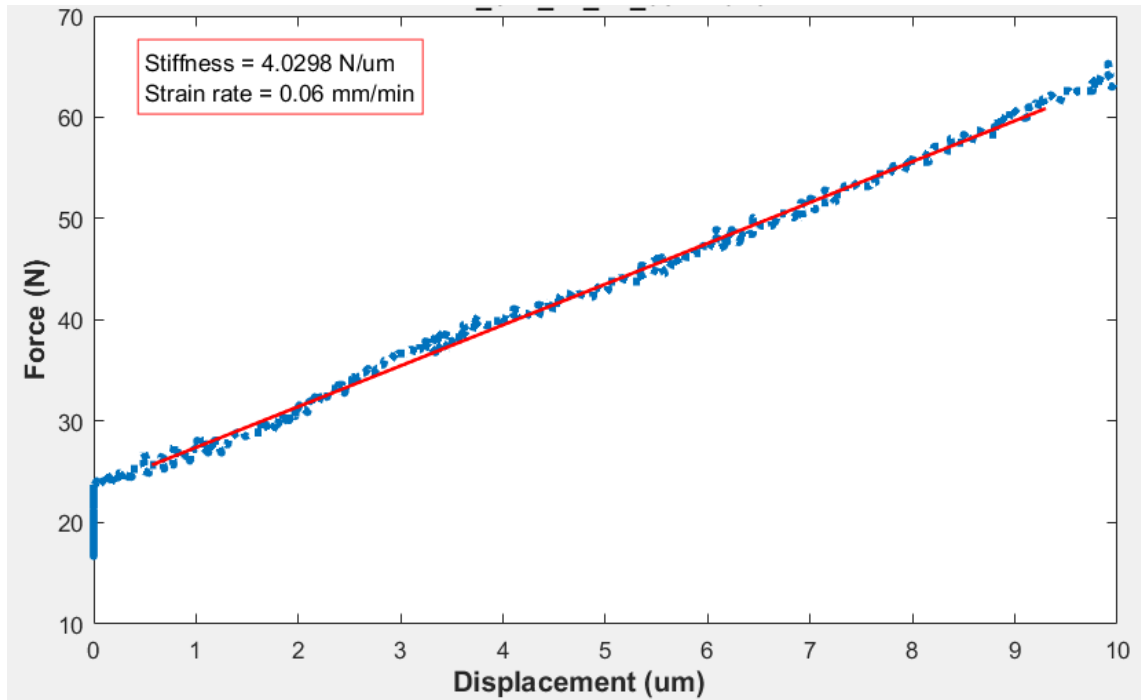
Figure C.27 - Representative force vs. displacement plot of human sample 27 during live bone study. Linear fit shown to determine bulk stiffness
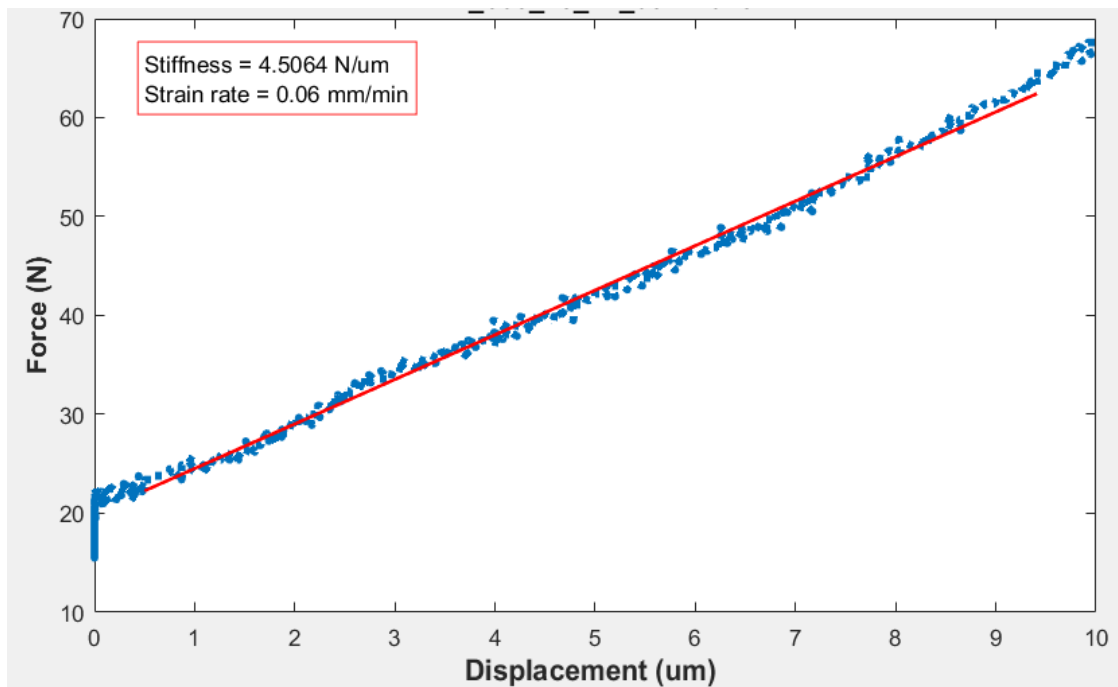
Figure C.28 - Representative force vs. displacement plot of human sample 28 during live bone study. Linear fit shown to determine bulk stiffness
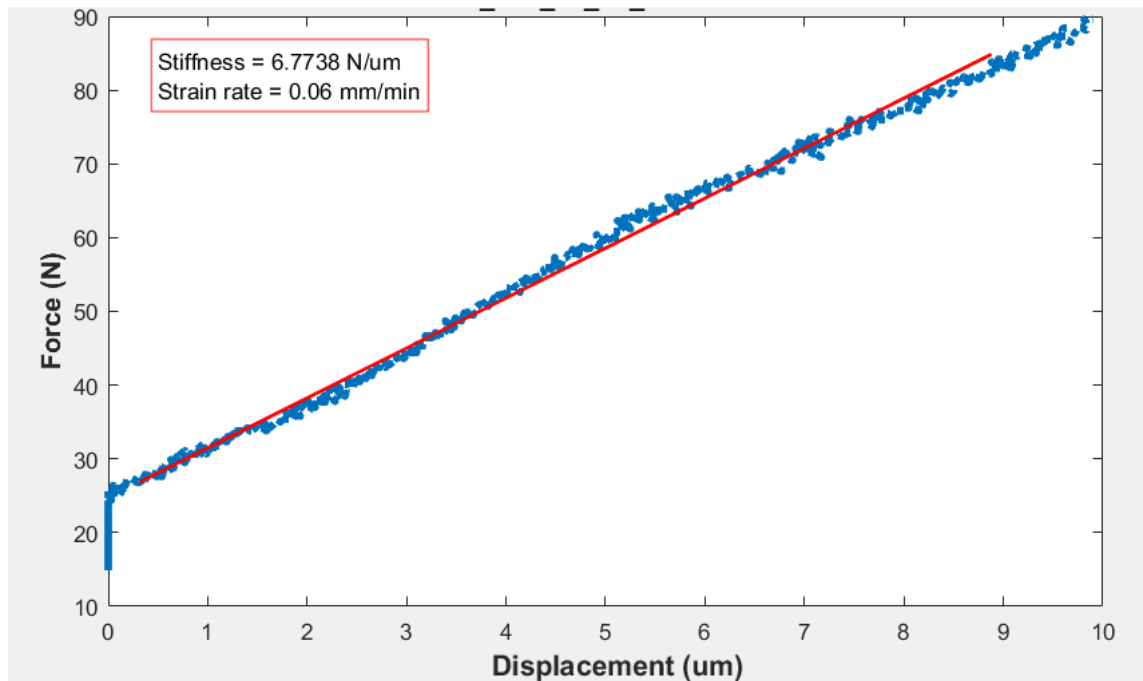
Figure C.29 - Representative force vs. displacement plot of human sample 29 during live bone study. Linear fit shown to determine bulk stiffness
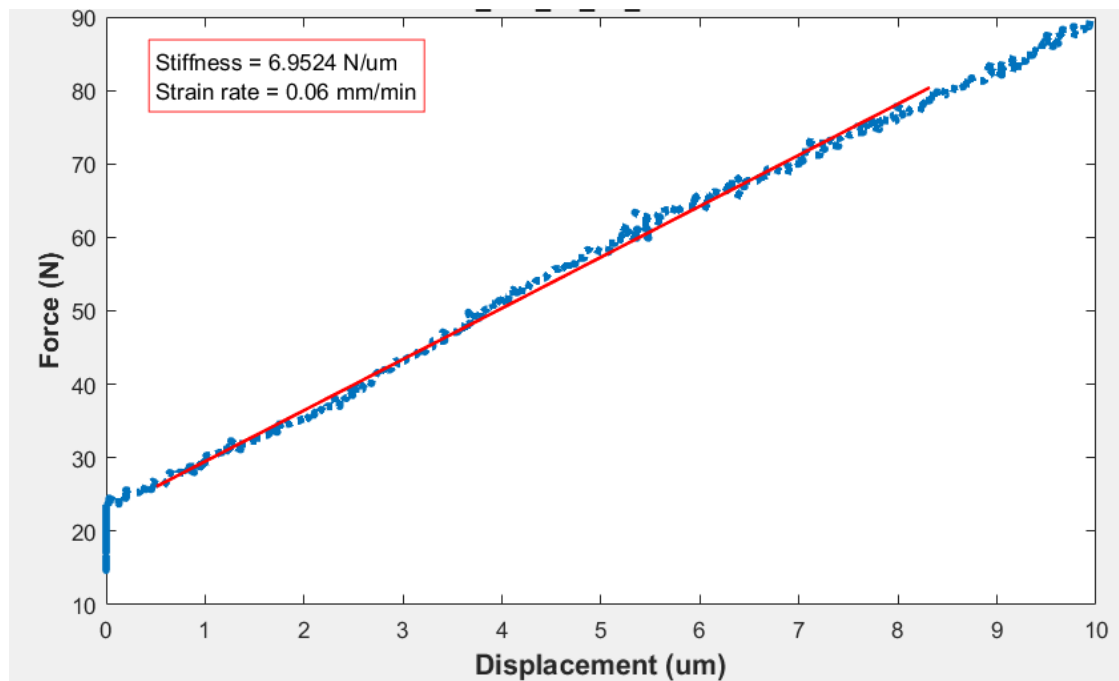
Figure C.30 - Representative force vs. displacement plot of human sample 30 during live bone study. Linear fit shown to determine bulk stiffness
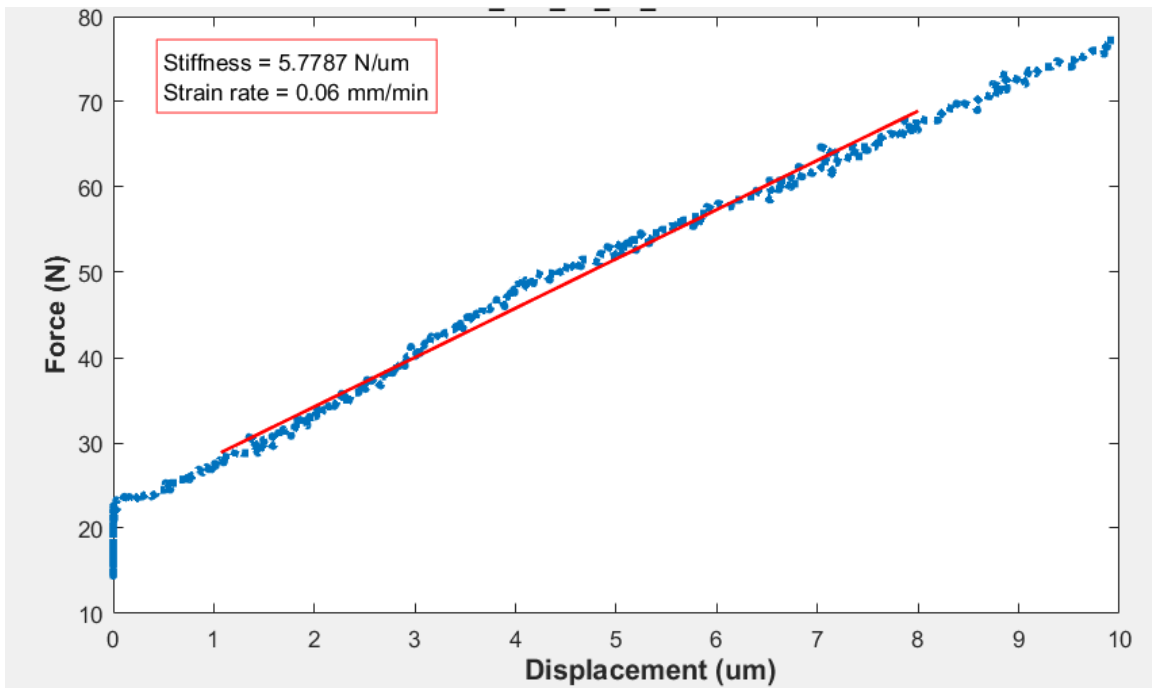
Figure C.31 - Representative force vs. displacement plot of human sample 31 during live bone study. Linear fit shown to determine bulk stiffness
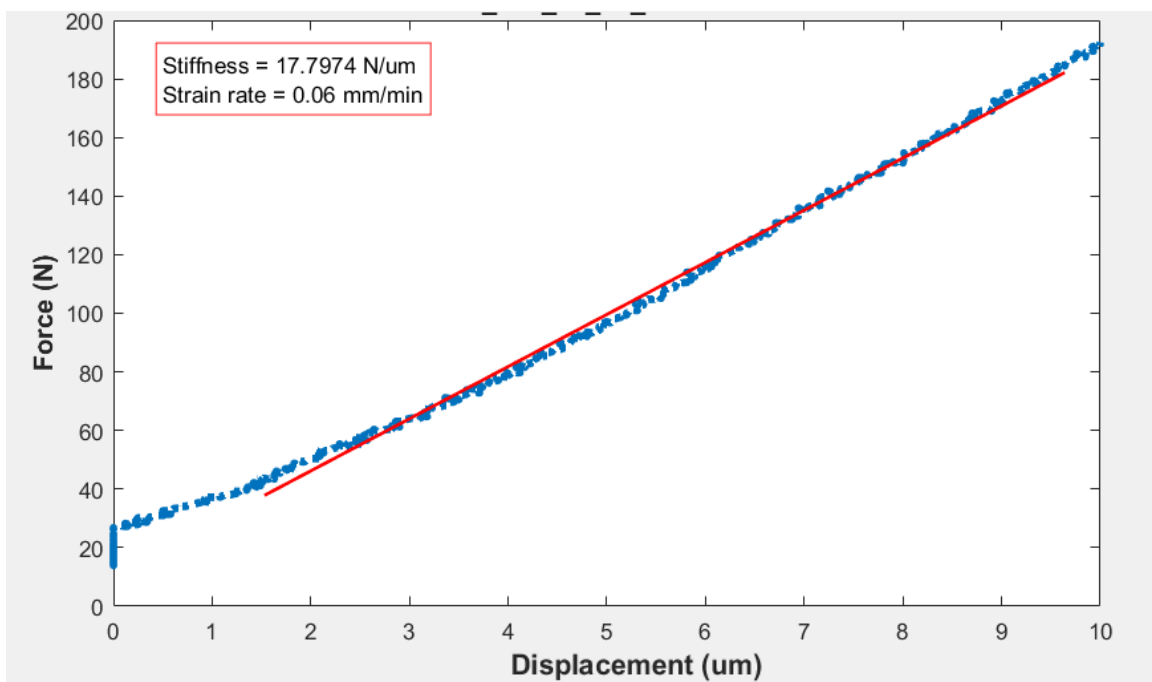
Figure C.32 - Representative force vs. displacement plot of human sample 32 during live bone study. Linear fit shown to determine bulk stiffness
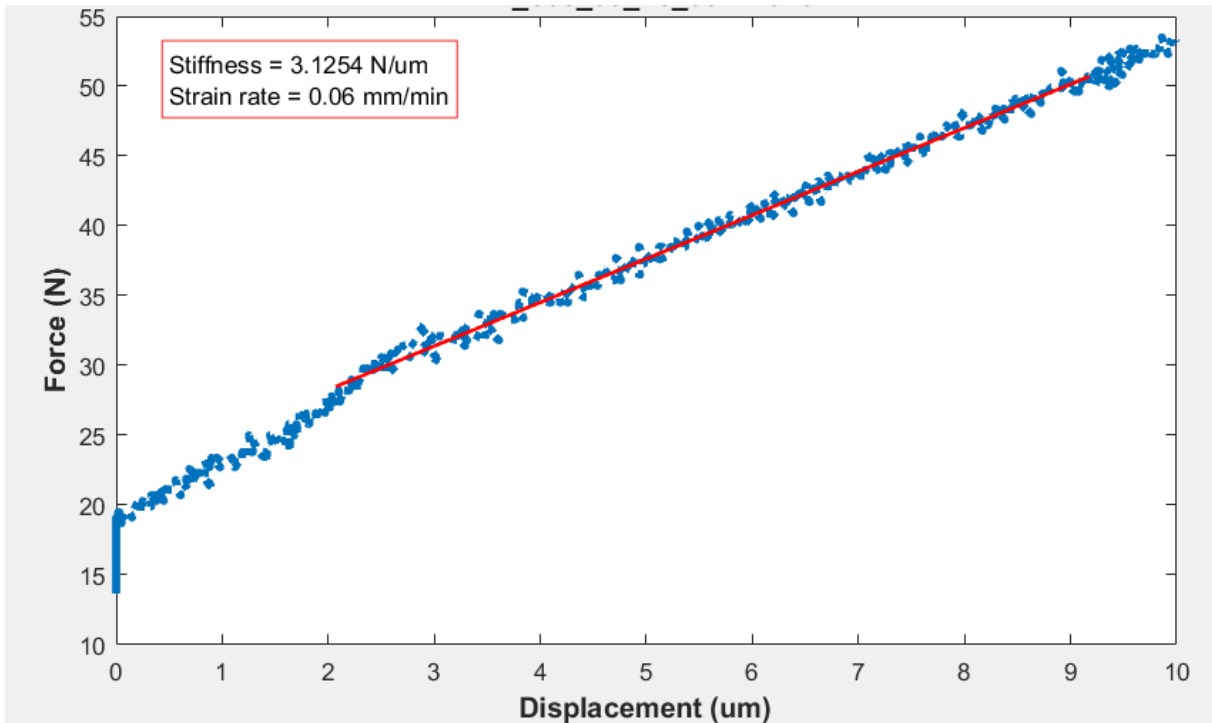
Figure C.33 - Representative force vs. displacement plot of human sample 33 during live bone study. Linear fit shown to determine bulk stiffness
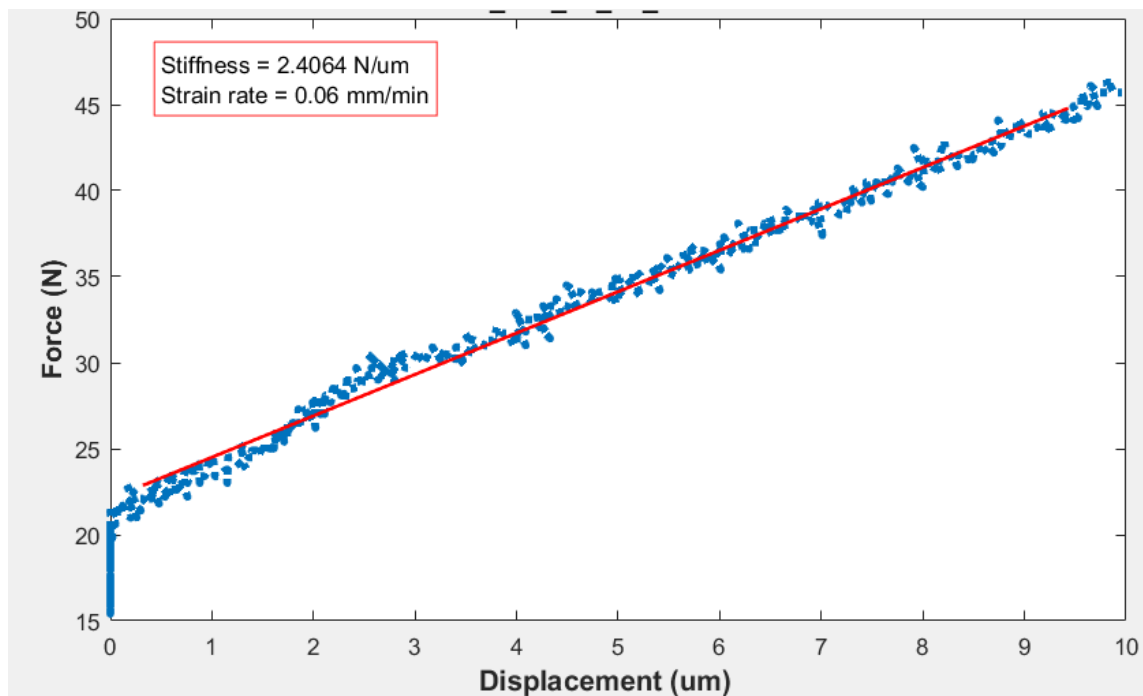
Figure C.34- Representative force vs. displacement plot of human sample 34 during live bone study. Linear fit shown to determine bulk stiffness
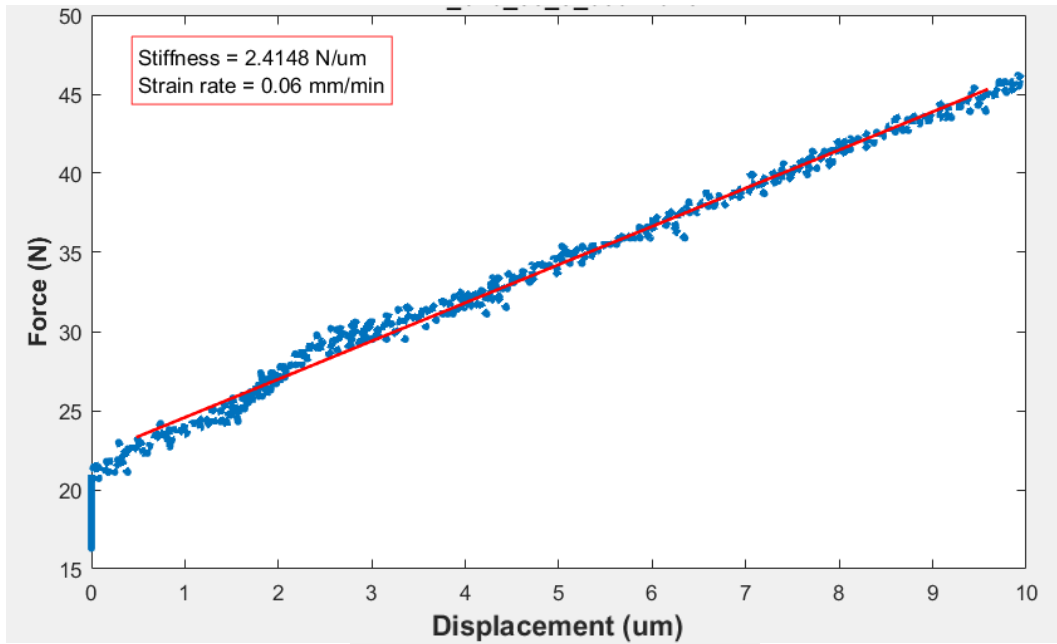
Figure C.35 - Representative force vs. displacement plot of human sample 35 during live bone study. Linear fit shown to determine bulk stiffness
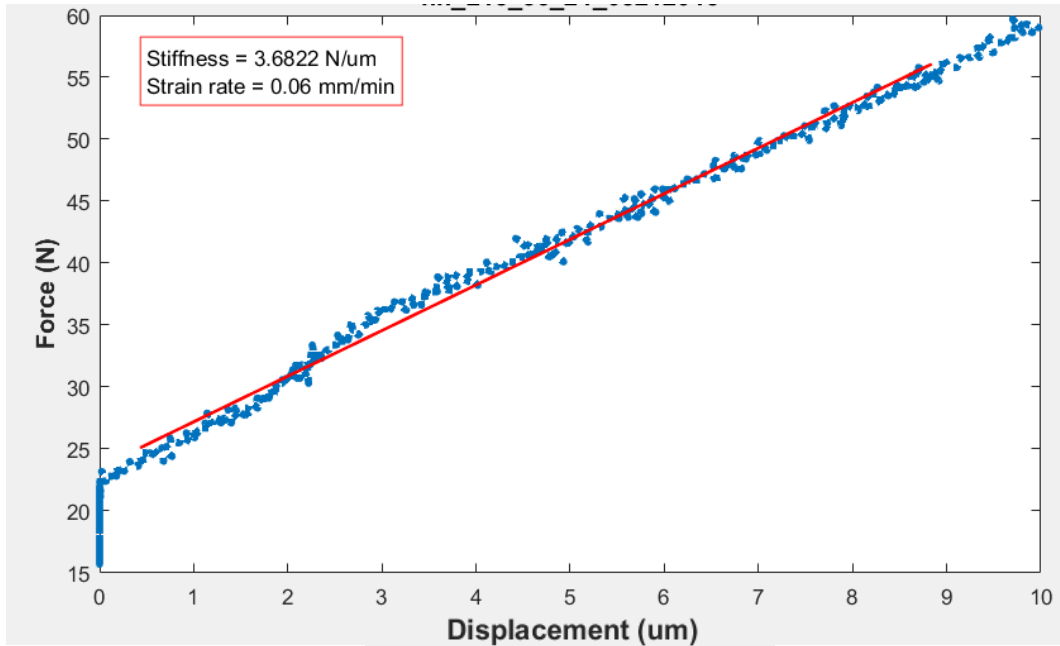
Figure C.36 - Representative force vs. displacement plot of human sample 36 during live bone study. Linear fit shown to determine bulk stiffness
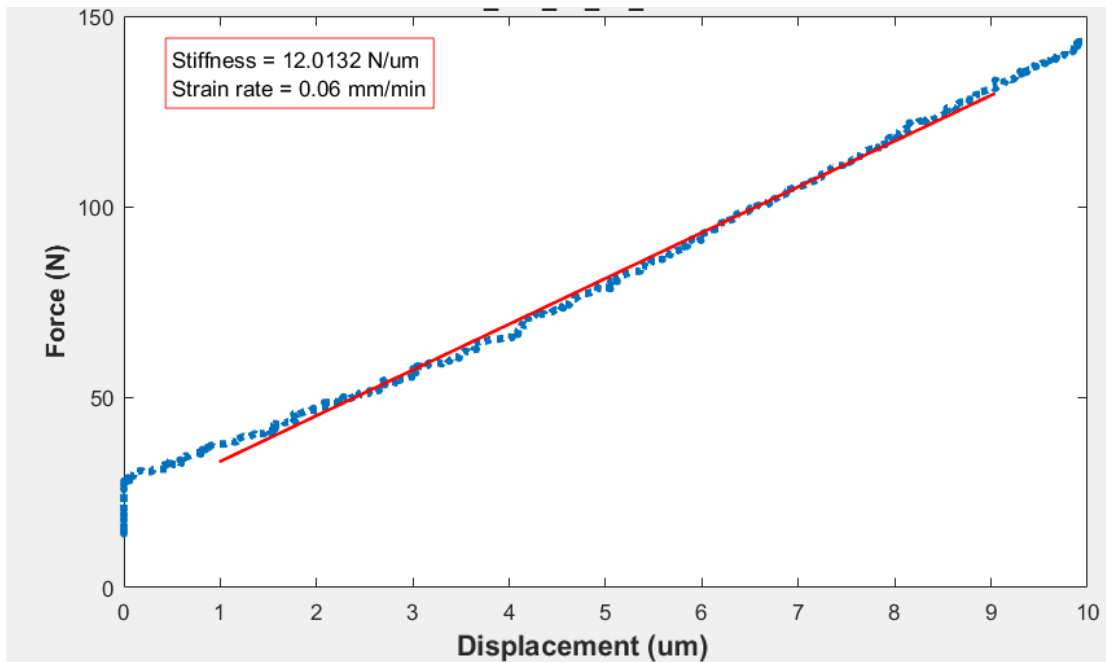
Figure C.37 - Representative force vs. displacement plot of human sample 37 during live bone study. Linear fit shown to determine bulk stiffness
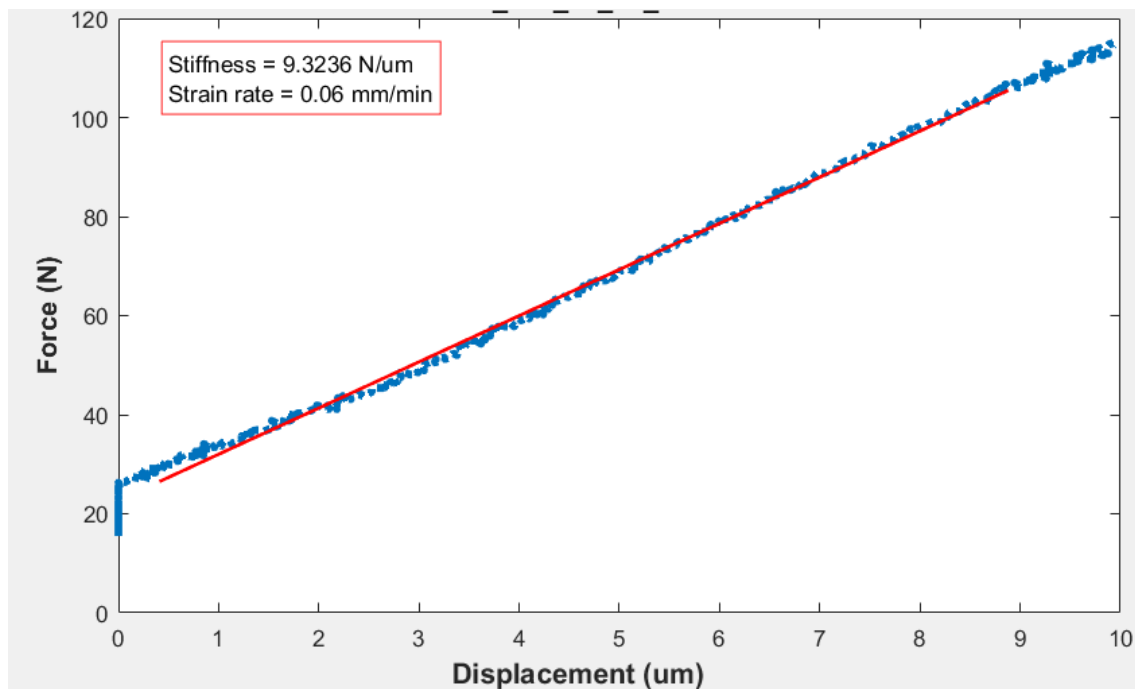
Figure C.38 - Representative force vs. displacement plot of human sample 38 during live bone study. Linear fit shown to determine bulk stiffness
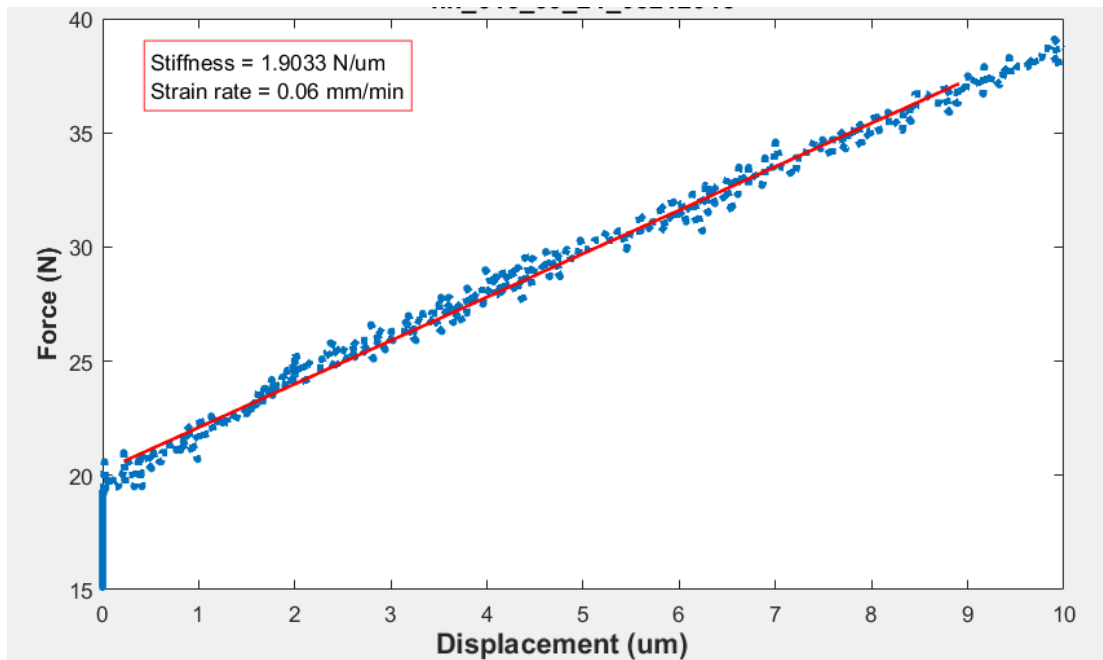
Figure C.39 - Representative force vs. displacement plot of human sample 39 during live bone study. Linear fit shown to determine bulk stiffness
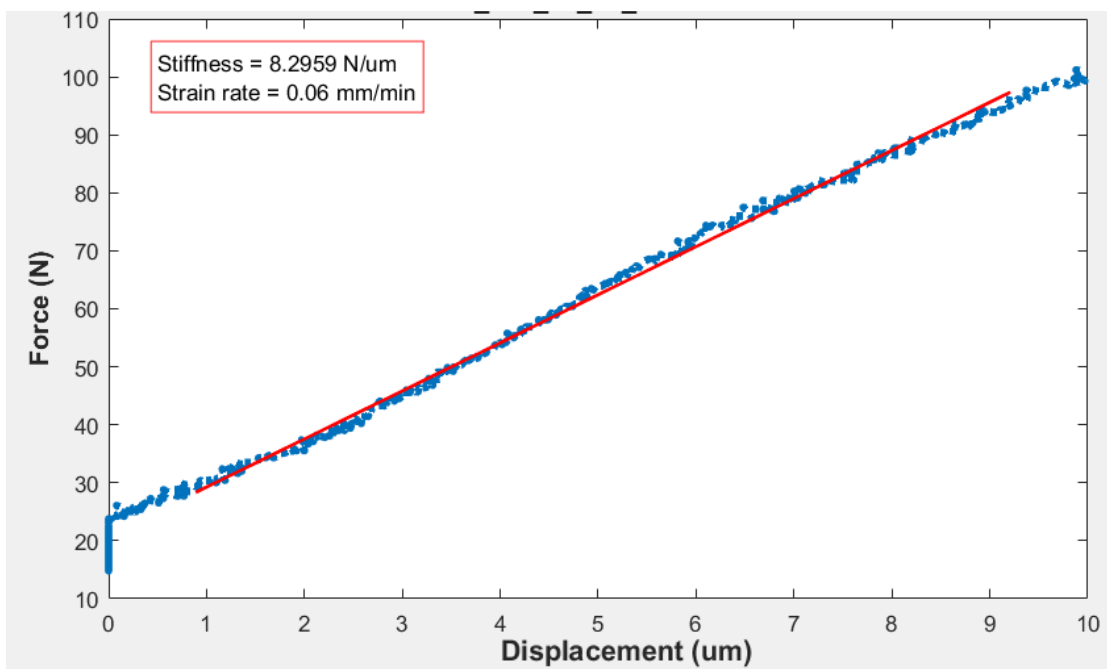
Figure C.40 - Representative force vs. displacement plot of human sample 40 during live bone study. Linear fit shown to determine bulk stiffness
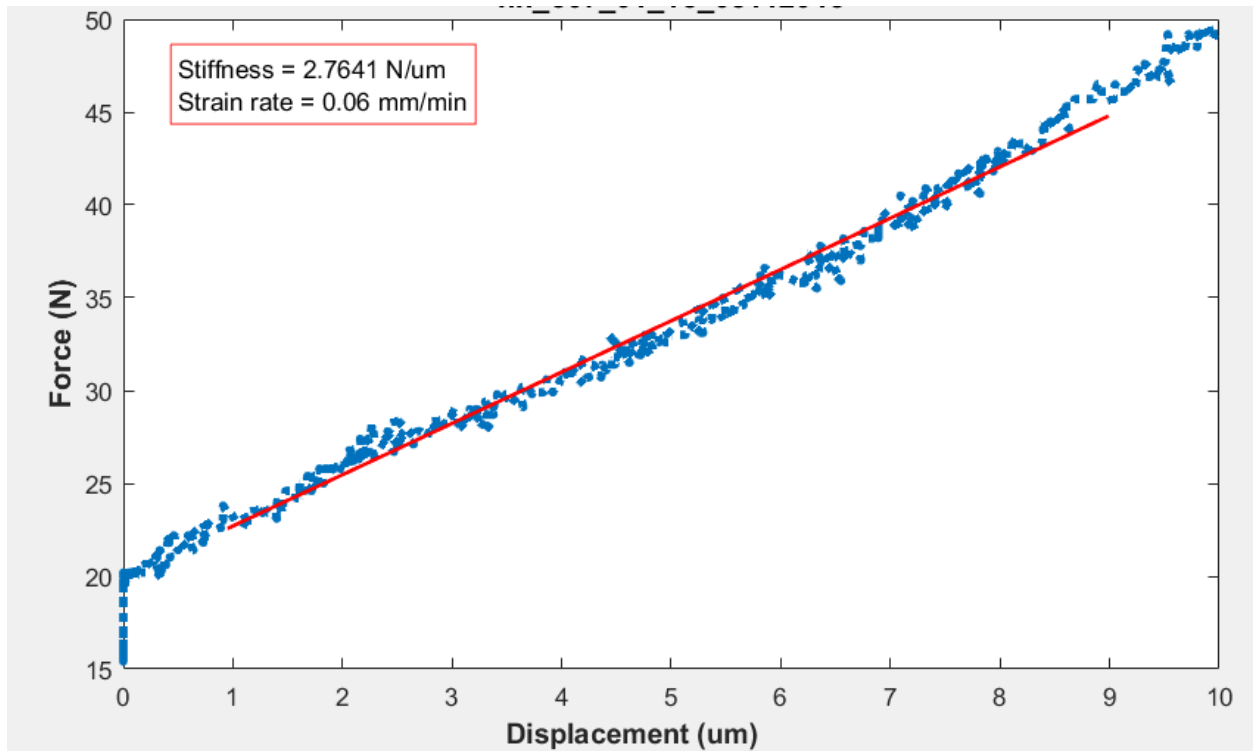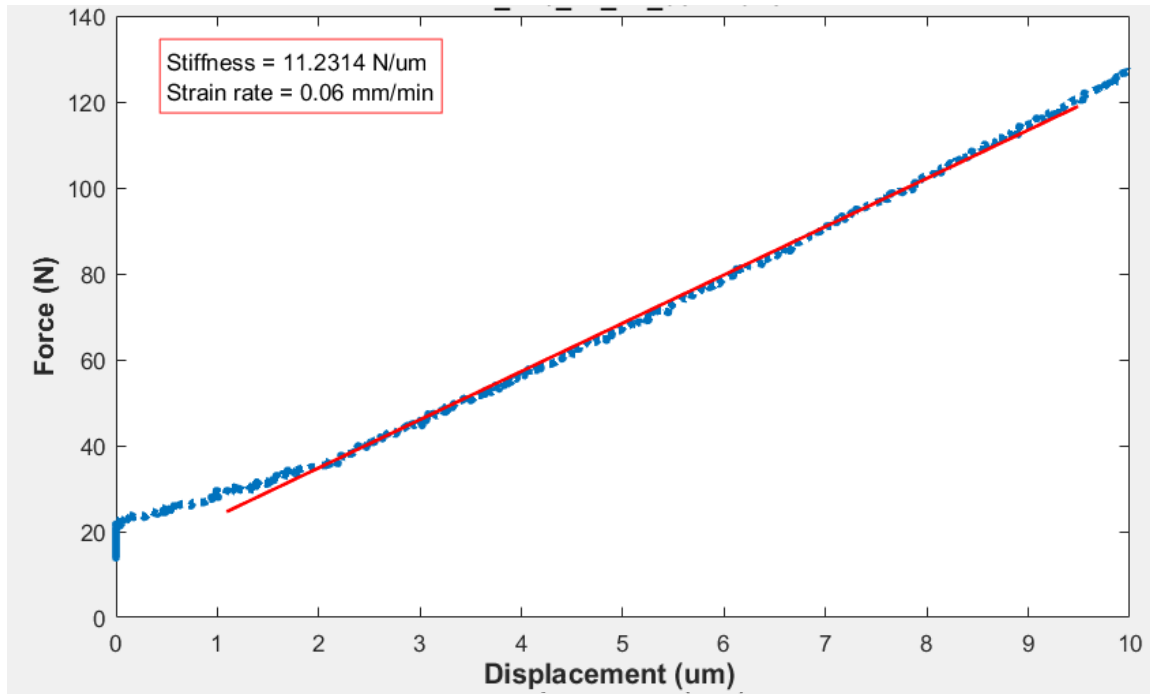
Figure C.41 - Representative force vs. displacement plot of human sample 41 during live bone study. Linear fit shown to determine bulk stiffness
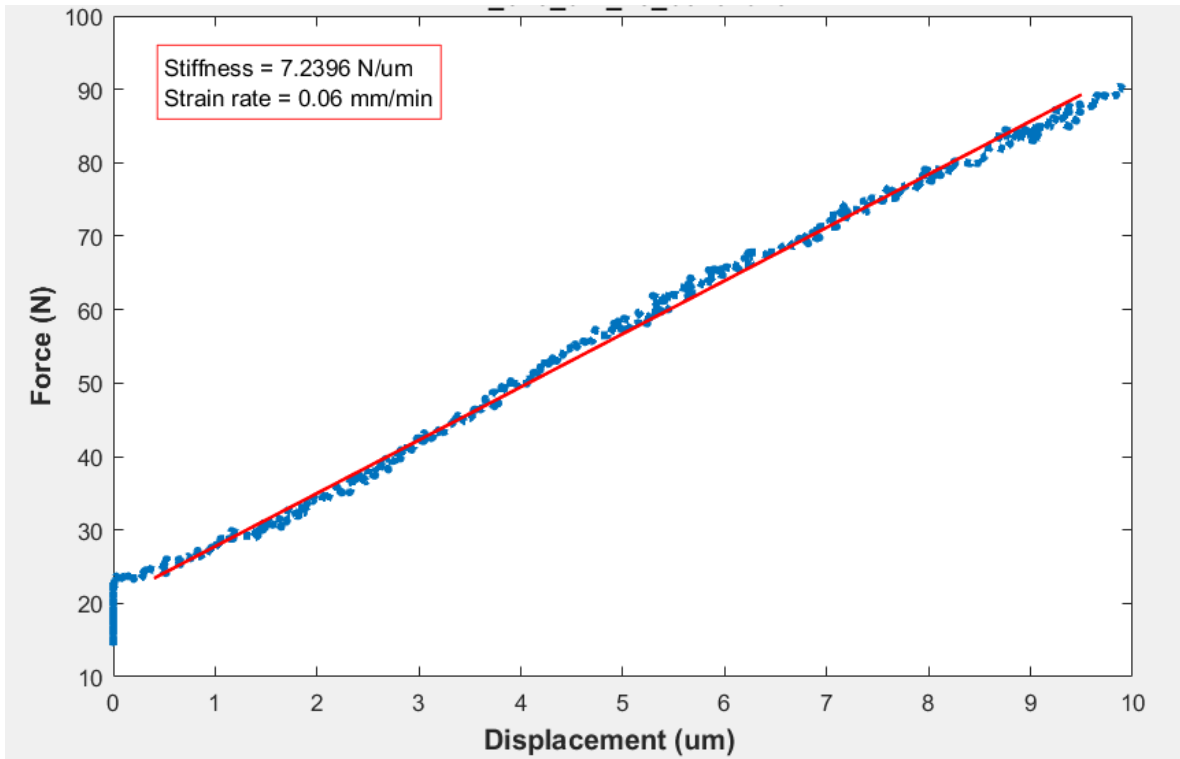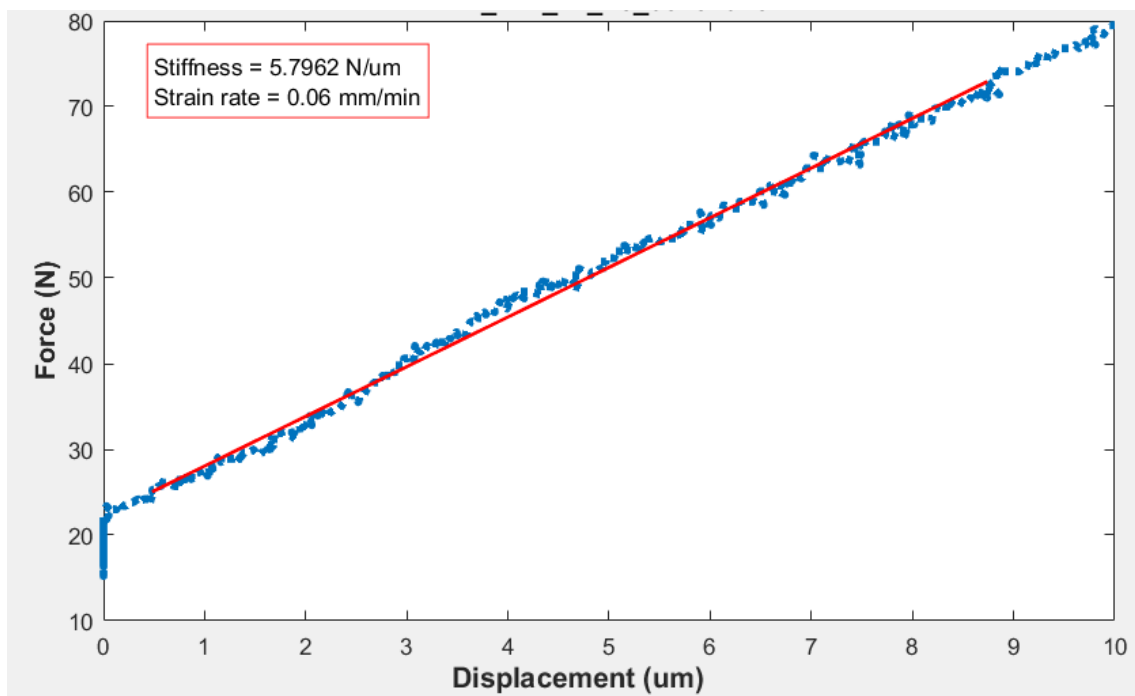

Figure C.42 - Representative force vs. displacement plot of human sample 42 during live bone study. Linear fit shown to determine bulk stiffness
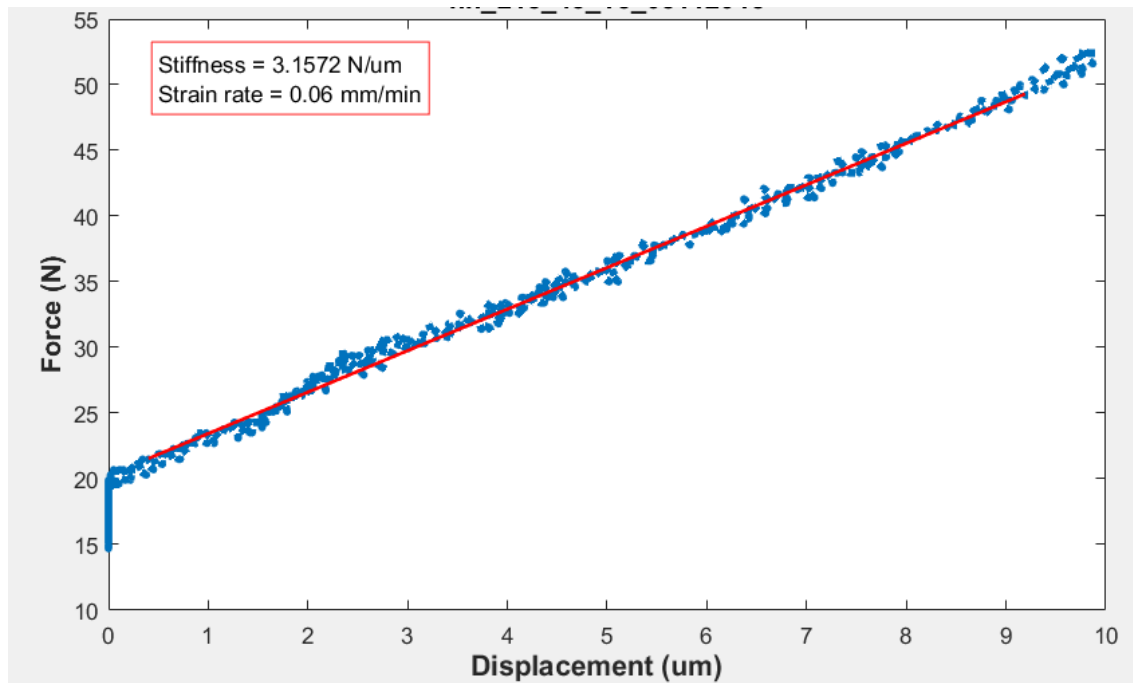
Figure C.4315 - Representative force vs. displacement plot of human sample 42 during live bone study. Linear fit shown to determine bulk stiffness
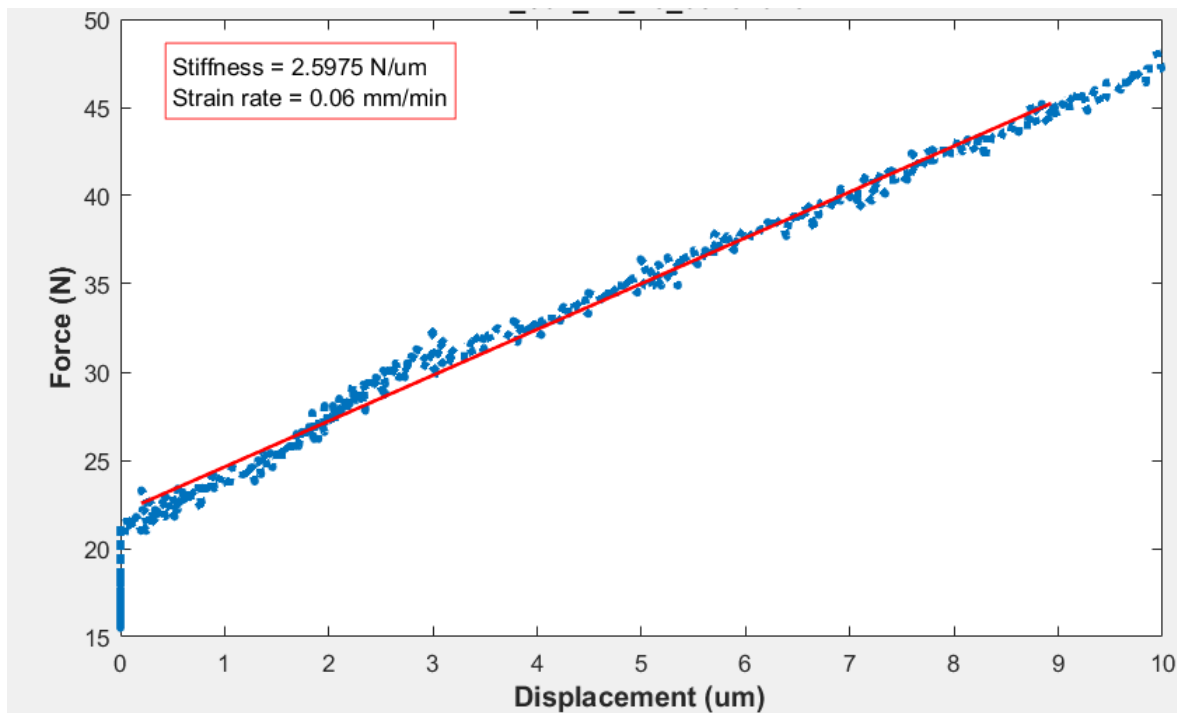
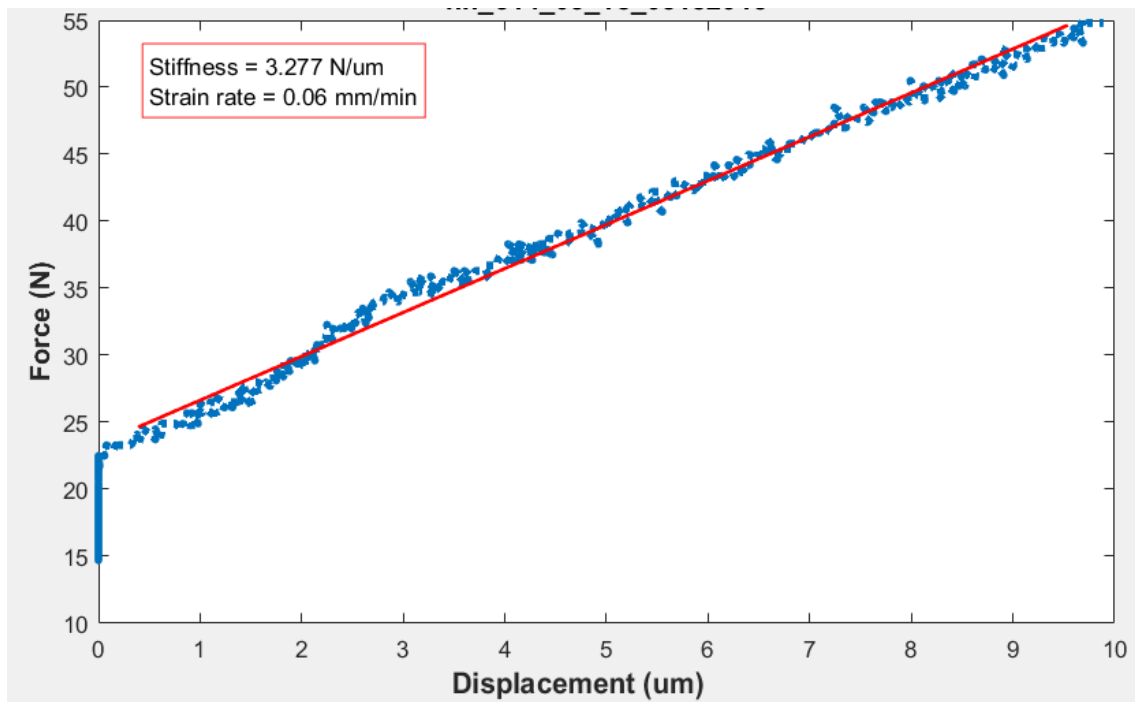
Figure C.44 - Representative force vs. displacement plot of human sample 44 during live bone study. Linear fit shown to determine bulk stiffness
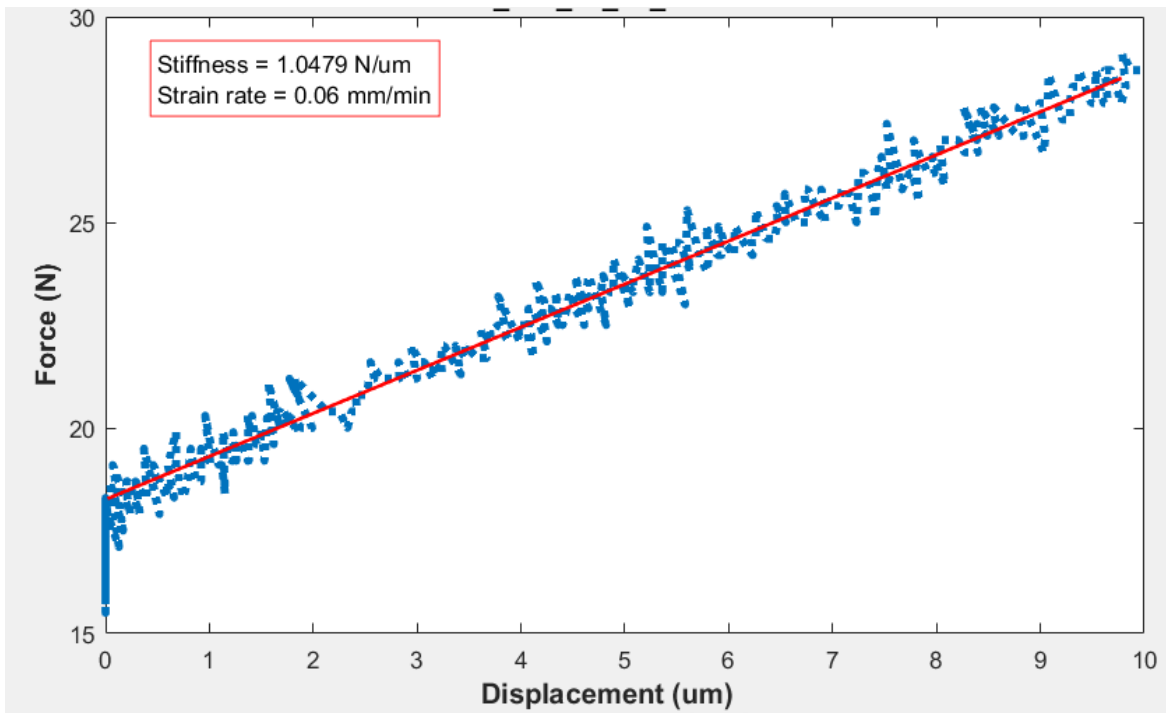
Figure C.45 Representative force vs. displacement plot of human sample 45 during live bone study. Linear fit shown to determine bulk stiffness
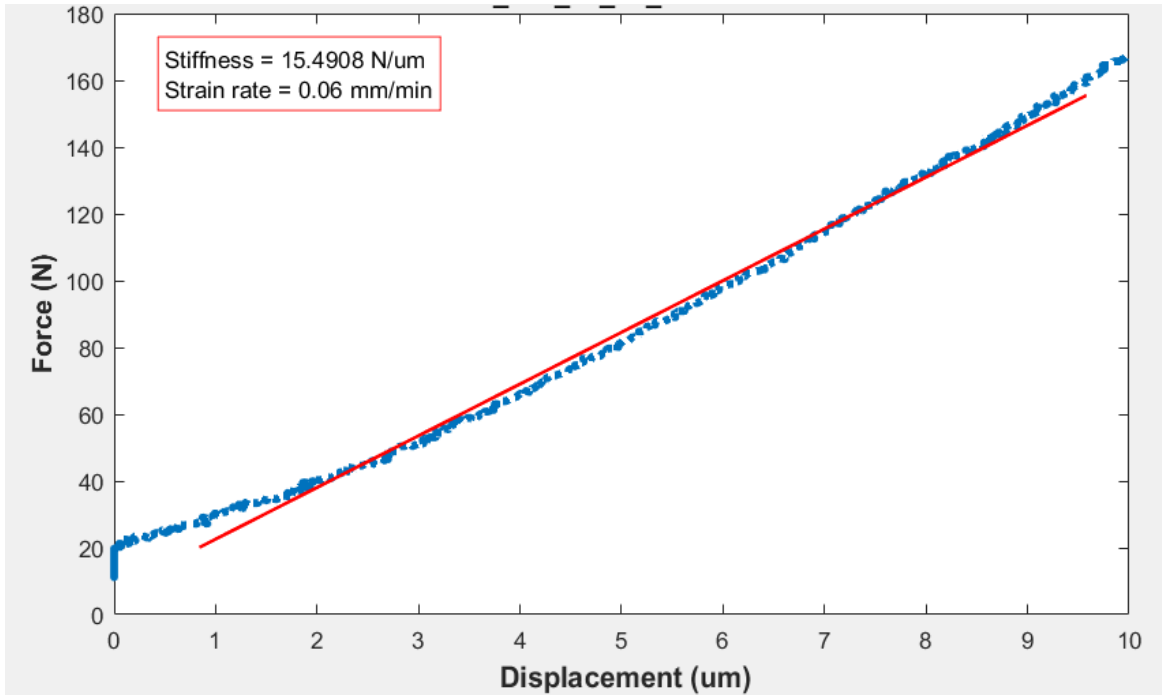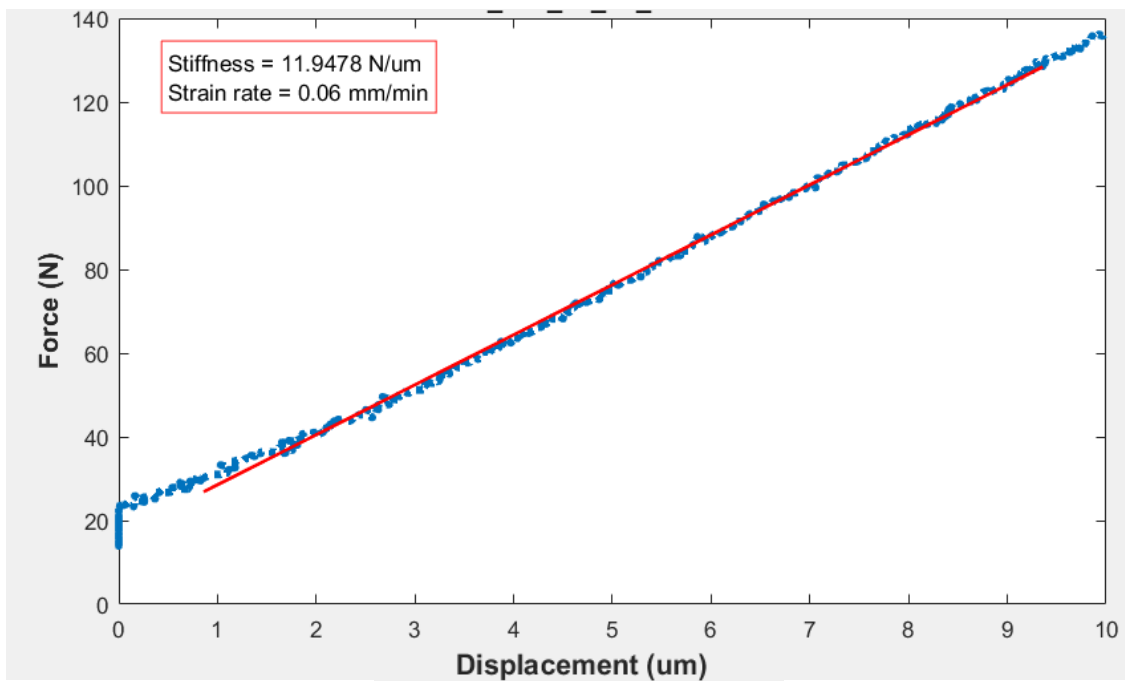

Figure C.46 - Representative force vs. displacement plot of human sample 46 during live bone study. Linear fit shown to determine bulk stiffness
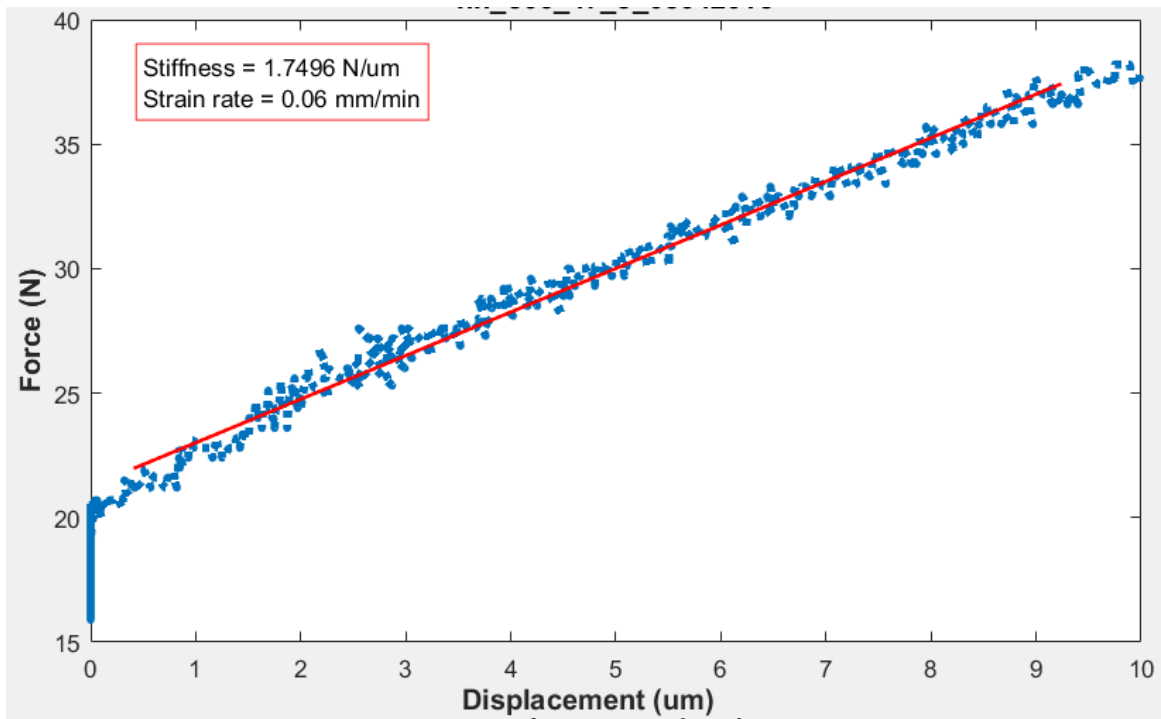
Figure C.4716 - Representative force vs. displacement plot of human sample 47 during live bone study. Linear fit shown to determine bulk stiffness
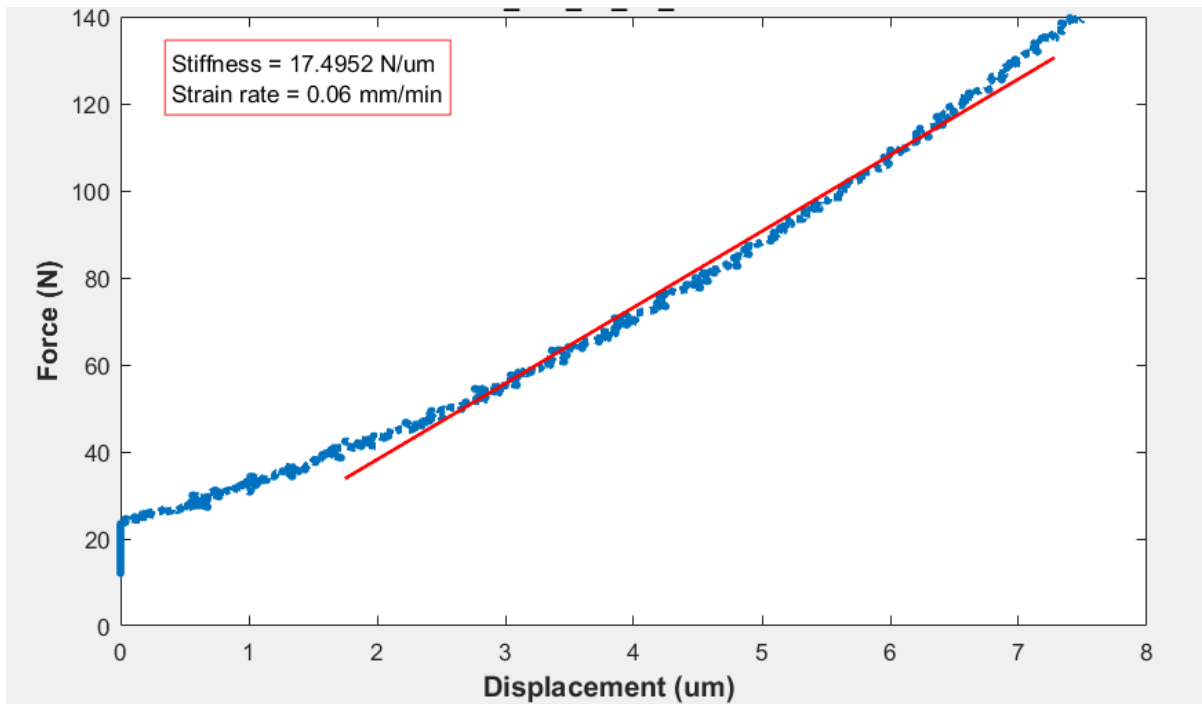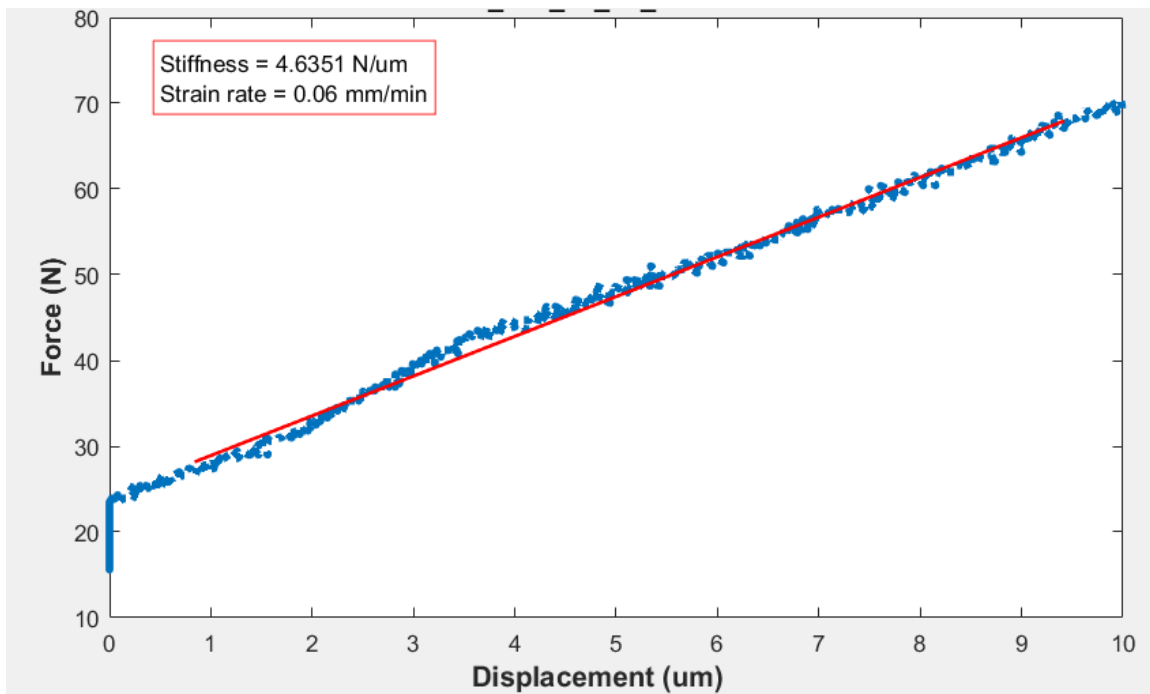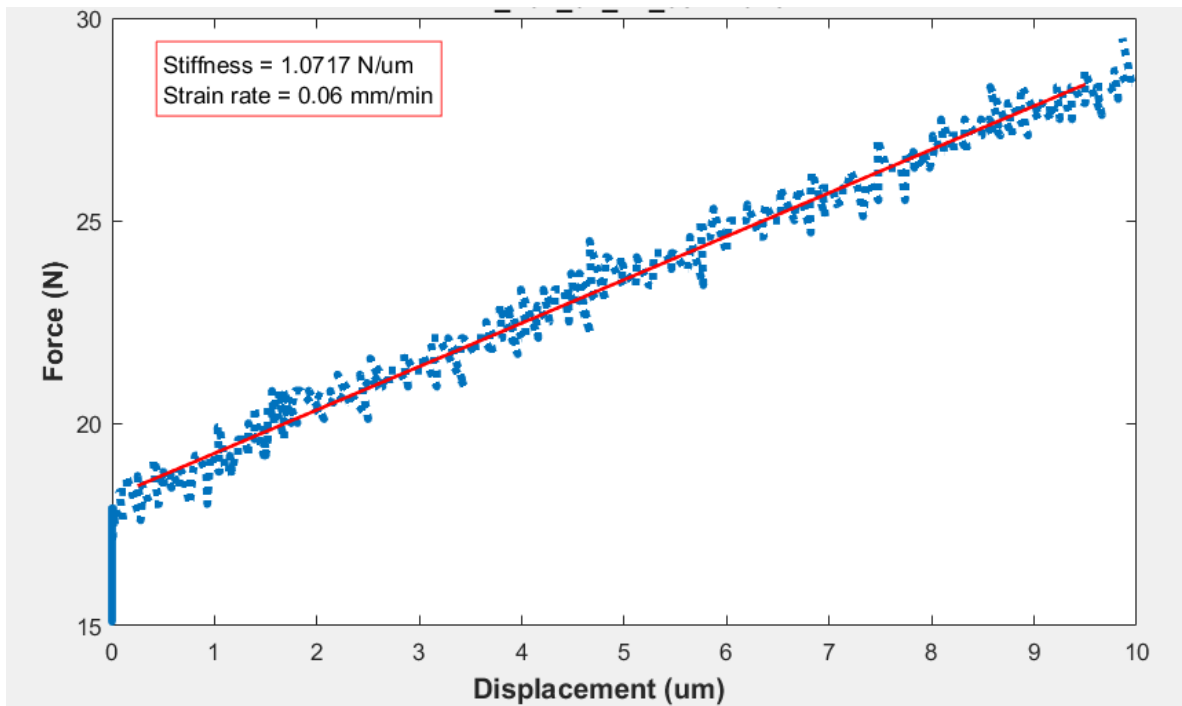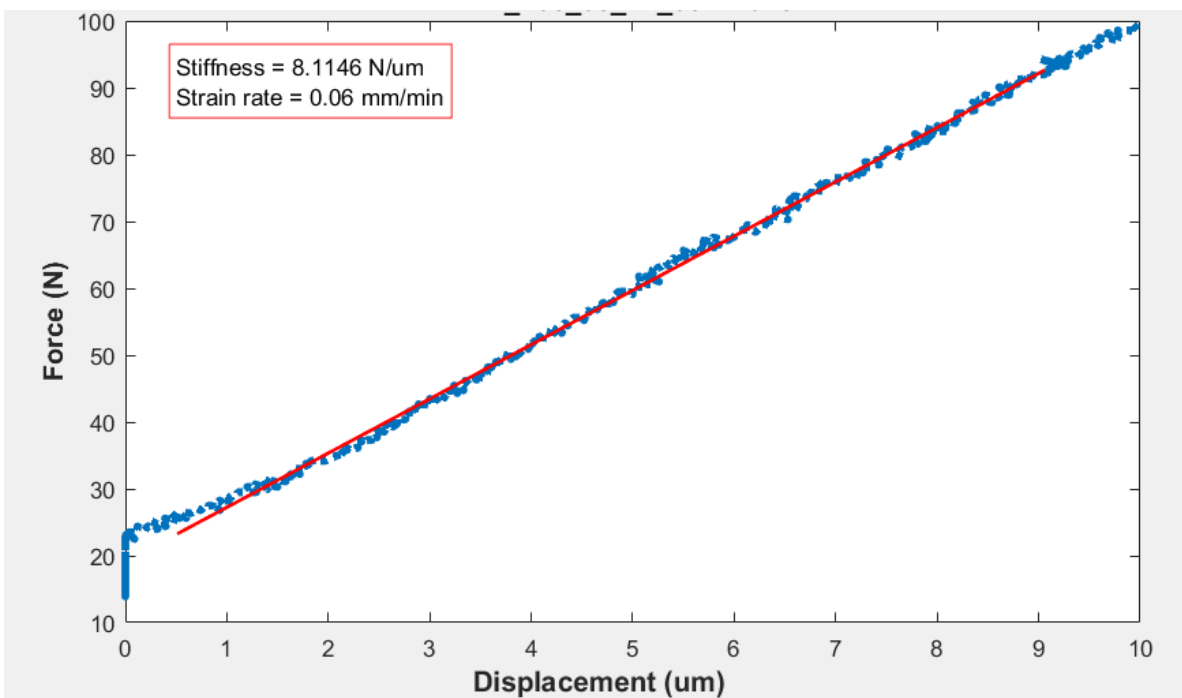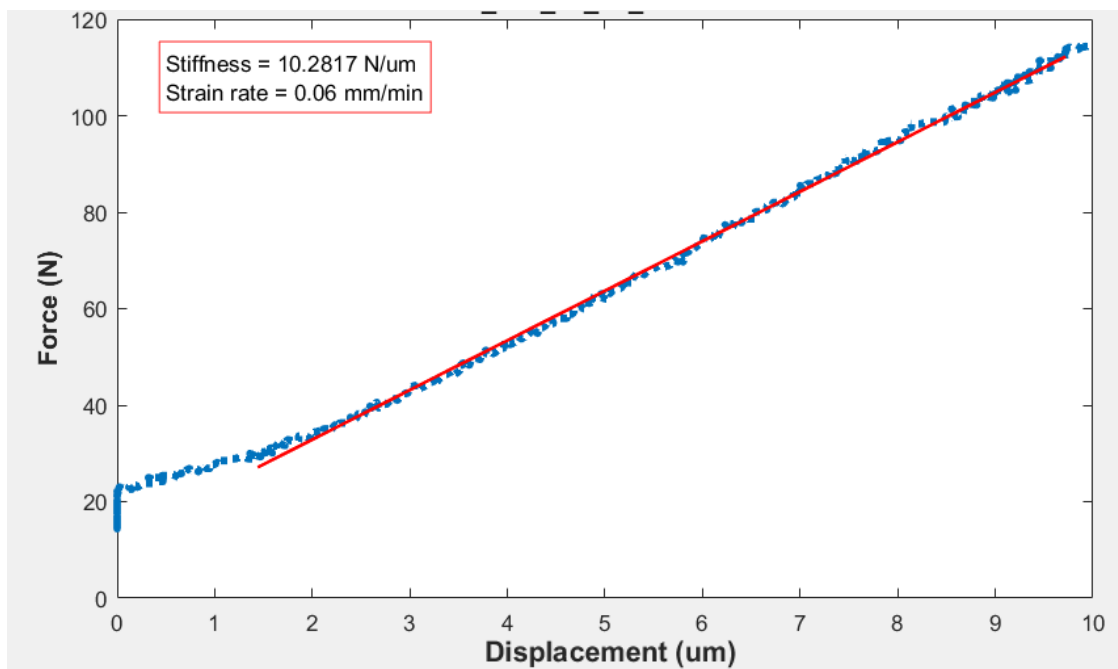

Figure C.48s17 - Representative force vs. displacement plot of human sample 48 during live bone study. Linear fit shown to determine bulk stiffness

Appendix D

D. Protocol for Analysis and Modeling of Bone Tissue

D.1 Segmentation in Mimics

1. Obtain DICOM type files for CT scanning images

2. Start new project by selecting "New Project Wizard"

3. Import DICOM file into Mimics (Materialise, Leuven, Belgium)

   - *File → Import Images*

   - Select appropriate folder and advance through screens

4. Assign orientation of object within the newly imported image

5. To improve visual rendering of the scan object, adjust the slider contrast controls

6. Section scanned object

   - Create profile line by selecting "Profile Line" icon

   - Use the pencil tool to draw a line through the object, making sure to include points from

     different grayscales

   - Select *"Scale to fit"* once profile line menu appears

   - Select "*Start thresholding"* and adjust threshold to isolate features of interest

   - Repeat process as necessary to obtain masks for different features (e.g. bone, fat, osteoid)

7. Refine masks

   - Implement *Region Growing*, *Edit Mask*, or *Morphology Operations* to refine existing

     masks

8. Obtain volume for each mask to determine ratios of feature components (e.g. osteoid to bone)

9. Obtain dimensions of scanned object

- Use *diameter* and *distance* functions to determine appropriate dimensions

10. Generate 3D volume for masks

   - Select "*Calculate 3D*" icon

   - Select desired mask, select "*optimal*" quality, and click "*calculate*"

D.2 Morphological Analysis in ImageJ

1. Download BoneJ plugin for ImageJ

2. Load CT images

   - *File → Import → Image Sequence*

   - Select appropriate folder containing DICOM images

   - Fill in appropriate information within the "*Sequence Options*" pop-up menu and select "*Sort names numerically*"

3. Adjust color scheme in view port if necessary

   - *Image → Adjustment → Threshold*

   - Click "*apply*" once appropriate adjustments have been made

4. An additional screen to "Convert Stack to Binary" will appear. Uncheck "*Calculate threshold for each image"* and select "*OK*."

5. Isolate features of interest by using selection tools

   - Scroll through slices to determine boundaries for features

   - Select "*Duplicate*" to create a copy stack. Title the stack appropriately and list the range of slices for the duplicate stack

   - Check "*Duplicate Stack*" and select "*OK*"

6. Analyze parameters of interest from duplicate stack

   - Determine Anisotropy

    i.   Select "*Auto Mode*" and check "*Record Eigens.*" Click "*OK.*" Results will appear in a new window.

    ii.   Use eigen vectors to determine the degree of anisotropy. Determine rotation of core by selecting "*rotation*" icon.

    iii.   Use the *dot product* and *magnitude* of eigen vectors to determine angle between vectors.

- Determine connectivity

    i.   "*Purify*" the duplicate stack

    ii.   Select "*Connectivity*" operation

- Determine Structural Model Index

    i.   Select "*Structural Model Index*" function

    ii.   Select "*Hildebrand & Ruegsegger*" as the *SMI Method*, enter "6" for *Voxel resampling*, and "0.5" for *Mesh smoothing*.

    iii.   Click "*OK*"

- Determine Thickness and Spacing

    i.   Select "*Thickness*" and "*Spacing*" in morphology prompt.

    ii.   Click "*OK*"

- Determine volume fractions

    i.   Select "*volume fraction*" function

    ii.   Ensure that the *Algorithm* is set to "*Voxel*" and *Surface and resampling* is set to "6."

    iii.   Check "*Use ROI manager*" within the prompt

Appendix E

E. Matlab Code for Determining K_{axial} from Force vs. Displacement

```
function find_Stiffness

    [infile, inpath]=uigetfile('*.txt','Select machine compliance input file'); %user selects file to be analyzed

    data=load([inpath infile]); %load the raw data

%    sampfreq = (rawdata(2,2)-rawdata(1,2))^-1; %FREQUENCY OF DATA COLLECTION

%    cutoff = .51; %used to establish cut-off frequency of filter

%    [B,A] = butter(6,cutoff/(sampfreq/3)); %set-up 6th order butterworth filter

%    data = filtfilt(B,A,rawdata); %filter the raw data with bidirectional filter

%

    force = data(:,1); %units = N

    disp = data(:,2); %units  = mm

    disp  = abs(min(disp))+disp; %shift the displacement so it starts at 0

    scrsz = get(0,'ScreenSize'); %captures the size of the user's screen (this may not work on some systems/monitors.
If there is a problem, comment out the next 2 lines)

    Figure('Position',[scrsz(3)/4 scrsz(4)/4 scrsz(3)/2 scrsz(4)/2]); %position the Figure in the center of the screen

     plot(disp,force,':','LineWidth',3.5);

    title(strrep(infile(1:length(infile)-4),'_','\_'),'fontsize',12,'fontweight','b'); %use strrep to replace the _ with the '\_'
so that the title appears correctly. The -4 removes the .txt from the title

    ylabel('Force (N)','fontsize',12,'fontweight','b');

    xlabel('Displacement (mm)','fontsize',12,'fontweight','b');

    hold on

    box = showinfowindow('Choose the start and endpoint of the linear region','NOTICE!!!');

    get(box,'Position');
```

```
set(box,'Position',[200 700 261 37]); %redefine position of the textbox. MAY NEED TO ADJUST BASED ON
MONITOR
    [x,y]=ginput(2); %select linear region of graph
    close(box);


    [leftpoint,d] = dsearchn(disp,x(1));%find the closest displacement value to the picked point
    [rightpoint,d] = dsearchn(disp,x(2));
    bounds = leftpoint:rightpoint;


    sample_K = polyfit(disp(bounds), force(bounds),1); %1st order curve fit on linear region of graph
    fit =  polyval(sample_K,disp(bounds)); %predictions
    dev = force(bounds) - mean(force(bounds)); %deviations, measure of spread
    SST = sum(dev.^2); %total variation to be accounted for
    resid = force(bounds) - fit; % residuals, measure of mismatch
    SSE = sum(resid.^2); % variation not accounted for
    R2 = 1- (SSE/SST); %the coefficient of determination


    h = plot(disp(leftpoint:rightpoint),
sample_K(1)*disp(leftpoint:rightpoint)+sample_K(2),'LineWidth',1.5,'Color','red'); %plot the curve fit


    r =(['R^2 = ' num2str(R2)]);
    h1 = textul(r,0.1); %write the R^2 value directly within the graph
    button_done=0;
    while button_done==0;
        button = questdlg('Is this curve fit accepTable?','User Action Required','Yes', 'No','Yes'); %generates user
prompt on screen. USES FUNCTION 'SHOWINFOWINDOW', IT MUST BE WITHIN THE WORKING
DIRECTORY
```

```matlab
switch button

    case 'Yes'

        button_done=1;

        appK = sample_K(1)*10^-3; %the apparent modulus

        delete(h1); %remove the R^2 value from the graph

    case 'No';

        delete(h);

        delete(h1);

        box = showinfowindow('Choose the start and endpoint of the linear region','NOTICE!!!');

        get(box,'Position');

        set(box,'Position',[200 700 261 37]); %redefine position of the textbox. MAY NEED TO ADJUST
BASED ON MONITOR

        [x,y]=ginput(2); %select linear region of graph

        close(box);


        [leftpoint,d] = dsearchn(disp,x(1));%find the closest displacement value to the picked point

        [rightpoint,d] = dsearchn(disp,x(2));

        bounds = leftpoint:rightpoint;


        sample_K = polyfit(disp(bounds), force(bounds),1); %1st order curve fit on linear region of graph

        fit =  polyval(sample_K,disp(bounds)); %predictions

        dev = force(bounds) - mean(force(bounds)); %deviations, measure of spread

        SST = sum(dev.^2); %total variation to be accounted for

        resid = force(bounds) - fit; % residuals, measure of mismatch

        SSE = sum(resid.^2); % variation not accounted for

        R2 = 1- (SSE/SST); %the coefficient of determination
```

```
        appK = sample_K(1); %the apparent modulus

        h = plot(disp(leftpoint:rightpoint),
sample_K(1)*disp(leftpoint:rightpoint)+sample_K(2),'LineWidth',1.5,'Color','red');

        r =(['R^2 = ' num2str(R2)]);

        h1 = textul(r,0.1); %write the R^2 value directly within the graph

    end

end


%    K = ((1/appK)-((1/5.2161)+(1/62.8931)+(1/62.8931)))^-1; %account for the compliance of the machine and
sapphires used to test the specimen
%    K = ((1/appK)-(1/5.2161))^-1; %account for the compliance of the machine used to test the specimen. This will
change based on the MTS frame used!!
K = ((1/appK))^-1; %the stiffness, assuming that machine compliance has already been accounted for
newK = K*1000;
txt1 =(['Stiffness = ' num2str(newK) ' N/um']);
txt2 = (['Strain rate = 0.06 mm/min']);
txt3 = (['Coefficient of Determination =' num2str(R2)]);
h2 = textul({txt1;txt2;txt3},0.1); %write the stiffness value directly within the graph


function h = textul(txt,place) %will add text to a graph in a specified location
    a = axis;
    wdth = a(2)-a(1);
    ht = a(4)-a(3);
    pos = [a(1)+0.05*wdth a(4)-place*ht]; %5 percent away from left
    h = text(pos(1),pos(2),txt,'EdgeColor','red');
```

Appendix F

F. Matlab Code for Bone Remodeling Algorithm, Chapter 8

F.1 BoneBio Class

```matlab
classdef Bonebio1_1v2Revised < QuadElasticity

    properties(GetAccess = 'public', SetAccess = 'private');

        myAge % model age

        myC_OBp % concentration of osteoblast precursors

        myC_OBa % concentration of active osteoblasts

        myC_OCp % Concentation of osteoclast precursors

        myC_OCa % Conentration of active osteoclasts

        myA_OBa % rate of active osteoblast apoptosis

        myD_OBp % max differentiation rate of osteoblast precursors


        myP_PTH_d % PTH dosage term

        myP_PTH_d_Nodes % PTH dosage at node


        myP_TGF_d % TGF dosage term

        myP_TGF_d_Nodes % TGF dosage at node


        myCounter

        myPhi_Nodes

        myMaxPhi
```

myMinPhi

myResultsMinPhi

myResultsMaxPhi

myResultsTime

myResultsMaxStress

myK_res % resorption rate

myK_form % formation rate

myRho % inital density

mylambda % anabolic strength parameter

myPhi % current porosity

myPi_PTH_REP_OB % repressor equilibrium constant

myPi_PTH_ACT_OB % activatior function of PTH

myB_PTH % intrinsic PTH production rate

myD_PTH % constant degradation rate of PTH

myK_PTH_ACT_OB % RANKL production-relevant equilibrium dissociation

%constant related to binding of PTH to its receptors expressed on osteoblasts

myK_PTH_REP_OB % OPG production-relevant equilibrium dissociation constant

%related to binding of PTH to its receptors expressed on osteoblasts

myPi_TGF_ACT_OB % activatior function of TGF

myPi_TGF_REP_OB % repressor equlibrium constant

```
        myB_TGF % intrinsic TGF production rate

        myD_TGF % constant degradation rate of TGF

        myK_TGF_ACT_OB % RANKL production-relevant equilibrium dissociation

        %constant related to binding of TGF to its receptors expressed on osteoblasts

        myK_TGF_REP_OB % OPG production-relevant equilibrium dissociation constant

        %related to binding of TGF to its receptors expressed on osteoblasts


        myPi_RANKL_ACT_OC % activatior function of RANKL


    end
    methods
        function obj = Bonebio1_1v2Revised(brepFileName,nElements,shape,class) % <insert pithy
comment here>
            obj = obj@QuadElasticity(brepFileName,nElements,shape,class);
        end
        function obj=setCellConc(obj,C_OBpo,C_OBao,C_OCpo,C_OCao) %set initial bone cell
concentrations
            obj.myC_OBp(1:obj.myNumElems)=C_OBpo; %initial molar concentration of osteoblast
precursor cells
            obj.myC_OBa(1:obj.myNumElems)=C_OBao; %initial molar concentration of active osteoblast
cells
            obj.myC_OCp(1:obj.myNumElems)=C_OCpo; %initial molar concentration of osteoclast
precursor cells
```

```
        obj.myC_OCa(1:obj.myNumElems)=C_OCao; %initial molar concentration of active osteoclast
cells
    end
    function obj=setRates(obj,D_OBp,A_OBa,K_res,K_form) %set differentiation and reaction rates
        obj.myD_OBp(1:obj.myNumElems)=D_OBp; %max differentiation rate of osteoblast precursor
cells
        obj.myA_OBa(1:obj.myNumElems)=A_OBa; %apoptosis rate of active osteoblasts
        obj.myK_res(1:obj.myNumElems)=K_res; %bone resorption rate
        obj.myK_form(1:obj.myNumElems)=K_form; %bone formation rate
    end


    function obj=setPTH(obj,P_PTH_d,B_PTH,D_PTH,K_PTH_ACT_OB,K_PTH_REP_OB) %grand
master PTH concentration control
%           if (nargin == 6)
%               members = 1:obj.myNumElems;
%           else
%               assert(max(members) <= obj.myNumElems);
%               assert(min(members) >=  1);
%           end
        obj.myB_PTH(1:obj.myNumElems)=B_PTH; %intrinsc PTH production rate
        obj.myD_PTH(1:obj.myNumElems)=D_PTH; %constant degradation rate of PTH
        obj.myK_PTH_ACT_OB(1:obj.myNumElems)=K_PTH_ACT_OB; %RANKL production-
relevant
```

% equilibrium dissociation constant related to binding of PTH to its receptors expressed on osteoblasts

```matlab
        obj.myK_PTH_REP_OB(1:obj.myNumElems)=K_PTH_REP_OB; %OPG production-relevant
        %equilibrium dissociation constant related to binding of PTH to its receptors expressed on
osteoblasts
        obj.myP_PTH_d(1:obj.myNumElems) =P_PTH_d.*rand(1,obj.myNumElems); %PTH dosage
        nElements=obj.myNumElems;
        for elem=1:nElements %assigning PTH concentrations to each element
        C_PTHElem=(obj.myB_PTH(elem)+obj.myP_PTH_d(elem))/obj.myD_PTH(elem);% molar
concentration of PTH
        obj.myPi_PTH_ACT_OB(elem)=C_PTHElem/(obj.myK_PTH_ACT_OB(elem)+C_PTHElem);
%activator function of carrying capacity of RANKL due to PTH
        obj.myPi_PTH_REP_OB(elem)=C_PTHElem/(obj.myK_PTH_REP_OB(elem)+C_PTHElem);
%repressor function of OPG production following PTH
        end
    end


    function obj=setTGF(obj,P_TGF_d,B_TGF,D_TGF,K_TGF_ACT_OB,K_TGF_REP_OB) %grand
master TGF concentration control
%        if (nargin == 6)
%            members = 1:obj.myNumElems;
%        else
%            assert(max(members) <= obj.myNumElems);
%            assert(min(members) >=  1);
```

```matlab
%        end
        obj.myB_TGF(1:obj.myNumElems)=B_TGF; %intrinsc TGF production rate
        obj.myD_TGF(1:obj.myNumElems)=D_TGF; %constant degradation rate of TGF
        obj.myK_TGF_ACT_OB(1:obj.myNumElems)=K_TGF_ACT_OB; %RANKL production-
relevant
        %equilibrium dissociation constant related to binding of PTH to its receptors expressed on
osteoblasts
        obj.myK_TGF_REP_OB(1:obj.myNumElems)=K_TGF_REP_OB; %OPG production-relevant
        %equilibrium dissociation constant related to binding of TGF to its receptors expressed on
osteoblasts
        obj.myP_TGF_d(1:obj.myNumElems) =P_TGF_d.*rand(1,obj.myNumElems); %TGF dosage
        nElements=obj.myNumElems;
        for elem=1:nElements %assigning TGF concentrations to each element
        C_TGFElem=(obj.myB_TGF(elem)+obj.myP_TGF_d(elem))/obj.myD_TGF(elem);% molar
concentration of TGF
        obj.myPi_TGF_ACT_OB(elem)=C_TGFElem/(obj.myK_TGF_ACT_OB(elem)+C_TGFElem);
%activator function of carrying capacity of RANKL due to TGF
        obj.myPi_TGF_REP_OB(elem)=C_TGFElem/(obj.myK_TGF_REP_OB(elem)+C_TGFElem);
%repressor function of OPG production following TGF
        end
    end


        function obj=setPorosity(obj,Phi) %change porosity of bone
        obj.myPhi(1:obj.myNumElems)=Phi; %bone porosity
```

```
end

function obj = simulateBone(obj)

    i=0;


    ResultsMaxPhi=zeros(1,5);

    ResultsMinPhi=zeros(1,5);

    ResultsMaxStress=zeros(1,5);

    ResultsTime=zeros(1,5);


    obj.myResultsMaxPhi = ResultsMaxPhi;

    obj.myResultsMinPhi = ResultsMinPhi;

    obj.myResultsTime = ResultsTime;

    obj.myResultsMaxStress = ResultsMaxStress;


    while i<=5

        obj=obj.solveLinearElasticityProblem();

        Figure(1)

        obj.plotPhi();

        pause(3)

        close(1)

        Figure(2)

        obj.plotStress();

        obj=obj.assemblePhi;
```

```matlab
        pause(3)

        close(2)

        counter = i+1;

        obj.myCounter = counter;

%        obj.myResultsMaxPhi(1,counter) = obj.myMaxPhi();

%        obj.myResultsMinPhi(obj.myCounter)= obj.myMinPhi;

%        obj.myResultsMaxStress(obj.myCounter)= obj.myMaxStress;

        i=i+1;

%        for j=1:counter

%            ResultsMaxPhi(j)= obj.myMaxPhi;

%            ResultsMinPhi(j)= obj.myMinPhi;

%            ResultsStress(j)=(obj.myMaxStress)

%        end

%

    end

end

function obj = assemblePhi(obj)

    nElements = obj.myNumElems;

    strainX = obj.myElemStrains(1:nElements,1,1);

    strainY = obj.myElemStrains(1:nElements,2,2);

    strainXY = obj.myElemStrains(1:nElements,1,2);


    devStrainX= (2/3)*strainX-(1/3)*strainY;

    devStrainY=(-1/3)*strainX+(2/3)*strainX;
```

```matlab
        gamXY=2*(strainXY);



        strain = 2/3*sqrt(1.5*(devStrainX.^2+devStrainY.^2)+.75*gamXY.^2);

        eMax = 0.8*abs(max(strain));

        eMin = 0.2*abs(max(strain));

        for elem=1:nElements
%           if strain(elem) >= eMax
%               C_OBpElem = .95*obj.myC_OBp; %decay of molar concentration of osteoblast precursor
cells in each element
%               deltaC_OBaElem = (obj.myD_OBp.*C_OBpElem.*obj.myPi_PTH_REP_OB)-
obj.myA_OBa.*obj.myC_OBa; %change in active osteoblasts
%               C_OBaElem = obj.myC_OBa+deltaC_OBaElem; %new value of active osteoblast
concentration
%               C_OCaElem = obj.myC_OCa; %concentration of active osteoclasts in each element
%               deltaPhiElem = -obj.myK_res.*C_OCaElem+obj.myK_form.*C_OBaElem; %change in
porosity
%               obj.myPhi = obj.myPhi+deltaPhiElem; %new porosity
%               obj.myPseudoDensity = ones(1,nElements)-obj.myPhi; %bone density as a result of
porosity
%           elseif strain <= eMin
%               C_OBpElem=.95*obj.myC_OBp; %decay of molar concentration of osteoblast precursor
cells in each element
```

```
%              deltaC_OBaElem=(obj.myD_OBp.*C_OBpElem.*obj.myPi_PTH_REP_OB)-
obj.myA_OBa.*obj.myC_OBa; %change in active osteoblasts

%              C_OBaElem=1.05*obj.myC_OBa+deltaC_OBaElem; %new value of active osteoblast
concentration

%              C_OCaElem=1.05*obj.myC_OCa; %concentration of active osteoclasts in each element

%              deltaPhiElem=-obj.myK_res.*C_OCaElem+obj.myK_form.*C_OBaElem; %change in
porosity

%              obj.myPhi=obj.myPhi+deltaPhiElem; %new porosity

%              obj.myPseudoDensity=ones(1,nElements)-obj.myPhi; %bone density as a result of
porosity

%         else

%              C_OBpElem=.95*obj.myC_OBp; %decay of molar concentration of osteoblast precursor
cells in each element

%              deltaC_OBaElem=(obj.myD_OBp.*C_OBpElem.*obj.myPi_PTH_REP_OB)-
obj.myA_OBa.*obj.myC_OBa; %change in active osteoblasts

%              C_OBaElem=obj.myC_OBa+deltaC_OBaElem; %new value of active osteoblast
concentration

%              C_OCaElem=obj.myC_OCa; %concentration of active osteoclasts in each element

%              deltaPhiElem=-obj.myK_res.*C_OCaElem+obj.myK_form.*C_OBaElem; %change in
porosity

%              obj.myPhi=obj.myPhi+deltaPhiElem; %new porosity

%              obj.myPseudoDensity=ones(1,nElements)-obj.myPhi; %bone density as a result of
porosity

%         end
```

```matlab
        C_OBpElem = .95*obj.myC_OBp(elem); %decay of molar concentration of osteoblast
precursor cells in each element
        if strain(elem) >= eMax
%            deltaC_OBaElem =
(obj.myD_OBp(elem).*C_OBpElem.*obj.myPi_TGF_REP_OB(elem))-
obj.myA_OBa(elem).*obj.myC_OBa(elem); %change in active osteoblasts
            deltaC_OBaElem =
(obj.myD_OBp(elem).*C_OBpElem.*obj.myPi_RANKL_ACT_OC(elem))-
(obj.myA_OBa(elem).*obj.myC_OBa(elem)*.myPi_TGF_REP_OB(elem)); %change in active
osteoblasts
            C_OBaElem = 1.05*obj.myC_OBa(elem)+deltaC_OBaElem; %new value of active
osteoblast concentration
            C_OCaElem = obj.myC_OCa(elem); %concentration of active osteoclasts in each element
            deltaPhiElem = -obj.myK_res(elem).*C_OCaElem+obj.myK_form(elem).*C_OBaElem;
%change in porosity
            obj.myPhi(elem) = obj.myPhi(elem)+deltaPhiElem; %new porosity
            if obj.myPhi(elem)<0
                obj.myPhi(elem)=0;
            elseif obj.myPhi(elem)>1
                obj.myPhi(elem)=1;
            else
                obj.myPhi(elem)=obj.myPhi(elem);
            end
            obj = obj.setPseudoDensity(elem, 1-obj.myPhi(elem)); %bone density as a result of porosity
```

```matlab
        elseif strain <= eMin

            deltaC_OBaElem = (obj.myD_OBp(elem).*C_OBpElem.*obj.myPi_TGF_REP_OB(elem))-
obj.myA_OBa(elem).*obj.myC_OBa(elem); %change in active osteoblasts

            C_OBaElem = obj.myC_OBa(elem)+deltaC_OBaElem; %new value of active osteoblast
concentration

            C_OCaElem = 1.05*obj.myC_OCa(elem); %concentration of active osteoclasts in each
element

            deltaPhiElem = -obj.myK_res(elem).*C_OCaElem+obj.myK_form(elem).*C_OBaElem;
%change in porosity

            obj.myPhi(elem) = obj.myPhi(elem)+deltaPhiElem; %new porosity

            if obj.myPhi(elem)<0

                obj.myPhi(elem)=0;

            elseif obj.myPhi(elem)>1

                obj.myPhi(elem)=1;

            else

                obj.myPhi(elem)=obj.myPhi(elem);

            end

            obj.myPseudoDensity(elem) = 1-obj.myPhi(elem); %bone density as a result of porosity

        else

            deltaC_OBaElem = (obj.myD_OBp(elem).*C_OBpElem.*obj.myPi_TGF_REP_OB(elem))-
obj.myA_OBa(elem).*obj.myC_OBa(elem); %change in active osteoblasts

            C_OBaElem = obj.myC_OBa(elem)+deltaC_OBaElem; %new value of active osteoblast
concentration

            C_OCaElem = obj.myC_OCa(elem); %concentration of active osteoclasts in each element
```

```matlab
            deltaPhiElem = -obj.myK_res(elem).*C_OCaElem+obj.myK_form(elem).*C_OBaElem;
%change in porosity
            obj.myPhi(elem) = obj.myPhi(elem)+deltaPhiElem; %new porosity
            if obj.myPhi(elem)<0
                obj.myPhi(elem)=0;
            elseif obj.myPhi(elem)>1
                obj.myPhi(elem)=1;
            else
                obj.myPhi(elem)=obj.myPhi(elem);
            end
            obj = obj.setPseudoDensity(elem,1-obj.myPhi(elem)) ; %bone density as a result of porosity
        end
      end
    end
%      function plotPTH(obj) %plot PTH
%        obj.myP_PTH_d_Nodes = zeros(1,obj.myNumNodes); %PTH at note
%       for elem = 1:obj.myNumElems
%         if (obj.myPseudoDensity(elem) == 0)
%             continue;
%         end
%         nodes = obj.myMesh.q(1:obj.myNodesPerElement,elem)'; %mesh
%         obj.myP_PTH_d_Nodes(nodes) = obj.myP_PTH_d_Nodes(nodes) + obj.myP_PTH_d(elem);
%       end
```

```matlab
function plotTGF(obj) %plot TGF

    obj.myP_TGF_d_Nodes = zeros(1,obj.myNumNodes); %TGF at note

    nElemsConnectedToNode  = zeros(1,obj.myNumNodes);

    for elem = 1:obj.myNumElems

        if (obj.myPseudoDensity(elem) == 0)

            continue;

        end

        nodes = obj.myMesh.q(1:obj.myNodesPerElement,elem)'; %mesh

        nElemsConnectedToNode(nodes) = nElemsConnectedToNode(nodes) + 1;

        obj.myP_TGF_d_Nodes(nodes) = (obj.myP_TGF_d_Nodes(nodes) + obj.myP_TGF_d(elem));

    end

    obj.myP_TGF_d_Nodes=obj.myP_TGF_d_Nodes./nElemsConnectedToNode(nodes);

    X = zeros(obj.myNumElems,5);

    Y = zeros(obj.myNumElems,5);

    Z = zeros(obj.myNumElems,5);

%        nodalField = obj.myP_PTH_d_Nodes;

%        nodalField(isnan(nodalField)) = 0;


    nodalField = obj.myP_TGF_d_Nodes;

    nodalField(isnan(nodalField)) = 0;


    for count = 1:obj.myNumElems

        if (obj.myPseudoDensity(count) == 0), continue;end

        nodes = obj.myMesh.q(:,count);
```

```matlab
    X(count,:) = obj.myMesh.p(1,[nodes' nodes(1)]);

    Y(count,:) = obj.myMesh.p(2,[nodes' nodes(1)]);

    Z(count,:) = nodalField([nodes' nodes(1)]);


  end

  fill( X', Y',Z','EdgeColor','none') % surface

  axis equal; axis on;view(2);

  obj.adjustFigScale();

  hold on;

  title(['TGF Conc = ' num2str(max(nodalField))]);

end

function plotPhi(obj) %plot Phi

  obj.myPhi_Nodes = zeros(1,obj.myNumNodes); %Phi at node

  nElemsConnectedToNode  = zeros(1,obj.myNumNodes);

  for elem = 1:obj.myNumElems

    if (obj.myPseudoDensity(elem) == 0)

       continue;

    end

    nodes = obj.myMesh.q(1:obj.myNodesPerElement,elem)'; %mesh

    nElemsConnectedToNode(nodes) = nElemsConnectedToNode(nodes) + 1;

    obj.myPhi_Nodes(nodes) = (obj.myPhi_Nodes(nodes) + obj.myPhi(elem));

  end

  obj.myPhi_Nodes=obj.myPhi_Nodes./nElemsConnectedToNode;

  X = zeros(obj.myNumElems,5);
```

```matlab
    Y = zeros(obj.myNumElems,5);

    Z = zeros(obj.myNumElems,5);


    nodalField = obj.myPhi_Nodes;

    nodalField(isnan(nodalField)) = 0;


    for count = 1:obj.myNumElems

        if (obj.myPseudoDensity(count) == 0), continue;end

        nodes = obj.myMesh.q(:,count);

        X(count,:) = obj.myMesh.p(1,[nodes; nodes(1)]);

        Y(count,:) = obj.myMesh.p(2,[nodes; nodes(1)]);

        Z(count,:) = nodalField([nodes; nodes(1)]);

    end

    MaxPhi= max(nodalField)

    MinPhi=min(nodalField)

    obj.myCounter

%       obj.myMaxPhi(1,obj.myCounter)= MaxPhi;

%       obj.myMinPhi(1,obj.myCounter)= MinPhi;

    obj.myMaxPhi = MaxPhi;

    obj.myMinPhi = MinPhi;

    obj.myMaxStress

%       pause

%       a=obj.myMaxPhi

%       b=obj.myMaxStress
```

```matlab
%           obj.myResultsMaxPhi(obj.myCounter) = obj.myMaxPhi(1,obj.myCounter);

%           obj.myResultsMinPhi(obj.myCounter)= obj.myMinPhi(1,obj.myCounter);

%           obj.myResultsMaxStress(obj.myCounter)= obj.myMaxStress;

%

        fill( X', Y',Z','EdgeColor','none') % surface

        axis equal; axis on;view(2);

        obj.adjustFigScale();

        hold on;

        title(['Phi Max = ' ,num2str(max(nodalField)),'Phi Min = ', num2str(min(nodalField))]);

    end

end


    end
```

F.2 Test Function for BoneBio Class

```matlab
%% Test Bone Bio

clc; clear all;  format compact; format long;

problem = 3;

nElements = 2000;

shape = 'Linear';

C_OBpo=0.001;% original concentration of osteoblast precursors

C_OBao=0.0005;% original concentration of active osteoblasts

C_OCpo=0.001;% original concentration of osteoclast precursors
```

C_OCao=0.0001;% original conentration of active osteoclasts

Phio=0.05;% Cortical bone porosity

elem=1:nElements;

A_OBa=2.1107e-1;

D_OBp=.1650;

K_res=2; % The Scheiner paper has 2 as value

K_form=0.4;

K_PTH_REP_OB=2.226e-1;% repressor equlibruim constant (pM)

K_PTH_ACT_OB=1.5e2;% activation equlibruim constant(pM)

D_PTH=8.6e1;% degredation rate (1/d)

B_PTH=2.5e2;% intrinsic production rate (pM/d)

P_PTH_d=5e4;% PTH dosage (pM)

K_TGF_REP_OB=1.7543e-4;% repressor equlibruim constant (pM)

K_TGF_ACT_OBu=5.6328e-4;% activation equlibruim constant(pM)

D_TGF=1;% degredation rate (1/d)

B_TGF=2.5e2;% intrinsic production rate (pM/d)

P_TGF_d=5e4;% TGF dosage (pM)

Kd_RANKL_RANK=5.6797;% repressor equlibruim constant (pM)

Ka_RANKL_RANK=3.4118e-2;% activation equlibruim constant(pM)

```matlab
D_RANKL=1.0132;% degredation rate (1/d)

B_RANKL=1.6842e2;% intrinsic production rate (pM/d)

P_RANKL_d=5e4;% RANKL dosage (pM)



b=Bonebio1_1v2Revised('RectangleHole.brep',nElements,shape,'PlaneStress');


b=b.setRANKL(P_RANKL_d,B_RANKL,D_RANKL,Kd_RANKL_RANK,Ka_RANKL_RANK)


b=b.setPTH(P_PTH_d,B_PTH,D_PTH,K_PTH_ACT_OB,K_PTH_REP_OB);


b=b.setTGF(P_TGF_d,B_TGF,D_TGF,K_TGF_ACT_OBu,K_TGF_REP_OB);


b=b.setCellConc(C_OBpo,C_OBao,C_OCpo,C_OCao);

b=b.setRates(D_OBp,A_OBa,K_res,K_form);


b=b.setPorosity(Phio);

b=b.setPseudoDensity(b.myNumElems,1);

b=b.fixEdge(7);

b=b.applyYForceOnEdge(3,-1);


%b=b.solveFEProblem();
```

```
b=b.simulateBone();


% Figure(4)

% b.plotMesh();

% b=b.solveFEProblem();

% Figure(5)

% b.plotStress();

% Figure(6);

%b.plotTGF()
```

Appendix G

G. Protocol for Statistical Analysis

G.1 Principal Component Analysis Using R 3.2.5

#PCA for human hip endo study

#author: Luisa Meyer

myData <- read.delim("clipboard", na.strings = c(".", "NA"))

summary(myData)

#check for mistakes

str(myData)

#define subsets

control <- subset(myData, Treatment == "CC")

endothelin <- subset(myData, Treatment == "CB")

load <- subset(myData, Treatment == "LC")

loadET <- subset(myData, Treatment == "LB")

female <- subset(myData, Sex == "FEMALE")

male <- subset(myData, Sex == "MALE")

F.control <- subset(myData, Treatment == "CC", Sex == "FEMALE")

F.endothelin <- subset(myData, Treatment == "CB", Sex == "FEMALE")

```
F.load <- subset(myData, Treatment == "LC", Sex == "FEMALE")

F.loadET <- subset(myData, Treatment == "LB", Sex == "FEMALE")


M.control <- subset(myData, Treatment == "CC", Sex == "MALE")

M.endothelin <- subset(myData, Treatment == "CB", Sex == "MALE")

M.load <- subset(myData, Treatment == "LC", Sex == "MALE")

M.loadET <- subset(myData, Treatment == "LB", Sex == "MALE")


LoadOnly <- subset(myData, Load == "YES")

ETBlockOnly <- subset(myData, ETBlock == "YES")

noLoad <- subset(myData, Load == "NO")

noETBlock <- subset(myData, ETBlock == "NO")


factors <- c("FinalEapp", "IGF1", "DKK1", "BoneVolume", "SurfaceArea", "BSA_BV", "BV_TV",

"T.Th", "T.Sp", "Connectivity", "Anisotropy", "SMI", "FabricTensor")


newData <-myData[factors]


FnewData<- female[factors]

MnewData <- male[factors]


CTRL <-control[factors]

ETonly <-endothelin[factors]

EX <-load[factors]
```

EXET <-loadET[factors]

F.CTRL <-F.control[factors]

F.ETonly <-F>endothelin[factors]

F.EX <-F.load[factors]

F.EXET <-F.loadET[factors]

M.CTRL <-M.control[factors]

M.ETonly <-M.endothelin[factors]

M.EX <-M.load[factors]

M/EXET <-M.loadET[factors]

LoadOnly <- LoadOnly[factors]

ETBlockOnly <-ETBlockOnly[factors]

noLoad <-noLoad[factors]

noETBlock <-noETBlock[factors]

```
# Look at the correlations
library(lattice)
library(gclus)
library(corrplot)
stuff <- cor(newData)
corrplot(stuff, method = "circle")
```

```r
# Do the PCA

my.prc <- prcomp(newData[,-1], center=TRUE, scale=TRUE)

screeplot(my.prc, main="Scree Plot", xlab="Components")

screeplot(my.prc, main="Scree Plot", type="line" )


#get PCA results

my.prc$rotation


# Now draw the BiPlot

biplot(my.prc, cex=c(1, 0.7))


# Apply the Varimax Rotation

my.var <- varimax(my.prc$rotation)


# Correlation plot

cors<-cor(stuff)

cor.mtest <- function(mat, conf.level = 0.95) {

mat <- as.matrix(mat)

n <- ncol(mat)

p.mat <- lowCI.mat <- uppCI.mat <- matrix(NA, n, n)

diag(p.mat) <- 0

diag(lowCI.mat) <- diag(uppCI.mat) <- 1

for (i in 1:(n - 1)) {
```

```
   for (j in (i + 1):n) {

      tmp <- cor.test(mat[, i], mat[, j], conf.level = conf.level)

      p.mat[i, j] <- p.mat[j, i] <- tmp$p.value

      lowCI.mat[i, j] <- lowCI.mat[j, i] <- tmp$conf.int[1]

      uppCI.mat[i, j] <- uppCI.mat[j, i] <- tmp$conf.int[2]

   }

}

return(list(p.mat, lowCI.mat, uppCI.mat))

}

res1 <- cor.mtest(stuff, 0.95)

res2 <- cor.mtest(stuff, 0.99)

corrplot(cors, p.mat = res1[[1]], sig.level=0.05, insig="blank", cl.align="r", tl.cex=0.6, order="hclust",

type="lower", tl.srt=60, cl.ratio=0.1)


#Get adjusted p-values

pAdj <- p.adjust(c(res1[[1]]), method = "BH")

resAdj <- matrix(pAdj, ncol = dim(res1[[1]])[1])

corrplot(cors, p.mat = resAdj, sig.level=0.05, insig="p-value", cl.align="r", tl.cex=0.6, order="hclust",

type="lower", tl.srt=60, cl.ratio=0.1)

corrplot(cors, p.mat = resAdj, sig.level=-1, insig="p-value", cl.align="r", tl.cex=0.6, order="hclust",

type="lower", tl.srt=60, cl.ratio=0.1)


--------------------------------------------------------------------------------

#my.abs     <- abs(cor(my.HHdata[,-1]))
```

```
#my.colors  <- dmat.color(my.abs)

#my.ordered <- order.single(cor(my.HHdata[,-1]))

#cpairs(my.HHdata[,-1], my.ordered, panel.colors=my.colors, gap=0.5)


# DotPlot PC1


load    <- my.prc$rotation

sorted.loadings <- load[order(load[, 1]), 1]

myTitle <- "Loadings Plot for PC1"

myXlab  <- "Variable Loadings"

dotplot(sorted.loadings, main=myTitle, xlab=myXlab, cex=1.5, col="red")


# DotPlot PC2


sorted.loadings <- load[order(load[, 2]), 2]

myTitle <- "Loadings Plot for PC2"

myXlab  <- "Variable Loadings"

dotplot(sorted.loadings, main=myTitle, xlab=myXlab, cex=1.5, col="red")
```

G.2 Best General Linear Model Using R 3.2.5

```
#Best GLM for human hip endo study

#author: Luisa Meyer


------
```

```
#Read in data sets

#for data in "Revised End Data for R" tab within "Human Hip 2015 all data LM.xls"
myData <- read.delim("clipboard", na.strings = c(".", "NA"))
summary(myData)


#check for mistakes
str(myData)


control <- subset(myData, Treatment == "CC")
endothelin <- subset(myData, Treatment == "CB")
load <- subset(myData, Treatment == "LC")
loadET <- subset(myData, Treatment == "LB")


female <- subset(myData, Sex == "FEMALE")
male <- subset(myData, Sex == "MALE")


F.control <- subset(myData, Treatment == "CC", Sex == "FEMALE")
F.endothelin <- subset(myData, Treatment == "CB", Sex == "FEMALE")
F.load <- subset(myData, Treatment == "LC", Sex == "FEMALE")
F.loadET <- subset(myData, Treatment == "LB", Sex == "FEMALE")


M.control <- subset(myData, Treatment == "CC", Sex == "MALE")
M.endothelin <- subset(myData, Treatment == "CB", Sex == "MALE")
```

```
M.load <- subset(myData, Treatment == "LC", Sex == "MALE")

M.loadET <- subset(myData, Treatment == "LB", Sex == "MALE")


LoadOnly <- subset(myData, Load == "YES")

ETBlockOnly <- subset(myData, ETBlock == "YES")

noLoad <- subset(myData, Load == "NO")

noETBlock <- subset(myData, ETBlock == "NO")


factors <- c("BoneVolume", "BSA_BV", "BV_TV", "T_Sp", "Anisotropy", "FinalEapp")


newData <-myData[factors]


FnewData<- female[factors]

MnewData <- male[factors]


CTRL <-control[factors]

ETonly <-endothelin[factors]

EX <-load[factors]

EXET <-loadET[factors]


F.CTRL <-F.control[factors]

F.ETonly <-F>endothelin[factors]

F.EX <-F.load[factors]

F.EXET <-F.loadET[factors]
```

M.CTRL <-M.control[factors]

M.ETonly <-M.endothelin[factors]

M.EX <-M.load[factors]

M/EXET <-M.loadET[factors]

LoadOnly <- LoadOnly[factors]

ETBlockOnly <-ETBlockOnly[factors]

noLoad <-noLoad[factors]

noETBlock <-noETBlock[factors]

#Generate

library(bestglm)

input <- newData

summary(input)

myout <-bestglm(input, family=gaussian, IC="AIC")

myout$BestModels

#add whatever factors come out of best GLM

model <- glm(formula = FinalEapp ~ BSA.BV , data=newData, family=gaussian)

summary(model)

glm(formula = FinalEapp ~ BSA.BV , family = gaussian, data = newData)

```
#Test for goodness of fit

library(ResourceSelection)

hoslem.test(newData$FinalEapp, fitted(model))

---

myDataF <- read.delim("clipboard", na.strings = c(".", "NA"))

summary(myDataF)


inputF <- myDataF

summary(inputF)


myoutF <-bestglm(inputF, family=gaussian, IC="AIC")

myoutF$BestModels

---


myDataM <- read.delim("clipboard", na.strings = c(".", "NA"))

summary(myDataM)


inputM <- myDataM

summary(inputM)


myoutM <-bestglm(inputM, family=gaussian, IC="AIC")


myoutM$BestModels
```

Appendix H

H. Conference Abstracts

H.1 American Society for Bone and Mineral Research 2012

Luisa Meyer[1], Michael Johnson[2], Juan Vivanco[1], Robert Blank[2], Heidi-Lynn Ploeg[1], Everett Smith[3]

[1]Department of Biomedical/Mechanical Engineering, University of Wisconsin – Madison

[2]Department of Medicine, University of Wisconsin – Madison

[3]Department of Population Health Sciences, University of Wisconsin – Madison

H.1.1 Exposure to big endothlin-1 in bovine sternal cores mimics some aspects of mechanical loading.

It is well established that mechanical loading increases bone strength by inducing bone remodeling. Endothelin-1 (ET1), a ubiquitous autocrine/paracrine signaling molecule, is known to promote osteogenesis in the setting of breast and prostate cancer. It was hypothesized that ET1 acts synergistically with mechanical loading to increase the apparent stiffness of bovine trabecular bone cores. In a 2x2 factorial trial of daily compressive loading and 25 ng/ml big ET-1, 48 bovine sternal cores were maintained in individual polycarbonate chambers. The cores were tested in compression with a piezoelectric controlled axial loading system with measurements of force and displacement. Apparent stiffness was calculated from the slope of the force-displacement data and apparent elastic modulus was determined assuming Hooke's Law and the bulk dimensions of the bone core. The cores in the "load" groups were subjected to dynamic loading once a day of -2000 microstrain for 120 cycles at a frequency of 2 Hz. Apparent elastic modulus was determined from a quasistatic measurement at baseline and on days 15, and 23. Culture media were changed daily and collected at baseline and every three days thereafter. Prostaglandin E2 production was measured by ELISA. Loading of the bone cores significantly ($p < 0.05$) increased the mean percent change in apparent elastic modulus (+26% in "load+ET-1" and +17% and in the "load" groups). Exposure to ET-1 contributed to an increase in stiffness from baseline to

day 23 in both the "load" and "no load" groups, 26% and 13% respectively. The effect of ET-1 alone (+13%) and exercise alone (+17%) were not significantly different. In all treatment groups prostaglandin production began at 8 days post osteotomy and continued throughout the remainder of the experiment, while in the control group prostaglandin production began to decrease at day 12 and by day 15 was 70% of the treatment groups. The study results suggest that exposure to ET1 mimicked exercise induced strain.

H.2 American Society for Bone and Mineral Research 2013

Diane M. Cullen[1], Gwendolyn Alvarez[1], Luisa Meyer[2], Michael Johnson[3], Juan Vivanco[4], , Heidi-Lynn Ploeg[2], Everett Smith[5]

[1]Creighton University, [2]University of Wisconsin, [3]Medical College of Wisconsin

H.2.1 Mechanical Loading And Big Endothelin-1 In Trabecular Bone Cores

Mechanical loads are anabolic stimuli for bone, increasing formation and strength in adaptation to the stresses. Endothelin-1 (ET1), a ubiquitous autocrine/paracrine signaling molecule promotes osteogenesis associated with breast and prostate cancer. In this ex vivo study we combined both anabolic stimuli and hypothesized that bone formation would increase synergistically. Bovine sternal trabecular bone cores (5x10mm) were maintained in individual polycarbonate chambers with media changed daily over 23 days. Cores were placed into four groups blocked by stiffness and treated daily with compressive loading (-2000 $\mu\epsilon$, 120 cyc, 2 Hz) and/or big ET-1 (25 ng/mL). Bone formation was labeled in culture with calcein on days 9 and 19. Bone stiffness and prostaglandin production was measured throughout the experiment. After collection cores were embedded in methylmethacrylate and sectioned for histomorphometric measurement of bone area, surface, label length, and label width. Differences among groups were analyzed by 2-way ANOVA for the effects of Load x Endothelin. There was no difference among groups in bone volume (BV/TV) of the cores. Due to the long labeling interval, single label predominated over double. Load cores had 50% more single label bone surface (sLS/BS) than NoLoad cores. Mineral apposition rate (MAR) showed a stair step pattern with a positive Load impact (P=0.007)

and ET-1 showing a positive trend (P=0.16). Bone formation rate (BFR), a product of label length and MAR, was twofold greater in Load than NoLoad (P=0.009), but not altered by ET-1 although the same pattern was observed. There was no significant interaction between Load and ET-1. The bone formation response to Load and ET-1 correlate with the change in stiffness across the experiment. In conclusion, ex vivo mechanical loads increased bone formation and stiffness of the cores. ET-1 response in this study was less than predicted from previous work. combined effects tended to be additive rather than synergistic.

Table H.1 - Summary of Histological results

Trt	Drug	N	BV/TV	sL/BS	MAR	BFR
NoLoad	Veh	10	17.9 (5.1)	27 (19)	0.89 (0.66)	63 (75)
	ET-1	10	16.5 (4.9)	30 (17)	1.08 (0.74)	76 (71)
Load	Veh	9	16.5 (2.4)	43 (21)	1.38 (0.67)	131 (107)
	ET-1	9	16.2 (5.4)	43 (11)	1.79 (0.41)	151 (49)
P value	Load		NS	0.01	0.007	0.009
	Drug		NS	NS	NS	NS

H.3 World Congress of Biomechanics 2014

Luisa Meyer[1], Michael Johnson[2], Diane Cullen[3], Juan Vivanco[1], Robert Blank[2], Heidi-Lynn Ploeg[1], Everett Smith[4]

[1]Department of Biomedical/Mechanical Engineering, University of Wisconsin – Madison

[2]Department of Medicine, University of Wisconsin – Madison

[3]Department of Biomedical Sciences, Creighton University

[4]Department of Population Health Sciences, University of Wisconsin – Madison

H.3.1 Mechanical Loading and Exposure to Big Endothlin-1 Increases Bone Formation in Ex Vivo Bovine Trabecular Cores

Mechanical loading increases bone formation by inducing bone remodeling. Endothelin-1 (ET-1), a ubiquitous autocrine/paracrine signaling molecule promotes osteogenesis in metastatic disease. In a 2x2 factorial trial of daily mechanical loading and big ET-1, 48 bovine sternal trabecular cores were maintained in polycarbonate chambers for 23 days. It was hypothesized that both ET-1 and mechanical

stimulation would contribute synergistically to bone formation. A uniaxial loading system was used to load cores ("jump" waveform ,-2000 $\mu\epsilon$, 120 cycles, 0.375 sec/cycle, daily), and ET-1 (25 ng/ml) was administered through the culture media. Prostaglandin E2 (PGE2) production was measuredevery 3 days; and, calcein labeling (days 9 and 19) tracked bone formation. Quasi-static force-displacement measurements (0.04-0.08 $\mu\epsilon$/sec, well below the threshold required for bone stimulation) were taken at baseline, days 15 and 23. The waveform for daily "exercise" was consistent across cores and the range of quasi-static strain rates did not affect bone formation. The effects of load and ET-1 were determined using 2-way ANOVA. The mean percent change in core stiffness over 23 days was increased in the "load+ET-1" group (+26%) and significantly ($p<0.05$) increased in the "load" group (+17%). Exposure to ET-1 contributed to an increase in stiffness over 23 days in both the "load" (+26%) and "no load" (+13%) groups. In treatment groups PGE2 production remained elevated for days 8-23; while, in the control group PGE2 decreased at day 12 and was 70% of the treatment groups by day 15. At the conclusion of the *ex vivo* study, the cores were embedded in methylmethacrylate and sectioned for histomorphometric measurement of bone area, bone surface, label length, and label width. Mechanically loaded cores had 50% more single label bone surface than non-loaded cores. Mineral apposition rate was higher than the control in the "ET-1"(+18%) and "load+ET-1" (+63%) groups, and was significantly ($p = 0.007$) higher in the "load" group (+45%). Bone formation rate was two times greater in the loaded versus non-loaded group ($p=0.009$), but not significantly altered by ET-1. The study results show that mechanical loading increases bone formation and suggest that exposure to ET-1 mimics exercise induced strain.
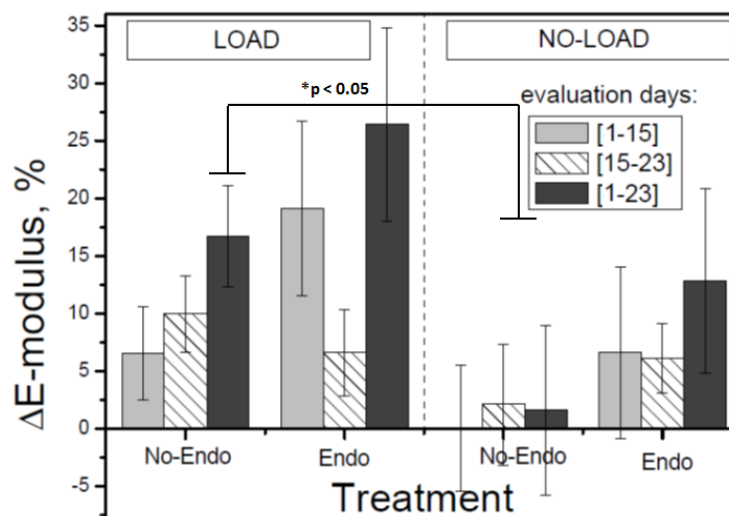
Figure H.1.1 - Percent Change in calculated apparent elastic modulus for each treatment group, arranged according to evaluation days. Asterisk indicates statistically significant increase from baseline to day 23 compared to control group at 95% confidence level

H.4 European Congress of Biomechanics 2015

Luisa Meyer[1], Caitlyn Collins[1], Krishnan Suresh[1], Heidi-Lynn Ploeg[1]

[1]Department of Mechanical Engineering, University of Wisconsin – Madison

H.4.1 Predictive Model for Simulating Trabecular Bone Remodeling in Two Dimensions

H.4.1.1 Introduction

Currently, about 55% of adults older than 50 years are affected by or at risk for osteoporosis—a systemic skeletal disease causing deterioration of bone tissue and associated with a high mortality risk [ACPM, 2009]. Understanding bone biomechanical behaviour is imperative to promote bone health throughout aging, preventing fractures, and improving treatment options. It is necessary to consider cellular level biological factors in addition to mechanical stimuli. Recently, Scheiner *et al* employed one-dimensional (1D) analytical stress analysis, and system's biology in tandem to develop mathematical models to predict the morphological changes in bone resulting from mechanical and biochemical stimuli [Scheiner, 2013]. The goal of the current study was to develop an algorithm that could simulate cortical bone adaptation on a simple two-dimensional (2D) geometric model, in real time.

H.4.1.2 Methods

The predictive algorithm was developed in MATLAB (version R2013a, Simulink) by modifying the analytical models determined by Scheiner *et al* bone cell interactions to interface with a 2D finite element (FE) solver. The inputs for biochemical factors (RANK, RANKL, OPG, PTH, and TGF-β) cell concentrations, initial bone porosity (5%), and isotropic mechanical properties were assumed from literature (elastic modulus=10 GPa, Poisson's ratio=0.3) (Scheiner, 2013). These properties were assigned to a simple 2D geometry under 500 N compressive uniaxial loading (Fig 1A) and a finite element analysis (FEA) with 4000 linear quadrahedral elements was performed. The algorithm uses calculated strain energy density (SED) and assumed biological factors to minimize the SED in load bearing tissue by changing the porosity in relevant areas. The algorithm was repeated for 5, 10, and 20 time steps to simulate bone adaptation with time.

H.4.1.3 Results

As expected, the simulation found the maximum Von mises stress located in the stress concentration caused by the hole (Fig 1B) and bone material adapted to reduce porosity at that location. After 20 iterations, the maximum Von mises stress increased by 11% and the maximum porosity in the bone decreased by 30% with a 3% difference between the maximum and minimum porosity values. The SED was decreased by nearly 100%.
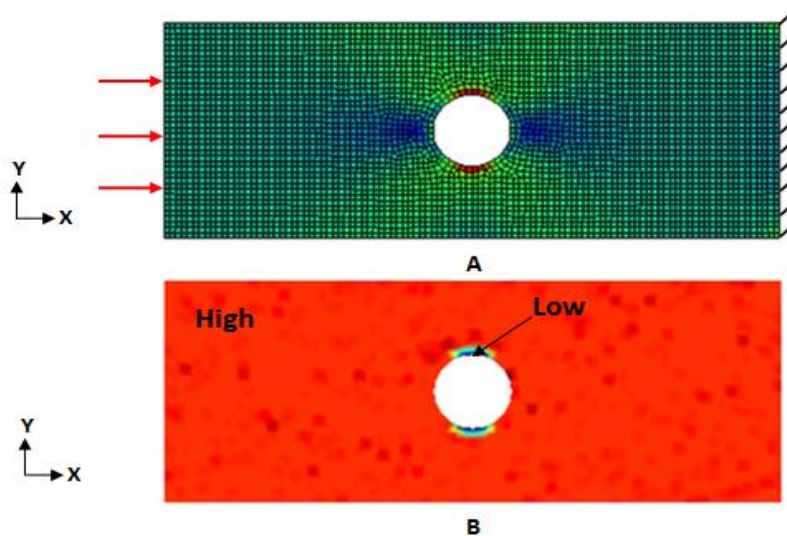
Figure H.4.1 - A) Von mises stress distribution at hole with high stresses in red and lower stresses in green. Applied load and boundary conditions shown. B) Predicted porosity distribution across hole after 20 iterations.

H.4.1.4 Discussion

The presented simulation successfully mimicked bone remodelling in 2D on a simplified geometry. The intent of the current research was to expand Scheiner's algorithm from 1D analytical stress analysis and show remodelling of simulated bone in response to initial concentrations of biochemical factors, porosities, and mechanical stimuli. The algorithm has shown promise in that the results were consistent with known physiological bone remodelling patterns. It will be tested on additional 2D structures more representative of bone. Future versions of the algorithm will be developed to include additional biochemical factors that contribute to the response of osteoblasts and osteoclasts. Finally, the algorithm will be expanded to three dimensions to model whole bone.

H.4.1.5 References

American College of Preventive Medicine, Am J Prev Med, 36(4):366-75, 2009.

Scheiner, S., *et al*., 254:181-196, 2013.

H.5 Computer Methods in Biomechanics and Biomedical Engineering 2015

Luisa Meyer[1], Caitlyn Collins[1], Krishnan Suresh[1], Heidi-Lynn Ploeg[1]

[1]Department of Mechanical Engineering, University of Wisconsin – Madison

H.5.1 Algorithm for Simulating Trabecular Bone Remodeling in Two Dimensions

H.5.1.1 Introduction

About 55% of adults older than 50 years are affected by or at risk for osteoporosis—a systemic skeletal disease causing deterioration of bone tissue and associated with a high mortality risk [ACPM, 2009]. Understanding bone biomechanical behavior is imperative to promote bone health throughout aging, preventing fractures, and improving treatment options. It is necessary to consider cellular level biological factors in addition to mechanical stimulH. Recently, Scheiner *et al* implemented one-dimensional (1D) analytical stress analysis, and system's biology in tandem to develop mathematical models to predict the morphological changes in bone resulting from mechanical and biochemical stimuli [Scheiner, 2013]. The goal of the current study was to develop an algorithm that could simulate cortical bone adaptation on a simple two-dimensional (2D) geometric model, in real time.

H.5.1.2 Methods

The predictive algorithm was developed in MATLAB (version R2013a, Simulink) by modifying the analytical models determined by Scheiner *et al* bone cell interactions to interface with a 2D finite element (FE) solver. The inputs for biochemical factors (RANK, RANKL, OPG, PTH, and TGF-β) cell concentrations, initial bone porosity (5%), and isotropic mechanical properties were assumed from literature (elastic modulus=10 GPa, Poisson's ratio=0.3) (Scheiner, 2013) and were assigned to a simple 2D geometry under 500 N compressive uniaxial loading (Fig 1A) and a finite element analysis (FEA) with 4000 linear quadrahedral elements was performed. Calculated strain energy density (SED) and assumed biological factors were used to minimize the SED in load bearing tissue by changing the porosity in relevant areas. Doses of PTH ($1-50 \times 10^4$ pM), PTH production rate ($2.5-20 \times 10^2$ pM/day), and

PTH deactivation rate (4.3-17.2 day^{-1}) were varied. Each time, the algorithm was repeated for 5, 10, and 20 time steps to simulate bone adaptation with time.

H.5.1.3 Results

As expected in every case, the simulation found the maximum Von mises stress located in the stress concentration caused by the hole (Fig 1B) and bone material adapted to reduce porosity at that location. After 20 iterations, the maximum Von mises stress increased by approximately 11% and the maximum porosity in the bone decreased by approximately 30% with a consistent 3% difference between the maximum and minimum porosity values. The SED was decreased by nearly 100%. Variation of PTH dose minimally affected the changes in stress, porosity and SED during the iterations, however changing PTH activation and deactivation altered the rates of stress increase and porosity decrease by approximately 5%.

H.5.1.4 Conclusions

The simulation effectively emulated bone remodeling in 2D on a simplified geometry. The intent of the current research was to expand Scheiner's algorithm from 1D analytical stress analysis and show remodeling of simulated bone in response to initial concentrations of biochemical factors, porosities, and mechanical stimuli. The algorithm shows promise in that the results were consistent with known physiological bone remodeling patterns. Incorporation of additional contributing biochemical factors is necessary to fully mimic physiological bone remodeling. Furthermore, the algorithm will be tested on additional 2D structures more representative of bone. Finally, the algorithm will be expanded to three dimensions to model whole bone.

H.5.1.5 References

American College of Preventive Medicine, Am J Prev Med, 36(4):366-75, 2009.

Scheiner,S. ,et.al., Comput. Methods Appl. Mech. Engrg. 254:181-96, 2013.

H.5.1.6 Figures
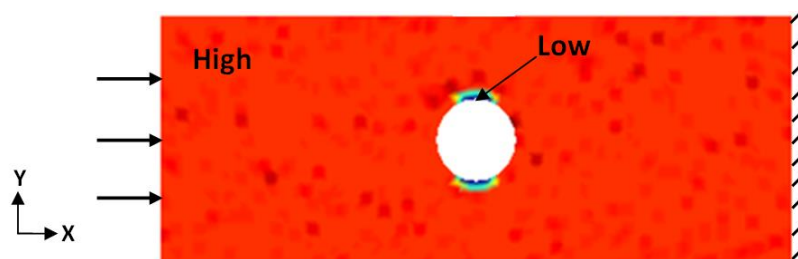
Figure H.5.1 - Predicted porosity distribution across hole after 20 iterations.

H.6 Computer Methods in Biomechanics and Biomedical Engineering 2015

Luisa Meyer[1], Juan Vivanco[2], Heidi-Lynn Ploeg[1]

[1]Department of Mechanical Engineering, University of Wisconsin – Madison

[2]Facultad de Ingeniería y Ciencias, Universidad Adolfo Ibáñez-Chile

H.6.1 Multi-scale Mechanical Analysis of Injection Molded Beta Tricalcium Phosphate Bone Scaffolds

H.6.1.1 Introduction

Currently, about 55% of adults older than 50 years are affected by or at risk for osteoporosis—a systemic skeletal disease causing deterioration of bone tissue and associated with a high mortality risk [ACPM, 2009]. A current method for repairing affected bone tissue is the implantation of porous three-dimensional (3D) scaffolds that support and stimulate existing tissue. Tricalcium phosphate (TCP), due to its biocompatibility and bioresorbability, is used extensively in clinical and research applications [Kasten, 2008]. Since the success of scaffolds is greatly dependent on their ability to osteointegrate, it is imperative to understand their mechanical behavior and appropriately select material to use for scaffolds that would mimic not only bone morphology, but also bone mechanical properties.

H.6.1.2 Methods

Fifty TCP scaffolds were injection molded (approximate bulk dimensions: 5.4x5.4x4.2mm^3) and sintered at 1150°C. Each scaffold was loaded in uniaxial compression twice to 5 µm (in two orthogonal directions) and then loaded until failure [Vivanco, 2011]. The apparent elastic modulus (E_{app}) was determined in two orthogonal directions using Hooke's law and the slope of the linear region of the force-displacement curve. Micro- [Vivanco, 2012] and nano-indentation [Vivanco, 2012] was performed on each scaffold to determine the micro- and nano-level mechanical properties of the TCP material. A finite element (FE) model was made using bulk dimensions of the scaffold. The model was compressively loaded in two orthogonal directions (Abaqus 6.11, Simulia) to mimic mechanical testing of the actual scaffold samples. The model used quadratic tetrahedral elements with a side length of 0.1 mm. The E_{app} of the simulated scaffold was calculated from the maximum force and deflection, assuming Hookean behavior. The analysis was done twice in each direction, using the micro-level elastic modulus (E_{μ}) and then the nano-level elastic modulus (E_n).

H.6.1.3 Results

The E_{app} determined from the mechanical testing was 11121±764 MPa and 4106±2000 MPa in the two orthogonal directions, respectively. Micro- and nano-indentaton yielded 98.67±3.5 GPa and 87.76±7.57 GPa, respectively. Using the FE model, the E_{app} was found to be 8064 MPa and 3214 MPa in two orthogonal directions when the nano-level elastic modulus was used for the scaffold material. The E_{app} was found to be 10900 MPa and 4360 MPa in two orthogonal directions when the micro-level elastic modulus was used for the scaffold material.

H.6.1.4 Conclusions

Based on the results of the FE analysis, the bulk properties of the bone scaffold more closely matched the material properties of the TCP on the micro-level. This implies that the bulk mechanical

properties of the scaffold are more affected by the micro-level material and mechanical properties than on the nano-level. Therefore, manufacturing control variables for injection molded TCP scaffolds should be selected based on their effect on the micro-level mechanical and material properties of the intended scaffold design. Future modeling is needed to determine if this pattern holds for multiple sintering temperatures and different TCP porosity levels.

H.6.1.5 References

American College of Preventive Medicine, Am J Prev Med, 36(4):366-75, 2009.

Kasten P, et.al. Acta Biomaterialia. 4:1904-15,2008

Vivanco,J. et.al. J Mech Behav Biomed Mater. 4.8:2150-60, 2011

Vivanco,J. et.al. Biomat. Sci. 237:101-09, 2012

Vivanco,J.,et.al. J Mech Behav Biomed Mater.9:137-52, 2012

H.6.1.6 Figures

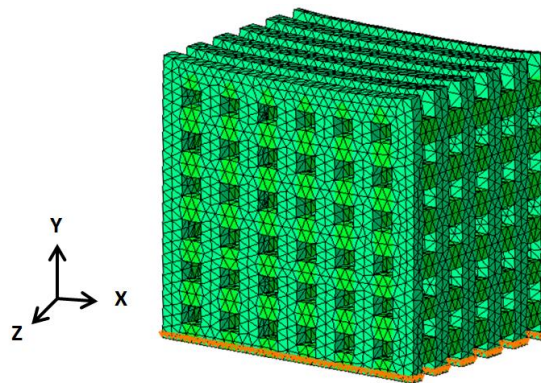**Figure H.6.1 - Von mises stress distribution with high stresses in yellow and lower stresses in green.**

H.7 American Society for Bone and Mineral Research 2015

Michael G Johnson[1,5], Luisa A. Meyer[2], Caitlyn J. Collins[2], Heidi-Lynn Ploeg[2], Everett L. Smith[3], Robert D. Blank[4,5] and Karen E. Hansen[1]

University of Wisconsin Department of Medicine[1], Department of Mechanical Engineering[2], Department of

Population Science[4], Medical College of Wisconsin[5] and William S. Middleton Veterans Hospital (GRECC),

Madison, WI[6].

H.7.1 Endothelin 1 Signaling is Required for SOST and IGF1 Secretion in Response to Mechanical Load

Previously we demonstrated that addition of exogenous big endothelin to *ex vivo* cultured bovine bone or application of -2000 µε elicits similar biochemical and physical responses, change in apparent elastic modulus (E_{app}), mineral apposition rate and secretion of PGE2. We hypothesized that endothelin (ET1) signaling was required for physical and biochemical responses of bone to mechanical load. To test this hypothesis, we conducted a 2x2 factorial trial of daily mechanical loading (-3000 µε, 120 cycles daily) and 10 □M BQ-123, an endothelin receptor A (ET_A) antagonist. Forty-eight human, trabecular bone cores (5 mm h x 10 mm d) were obtained from 2 male donors undergoing hip replacement. Donor cores and E_{app} were blocked to blocked to equivalency. The cores were maintained in bioreactors for 25 days post initiation of treatment. There were four groups: control (CC), control+BQ-123 (CB), load+control (LC) and load+BQ-123 (LB). Each specimen was tested quasi-statically with a maximal compression of ~4000 µε on days 0 and 25 of the study to measure E_{app}. Culture medium from each sample was analyzed for secretion of IGF1, SOST and ET1 on days 0, 8, 11, 18, and 25. Biochemical data over time were analyzed by Wilcoxin test, followed by paired analysis by Kruskal-Wallace. There were significant differences in IGF1, SOST and ET1 secretion over time and between the LC and LB groups with the LB group having increased secretion of SOST and ET1 and decreased secretion of IGF1. The percent change in apparent elastic modulus over the duration of the experiment was not significantly different between groups; however, the LC group tended to be higher than the other groups. The increase in ET1 secretion in the CB and LB groups indicates the presence of a feedback loop. The decrease in SOST secretion in the LC group is similar to the change in SOST seen *in vivo* in response to mechanical load. Blockade of ET1 signaling prevents the decrease in SOST secretion in response to mechanical load.

The increase in IGF1 secretion in response to mechanical load and the decrease in secretion seen when ET1 signaling is blocked suggest that ET1 signaling interacts with pathways that respond to mechanical load. This is the first study to show that autocrine ET1 signaling is required for response to mechanical load in human trabecular bone cores and that ET1 signaling is required for transduction of mechanical into biochemical signals during the anabolic response of bone to mechanical load.

H.8 Orthopaedic Research Society 2016

Luisa A. Meyer[1], Michael G. Johnson [1], Everett L. Smith[1], Matthew W. Squire[2], Karen E. Hansen[1,2], Robert D. Blank[3,4], Heidi-Lynn Ploeg[1]

[1]University of Wisconsin – Madison, Madison, WI, [2]University of Wisconsin Hospital and Clinics, Madison, WI, [3]Medical College of Wisconsin, Milwaukee, WI, [4]The Clement J. Zablocki VA Medical Center, Milwaukee, WI

H.8.1 Human Trabecular Bone Response to Mechanical Load is Dependent on Endothelin-1 Signaling

H.8.1.1 Introduction

Fifty five percent of adults older than 50 years are affected by or at risk for osteoporosis—a systemic skeletal disease causing deterioration of bone tissue and associated with a high mortality risk [1]. It is important to understand bone biomechanical behavior to promote bone health throughout aging, prevent fractures, and improve treatment options. While it is widely recognized that mechanical loading promotes bone modeling, remodeling, and homeostasis, the interactions of the mechanotransduction pathways are not as well understood [2]. Research has demonstrated that the WNT signaling pathway, the activity of which is indicated by secretion of certain genes including endothelin (ET1) and sclerostin (SOST), plays a critical role in regulating mechanotransduction [3]. SOST is a WNT signaling antagonist and is tonically secreted by osteocytes. The secretion of SOST is suppressed in the setting of mechanical loading. The purpose of this study was to investigate if pharmacological antagonism of the endothelin receptor A would inhibit relevant mechanotransduction pathways leading to bone modeling and

remodeling in human trabecular bone. The hypothesis was that ET1 signaling was essential for physical and biochemical responses of bone to mechanical loading.

H.8.1.2 Methods

The study hypothesis was tested by conducting a 2x2 factorial trial whereby human trabecular bone cores were subjected to daily mechanical loading (-3000 µε, 120 cycles daily) and 10 µM BQ-123, an endothelin receptor A antagonist. Using a protocol approved by the University of Wisconsin – Madison Institutional Review Board and after acquiring informed consent, 48 cores (5 mm x 10 mm) were obtained from 2 donors (1 male, 1 female) undergoing total hip arthroplasty. Cores were assigned to groups according to block randomization based on the donor and apparent elastic modulus (E_{app}) on day 1. The cores were maintained in individual bioreactors for 25 days post initiation of treatment. There were four groups: control (CC), control+BQ-123 (CB), load+control (LC) and load+BQ-123 (LB). Each specimen was tested quasi-statically with a maximal bulk compression of 4000 µε on days 1,8,15, and 22 of the study to measure E_{app}. Culture medium from each sample was analyzed for secretion of insulin-like growth factor (IGF1), SOST, and ET1 on days 0, 8, 11, 18, and 25. Biochemical data were analyzed by Kruskal-Wallace tests, followed by paired analysis via Wilcoxon tests.

H.8.1.3 Results

Significant differences were found in IGF1, SOST and ET1 secretion over time and between the LC and LB groups. The LB group showed increased secretion of SOST and ET1 and decreased secretion of IGF1. The percent change in E_{app} over the duration of the experiment was not significantly different between groups, however, the mean percent change in E_{app} in the LC group (37.4±18.2 %, p=0.096) tended to be higher than the other groups (CC 24.5%, CB 13.3%, LB 31.2%).

H.8.1.4 Discussion

This is the first study to show that autocrine ET1 signaling is required for response to mechanical load in human trabecular bone cores and that ET1 signaling is required for transduction of mechanical into biochemical signals during the anabolic response of bone to mechanical load. The results of the study show that blockade of ET1 signaling is associated with an increase in SOST secretion in response to mechanical load. Increases in IGF1 secretion in response to mechanical load and the decrease in secretion when ET1 signaling is blocked suggest that ET1 signaling interacts with pathways that respond to mechanical load. The increase in ET1 secretion in the CB and LB groups indicates the presence of a feedback loop. The decrease in SOST secretion in the LC group is similar to the change in SOST seen *in vivo* in response to mechanical load [4]. Study limitations include the variability observed among the samples which was likely caused by inherent variability in trabecular tissue from hip arthroplasty patients, and well-documented limitations of compression testing of bone cores.

H.8.1.5 Significance

The presented study examines the role of ET1 signaling in the physical and biochemical response of human trabecular bone to mechanical loading to better understand interactions of factors in the bone mechanotransduction pathways. The blockade of ET1 pathways inhibits bone response to mechanical loading as shown by decreased secretion in relevant biochemical factors and limited increases in elastic modulus.

H.8.1.6 References

[1] American College of Preventive Medicine, American Journal of Preventive Medicine, 36(4):366-75, 2009

[2] Klein-Nulend J, *et al*, Bone, 2013;54: 182-90

[3] Robling, AG, *et al*, Critical Reviews in Eukaryotic Gene Expression, 2009, 19(4): 319-38.

[4] Robling, AG, *et al*, Journal of Biological Chemistry, 2008, 283(9): 5866-75.

H.8.1.7 Acknowledgements

H.8.1.8 Images and Tables
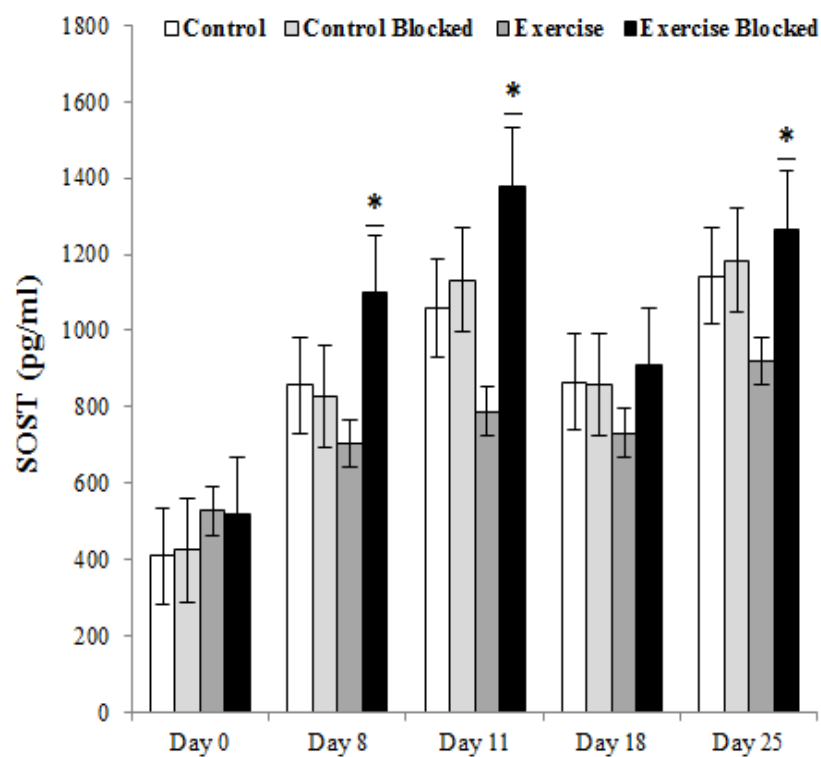
Figure H.8.18 - SOST secretion over duration of experiment. Asterisks indicate significant increase from baseline between the LB and the CL groups (α=0.05).
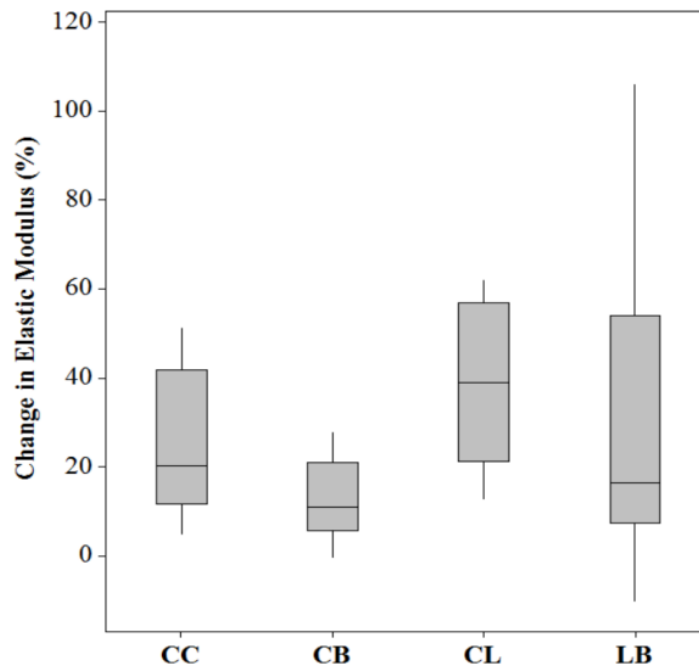
Figure H.8.2 – Change in E_{app} between days 1 and 22. Graph shows medians, first and third quartiles, and the lowest/highest datum within 1.5 interquartile lower/higher range.

H.9 European Congress of Biomechanics 2016

Luisa A. Meyer(1), Dalton J. Hess(1), Michael G. Johnson(1), Everett L. Smith(1), Karen E. Hansen(2), Heidi-Lynn Ploeg(1)

1. University of Wisconsin – Madison, United States 2. University of Wisconsin Hospital and Clinics

H.9.1 Using Morphological and Biochemical Factors to Predict Human Trabecular Bone Stiffness

H.9.1.1 Introduction

Fifty percent of women older than 50 years will sustain an osteoporotic fracture, which causes increased morbidity and mortality. Osteoporosis is a systemic skeletal disease that causes deterioration of bone tissue [1]. Understanding bone biomechanical behaviour is necessary to identify the causes and improve treatment of osteoporosis. Mechanical loading promotes bone modelling and remodelling. However, the additional contributions from mechanotransduction pathways and tissue level morphology are less understood [2]. Previous studies have investigated the ability of clinical computed tomography

(CT) imaging to non-invasively determine bone stiffness [3], but metrics ascertained from CT are not the only contributors to bone mechanical properties and do not encompass pathological factors. The purpose of this study was to investigate the impact of biochemical factors on bone stiffness in cores donated by two hip arthroplasty patients.

H.9.1.2 Methods

Twenty four human trabecular bone cores (5 mm x 10 mm) were prepared from bone removed during two hip arthroplasties (48 year old male, 68 year old female). The bone cores were allocated to two groups using block randomization based on the donor and apparent elastic modulus (E_{app}) determined on day 0. One group was the control group ("CC") and the other ("LC") was subjected to daily mechanical loading (-3000 µε, 120 cycles daily). The cores were maintained in individual bioreactors for 25 days. A quasi-static compression test of 4000 µε measured E_{app} on day 22. Culture medium from each sample was analysed for secretion of prostaglandin E2 (PGE2), insulin-like growth factor (IGF1), sclerostin (SOST) and endothelin-1 (ET1) on days 0, 8, 11, 18 and 25. At the end of the *ex vivo* study, the cores were imaged using a micro-CT scanner at a resolution of 10 µm to calculate the core volume, bone volume/total volume (BV/TV), bone surface area (BSA), trabecular thickness (T.Th), trabecular spacing (T.Sp), connectivity, degree of anisotropy (DoA) and the structural model index (SMI). The measured biochemical factors and the calculated morphological factors were then combined to generate a linear mixed effects model to predict the E_{app} of each bone core.

H.9.1.3 Results

Using a linear mixed effects model approach on the cores from each individual patient, the E_{app} of each core could be predicted by evaluating the bone morphology (BV, SA, T.Th, DoA, SMI) with a coefficient of determination of 94% (R^2-adj=83%, p=0.02). Modelling cores from both patients resulted in a much lower coefficient of determination (R^2=52%, p=0.12), but including biochemical factors

(SOST, DKK1, IGF1, PGE2) improved the accuracy of the model such that the prediction capabilities approached those of the individual models ($R^2 > 79\%$, p=0.006).
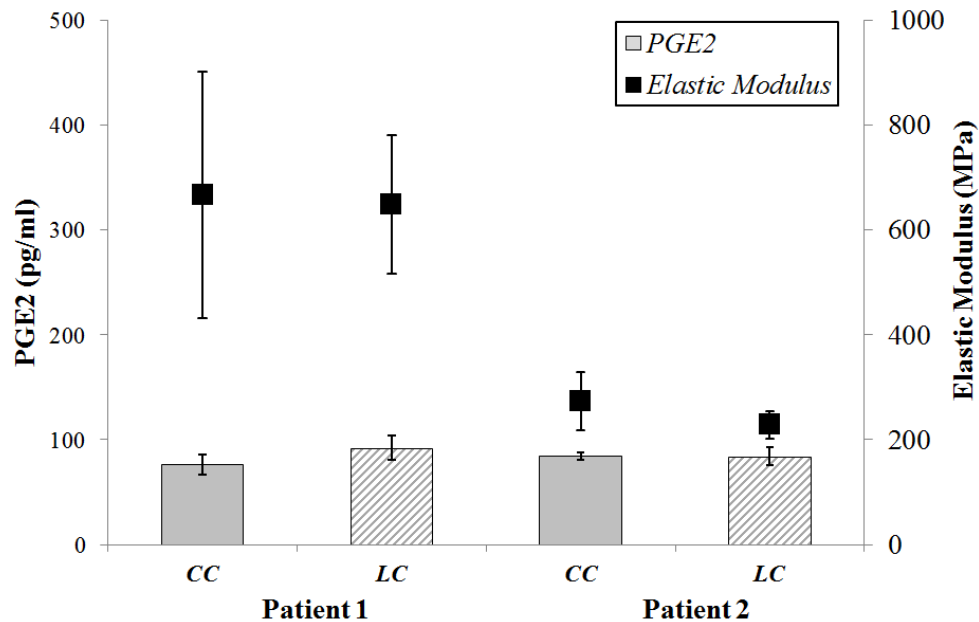
Figure H.9.1 - Measured PGE2 and elastic modulus (E_{app}) at the end of the experiment. Standard error is shown for each group.

H.9.1.4 Discussion

The study demonstrates that E_{app} can be predicted by CT-based metrics alone, but inclusion of biochemical factors improves ability to predict E_{app}. The study also demonstrates that individual bone cores behave uniquely. Additional studies should be conducted that include more bone cores, to determine if the number of factors contributing to the predictive model can be reduced and still accurately predict E_{app}.

H.9.1.5 References

1. Lim, S.L., *et al*, Am J Prev Med, 36(4):366-75, 2009

2. Klein-Nulend, J, *et al*, Bone, 54: 182-90, 2013

3. Liu, X.S., *et al*, J Bone Miner Res, 25(10): 2229-38, 2010

H.9.1.6 Acknowledgements

Appendix I

H. Curriculum Vitae

EDUCATION: *University of Wisconsin – Madison, Madison, WI*
Ph.D. Mechanical Engineering, expected May 2016, GPA: 3.82/4.0
Advisor: Professor Heidi-Lynn Ploeg
Thesis: Modeling and Testing Macro and Micro Mechanical Properties of *Ex Vivo* Trabecular Bone

M.S. Biomedical Engineering, December 2012, GPA: 3.7/4.0
Advisor: Professor Heidi-Lynn Ploeg
Thesis: *Ex vivo* Testing of Live Trabecular Bone Using ZETOS Bone Loading System and Bioreactor

B.S. Biomedical Engineering, May 2011, GPA: 3.08/4.0
Focus: Biomechanics
Biology in Engineering Certificate

Awards and Honors:
Interdisciplinary Research Competition Funding, September 2015-May 2016
Student Research Travel Grant - Conference Presentation Funds, September 2015
Outstanding Poster Award, Symposium on Therapeutics Discovery and Development, April 2015
Mechanical Engineering Graduate School Funding, September 2013-January 2014

RESEARCH EXPERIENCE: *University of Wisconsin – Madison, Madison, WI*
Research Assistant, Bone and Joint Biomechanics Lab, June 2011-present
Advisor: Heidi-Lynn Ploeg, PhD
Modeled and mechanically tested human trabecular bone to characterize its remodeling response.

Undergraduate Researcher, Biomedical Engineering, January 2010-May 2011
Advisor: Thomas Yen, PhD
Leader of a team that developed an automated lift platform to assist patients access an exam Table.

Undergraduate Researcher, Biomedical Engineering, September 2009-December 2009
Advisor: Wan-Ju Li, PhD
Client correspondent of team that designed live cartilage bioreactor for use with MRI.

Undergraduate Researcher, Ecology/Entomology, May 2009-August 2009
Advisor: Richard Lindroth, PhD
Determined the effects of browsing and nutrients on the fitness and defense of aspen trees
by studying physical and chemical responses

Undergraduate Researcher, Biomedical Engineering, January 2009-May 2009
Advisor: Paul Thompson, PhD
Client correspondent of team that designed and fabricated a low-cost grip dynamometer
that could provide digital user feedback for rehabilitation use.

Undergraduate Researcher, Biomedical Engineering, September 2008-December 2008
Advisor: Walter Block, PhD
Website manager for a team that simulated a magnetic field for a magnetic resonance
imaging (MRI) system given a coil design. The simulation was then used for further study
in the development of a miniature MRI setup that could be used for research purposes.

TEACHING
EXPERIENCE: *University of Wisconsin – Madison, Madison, WI*

Guest Lecturer, Therapeutic Medical Devices, February 2015
Presented 50 min lecture on current research in the area of bone deformity correction
devices, design of biomedical devices, and bioethics.

Teaching Assistant, Design of Machine Elements, January 2013-December 2014
Prepared and presented 50 min lectures for senior undergraduate students twice a week
throughout semester. Mentored and facilitated group work on student design projects.
Graded all students' written work including all exams.

Guest Lecturer, Therapeutic Medical Devices, March 2014
Presented 50 min lecture on prosthetic joints and bone implants. Discussed appropriate
device design steps, analytical methods, and current research in the field.

Teaching Assistant, Mechanics of Materials Laboratory, September 2012-May 2013
Prepared and presented 30 min lectures twice a week for sophomores and junior
undergraduate students. Generated course syllabus, homework assignments, laboratory
report rubrics, and exams. Facilitated and supervised laboratory activities using
mechanical testing equipment.

Teaching Assistant, Statics, January 2012-May 2012
Prepared and presented 50 min lectures twice a week throughout semester for freshman
undergraduate students. Mentored and facilitated group work on student design projects.
Graded all students' written work, including all exams.

RELATED
EXPERIENCE: *Silatronix, Inc., Madison, WI*

Research Associate, November 2012 – Present
Design experiments, conduct data analysis and present results periodically to technical
team. Support additional company research projects with data processing and analysis.
Coordinate Chemical Registration for global business development efforts.

Laboratory Technician, June 2010 – October 2012
Manufacture electrolytes and coin cells for research. Perform physical characterization test of solvents used to make coin cell electrolyte

University of Wisconsin – Madison, Madison, WI
Project Assistant, Senior Design Course Development, May 2015-August 2015
Part of a multi-disciplinary team tasked with re-designing the senior level design course for mechanical engineering students. Generated and refined course material on various topics including design thinking, technical communication, prototyping, and ethical and professional conduct.

Grader, Applied Thermal and Structural Finite Element Analysis, January 2013-May 2013
Graded student assignments on basic uses of finite element analysis and relevant applications.

Project Assistant, Limb Lengthening Device Design, May 2015
Contributed to the design of a limb deformity correction device for pediatric applications.

University of Wisconsin Hospital & Clinics, Madison, WI
Clinical Labs Student Help, March 2010 - April 2011
Responsible for processing internal medical billing and patient medical request forms and delivering them to proper destinations
Monitored functionality of lab equipment and contributed to general lab upkeep and cleanliness

SOFTWARE: MATLAB, Abaqus, ANSYS, SolidWorks, Minitab, Maple, Mimics, R, ImageJ, Geomagic, MIMS client

SKILLS/
EQUIPMENT: Mechanical testing apparati, Bio-Logic Science Instrumentation, Micro-CT, Load and displacement transducer, Differential scanning calorimetry, Machining, Biosafety

MEMBERSHIPS: European Society of Biomechanics (ESB), Institute for Clinical and Translational Research (ICTR)

PUBLICATIONS:
Thesis
Meyer, L. *Ex Vivo* Testing of Live Trabecular Bone Using ZETOS Bone Loading System and Bioreactor. MS Thesis. University of Wisconsin-Madison, Madison, WI, USA, December 2012.

Journal
Meyer, L.A., Johnson, M.G., Cullen, D.M., Vivanco, J.F., Blank, R.D., Ploeg, H-L, Smith, E.L. Combined exposure to big endothelin-1 and mechanical loading in bovine sternal cores promotes osteogenesis. *Bone*, 2016, volume 85, pages 115-122.

PRESENTATIONS:

Conference Posters:
Meyer, L.A., Johnson, M.G., Smith, E.L., Squire, M.W., Hansen, K.E., Blank, R.D., Ploeg, H-L. Human Trabecular Bone Response to Mechanical Load is Dependent on Endothelin-1 Signaling. Orthopaedic Research Society Annual Meeting. Orlando, Florida, March 2016. Poster.

Johnson, M.G., Meyer, L.A., Collins, C.J., Ploeg, H-L., Smith, E.L., Blank, R.D., Hansen, K.E. Endothelin 1 Signaling is Required for SOST and IGF1 Secretion in Response to Mechanical Load. 2015 ASBMR 37th Annual Meeting. Seattle, Washington, October 2015. Poster.

Meyer, L.A., Collins, C.J., Suresh,K., Ploeg, H-L., Predictive Model for Simulating Trabecular Bone Remodeling in Two Dimensions. 21st European Congress of Biomechanics. Prague, Czech Republic. July 2015. Poster.

Meyer, L.A., Johnson, M.G., Cullen, D.M., Vivanco, J.F., Blank, R.D., Ploeg, H-L, Smith, E.L. Big Endothelin-1 in Bovine Sternal Cores Causes Response Similar to Mechanical Loading. 2nd Annual Symposium on Therapeutics Discovery & Development. Madison, Wisconsin, April 2015. Poster.

Johnson M.G., Kristianti J., Konicke K., Gustavson A., Garbo R., Wang X., Yuan B., Meyer L.A., Collins C., Ploeg H-L, Smith E., Blank R., ECE1 dependent endothelin signaling regulates the production of IGF-1, the WNT signaling inhibitors sclerostin and DKK1, and is critical for osteogenesis, ASBMR 36th Annual Meeting, Houston, Texas, September 2014. Poster.

Meyer, L.A., Johnson, M.G., Cullen, D.M., Vivanco, J.F., Blank, R.D., Ploeg, H-L, Smith, E.L. Exposure to Big Endothelin-1 in Bovine Sternal Cores Mimics Aspects Mechanical Loading. 7th World Congress of Biomechanics. Boston, Massachussets, July 2014. Poster.

Cullen, DM., Alvarez, G, Meyer, L.A., Johnson, M, Vivanco, J. Ploeg, H-P, Smith, E. EMechanical loading and big endothelin-1 in trabecular bone cores. 2013 ASBMR 35th Annual Meeting. Baltimore, Maryland, October 2013. Poster.

Meyer, L.A., Johnson, M.G., Vivanco, J.F., Blank, R.D., Ploeg, H-L, Smith, E.L. Exposure to Big Endothelin-1 in Bovine Sternal Cores Mimics Mechanical Loading. 2012 ASBMR 34th Annual Meeting. Minneapolis, Minnesota, October 2012. Poster.

Meyer, L.A., Johnson, M.G., Vivanco, J.F., Blank, R.D., Ploeg, H-L, Smith, E.L. Exposure to Big Endothelin-1 in Bovine Sternal Cores Mimics Mechanical Loading. 2012 UW-Madison DOM Poster Session. Madison, Wisconsin, June 2012. Poster.

Conference Podiums:

Meyer, L.A., Collins, C.J., Suresh,K., Ploeg, H-L., Predictive Model for Simulating Human Bone Remodeling. Computer Methods in Biomechanics and Biomedical Engineering. Montreal, Quebec, Canada. September 2015, Oral.

Meyer, L.A., Vivanco, J.F., Ploeg, H-L., Macro-, Micro-, and Nano-level Mechanical Analysis of Injection Molded Beta Tricalcium Phosphate Bone Scaffolds. Computer Methods in Biomechanics and Biomedical Engineering. Montreal, Quebec, Canada. September 2015. Oral.